

SAINT PETERSBURG STATE UNIVERSITY
Department of Nuclear Physics Research Methods

22nd International School-Conference

**MAGNETIC RESONANCE AND ITS APPLICATIONS.
SPINUS**

Proceedings

31 March — 4 April, 2025
Saint Petersburg, Russia

Magnetic Resonance and its Applications. Spinus – 2025.

Proceedings. Saint Petersburg State University, **2025**. 267 pp.

Volume 22

ISSN 2542-2049

Reviewer of Proceedings: Vasily T. Lebedev, Doctor of Physics and Mathematics, Head of Laboratory of Neutron Physicochemical Research, PNPI RAS

Schola Spinus



**22nd International School-Conference
MAGNETIC RESONANCE AND ITS APPLICATIONS
SPINUS-2025**

ORGANIZING COMMITTEE

Chairman	Prof. Denis Markelov, SPSU
Vice-chairman	M. Sc. Alexandr Ievlev, researcher, SPSU
Committee members	Dr. Andrey Egorov, associate professor, SPSU Dr. Andrey Komolkin, associate professor, SPSU Prof. Marina Shelyapina, SPSU Dr. Nadezhda Sheveleva, senior teacher, SPbU Dr. Pavel Kupriyanov, associate professor, GTU (Gebze, Turkey) M. Sc. Timofey Popov, SPSU
Layout of proceedings	M. Sc. Aleksandra Koroleva
Reviewer of Proceedings	Vasily T. Lebedev, Doctor of Physics and Mathematics, Head of Laboratory of Neutron Physicochemical Research, PNPI RAS

CONTACTS

1, Ulyanovskay st., Peterhof, 198504, St. Petersburg, Russia
Department of Nuclear Physics Research Methods
St. Petersburg State University

Tel.: +7-953-350-0640
E-mail: spinus@spinus.spb.ru
Website: spinus.spb.ru

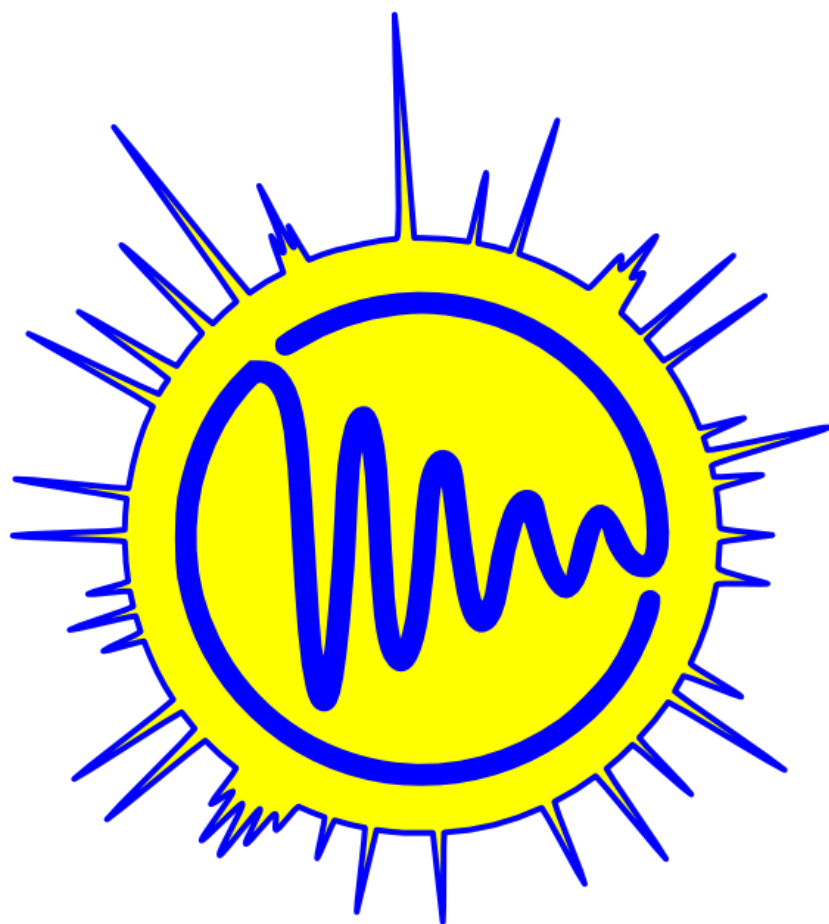
PROGRAM COMMITTEE

SCIENTIFIC ADVISER OF THE SCHOOL-CONFERENCE

Vladimir Chizhik	Honored Scientist of Russian Federation Honorary Professor of Saint Petersburg State University
------------------	--

ADVISORY BOARD

Yu. M. Bunkov	Professor, Russian Quantum Center, Moscow, Russia
C. Cabal	Merit researcher, Cuban Neuroscience Center, Cuba.
V. I. Chizhik	Professor, St. Petersburg State University, Russia
S. V. Dvinskikh	Professor, Royal Institute of Technology, Stockholm, Sweden
L. Yu. Grunin	Associate Professor, CEO, Resonance Systems, Russia
Yu. A. Pirogov	Professor, Moscow State University, Russia
B. Rameev	Professor, Gebze Technical University, Turkey
M. S. Tagirov	Professor, Kazan Federal University, Russia
L. M. Varela	Professor, University Santiago de Compostela, Spain



SpinuS



Saint-Petersburg State University
spbu.ru



ELEMENT Company
element-msc.ru



Magicplot Systems, LCC
magicplot.com



TerraQuanTech, LCC

Contents

SCHEDULE.....	16
LECTURES	27
<i>Yury M. Bunkov, Aleksey N. Kuzmichev, Danila A. Samodelrin</i>	
Quantum self-oscillator based on magnon Bose-Einstein condensate.....	28
<i>Carlos Cabal-Mirabal, Evelio González-Dalmau</i>	
Wound healing rate and treatment effectiveness determined by MRI.....	30
<i>Elena V. Charnaya, Allisher A. Vasilev, Andrei V. Uskov, Denis Yu. Nefedov</i>	
Metals under nanoconfinement: NMR studies.....	33
<i>Vladimir I. Chizhik</i>	
A few little-known facts in the history of NMR in Russia and a couple of thoughts on unfortunate terminology in magnetic resonance.....	35
<i>Ilya D. Gridnev</i>	
Use of various NMR techniques in the study of mechanism of Rh-catalyzed asymmetric hydrogenation.....	38
<i>Abinaya Gayathri, Kumaravel Kaliaperumal, Thiruchelvi Ramakrishnan</i>	
Antiviral metabolite isolation and characterization from Acremonium sp (SIMATS2121) endophytic fungi from medicinal plant.....	41
<i>Daniil I. Kolokolov, Alexander E. Khudozhnikov, Ralf Ludwig</i>	
Hydrogen bonds types, strengths and dynamics in	42
<i>William S. Price</i>	
Accurate NMR Diffusion Measurements in Reacting Systems.....	43
<i>Bin Xia</i>	
DNA Binding Mechanism of the Virulence Regulator SarA of Staphylococcus aureus.....	44
ORAL REPORTS	47
<i>Nikolay V. Anisimov</i>	
MRI of wildlife	48
<i>Anastasia V. Batueva, Roman A. Babunts, Aleksandr S. Gurin, Daria D. Kramushchenko, Pavel G. Baranov</i>	
Registration of nickel and nitrogen spin centers signals by their interactions with negative NV centers in diamond by photoluminescence.....	50
<i>Georgii A. Bochkin, Sergey G. Vasil'ev, Elena I. Kuznetsova, Edward B. Fel'dman</i>	
Quantum entanglement in quasi-equilibrium states in NMR multi-pulse spin locking.....	52

<u>E.I. Boltenkova</u> , A.V. Bogaychuk, M.Yu. Volkov, A.M. Garaeva, E.M. Alakshin The hydrothermal treatment effect on the relaxivity of DyF ₃ nanoparticles colloidal solution	55
<u>Bystrov S. S.</u> , Kirilenko V. D, Zolotov D. R, Khrustalev A.A, Bystrov E.S. Unified NMR: towards universally accessible NMR workflow with TQT “Nuclei”	57
Alexandr V. Ievlev, <u>Daria A. Chetverikova</u> , Nadezhda V. Pokhvishcheva, Maria A. Peshkova NMR Diffusometry for Studying Ionic Association in Plasticized Polymers.....	60
<u>G.A. Dolgorukov</u> , V.V. Kuzmin, A.S. Makarchenko Low field setup for DNP studies in stray field of superconducting magnet.....	63
Sergey V. Dvinskikh Ion dynamics in liquid crystal-electrolyte mixtures	65
<u>Dmitry S. Filimonenko</u> , Alexander P. Nizovtsev, Sergei Ya. Kilin, B. I. Stepanov Zero-field cross-relaxation resonances in ensembles of NV centers in diamond and fully optical magnetic field detection.....	66
<u>Aliya Galimova</u> , Hasan Pişkin, Rustem Khusnutdinov, Faik Mikailzade, Sergey A. Moiseev, Bulat Rameev Theory of two-stage quantum transduction based on use of magnetic material coupled to erbium-doped crystal.....	69
<u>Naira R. Gromova</u> , Andrei V. Komolkin, Amina D. Muratova, Denis A. Markelov Cell size dependence of diffusion properties of PAMAM dendrimers by MD simulations	73
<u>Leonid Grunin</u> , Yurii Grunin, Mariia Ivanova NMR Transverse Relaxation as the Tool for Structure and Thermodynamics Analysis	75
<u>Alexandr V. Ievlev</u> , Konstantin V. Tyutyukin, Oscar Cabeza, Luis M. Varela Study of complex ionic liquids according to NMR relaxation and diffusion measurements...77	77
<u>Alexander E. Khudozhnikov</u> , Daniil I. Kolokolov ² H NMR study of [P ₄₄₄ -D][OMs] and [N ₄₄₄ -D][OMs] ionic liquids	80
<u>Gaspar Kocharyan</u> , Makich Musaelyan Determination of anti-peroxyl radical capacity of flavonoids (quercetin, morin and rutin) by the kinetic EPR method with pulse reactant injection.	81
<u>P. Kupriyanov</u> , G. Mozhukhin, N.G. Sarıbaş, B. Rameev RFI suppression in the absence of magnetic resonance sensor shielding.....	83
<u>Galina Kupriyanova</u> , Mark Smirnov, Andrey Zyubin, A. Zozulya, Ivan Lyatun Study of the influence of Au nanoparticles of various shapes on the dynamics and structure of tyrosine using ¹ H NMR methods	86

<u>Néstor Juan Rodríguez de la Cruz</u> , Carlos Alberto Cabal Mirabal, Robert N. Muller, Sophie Laurent, Fabian Tamayo Delgado, Juan Carlos García Naranjo and Manuel Arsenio Lores Guevara Proton MRD profile analysis in Human Serum Albumin solutions: a two site exchange model approach	89
<u>Kiryutin A. S</u> , <u>Markelov D. A.</u> , Kosenko I. D, Osmanov V. K, Godovikov I. A, Yurkovskaya A. V. Spin Hyperpolarization Of ^{77}Se Nuclei Using Signal Amplification By Reversible Exchange (SABRE) At Microtesla Fields	92
<u>B.M. Mukhamadullin</u> , E.M. Alakshin, E.I. Boltenkova, A.M. Garaeva, A.V. Bogaychuk Study of fluoride nanoparticles nucleation processes by NMR in the capillary system	95
<u>Cengiz Okay</u> , A.Talha Demir, Bulat Rameev Investigation of Relaxation Times of Cotton Oil-Diesel Fuel Mixtures by TD-NMR	97
<u>Daria A. Pomogailo</u> , Anastasiya S. Kovalenko, Anton M. Nikolaev, Leonid M. Kustov, Olga A. Shilova Electron Spin Resonance of Fe-doped TiO_2 nanoparticles	100
<u>Salikhov K.M.</u> Further development of the theory of spin exchange in dilute solutions of paramagnetic particles	102
<u>Nikita A. Slesarenko</u> , Alexander V. Chernyak, Kyunsylu G. Khatmullina, Anna A. Slesarenko, Olga V. Yarmolenko Competitive ion transport in polymer gel electrolytes studied by NMR	104
<u>Mark Smirnov</u> , Galina Kupriyanova Influence of the shape of gold nanoparticles on the structural and dynamical properties of L-tyrosine.....	Ошибка! Закладка не определена.
<u>Alexander V. Snadin</u> , Alexey S. Kiryutin, Natalya N. Fishman, Nikita N. Lukzen Development of a new class of adiabatic inverting MCA pulses combining constant and offset-independent adiabaticity	107
<u>Milosh Ubovich</u> , Kirill A. Mukhin, Vladimir V. Matveev, Andrey V. Egorov, Vladimir I. Chizhik “Ionic Liquid EAN/ $\text{Al}(\text{NO}_3)_3/\text{H}_2\text{O}$ ” System Studied by NMR and Computational Methods	111
<u>Sergey G. Vasil’ev</u> , Elena I. Kuznetsova, Elizaveta I. Shipulya, Edward B. Fel’dman, Alexander I. Zenchuk Equation Chapter 1 Section 1 Lindblad dephasing relaxation and quantum entanglement in two-spin systems	117

<u>Ilya V. Yakovlev, Aleksandr V. Toktarev, Aleksandr A. Shubin, Evgeniy S. Papulovskiy, Olga B. Lapina</u> Silicon-enhanced incorporation of boron into AlPO-11 framework according to ^{11}B solid-state NMR	120
<u>Natalia P. Yevlampieva, Vasily T. Lebedev, Maria V. Popova, Mikhail A. Vovk, Alexander V. Shvidchenko, Biligma B. Tudupova, Victor I. Kuular</u> Magnetic relaxation properties of metal-carbon heterostructures	121
<u>Anna P. Yi, Ivan A. Trofimov, Oleg G. Salnikov, Andrey N. Pravdivtsev, Henri de Maissin, Eduard Y. Chekmenev, Jan-Bernd Hövener, Andreas B. Schmidt, Igor V. Koptuyug</u> Intra- and intermolecular transfer of parahydrogen-induced hyperpolarization via nuclear Overhauser effect induces RASER.....	124
<u>Pavel Yushmanov</u> Electrophoretic NMR and its application in studying the electro kinetic transport of water and methanol in Nafion membranes.....	127
<u>Zefirova P.M., Kadnikov M.V., Fetin P.A., Zorin I.M.</u> ^1H NMR spectroscopy application for assessment catalytic behavior of comb-like polyelectrolytes in Suzuki reaction	129
POSTER SESSION	132
<u>Artem S. Alexandrov, Daria L. Melnikova, Vladimir D. Skirda</u> Generator of arbitrary sequences of commands/pulses	133
<u>Omar Alkhuder, Mikhail A. Kostin, Peter M. Tolstoy</u> Exploring the Ability of the P=O Group to Form Multiple Hydrogen Bonds	134
<u>Alonso-Geli, Yamirka, López-Alexander, Rosmery, Lores-Guevara, Manuel A.</u> Physicochemical characterization of carbon-coated magnetic cobalt nanoparticles	137
<u>Andronenko S.I., Nikolaev A.M., Suharzhevsky S.M., Sinelnikov A.A., Kovalenko A.S., Abiev R.Sh, Ivanova A.G, Shilova O.A.</u> The FMR/EPR studies of magnetite/maghemite nanoparticles, synthesized by different methods.....	142
<u>Nikolay V. Anisimov, Pavel Tikhonov, Anna Hurshkainen</u> Construction of sensitivity maps for wireless coils using ^{19}F MRI.....	145
<u>Nikolay V. Anisimov, Arina A. Tarasova</u> Simultaneous detection of nuclei ^{13}C , ^{23}Na , ^{27}Al and ^{55}Mn at 0.5 Tesla.....	145
<u>Antonenko A.O., Charnaya E.V, Marchenkov V.V, Naumov S.V, Lee M.K, Chang L.J.</u> ^{125}Te NMR spectra in Td -phase WTe_2	149

<u>E.E. Batueva, A.R. Sharipova, E.N. Frolova, A.A. Sukhanov, O.A. Turanova, A.N. Turanov</u> Multifunctional Heptanuclear Iron Complex: Magnetic Properties and Potential Applications in MRI	152
<u>Valeriy V. Bezrodnyi, Sofia E. Mikhianiuk, Oleg V. Shavykin, Igor M. Neelov, Nadezhda N. Sheveleva and Denis A. Markelov</u> Molecular dynamics simulation of C ₆₀ /C ₇₀ fullerene complexes with peptide dendrimer containing histidine spacers	153
<u>K.V. Bozhenko, A.N. Utenyshev, L.G. Gutsev, S.M. Aldoshin, and G.L. Gutsev</u> Quantum-Chemical study of Interactions of Fe ₂ O _n (n=7, 9) Clusters with H ₂ and O ₂ Molecules	156
<u>Cheremensky S.O., Egorov A.V.</u> Microstructure and molecular mobility in the ternary LiCl-CsCl- H ₂ O system. A molecular dynamics simulation study	157
<u>Nina Djapic</u> Proton attached to nitrogen in porphyrins and tetrapyrroles	158
<u>Anastasia S. Dmitrieva, Boris P. Nikolaev, Ludmila Yu. Yakovleva, Viacheslav S. Fedorov, Maxim Shevtsov</u> Potential of NMR spectroscopy for assessing the hydrophobicity of microsphere cellulose carriers for spiking cancer cells	160
<u>E.V. Dmitrieva, G.V. Mamin, F.F. Murzakhanov, I.N. Gracheva, M.R. Gafurov, V.A. Soltamov</u> Analysis of hyperfine and quadrupole interactions in the first coordination sphere of ¹⁴ N in hexagonal boron nitride	163
<u>A.R. Gafarova, G.G. Gumarov, R.B. Zaripov, D.S. Rybin</u> Study of conformation of mechanically activated calcium gluconate irradiated with gamma quanta	166
<u>Galiakhmetov S.A., Mulloyarova V.V, Antonov A.S.</u> Influence of substitutes and chalcogen atom nature on the akylation of phosphine chalcogenides	168
<u>Vyacheslav E. Gonyalin, Polina V. Egorova, Natalia S. Garaeva, Marat M. Yusupov and Konstantin S. Usachev</u> NMR assignment of eucaryotic initiation translation factor 5A of <i>Candida albicans</i>	170
<u>Kristina S. Gorkovaia, Victoria V. Abzianidze, Alexander S. Bogachenkov, Denis V. Krivorotov, Leonid S. Chisti, Diana S. Suponina</u> NMR control of the synthesis of pharmaceutical intermediates	172
<u>Ilya A. Grishanovich, Semyon L. Shestakov, Alexander Yu. Kozhevnikov</u> The optimization of the conditions of 2D NMR spectra registration for the analysis of thermoplastic organic compounds in molten state	174

<i>Roman V. Haponchyk, Alexey B. Ustinov</i> Investigation of the magnonic nonlinear phase shifter based on forward volume spin waves	176
<i>Artem S. Igonin, Ekaterina I. Isaeva, Ivan A. Godovikov, Ruslan I. Baichurin</i> Effect of palladium(II) on NMR spectra of coordinated semicarbazones	179
<i>Dmitry Ivanov, Vladimir Skirda</i> Features of the study of the pore space of the core by the method of nuclear magnetic resonance	182
<i>Nataliya V. Karmanova, Aydar R. Yulmetov</i> Modelling localization of various statins within a POPC bilayer by molecular dynamics and metadynamics	185
<i>Daniil A. Khroshin, Alexey B. Ustinov</i> Modeling of spin-wave spectrum for YIG films at sub-THz frequencies	188
<i>Alexey Kiryutin, Danil Markelov, Alexandra Yurkovskaya</i> Determination of Rotational Correlation Time of and Iridium Dihydride Complex in Aqueous Medium by Means of NMR Relaxometry with High-resolution	190
<i>Andrei V. Komolkin, Natalia P. Yevlampieva, Alexandr V. Sokol, Olga L. Alikhanova, Alexandr V. Serbin, Mikhail A. Vovk</i> NMR $^1\text{H}/^{13}\text{C}$ study of biocompatible copolymer of divinyl ether and maleic anhydride	193
<i>S.I. Levit, M.V.Kadnikov, P.A.Fetin, I.M.Zorin</i> NMR analysis of surfactants characteristics based on methacrylic acid.	196
<i>Daria A. Malakhova, Alexandr V. Ievlev, Konstantin V. Tyutyukin</i> Study of intramolecular mobility in ionic liquid $[\text{Bmim}]_2\text{Cd}(\text{SCN})_4$ using NMR relaxation data.	198
<i>Daria Melnikova, Irina Nesmelova, Vladimir Skirda</i> Effect of the disulfide reducing agent TCEP on the translational mobility of α - and κ -casein and their ability to form supramolecular structures	201
<i>Daria L. Melnikova, Artem S. Alexandrov, Ruslan V. Arkhipov, Victor P. Arkhipov</i> NMR diffusometry and micellar solubilization using biological surfactants	204
<i>Yulianela Mengana Torres, Manuel Arsenio Lores Guevara, Lilian Somoano Delgado, Claudia Camila García Cruz, Yamirka Alonso Geli, Fabián Tamayo Delgado, Juan Carlos García Naranjo, Yomaidis Araujo Durán, Lidia Clara Suárez Beyries, Yanet Obregón Segura, Yasmin Estrada Garrido</i> Evaluation of plasma viscosity in patients with hyperviscosity syndrome using Proton Magnetic Relaxation	205

<u>Olga Mikhailovskaya, Anna Kuzminova, Anton Mazur, Anastasia Penkova, Mariia Dmitrenko</u> Modification approaches to the development of pervaporation sodium alginate-based membranes with enhanced properties	208
<u>Mikhailap M. V., Pelipko V. V., Gomonov K. A., Makarenko S. V.</u> Determination of the spirocyclopropanoxindole fine structure using NMR spectroscopy....	210
<u>Anna Mikulan, Roman Dubovenko, Mariia Dmitrenko, Anna Kuzminova, Anton Mazur, Anastasia Penkova</u> Novel blend cellulose nitrate/cellulose acetate ultrafiltration membranes for enhanced water treatment.....	212
<u>Minaeva V. Yu, Ozerova O. Yu, Makarenko S. V.</u> Determination of the structure of regioisomeric furan-containing naphthofuranes based on 1D and 2D NMR spectroscopy experiments	214
<u>Guzel A. Minnullina, Islam N. Garifullin, Sergey V. Efimov, Vladimir V. Klochkov</u> Conformational behavior of cyclic peptides cyclosporin C and alisporivir in acetonitrile and their interaction with Dy ³⁺ ions.....	217
<u>D.A. Mizyulin, A.V. Egorov</u> Hydrogen/deuterium isotope effects on the microstructure and molecular mobility in the aqueous solution of uropium nitrate. A molecular dynamics simulation study	220
<u>Polina A. Anufrieva, Sofia E.Mikhtaniuk, Alina S. Zaitseva, Valeriy V. Bezrodnyi, Emil I. Fatullaev, Igor M. Neelov</u> Computer simulation of interaction of fullerenes C60 with short amyloid peptides	221
<u>Alexey V. Vakulyuk, Sofia E.Mikhtaniuk, Valeriy V. Bezrodnyi, Emil I. Fatullaev, Igor M. Neelov</u> Investigation of interaction of cyclic peptide with short amyloid peptides by computer simulation.....	224
<u>Yaroslav Yu. Marchenko, Vyacheslav A. Ryzhov, Vladimir V. Deriglazov, Anastasia S. Dmitrieva, Anastasia V. Nikitina, Yuriy V. Bogachev</u> Investigation of magnetic characteristics of magnetite nanoparticles in various organic shells.....	227
<u>Pilipenko I. A, Ozerova O.Yu, Makarenko S. V.</u> Application of ¹ H- ¹³ C HMBC NMR spectroscopy for identification of regioisomeric polycyclic dihydrofurans.....	230
<u>Julia A. Pronina, Alexander V. Stepanov, Stanislav I. Selivanov</u> The spiro[1-azabicyclo[3.2.0]heptane] frameworks: structures determination using NMR methods	232
<u>Julia A. Pronina, Ekaterina V. Berezhnaya, Alexander V. Stepanov, Stanislav I. Selivanov</u> The spiro[1-azabicyclo[3.3.0]octane] frameworks: structures determination using NMR methods	235

<u>Andrey M. Rochev, Vladimir M. Mikushev, Elena V. Charnaya, Denis Yu. Nefedov</u> Different mechanisms of spin-lattice relaxation of gallium in semi-insulator GaAs	238
<u>Margarita A. Sadovnikova, George V. Mamin, Darya V. Shurtakova, Margarita A. Goldberg, Nataliya V. Petrakova, Vladimir S. Komlev, Marat R. Gafurov</u> Effect of rare earth impurities on structural properties of calcium phosphate-based materials by EPR spectroscopy	241
<u>A. Samadov, I.A. Zvereva, G.A. Valkovskiy, M.G. Shelyapina, V. Petranovskii</u> Effect of alkaline treatment on structure, morphology, CO ₂ sorption of mesoporous ZSM-5 zeolites	243
<u>A.N. Sashina, A.V. Filippov, A.V. Khaliullina</u> Phase structure and molecular mobility of drug delivery systems based on liposomes with Pluronics by nuclear magnetic resonance method	246
<u>G.A. Shonin, I.A. Balova, A.I. Govdi</u> Synthesis of 4,5-diethynyl-1,2,3-triazoles and structure analysis by NMR spectroscopy	248
<u>Artyom S. Tarasov, Anastasia F. Petrova, Sergey V. Efimov, Vladimir V. Klochkov</u> Spectral characteristics of cyclosporin G and L in deuterated acetonitrile with water solution determined by NMR spectroscopy	250
<u>Anastasia A. Troshkina, Dmitriy S. Blokhin, Vladimir V. Klochkov</u> The structural features of the fibril-forming peptide SEM2(49-107) by NMR spectroscopy and its role in enhancing HIV activity	253
<u>Konstantin V. Tyutyukin, Alexandr V. Ievlev</u> Study of slow molecular motions by NMR relaxation.	255
<u>Valentina V. Yakovleva, Kirill V. Likhachev, Marina V. Muzafarova, Anna P. Bundakova, Roman A. Babunts, Sergey V. Titkov, Pavel G. Baranov</u> Study of NV ⁻ centers in natural diamonds (carbonado) by micron scale scanning spectroscopy	257
<u>Ekaterina M. Zaitseva, Aydar R. Yulmetov, Daria A. Osetrina, Dmitriy S. Blokhin</u> NMR study of the fibril-forming peptide SEM(86-107)	259
POEMS ABOUT SCHOOL.....	262
AUTHOR INDEX.....	264

Schedule

22nd International School-Conference

«Magnetic Resonance and its Applications.

Spinus-2025»

31 March - 4 April, 2025

St. Petersburg



MONDAY –31 March, 2025	
Chairman	Prof. Denis Markelov (Saint-Petersburg, Russia)
10:00-10:10	Opening
10:10-10:40	Vladimir Chizhik (Saint Petersburg, Russia) Lecture: A few little-known facts in the history of NMR in Russia and a couple of thoughts on unfortunate terminology in magnetic resonance
10:40-11:20	Bin Xia (Beijing, China) Lecture: DNA Binding Mechanism of the Virulence Regulator SarA of <i>Staphylococcus aureus</i>
11:20-11:40	Ekaterina Boltchenkova (Kazan, Russia) Oral report: The hydrothermal treatment effect on the relaxivity of DyF ₃ nanoparticles colloidal solution
11:40 – 12:10	‘COFFEE’ BREAK
Chairman	Prof. Cabal-Mirabal Cabal (Havana, Cuba)
12:10-12:50	Kumaravel Kaliaperumal (Chennai, India) Lecture: Antiviral metabolite isolation and characterization from <i>Acremonium</i> sp (SIMATS2121) endophytic fungi from medicinal plant
12:50-13:10	Galina Kupriyanova (Kaliningrad, Russia) Oral report: Study of the influence of Au nanoparticles of various shapes on the dynamics and structure of tyrosine using ¹ H NMR methods.

13:10 – 13:25	Mark Smirnov (Kaliningrad, Russia) Oral report: Influence of the shape of gold nanoparticles on the structural and dynamical properties of L-tyrosine
13:25 – 14:05	Ilya Gridnev (Moscow, Russia) Lecture: Use of various NMR techniques in the study of mechanism of asymmetric hydrogenation
14:05 – 15:10	LUNCH
Chairman	Prof. Galina Kupriyanova (Kaliningrad, Russia)
15:10 – 15:50	Carlos Cabal-Mirabal (Havana, Cuba) Lecture: Wound healing rate and treatment effectiveness determined by MRI
15:50 – 16:10	Nikolay Anisimov (Moscow, Russia) Oral report: MRI of wildlife
16:10 – 16:25	Anna Yi (Novosibirsk, Russia) Oral report: Intra- and intermolecular transfer of parahydrogen-induced hyperpolarization via nuclear Overhauser effect induces RASER
16:25 – 16:40	Manuel Arsenio Lores Guevara (Santiago de Cuba, Cuba) Oral report: Proton MRD profile analysis in Human Serum Albumin solutions: a two site exchange model approach
16:40 – 17:00	Leonid Grunin (Yoshkar-Ola, Russia) Lecture: NMR Transverse Relaxation as the Tool for Structure and Thermodynamics Analysis
17:00 – 17:20	Cengiz Okay (Istanbul, Turkey) Oral report: Investigation of Relaxation Times of Cotton Oil-Diesel Fuel Mixtures by TD-NMR
17:20 – 17:40	Dmitry Filimonenko (Minsk, Belarus) Oral report: Zero-field cross-relaxation resonances in ensembles of NV centers in diamond and fully optical magnetic field detection
18:30 – 22:00	Welcome Party
TUESDAY – 1 April, 2025	
Chairman	Prof. Marina Shelyapina (Saint-Petersburg, Russia)
10:00 – 10:40	William Price (Sydney, Australia) Lecture: Accurate NMR Diffusion Measurements in Reacting Systems
10:40 – 10:55	Bulat Mukhamadullin (Kazan, Russia) Oral report: Study of fluoride nanoparticles nucleation processes by NMR in the capillary system
10:55 – 11:10	Polina Zefirova (Saint-Petersburg, Russia) Oral report: ^1H NMR spectroscopy application for assessment catalytic behavior of comb-like polyelectrolytes in Suzuki reaction
11:10 – 11:25	Naira Gromova (Saint-Petersburg, Russia) Oral report: Cell size dependence of diffusion properties of PAMAM dendrimers by MD simulations

11:25 – 11:40	Milosh Ubovich (Saint-Petersburg, Russia) Oral report: “Ionic Liquid EAN/Al(NO ₃) ₃ /H ₂ O” System Studied by NMR and Computational Methods
11:40 – 12:10	‘COFFEE’ BREAK
Chairman	Prof. Peter Tolstoy (Saint-Petersburg, Russia)
12:10 – 12:50	Daniil Kolokolov (Novosibirsk, Russia) Lecture: Hydrogen bonds types, strengths and dynamics in hydroxyl- and carboxyl-functionalized ionic liquids
12:50 – 13:10	Alexander Khudozhitkov (Novosibirsk, Russia) Oral report: ² H NMR study of [P444-D][OMs] and [N444-D][OMs] ionic liquids
13:10 – 13:25	Daria Chetverikova (Saint Petersburg, Russia) Oral report: NMR Diffusometry for Studying Ionic Association in Plasticized Polymers
13:25 – 13:45	Alexandr Ievlev (Saint Petersburg, Russia) Oral report: Study of complex ionic liquids according to NMR relaxation and diffusion measurements
13:45 – 14:05	Nikita Slesarenko (Chernogolovka, Russia) Oral report: Competitive ion transport in polymer gel electrolytes studied by NMR
14:05 – 15:10	LUNCH
Chairman	Prof. Denis Markelov (Saint-Petersburg, Russia)
15:10– 16:20	Oral blitz reports of young scientists
16:20-16:30	CONFERENCE PHOTO
16:30-18:30	Oral blitz reports of young scientists POSTER SESSION I
	WEDNESDAY – 2 April, 2025
11:00 – 14:00	Excursion to the Grand Menshikov Palace
14:00 – 15:00	LUNCH
15:00– 17:00	Excursion to Magnetic Resonance Research Centre of St. Petersburg State University

	THURSDAY – 3 April, 2025
Chairman	Dr. Andrei Egorov (Saint-Petersburg, Russia)
10:00 – 10:40	Elena Charnaya (Saint Petersburg, Russia) Lecture: Metals under nanoconfinement: NMR studies
10:40 – 11:00	Ilya Yakovlev (Novosibirsk, Russia) Oral report: Silicon-enhanced incorporation of boron into AlPO-11 framework according to ^{11}B solid-state NMR
11:00– 11:15	Danil Markelov (Novosibirsk, Russia) Oral report: Hyperpolarization of ^{77}Se nuclei using signal amplification by reversible exchange (SABRE) at microtesla fields
11:15– 11:30	Allisher Vasilev (Saint Petersburg, Russia) Oral report: Directional solidification in gallium under strong magnetic field: NMR studies
11:30– 11:45	Aliya Galimova (Kazan, Russia) Oral report: Theory of two-stage quantum transduction based on use of magnetic material coupled to erbium-doped crystal
11:45 – 12:10	‘COFFEE’ BREAK
Chairman	Prof. Elena Charnaya (Saint-Petersburg, Russia)
12:10 – 12:40	Kev Salikhov (Kazan, Russia) Oral report: Further development of the theory of spin exchange in dilute solutions of paramagnetic particles
12:40 – 13:00	Kocharyan Gaspar (Yerevan, Armenia) Oral report: Determination of anti-peroxyl radical capacity of flavonoids (quercetin, morin and rutin) by the kinetic EPR method with pulse reactant injection.
13:00– 13:15	Daria Pomogailo (Moscow, Russia) Oral report: Electron Spin Resonance of Fe-doped TiO_2 nanoparticles
13:15 – 13:30	Anastasia Batueva (Saint Petersburg, Russia) Oral report: Registration of nickel and nitrogen spin centers signals by their interactions with negative NV centers in diamond by photoluminescence
13:30 – 14:10	Alexandr Trifonov (CIQTEK, Moscow, Russia) Lecture: The development and results of magnetic resonance technology and instruments EPR Round Table and connected demonstration
14:10 – 15:10	LUNCH
Chairman	Prof. Denis Markelov (Saint-Petersburg, Russia)
15:10– 16:30	Oral blitz reports of young scientists

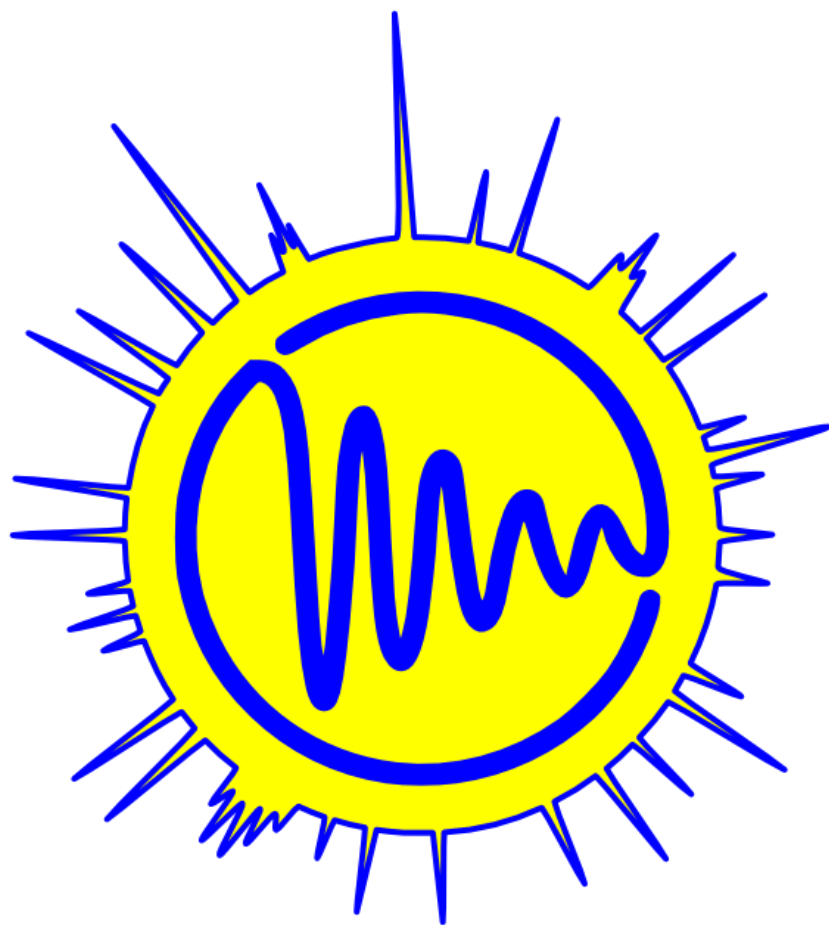
16:30-18:30	POSTER SESSION II
19:00– 23:00	Conference Dinner
	FRIDAY – 4 April, 2025
Chairman	Prof. Yury Bunkov (Moscow, Russia)
10:10 – 10:30	Sergey Dvinskikh (Stockholm, Sweden) Oral report: Ion dynamics in liquid crystal-electrolyte mixtures
10:30 – 10:50	Sergei Bystrov (Saint Petersburg, Russia) Oral report: Unified NMR: towards universally accessible NMR workflow with TQT “Nuclei”
10:50 – 11:10	Pavel Kupriyanov (Gebze, Turkey) Oral report: RFI suppression system for NQR detection in unshielded conditions
11:10– 11:25	Alexander Snadin (Novosibirsk, Russia) Oral report: Development of a new class of adiabatic inverting MCA pulses combining constant and offset-independent adiabaticity
11:25 – 11:40	Gleb Dolgorukov (Kazan, Russia) Oral report: Low field setup for DNP studies in stray field of superconducting magnet
11:40 – 12:10	‘COFFEE’ BREAK
Chairman	Dr. Andrei Komolkin (Saint-Petersburg, Russia)
12:10 – 12:30	Pavel Yushmanov (Stockholm, Sweden) Oral report: Electrophoretic NMR and its application in studying the electrokinetic transport of water and methanol in Nafion membranes
12:30 – 12:50	Natalia Yevlampieva (Saint-Petersburg, Russia) Oral report: Magnetic relaxation properties of metal-carbon heterostructures
12:50 – 13:10	Sergey Vasil'ev (Chernogolovka, Russia) Oral report: Lindblad dephasing relaxation and quantum entanglement in two-spin systems
13:10 – 13:30	Georgii Bochkina (Chernogolovka, Russia) Oral report: Quantum entanglement in quasi-equilibrium states in NMR multi-pulse spin locking
13:30 – 14:10	Yury Bunkov (Moscow, Russia) Lecture: Quantum self-oscillator based on magnon Bose-Einstein condensate
14:10 – 15:10	LUNCH
15:10– 15:40	Awarding, Closing and “Related Phenomena”

POSTER SESSION I (TUESDAY, 16:30-18:30)			
1	Omar	Alkhuder	Exploring the Ability of the P=O Group to Form Multiple Hydrogen Bonds
2	Anastasiia	Antonenko	^{125}Te NMR spectra in Td-phase WTe_2
3	Ekaterina	Batueva	Multifunctional Heptanuclear Iron Complexes: Magnetic Properties and Potential Applications in MRI
4	Aleksandra	Sashina	Phase structure and molecular mobility of drug delivery systems based on liposomes with Pluronics by nuclear magnetic resonance method
5	Vyacheslav	Gonyalin	NMR assignment of eucaryotic initiation translation factor 5A of <i>Candida albicans</i>
6	Anastasia	Dmitrieva	Potential of NMR spectroscopy for assessing the hydrophobicity of microsphere cellulose carriers for spiking cancer cells
7	Ekaterina	Dmitrieva	Analysis of hyperfine and quadrupole interactions in the first coordination sphere of ^{14}N in hexagonal boron nitride
8	Albina	Gafarova	Study of conformation of mechanically activated calcium gluconate irradiated with gamma quanta
9	Ekaterina	Zaitseva	NMR Study of the fibrile-forming peptide SEM1(86-107)
10	Kristina	Gorkovaia	NMR control of the synthesis of pharmaceutical intermediates
11	Ilya	Grishanovich	The optimization of the conditions of 2D NMR spectra registration for the analysis of thermoplastic organic compounds in molten state
12	Roman	Haponchyk	Investigation of the magnonic nonlinear phase shifter based on forward volume spin waves
13	Artem	Igonin	Effect of palladium(II) on NMR spectra of coordinated semicarbazones
14	Dmitry	Ivanov	Features of the study of the pore space of the core by the method of nuclear magnetic resonance
15	Natalya	Karmanova	Modelling localization of various statins within a POPC bilayer by molecular dynamics and metadynamics
16	Daniil	Khroshin	Modeling of spin-wave spectrum for YIG films at sub-THz frequencies
17	Savelii	Levit	NMR analysis of surfactants characteristics based on methacrylic acid.
18	Daria	Malakhova	Study of intramolecular mobility in ionic liquid $[\text{BMIM}]_2\text{Cd}(\text{SCN})_4$ using NMR relaxation data.
19	Daria	Melnikova	Effect of the disulfide reducing agent TCEP on the translational mobility of α - and κ -casein and their ability to form supramolecular structures
20	Daria	Melnikova	NMR diffusometry and micellar solubilization using biological surfactants
21	Artem	Alexandrov	Generator of arbitrary sequences of commands/pulses
22	Sergey	Andronenko	The FMR/EPR studies of magnetite/maghemite nanoparticles, synthesized by different methods

23	Nikolay	Anisimov	Simultaneous detection of nuclei ^{13}C , ^{23}Na , ^{27}Al and ^{55}Mn at 0.5 Tesla
24	Nikolay	Anisimov	Construction of sensitivity maps for wireless coils using ^{19}F MRI
25	Konstantin	Bozhenko	Quantum-Chemical study of Interactions of Fe_2O_n ($n=7, 9$) Clusters with H_2 and O_2 Molecules
26	Nina	Djapic	Proton attached to nitrogen in porphyrins and tetrapyrroles
27	Alexey	Kiryutin	Determination of Rotational Correlation Time of and Iridium Dihydride Complex in Aqueous Medium by Means of NMR Relaxometry with High-resolution

POSTER SESSION II (THURSDAY, 16:30-18:30)			
1	Olga	Mikhailovskaya	Modification approaches to the development of pervaporation sodium alginate-based membranes with enhanced properties
2	Marina	Mikhalap	Determination of the spirocyclopropanoxindole fine structure using NMR spectroscopy
3	Anna	Mikulan	Novel blend cellulose nitrate/cellulose acetate ultrafiltration membranes for enhanced water treatment
4	Veronika	Minaeva	Determination of the structure of regioisomeric furan-containing naphthofuranes based on 1D and 2D NMR spectroscopy experiments
5	Guzel	Minnullina	Conformational behavior of cyclic peptides cyclosporin C and alisporivir in acetonitrile and their interaction with Dy^{3+} ions
6	Dmitriy	Mizyulin	Hydrogen/deuterium isotope effects on the microstructure and molecular mobility in the aqueous solution of europium nitrate. A molecular dynamics simulation study
7	Ilya	Pilipenko	Application of ^1H - ^{13}C HMBC NMR spectroscopy for identification of regioisomeric polycyclic dihydrofurans
8	Julia	Pronina	The spiro[1-azabicyclo[3.2.0]heptane] frameworks: structures determination using NMR methods
9	Julia	Pronina	The spiro[1-azabicyclo[3.3.0]octane] frameworks: structures determination using NMR methods
10	Andrej	Rochev	Different mechanisms of spin-lattice relaxation of gallium in semi-insulator GaAs
11	Margarita	Sadovnikova	Effect of rare earth impurities on structural properties of calcium phosphate-based materials by EPR spectroscopy
12	Azamat	Samadov	Effect of alkaline treatment on structure, morphology, CO_2 sorption of mesoporous ZSM-5 zeolites
13	Stepan	Galiakhmetov	Influence of substitutes and chalcogen atom nature on the alkylation of phosphine chalcogenides
14	Georgiy	Shonin	Synthesis of 4,5-diethynyl-1,2,3-triazoles and structure analysis by NMR spectroscopy
15	Artyom	Tarasov	Spectral characteristics of cyclosporin G and L in deuterated acetonitrile with water solution determined by NMR spectroscopy

16	Anastasia	Troshkina	The structural features of the fibril-forming peptide SEM2(49-107) by NMR spectroscopy and its role in enhancing HIV activity
17	Sergey	Cheremensky	Microstructure and molecular mobility in the ternary LiCl-Cs-Cl-H ₂ O system. A molecular dynamics simulation study
18	Valentina	Yakovleva	Study of NV- centers in natural diamonds (carbonado) by micron scale scanning spectroscopy
19	Andrei	Komolkin	NMR ¹ H/ ¹³ C study of biocompatible copolymer of divinyl ether and maleic anhydride
20	Yulianela	Mengana	Evaluation of plasma viscosity in patients with hyperviscosity syndrome using Proton Magnetic Relaxation.
21	Valerii	Bezrodnyi	Molecular dynamics simulation of C ₆₀ /C ₇₀ fullerene complexes with peptide dendrimer containing histidine spacers
22	Igor	Neelov	Computer simulation of interaction of fullerenes C ₆₀ with short amyloid peptides
23	Igor	Neelov	Investigation of interaction of cyclic peptide with short amyloid peptides by computer simulation
24	Anastasia	Nikitina	Investigation of magnetic characteristics of magnetite nanoparticles in various organic shells
25	Konstantin	Tyutyukin	Study of slow molecular motions by NMR relaxation
26	Yamirka	Alonso	Physicochemical characterization of carbon-coated magnetic cobalt nanoparticles



SpinuS

The School-Conference “Spinus” of Saint Petersburg State University

The St. Petersburg State University (SPbSU) holds International School-Conference “Magnetic resonance and its application” (Spinus) since 2004. “Spinus” is organized in according to the subjects of researches and educational programs, which have been developed and implemented in the SPbSU. In modern physics, the term “magnetic resonance” refers to a set of phenomena accompanied with the emission or absorption of electromagnetic waves of the radiofrequency diapason by quantum systems (nuclei, electrons, atoms, molecules, etc.). These phenomena, the physical nature of which is of independent interest, provided the basis of radiospectroscopic methods for studying the structure of matter and physical-chemical processes in it. They are also used for the creation of quantum generators, amplifiers, and magnetometers. For the development of ideas and applications of magnetic resonance six Nobel Prizes were awarded in the areas of physics, chemistry, biology, physiology and medicine (the latter was in 2003).

Primarily, magnetic resonance methods are:

- Nuclear Magnetic Resonance (NMR)
- Electron Paramagnetic Resonance (EPR)
- Nuclear Quadrupole Resonance (NQR)

These methods, being contactless, do not destroy an object under a study, that makes them unique and in demand not only in physics and chemistry, but also in medicine, geology, biology, archeology. Now, any medical center with high reputation has a magnetic resonance imaging (MRI). In Russia, NMR is used in oil well logging, laboratory analysis of the productivity of oil-bearing reservoirs, analysis of oil content and moisture of seeds; EPR technique is used for geological research, non-destructive control of precious stones, as well as for the dating of paleontological artifacts; there are NQR applications for remote detection of solid explosives and narcotics. Magnetometry methods based on magnetic resonance are indispensable for carrying out archaeological researches.

Earlier the school organizers worked at the Department of quantum magnetic phenomena (QMPh) of the St. Petersburg State University, which was founded in 1993 on the initiative of Professor V. I. Chizhik on the basis of the laboratory, created in the 50s of the last century by F. I. Skripov at the Department of Radio Physics (the branch “Quantum Radiophysics”). On January 1, 2014, the Department of QMPh joined the united Department of nuclear-physics research methods (Head of the Department is Corresponding Member of the Russian Academy of Sciences, Professor Mikhail Kovalchuk). The QMPh collective has a number of priority works in the field of nuclear magnetic resonance. One of the most significant achievements was the first in the world implementation (in 1958) of the Fourier transform of a free induction signal in order to obtain a NMR spectrum (see the details in [1]). Concurrently with the research activity, the staffs of the department are involved in the development of practical applications of magnetic resonance. The department graduates work not only in Russia and the CIS, but also in Sweden, China, Australia, New Zealand, England, Cuba, Germany, France, USA, Italy, Turkey, occupying positions from a highly advanced operator of radiospectrometers to a professor.

The main research areas developing by the collective:

- Nuclear magnetic resonance in liquids (spectra, relaxation, diffusometry, ...);
- Nuclear magnetic resonance in solids;
- NMR in liquid crystals;
- NMR in heterogeneous systems;
- Nuclear magnetic resonance in the magnetic field of the Earth;
- The quantum magnetometry in archeology and industry;

- Computing modeling in magnetic resonance.

It is evident from the above that the scope of our research interests is quite wide. We are always open for the collaboration with researchers from various fields of science.

Our team has published a series of monographs, textbooks and training manuals on Magnetic Resonance. For example:

1. Vladimir I. Chizhik, Yuri S. Chernyshev, Alexey V. Donets, Viatcheslav Frolov, Andrei Komolkin, Marina G. Shelyapina. *Magnetic Resonance and Its Applications*. 2014, Springer-Verlag. 782 pp. (*Now more than 40000 chapters download*).
2. Квантовая радиофизика: магнитный резонанс и его приложения. Учеб. пособие. 2-е изд., перераб. Под ред. В. И. Чижики. – СПб.: Изд-во С.-Петерб. ун-та, 2009. 700 с.
3. В. И. Чижик. Ядерная магнитная релаксация. Учеб. пособие. 3-е изд. – СПб.: Изд-во С.-Петерб. ун-та, 2004. 388 с.
4. Практикум по магнитному резонансу. Учебное пособие. Под ред. В. И. Чижики. – СПб.: Изд-во С.-Петерб. ун-та, 2003. 184 с.

The goal of “Spinus” is to provide a forum for young scientists to discuss the use of all aspects of magnetic resonance methods and techniques, as well as computational and theoretical approaches, for the solving of fundamental and applied problems in physics, chemistry, medicine and biology.

Annually, selected papers of participants are published in a special issue of the journal “Applied Magnetic Resonance”

Welcome to the annual “Spinus”!

*Dr. Sci., Professor, SPbSU, Denis A. Markelov
Chairman of Organizing committee of the 22nd School-conference
“Magnetic resonance and its applications” Spinus-2025*



[1] V.I. Chizhik. On the history of the Fourier transform in NMR spectroscopy. 2018, BULLETIN DU GROUPEMENT AMPERE, 67, № 4 (273), p 5-6.

Lectures

Quantum self-oscillator based on magnon Bose-Einstein condensate

Yury M. Bunkov, Aleksey N. Kuzmichev, Danila A. Samodelrin.

M-Granat, Russian Quantum Center, B. Boulevard, 30, Skolkovo, Moscow 121205

E-mail: y.bunkov@rqc.ru

The objective of our research is to create a narrow-band low-noise microwave generator for use in computing devices such as the Ising Machine and/or Reservoir Computer. The basis of this device is a coherent quantum state of the magnon BEC, which emits a coherent microwave signal. This signal is fed to an amplifier and a YIG crystal, which leads to the excitation of new magnon quasiparticles. According to the principles of quantum mechanics, new quasiparticles are excited only in the state of already existing BEC quasiparticles. As a result, the magnon BEC exists continuously without attenuation. This problem of the continuous existence of the BEC state in atomic systems can be solved with very great technical difficulties, using a flow of cooled atoms from an external source. In the case of the magnon BEC, this problem has already been solved by us in preliminary experiments. This experiment expands the possibilities of experimental study of the properties of BEC, and, in particular, the processes of BEC dynamics, which go beyond the applicability of the semiclassical theory of the dynamics of the Gross-Pitaevsky Bose condensate and the semiclassical theory of Landau-Lifshitz magnetic precession [1,2].

The first experimental results have already shown nontrivial behavior of such a system with enhanced feedback. It was shown that the self-excited magnon Bose condensate reaches a magnon density of the order of 10^{21} cm^{-3} , which corresponds to precessing magnetization deviation angles of 15° , which corresponds to 25% of the magnon density in the Bose condensate. At the same time, due to the repulsion interaction between magnons, a frequency shift of the order of 100 MHz occurs at the resonance frequency of 3 GHz. The presence of a frequency shift from the excitation amplitude leads to ambiguity of the precession frequency in a stationary magnetic field. Two frequencies of self-excitation precession are observed, corresponding to two different magnon densities. In this case, the separation of these equilibrium states is determined by the phase incursion in the radio engineering circuits of the reverse pumping. Naturally, the returning excitation signal must correspond in phase to the resonance signal. That is, two minima of the Hamiltonian of the system with a phase difference of 2π in the return signal circuit are realized. One can assume an analogy with systems using superconductor qubits. Experimentally, it was possible to initiate a transition between two solutions with a weak short pulse of an external magnetic field. To our surprise, within a time of about 4 μs , it was possible to simultaneously observe radiation at two frequencies, as shown in Fig. 1.

We fitted the signals by sinusoids with two frequencies and arbitrary phase. Fig. 2 shows the time dependences of the amplitudes of these fits. Thus, we have obtained a mixed state of two Bose condensates. The possibility of using this state to create a qubit is debatable. To resolve this issue, it is necessary to conduct appropriate tests. Theoretically, this issue cannot be resolved, since there is no adequate quantum description of the dynamics of magnon condensates.

The work was supported by the Russian Science Foundation. Grant No. 22-12-00322.

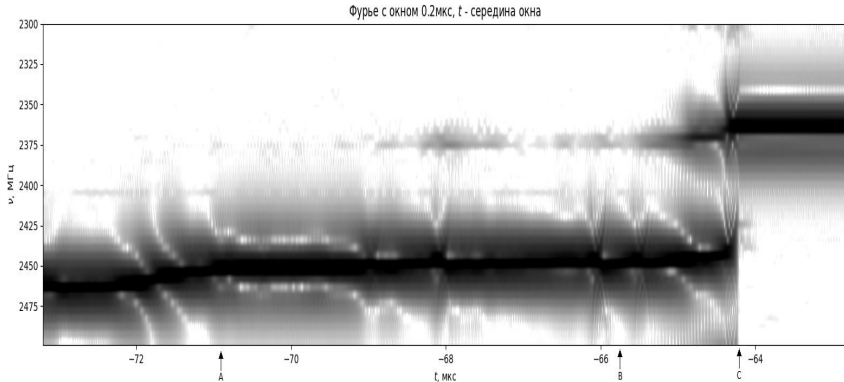


Fig. 1. Fourier analysis of the radiation signal of magnon Bose condensates. Point A is the end of a small change in the external field by 1 Oe. B is the formation of the second Bose condensate; C is the destruction of the initial Bose condensate.

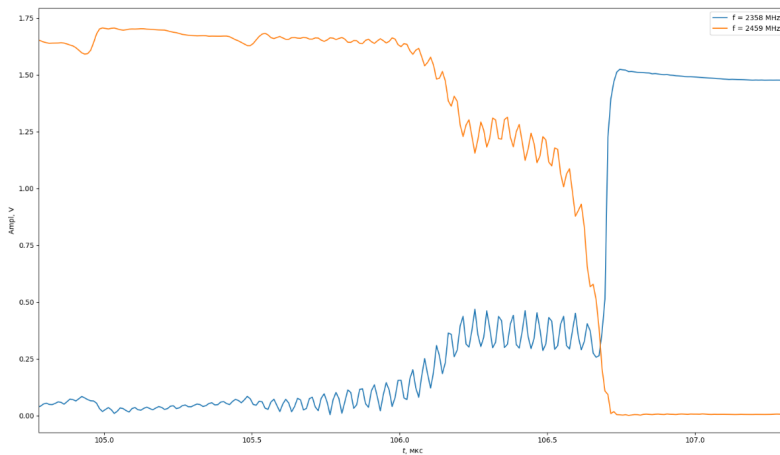


Fig. 2. Dependence of the amplitude of signals at two frequencies. At 105.0 the magnetic field was changed. At 105.5 a signal at the second frequency began to appear. Then the coexistence of two frequencies of BEC signal generation is observed. At 106.7 a stable coherent signal at the second frequency was formed.

1. Yu. M. Bunkov et al., // JETP Letters, 120, 421 (2024).
2. G. A. Knyazev, et al. // Optics Express 32, 13761 (2024).
3. P. E. Petrov et al., // JETP Letters, 119, 118 (2024).

Wound healing rate and treatment effectiveness determined by MRI

Carlos Cabal-Mirabal¹, Evelio González-Dalmau¹

¹Cuban Neuroscience Center

carlos.cabal@quimica.unlp.edu.ar

Introduction

The majority of MRI reports perform a qualitative assessment of the status of the feet, without giving continuity to the evolution (longitudinal studies), and those that do it, do not show guarantees of making it under equal conditions. [1,3-5].

In this article, quantitative data on the evolution of skin lesions throughout treatment are presented. Particular emphasis is placed on one of the most complex healing processes: diabetic foot ulcers (DFU). [2-5].

Materials and Method

Magnetic Resonance Sequences: MRI examination was performed with a 1,5 T Symphony Master Class system (Siemens, Germany). The sequences used were T1 Spin Echo (coronal, axial, and sagittal) with Echo Time (TE) and Repetition Time (TR) of 12 ms and 478 ms, respectively. The Short Tau Inversion Recovery (STIR) images were performed with TR = 4800 ms, TE = 45 ms, and Inversion Time (TI) = 150 ms. In all cases, the slice thickness was 3 mm, and the slice gap was zero mm. The diffusion-weighted images (DWI) were registered by Single Shot Echo Planar Imaging (SSEPI) sequence for five b values (0, 100, 300, 500, and 750 s/mm²), TE=85ms; TR= 8000 ms, slice thickness 6 mm and, interslice gap 0, 6 mm. The ADC values were calculated from the DWI by Matlab. 7. x software. "In vivo" ¹H MRS was obtained using a single voxel (1 cm³) localized in the ulcer region and the equivalent region of the corresponding contralateral healthy foot.

Our group has developed a stereotaxic frame (SF) to better assist in reproducibility [2-4]. There are four external markers, which are parallel ampules (containing paramagnetic solution) at the same level in order to control the right position of the feet during the serial MRI evaluations.

Image Storage and Processing: MRI data were stored and processed in DICOM format in a database using eFilm 2.x. The areas and volume calculations were performed manually using Amira 5.1.0 and Matlab.7.x. The existence of statistically significant differences between the values obtained for each volunteer and patient was examined with an ANOVA test for normally distributed data of homogeneous variance. Statistical significance was set at $p < 0.05$. For each healthy volunteer, the variation coefficient for calcaneus

Results and discussion

Figure 1 as an example, shows the evolution of a patient's lesion through the axial T1 slice at three different times. It is marked with an arrow to indicate the position of the injury. It is observed that the size of the lesion decreases and at the same time a hyperintense area appears in the image that corresponds to the new epithelial tissue. Additionally, a 3D reconstruction of another patient's lesion and the evolution of the edema, are shown in pink. The decrease in the size of the lesion due to healing goes hand in hand with the decrease in the associated edema. The lesion's ADC tends to the ADC's value in the same area of the healthy foot.

Figure 2 A is observed most of the curves can be fixed by 2 exponents. However, there are few patients whose evolution curves only present one exponent. This fact is discussed.

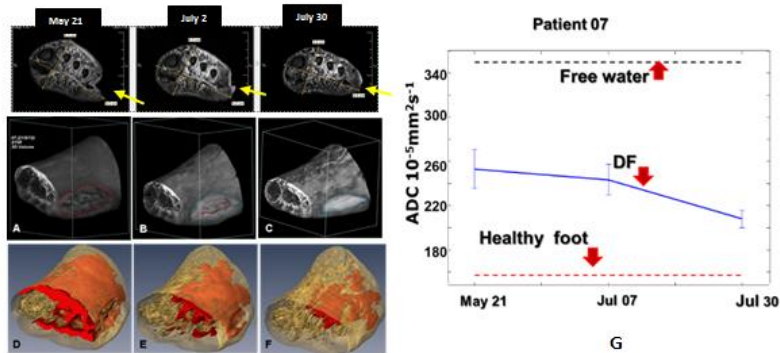


Fig. 1: Axial T1. The lesion studied over time was marked with a yellow arrow. It can be seen that the position of the foot is maintained throughout the studies. STIR 3D Reconstruction. Wound (A-C) and Edema (D-F) Changes during EGF Treatment: A and D: before Treatment; B and E: Week 6 after Treatment; C and F: Week 10 after Treatment. Edema is represented in pink color in D, E, and F. The Calculated Edema Volumes were 137 cm³ (D), 94 cm³ (E) and 54 cm³ (F). An example of ADC measurements in a patient is shown in Figure G. The dotted black line is the ADC of free water (control). The blue line shows the change in ADC during the healing process of the diseased foot, and the red line (dotted) shows the ADC of the same area and injury of the healthy foot.

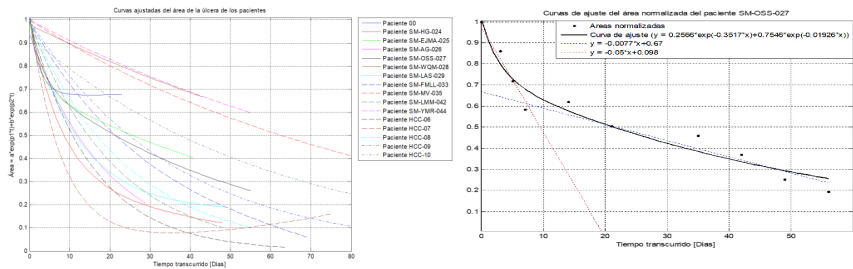


Fig. 2 The variation of the area during the healing process. In most cases, they can be adjusted to two exponentials.

These curves of temporal variation of the lesion areas provide significant data regarding the kinetics of healing. A multi-exponential dependence of the variations in the lesion areas can be explained if one takes into account that the healing process of skin lesions takes place through two interrelated processes: the mechanical contraction process of the wound, bringing the edges of the lesion closer together, and the granulation process, the formation of new tissue [5-7].

$$Z(t) = (Z_0 - Z_K)\exp[-tV_C] + Z_K\exp[-tV_G] + \aleph(tt_K, F, \dots)$$

Where $Z(t)$ is the area of the lesion at time t , measured from the images V_C is the mechanical contraction velocity, slope of the first exponential, and V_G represents the speed of

healing due to the granulation process. $\aleph(tt_K, F, \dots)$ is disturbing complex term which include several physio pathological processes likes the infection, edema, etc. which act again the healing.

If $(Z_0 - Z_K)\exp[-tV_C] + Z_K\exp[-tV_G] \gg \aleph(tt_K, F, \dots)$ healing (and its treatment) is successful, the higher the contributions of the exponents, the more effective and faster the healing would be. In the opposite case, $\aleph(tt_K, F, \dots) \geq (Z_0 - Z_K)\exp[-tV_C] + Z_K\exp[-tV_G]$ where the kinetics of the healing process is significantly slowed, a sign that the response to the therapy is deficient.

An important piece of information to take into account is the shape of the evolutionary curves of the lesion areas. An area under the kinetic curve equal to zero will correspond to instantaneous healing. An area tending to infinity would correspond to NO healing. It can then be inferred that a patient with a smaller area under the evolutionary curve of the lesion than another will be a patient who will heal more quickly. Ade tails discussion regarding Diffusion and Edema's role in the healing process is done.

Conclusion

The variation in area, volume, associated edema, and apparent diffusion coefficient are highly valuable biomarkers for quantifying the speed of healing and evaluating the effectiveness of treatments for each patient. A healing model can be formulated from the data obtained from the MRI.

Acknowledgments

The authors would like to thank the healthy volunteers and patients who participated in the study. They also thank the CIMEQ Clinical Surgical Hospital.

References.

1. T. Gorbachova "Magnetic resonance imaging of the ankle and foot" Pol J Radiol. 2020; 85: e 532–e549. Doi: 10.5114/pjr.2020.99472
2. C. Cabal Mirabal, et al "Feet Positioning System for MRI studies" US Patent Application Publication US 2016/0157750, 2016.
3. C. Cabal-Mirabal, E. González Dalmau, J. Berlanga Acosta, D. Darias Zayas, et al (2014), "Quantitative Studies of the Evolution of Diabetic Foot Lesions under EGF Treatment by Magnetic Resonance Imaging," Journal of Radiology Research and Practice Vol. 2014 (2014), Article ID 783980, DOI:10.5171/2014.783980
4. Cabal Mirabal, C., Fernández García, A., Lores Guevara, M. et al. "Kinetics of Complex Biomedical Problems by Magnetic Resonance. Cuban Experiences". Appl Magn Reson (2018) pp.1/10 <https://doi.org/10.1007/s00723-018-0985-2>
5. C. Cabal Mirabal, J. Berlanga Acosta, J. Fernández Montequín, L. Oramas Díaz, E. González et al "Quantitative Studies of Diabetic Foot Ulcer Evolution Under Treatment by Digital Stereotactic Photography" Journal of Diabetes Science and Technology, 2019, 1-6 doi.org/10.1177/1932296819853843
6. V. W. Wong, S. Akaishi, M. T. Longaker and G. C. Gurtner "Pushing Back: Wound Mechanotransduction in Repair and Regeneration"; Journal of Investigative Dermatology (2011), Volume 131 p. 2186-2196
7. V. W. Wong, M. T. Longaker, G. C. Gurtner "Soft tissue mechanotransduction in wound healing and fibrosis" Seminars in Cell & Developmental Biology Volume 23, Issue 9, December 2012, Pages 981-986

Metals under nanoconfinement: NMR studies

Elena V. Charnaya, Allisher A. Vasilev, Andrei V. Uskov, Denis Yu. Nefedov

Faculty of Physics, St. Petersburg State University, St. Petersburg 198504 Russia

E-mail: e.charnaya@spbu.ru

Introduction

NMR gives valuable information about properties of metals and metallic alloys in the solid and liquid states through measurements of the shift in the resonance frequency, the Knight shift, and the nuclear spin-lattice relaxation rate caused by coupling with conduction electrons and with dynamic electric fields due to lattice vibrations and ionic mobility. Moreover, NMR allows studying properties of metallic nanostructures, then opening a wide modern area in nanophysics. In particular, substances confined to nanoporous templates were recently studied by NMR, revealing new crucial properties related to the impact of nanoconfinement and size effects. Different nanoporous templates were used such as synthetic opals (photonic crystals), porous glasses, and porous alumina, which have various pore geometry, pore network connectivity, and very large diapason of pore sizes from several to hundreds nanometers. First, NMR proved to be extremely effective in demonstrating the specific features of confined metals during the melting and freezing phase transitions, for instance, the pronounced supercooling and highly reproducible thermal hysteresis between freezing and melting as well as reduction of the melting temperature. Later, it was shown as a result of tight cooperation between St. Petersburg State University, Ioffe Institute RAS, Leipzig University and National Cheng Kung University that NMR revealed the drastic slowdown of the atomic mobility in liquid and supercooled metals and alloys in confined geometry compared to their bulk counterparts and found the structural phase transitions in nanoconfined melts (the liquid-liquid transition), occurrence of new polymorph crystalline modifications under nanoconfinement, shift of the temperatures of polymorph transitions, and the influence of nanoconfinement on the phase diagrams for metallic eutectic alloys.

Here we review briefly these results.

Experimental

The nanostructured fusible metals and alloys were obtained by embedding the melts into opal matrices, porous glasses and porous alumina under pressure up to 10 kbar in Ioffe Institute RAS.

Studies were carried out using NMR Bruker Avance 400, Avance 500, and Avance 750 pulse spectrometers within a broad temperature range. We observed the variations with temperature of the Knight shift, integral intensity of the NMR lines, and relaxation rates in the melts and solid phases. At each target temperature the samples were stabilized for about 20 min. The rate of changing temperature did not exceed 0.5 K/min to prevent the temperature overshoots.

Results and discussion

Atomic mobility

Drastic slowdown of the in-pore self-diffusion was observed for liquid metals and alloys: pure gallium and indium, their binary alloy, triple gallium-indium-tin alloy, and melted sodium. The self-diffusion reduction was evidenced by a strong increase in the correlation time of atomic mobility. Pronounced increase was obtained for the atomic mobility in nanoconfined solid sodium. This was seen due to participation in spin-lattice relaxation of the nuclear quadrupole moments coupling with dynamic electric fields ([1-3] and references therein).

Liquid-liquid phase transition

The liquid-liquid phase transition (LLPT) was found in the nanoconfined supercooled gallium and gallium-indium alloys of different compositions. LLPT was evidenced as splitting the NMR lines within some temperature ranges upon cooling and surviving the only one component at lower temperatures. Detailed measurements of the line shift and lineshape were performed to justify LLPT in the alloys ([4,5] and references therein).

Polymorphism under nanoconfinement

Polymorphism in pure gallium and gallium alloys under nanoconfinement was observed as the step-like freezing and melting processes and justified using the x-ray powder diffraction. The crystalline modifications emerged upon crystallization within nanopores were found to be strongly dependent on pore sizes and geometry. The stabilization of β -Ga, which is metastable in bulk, were demonstrated by obtaining the relevant NMR signal ([6] and references therein).

The drastic increase in the temperature of partial polymorph transition in confined solid sodium was found by observing the emergence of the second component of the NMR line [7].

Eutectic alloys: phase diagram and abnormal melting and freezing

NMR is very useful in studying the impact of nanoconfinement on the phase diagrams of the eutectic metallic alloys. The gallium alloys and the sodium-potassium alloy were investigated. The changes in the liquidus and solidus lines were observed. The freezing and melting transitions in the confined Na-K alloy were found to differ remarkably from those in the bulk alloy ([8,9] and references therein).

Acknowledgements

Part of measurements was carried out using the equipment of “Center for Diagnostics of Functional Materials for Medicine, Pharmacology and Nanoelectronics”, St. Petersburg State University.

References

1. E. V. Charnaya, T. Loeser, D. Michel, et al. – Phys. Rev. Lett., 88, 097602 (2002).
2. C. Tien, E. V. Charnaya, W. Wang, Y. A. Kumzerov, D. Michel. – Phys. Rev. B, 74, 024116 (2006).
3. A. V. Uskov, D. Yu. Nefedov, E. V. Charnaya, et al. - Appl. Magn. Reson., 54, 905 (2023).
4. A. A. Vasilev, D. Yu. Nefedov, E. V. Charnaya, Yu. A. Kumzerov, A. V. Fokin – Appl. Magn. Reson., 55, 795 (2024).
5. D. Y. Nefedov, D. Y. Podorozhkin, E. V. Charnaya, et al. – J. Phys.: Condens. Matter, 31, 255101 (2019).
6. D. Yu. Nefedov, E. V. Charnaya, A. V. Uskov, et al. – Appl. Magn. Reson., 52, 1721 (2021).
7. A. V. Uskov, D. Yu. Nefedov, E. V. Charnaya, et al. - NanoLetters, 16, 791 (2016).
8. E. V. Charnaya, M. K. Lee, Cheng Tien, et al. - Phys. Rev. B, 87, 155401 (2013).
9. A. A. Vasil'ev, D. Yu. Podorozhkin, D. Yu. Nefedov, et al. - Appl. Magn. Reson., 53, 1649 (2022).

A few little-known facts in the history of NMR in Russia and a couple of thoughts on unfortunate terminology in magnetic resonance

Vladimir I. Chizhik

Faculty of Physics, Saint Petersburg State University, Saint Petersburg, Russia

E-mail: v.chizhik@spbu.ru

After the existence of magnetic moments of electrons and nuclei had been proven at the turn of the 20s and 30s of the last century, the era of magnetic resonance research and its applications began. Magnetic resonance includes, first of all, nuclear magnetic resonance (NMR), electron paramagnetic resonance (EPR) and nuclear quadrupole resonance (NQR), as well as some of their combinations (so-called double resonances). Nuclear magnetic resonance is characterized by the greatest breadth of research due to the fact that it can be observed for any chemical elements (for any element there is at least one isotope with a magnetic moment) and in any aggregate states of matter.

NMR was initially observed in 1937 by I. Rabi in experiments on atomic and molecular beams [1], for which he was awarded the Nobel Prize in Physics in 1942. However, the heyday of NMR research began after 1946, when articles by two groups of American scientists were published on the observation of NMR in condensed matter [2, 3]. The importance of the works [2, 3] is so great that in many articles and books they are erroneously qualified as pioneering in the field of NMR (without specifying that this refers to NMR in the condensed state).

It is worth noting that attempts to detect NMR in the condensed state were made in the very early 40s (this was discussed, in particular, at the AMPERE Congress held in Kazan in 1994). Most of these attempts were unsuccessful, but without questioning the fair slogan “not published -- not done”, I would like to briefly describe the attempts of E. K. Zavoisky to register the proton (^1H) resonance in condensed matter (Kazan University, Russia). There are evidences in the form of notes in his laboratory notebook that he was able to observe proton magnetic resonance repeatedly in the spring of 1941. Unfortunately, E. K. Zavoisky failed to obtain a stable NMR effect due to the design imperfections of the magnet used. Due to the intervention of German troops into the territory of the USSR on June 22, 1941, many civilian studies were closed, including the experiments of E. K. Zavoisky. While carrying out the mentioned experiments, E. K. Zavoisky made several important improvements that allowed him to discover/register the phenomenon of electron paramagnetic resonance (EPR) in 1944.

The second sad story connected with the slogan “not published -- not done” is about the magnetic resonance imaging (MRI). In 1960, a young army lieutenant Vladislav A. Ivanov applied for registration of an invention: obtaining information about the macroscopic structure of material bodies by means of NMR registration in an inhomogeneous magnetic field (№ 659411/26 “Способ исследования внутреннего строения материальных тел”). The application was reviewed negatively and rejected. The history of the successful development of MRI in the 1970s in many countries is well known. As a result, it was decided to return to reviewing V. A. Ivanov's application, and a positive decision was issued in 1984 with a priority of 1960 (!) (see Fig. 1). As a result of the fact that the application was not published in time, in 2003 the Peter Mansfield and Paul Christian Lauterbur the Nobel Prize for the development of MRI (in Physiology or Medicine).



Figure 1. The Ivanov's patent No. 659411/26 "Method of investigating the internal structure of material bodies"

The next story concerns the fate of a paper published in 1958. We will only cite a publication on the worldwide first high-resolution NMR spectrum obtained from a free induction decay (FID) using the Fourier transform [4] (see Fig. 2). The work [4] did not attract the attention of contemporaries, probably, because in the absence of computers it took a very long time (many days) to calculate one spectrum.

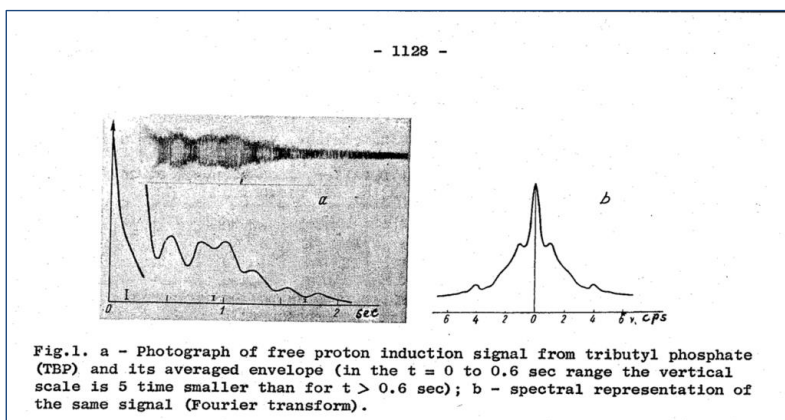


Figure 2. The first high-resolution NMR spectrum obtained from a free induction decay (FID) using the Fourier transform [4].

Unfortunately, this article was never cited by R. R. Ernst, who joined Varian Associates in 1963 and witnessed the lawsuit of Varian Associates against Bruker Corporation in the 70's and its rejection based on the article [4]. As a result, the work [5] is traditionally considered as the "source" of the Fourier NMR spectroscopy. Without belittling the achievements of the R.R. Ernst, who was awarded the Nobel Prize in 1991 for his contributions towards the development of Fourier Transform nuclear magnetic resonance spectroscopy and the subsequent development of multi-dimensional NMR techniques, we would like to draw the attention of the scientific community to the undeservedly forgotten article [4].

Further, the lecture will discuss the inappropriateness of using the concept of "precession" for the individual (single) magnetic moment of a nucleus (or electron). Unfortunately, this term is quite popular in the literature. It should be kept in mind that the concept of the "precession" effect arises from the equation of Classical Physics and, therefore, can be applied only to the macroscopic magnetization or to the average expected value of the transverse (relative to the static magnetic field) component of the magnetic moment.

I would also like to discuss the appropriateness of retaining the term "spin-spin relaxation rate (time)". I cannot get used to the term/understand the term (during 60 years), since the spin-lattice relaxation is also included in this process. In my opinion, it is better to use simply „spin relaxation time“[6] (see also [7]).

References

1. I. I., Millman S., Kusch P., Zacharias J. R. The molecular beam resonance method for measuring nuclear magnetic moments. *Phys. Rev.*, vol., 55, p. 526-535 (1939).
2. Bloch F., Hansen W. W., Packard M. Nuclear induction. *Phys. Rev.*, vol. 69, p. 127 (1946).
3. Purcell E. M., Torrey N. C., Pound R. V. Resonance absorption by nuclear magnetic moments in a solid. *Phys. Rev.*, vol. 69, p. 37-38 (1946).
4. A.A. Morozov, A.V. Melnikov, F.I. Skripov. Applications of the weak-field free nuclear induction technique in high-resolution radio spectroscopy. *Bulletin of the Academy of Sciences of the USSR, Physical Series*, vol. 22, 1127 (1958).
5. R.R. Ernst, W.A. Anderson. Application of Fourier transform spectroscopy to magnetic resonance. *Rev. Sci. Instr.*, vol. 47, 93 (1966).
6. Chizhik V. I. *Bulletin du groupement AMPERE*, # 281, 2–4 (2020).
7. Gupta, A., Stait-Gardner, T., & Price, W. S. Is It Time to Forgo the Use of the Terms "Spin-Lattice" and "Spin-Spin" Relaxation in NMR and MRI? *J. Phys. Chemistry Letters*, 12 (27), 6305-6312 (2021).

Use of various NMR techniques in the study of mechanism of Rh-catalyzed asymmetric hydrogenation

Ilya D. Gridnev

N.D. Zelinsky Institute of Organic Chemistry, Leninsky prosp. 47, 119991 Moscow, Russia

E-mail:ilyaiochem@gmail.com

Introduction

NMR Experiments designated to clarify the mechanism of enantioselection in Rh-catalyzed asymmetric hydrogenation are facilitated by several happy features of the studied compounds. Thus, vast majority of the catalytic precursors, catalysts and reactive intermediates are perfectly soluble in the most common solvents applied in synthetic procedures, viz. methanol and methylene chloride, although with the latter the situation is slightly worse. Both corresponding deuterated solvents have very low melting points and sharp and intensive signals of deuterium that allows effectively adjust resolution even at 173–183K. High solubility of intermediates makes possible acquisition of ^{13}C signals of the carbons belonging to the coordinated double bond, that are coupled to Rh and two phosphorus atoms.

This talk summarizes the author's ample experience in NMR studies of the mechanism of Rh-catalyzed asymmetric hydrogenation.

NMR characterization of BisP*-Rh solvate dihydrides

Initial theory concerning the mechanism of Rh-catalyzed asymmetric hydrogenation considered as very unlikely formation of solvate dihydrides upon hydrogenation of the chelate catalyst-substrate complexes. We have characterized the corresponding dihydrides upon hydrogenation of the $\text{BisP}^*\text{RhS}_2$ complex in deuteriomethanol in the temperature interval 173–243K (Figure 1) [1]

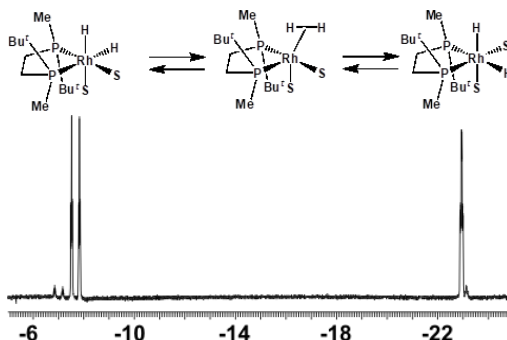


Figure 1. Hydride signals in the ^1H NMR spectrum of the equilibrium mixture (600 MHz, CD_3OD , 183K)

Low-temperature hydrogenation of TCFP-Rh catalyst-substrate complexes

Three different catalyst-substrate complexes were characterized for the catalytic system TricheckenfootPHOS-Rh and methyl (*Z*)- α -acetamidocinnamate: with *re*- and *si*-coordinated double bond nearby the the chiral phosphorus atom and with *re*-coordinated double bond nearby the non-chiral phosphorus atom (Figure 2). Low-temperature

hydrogenation of each of these three complexes was monitored by ^{31}P NMR and gave *R* product independently on the mode of coordination of the double bond [2].

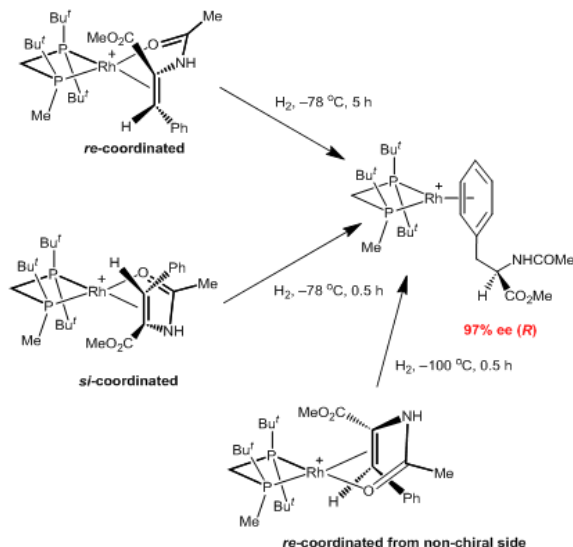


Figure 2. Low-temperature hydrogenation of TCFP-Rh catalyst-substrate complexes monitored by NMR

Detection and characterization of *gauche*-coordinated catalyst-substrate complex

Low temperature reaction between BenzP* Rh complex and (*Z*)- α -acetamidocinnamate gave an unstable intermediate with previously unknown structure. Multinuclear NMR experiments coupled with DFT computations made possible to assign the structure of the intermediate as a catalyst-substrate complex with *gauche*-coordinated double bond [3]. Figure 3 demonstrates a convincing correlation of the experiments and computed ^{13}C chemical for the *gauche*-coordinated double bond.

Other NMR studies of the intermediates in Rh-catalyzed asymmetric hydrogenation will be discussed in the talk.

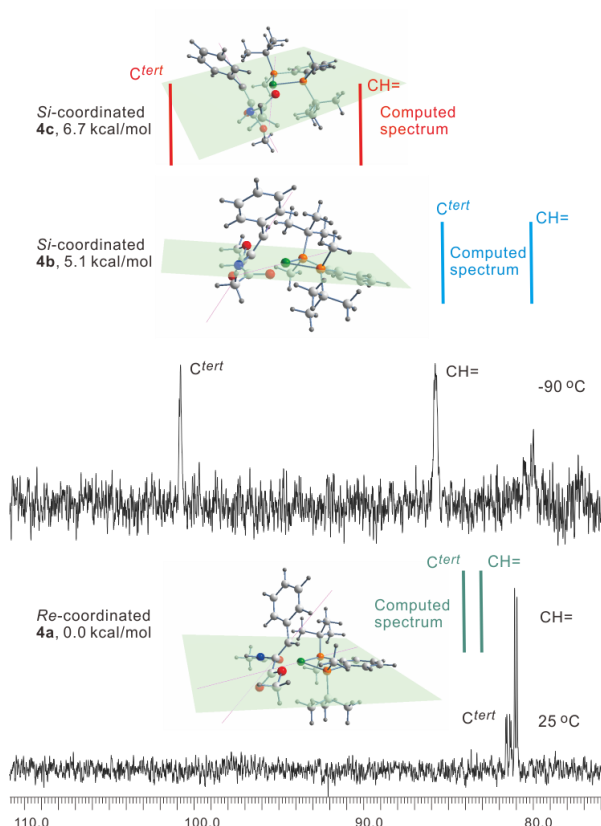


Figure 3. Comparison of the experimental and computed ^{13}C chemical shifts for complexes with different type of the double bond coordination.

Acknowledgements

This work is supported by the Russian Foundation (grant #24-13-00011).

References

1. I. D. Gridnev, N. Higashi, K. Asakura, T. Imamoto.1 – J. Am. Chem. Soc., 122, 7183-7194 (2000).
2. I. D. Gridnev, T. Imamoto, G. Hoge, M. Kouchi, H. Takahashi.– J. Am. Chem. Soc., 130, 2560-2572 (2008).
3. T. Imamoto, K. Tamura, Z. Zhang, Y. Horiuchi, M. Sugiya, K. Yoshida,; A. Yanagisawa, I. D. Gridnev.– J. Am. Chem. Soc. 134, 1754-1769 (2012).

Antiviral metabolite isolation and characterization from *Acremonium* sp (SIMATS2121) endophytic fungi from medicinal plant

Abinaya Gayathri ¹, Kumaravel Kaliaperumal ¹, Thiruchelvi Ramakrishnan ²

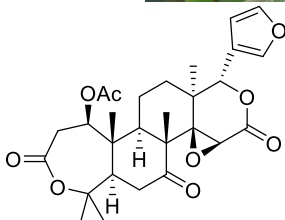
Email: kumarbio06@gmail.com

¹Unit of Biomaterials Research, Department of Orthodontics, Saveetha Dental College and Hospitals, Saveetha Institute of Medical and Technical Sciences (SIMATS), Saveetha University, Chennai, India.

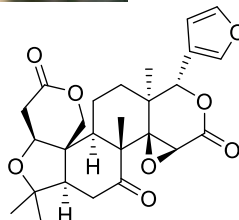
²Department of Biotechnology, St. Joseph College of Engineering, Anna University, Chennai, India.

Abstract

Endophytic fungi are microorganisms that live within plant tissues without causing any apparent harm to the host. They can be found in various plant species and have garnered significant interest in the field of biomedical research due to their potential applications. *Mimusops elengi*, commonly known as the Spanish cherry or bullet wood, is a tropical tree species that has several biomedical and pharmacological significances. *Mimusops elengi* contains various bioactive compounds, including flavonoids, tannins, and alkaloids which seems to be used as antimicrobial, anticancer and anti-inflammatory. An endophytic fungus *Acremonium* sp (SIMATS2121) isolated from *Mimusops elengi* leaves was cultivated under large scale fermentation in solid rice medium for 45 days. The fungal culture yielded 24 different secondary metabolites of class alkaloid, and terpenoids and its structural characterization predicted through ¹H-NMR, ¹³C-NMR (500MHz) revealed that its cyclic isomeric compounds. Biological screening of all 24 isolated compounds revealed that Compound-147AC and Compound 149AC has significant antiviral effect against HPV18 viral strains with EC₅₀ value of 1.89µg/mL. Further molecular screening of antiviral effect is still under validation.



Compound 147AC



Compound -149AC

Hydrogen bonds types, strengths and dynamics in hydroxyl- and carboxyl-functionalized ionic liquids

Daniil I. Kolokolov^{1,2}, Alexander E. Khudozhitkov^{1,2}, Ralf Ludwig³

¹ Novosibirsk State University, Pirogova Street 2, Novosibirsk 630090, Russia

E-mail: kdi@catalysis.ru

² Borekov Institute of Catalysis, Siberian Branch of Russian Academy of Sciences, Prospekt Akademika Lavrentieva 5, Novosibirsk 630090, Russia

³ Universität Rostock, Institut für Chemie, Abteilung für Physikalische Chemie, Albert-Einstein-Str. 27, 18059 Rostock

Like-charge attraction has been observed in hydroxyl- and carboxyl-functionalized ionic liquids (ILs), challenging the general wisdom that “opposite charges attract but like charges repel”. Therein, hydrogen bonded cationic clusters (c-c) successfully compete with hydrogen bonded ion pairs (c-a), despite repulsive in the first and attractive Coulomb interactions in the latter case. We showed that the equilibrium between both types of H-bonds is controllable by the shape, charge distribution and functionality of the ions. Surprisingly, the (c-c) hydrogen bonds are stronger than (c-a) hydrogen bonds as indicated by redshifted OH frequencies, smaller NMR deuteron quadrupole coupling constants and shorter intermolecular distances $R(\text{O}\cdots\text{O})$ and $R(\text{H}\cdots\text{O})$. Even the life times of (c-c) H-bonds may be longer than those of (c-a) hydrogen bonds.

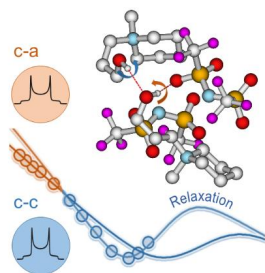


Figure 1. Hydroxyl- and carboxyl-functionalized pyridium-based ionic liquids (ILs) are capable to form cationic cluster, which are stabilized by cation-cation (c-c) hydrogen bonds, notably stronger, than the usual cation-anion (c-a) ones. These clusters govern the ILs local structure, dynamics and phase behavior. We provided in-depth characterization of the (c-a) and (c-c) hydrogen bonds by means of the ^2H NMR

We also demonstrate that (c-c) clusters influence the dynamics of the cations in a characteristic way. Our results confirm that the solid-state ^2H NMR spectroscopy is perfectly suited to study molecular mobility of distinct molecular species in complex fluids such as the hydrogen-bonded ionic liquids. Here we provide valuable information about the applicability of well-accepted relaxation models and show that the simple Bloembergen-Purcell-Pound (BPP) approach is not suitable to describe the dynamics in such complex systems.

We further show, that the carboxylic-functionalized ionic liquids provide stronger and more stable hydrogen bonded cationic cluster than the hydroxylated ones, which specifically affects the ionic liquids phase behavior and local ions dynamics in the liquids state.

Acknowledgements

This work was supported by the Russian Science Foundation (project No 24-13-00129) <https://rscf.ru/project/24-13-00129/>

References

A. E. Khudozhitkov, D. Paschek, A.G. Stepanov, D. I. Kolokolov, R. Ludwig, R. J. Phys. Chem. Lett. 2023, 14, 17, 4019–4025.

Accurate NMR Diffusion Measurements in Reacting Systems

William S. Price

Nanoscale Organisation and Dynamics Group, Western Sydney University, Penrith, NSW, Australia

E-mail: w.price@westernsydney.edu.au

<https://westernsydney.edu.au/nanoscale>

NMR diffusion measurements greatly expand on the information that can be obtained from NMR [1, 2] and are now a widely available technique possible of being conducted on most commercial spectrometers. Being able to measure diffusion in freely diffusing systems offers a direct connection with molecular size and intermolecular interactions. NMR diffusion measurements have traditionally been performed with gradient spin-echo (or stimulated echo) based sequence and in such measurements it has generally been assumed that it is possible to accurately separate the relaxation-based attenuation from the diffusion-related attenuation. Further, the majority of measurements have been conducted under the assumption that the relaxation-based attenuation occurs under conditions of constant relaxivity and that the populations of the diffusing species do not change during the measurement.

Although having the potential to provide simultaneous measurement of the diffusion of each species and the kinetics of a reaction, such measurements and the subsequent analysis can be complicated. Performing the NMR diffusion measurement more quickly so as to turn a changing system into a pseudo-stationary one alleviates some but not all of the difficulties. As the timescale for the changes decrease and approach the timescale of the NMR diffusion measurement further alterations to the how the measurements are performed are required if the diffusion data is to be correctly interpreted (e.g., [3-6]).

References

1. W.S. Price, *NMR Studies of Translational Motion: Principles and Applications* 1st ed., Cambridge University Press, Cambridge, 2009.
2. S.A. Willis, T. Stait-Gardner, A.M. Torres, G. Zheng, A. Gupta, W.S. Price. Expanding NMR Versatility, in: A. Bunde, J. Caro, C. Chmelik, J. Kärger, G. Vogl (Eds.) *Diffusive Spreading in Nature, Technology and Society*, Springer International Publishing, Cham, 2023, pp. 247-277.
3. M. Urbańczyk, D. Bernin, A. Czuroń, K. Kazimierczuk. Monitoring Polydispersity by NMR Diffusometry with Tailored Norm Regularisation and Moving-Frame Processing. *Analyst*, 141, 1745-1752 (2016).
4. T.S.C. MacDonald, W.S. Price, J.E. Beves. Time-Resolved Diffusion NMR Measurements for Transient Processes. *ChemPhysChem*, 20, 926-930 (2019).
5. J.-P. Günther, L.L. Fillbrook, T.S.C. MacDonald, G. Majer, W.S. Price, P. Fischer, J.E. Beves. Comment on “Boosted Molecular Mobility during Common Chemical Reactions”. *Science*, 371, eabe8322 (2021).
6. L.L. Fillbrook, M.D. Nothling, M.H. Stenzel, W.S. Price, J.E. Beves. Rapid Online Analysis of Photopolymerization Kinetics and Molecular Weight Using Diffusion NMR. *ACS Macro Letters*, 11, 166-172 (2022).

DNA Binding Mechanism of the Virulence Regulator SarA of *Staphylococcus aureus*

Bin Xia

Beijing Nuclear Magnetic Resonance Center, Peking University, Beijing, 100871, China

Staphylococcus aureus infections have long been a significant challenge to public health, particularly due to the emergence of multiple drug-resistant strains. SarA is a critical global regulator in *S. aureus* which binds to AT-rich sequences in the promoter regions of various genes, but the DNA-binding mechanism of SarA remains unclear.

We have determined the solution structures of a monomeric DNA binding domain of SarA (SarA^{ΔN19}) and its complex with an AT-rich double-stranded DNA. The winged helix domain of SarA^{ΔN19} binds to DNA in a classic way, with the α4 helix binding to the major groove of DNA, while the L5 loop binding to the minor groove, covering 10 AT base pairs. Residues L53, P65, and V68 of the α4 helix have hydrophobic interactions with thymine bases and sugar rings. The side chains of Arg90 and Arg84 from the wing are inserted into the minor groove, forming hydrogen bonds with A/T bases. Multiple positively charged or hydrophilic residues, including Lys54, Lys63, Lys69, Lys72, Lys82, and Gln64, interact with the phosphate groups on the DNA backbones.

This complex structure provides an in-depth understanding of the molecular mechanism for SarA to bind DNA, and a better structure basis for future anti-bacterial drug design targeting SarA.

1. Fu D, Duan B, Dong X, & Xia B* “1H, 13C, and 15N resonance assignments of SarA monomer from *Staphylococcus aureus* in complex with DNA”, *Biomol NMR Assign* 17: 193-197 (2023).
2. Fu D, Guo X, Duan B*, & Xia B* “DNA Binding Mechanism of The Virulence Regulator SarA in *Staphylococcus aureus*”, *J Magn Reson Open* 22: in press (2025).



ABOUT THE COMPANY



Selection of equipment in accordance with user tasks



Installation of equipment, user training



Direct supplies of equipment from manufacturers



Equipment maintenance and repair

NMR spectrometers



Cryogen free NMR spectrometer HT-PNMR series

Equipment for synthesis and purification

Flash chromatographs

Microwave synthesizers

Automatic peptide synthesizers (SPPS)

General laboratory equipment



Laboratory centrifuges

Water purification systems

Gas generators

Analytical columns for HPLC and GC, flash columns

Automated sample preparation

Automatic extractors

Homogenizers

Microwave sample digestion systems

Solvent evaporators

Consumables and spare parts for analytical instruments

Hollow cathode lamps deuterium lamps

Cuvettes

The ELEMENT LLC company is the official representative in Russia of the manufacturer of high-tech equipment - the ZHONGTAI company (China). The main business includes Scanning Electron Microscopes (SEMs), Electron Paramagnetic Resonance (Electron Spin Resonance) Spectroscopy, Scanning NV Probe Microscopes, and BET Surface Area & Pore Analyzers.

ELECTRON PARAMAGNETIC RESONANCE



Benchtop EPR Spectrometer
ZT6500



X-Band* CW-EPR Spectrometer
ZT15C



X-Band* Pulse-EPR Spectrometer
ZT15P



W-Band High-frequency EPR Spectrometer
ZT60W

*Optional Q-band extension available

Modernize your old EPR spectroscopy for the cutting-edge EPR research:

CW Microwave Bridge (X-band, Q-band), Pulsed Microwave Amplifier (X-band, Q-band), EPR Spectrometer Console & Magnetic Power Supply, Resonators (High-Q, Dual Mode, Pulsed, ENDOR Pulsed), Cryogenic Systems



NITROGEN-VACANCY (NV) MAGNETOMETRY



NV Magnetometer based on AFM

Magnetic field imaging with high spatial resolution by using the principles of nitrogen-vacancy (NV) center optically detected magnetic resonance (ODMR)



Widefield NV Microscope

Oral Reports

MRI of wildlife

Nikolay V. Anisimov

Faculty of Fundamental Medicine, Lomonosov Moscow State University, Moscow, Russia

E-mail: anisimovnv@mail.ru

Introduction/Purpose

In addition to medical diagnostics, MRI is used to scan wildlife - plants and animals. Small laboratory animals (mainly mice and rats) are used in experiments to model human pathologies. MRI of domestic animals - cats, dogs, etc. is used in veterinary practice. Of interest are MR images of other animals in the study of morphology. MRI of plants is also used, mainly in technological applications - for non-invasive assessment of the quality of products (fruits, berries). This paper provides a brief overview of the results obtained in the practice of MRI of living objects on a clinical 0.5T MR scanner Bruker Tomikon S50.

Immobilization

Of interest are some behavioral aspects identified in some animals regarding immobilization, which allows in some cases to perform MRI without anesthesia – Fig. 1.

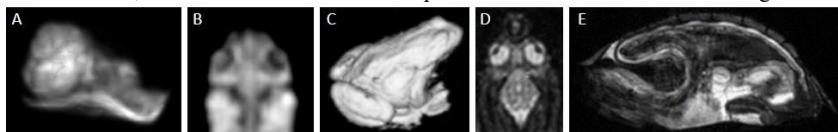


Figure 1. Animals scanned without immobilization. A – 3D MRI of mollusk (*Helix pomatia*), B and C – frog (*Pelophylax lessonae*): head (axial) and 3D image, D and E – turtle (*Swamp turtle*): head (axial) and whole body (sagittal)

Some plants (*Riccia*) were also used to immobilize the aquarium inhabitants (fish, mollusk, etc.) inside the wireless coil.

Wireless coil without lumped capacitance for underwater MRI

It turned out to be possible to use a solenoid as a resonant wireless coil (21.1 MHz) without connecting a concentrated capacity to it. Its functions are performed by the self (interturn) capacity, which increases 80 times in water [1]. Fig. 2 shows the use of a solenoid immersed in water for MRI of an underwater plant.

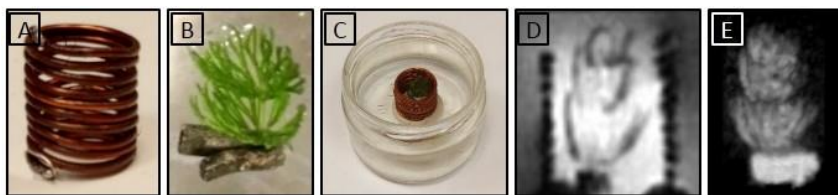


Figure 2. A - solenoid; B - underwater plant (*Ceratophyllum*); C - solenoid in a vessel with water; inside which a plant is placed; D – 3D image of a vessel with water (inside the solenoid the signal is 2.5 times greater than outside it); E - 3D image of a plant

Simultaneous MRI of several objects. Different orientation of objects and coils

The specificity of a typical clinical scanner as applied to the study of small laboratory animals is noted in comparison with what is possible on a typical research scanner with a small gap. In particular, the possibility of placing several animals simultaneously, as well as

the possibility of changing the orientation of the coil and the object itself relative to the B_0 field. Sometimes this gives a more even distribution of sensitivity in the area of interest.

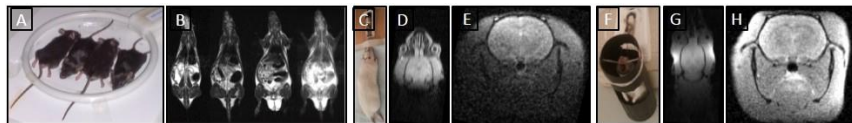


Figure 3. A - Four mice inside a loop coil. B – Their MRI, C - rat (Wistar) in horizontal position, D and E - MRI of the rat's head in a horizontal position in two projections; F - rat in vertical position, G and H - MRI of the rat's head in a vertical position in two projections

MRI of plant development in real time

Real-time MR visualization of the process of development of a flowering plant has been implemented. For this purpose, MR scanning was performed daily for a bulb planted in the ground with its localization in relation to the center of the magnet. The resulting images were composed as frames for a video film, which shows the growth of the stem, leaves, blossoming of the flower, with the subsequent withering of the plant – Fig. 4.

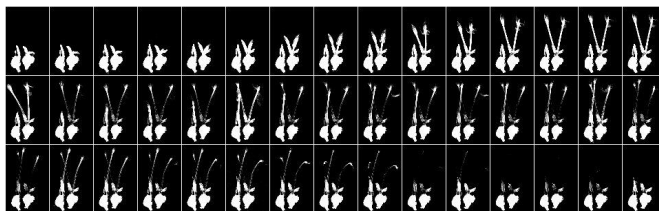


Figure 4. MRI of the colchicum plant, showing stages of its 30-day development in autumn

^{19}F and ^{23}Na MRI

^{19}F MRI were conducted with the injection of perfluoroorganic substances, in particular Perftoran, into the body of rats [2]. A series of experiments on ^{23}Na MRI were conducted on fresh fish (euthanized a few minutes before MR scanning), which made it possible to obtain their anatomical images and, based on the decrease in the ^{23}Na signal, to track the dynamics of necrotic changes in various organs [3].

Acknowledgment

The study was conducted under the State Assignment of Lomonosov Moscow State University.

References

1. N. V. Anisimov, Yu. A. Pirogov. – Electromagn. Waves and Electron. Syst., 24, 44-54 (2024) (in Russian).
2. N.V. Anisimov, et al. - J. Phys. Conf. Ser., 886(1), 012006 (2017).
3. N. V. Anisimov, et al. – Appl. Magn. Reson., 54, 1467-1479 (2022).

Registration of nickel and nitrogen spin centers signals by their interactions with negative NV centers in diamond by photoluminescence

Anastasia V. Batueva, Roman A. Babunts, Aleksandr S. Gurin, Daria D. Kramushchenko, Pavel G. Baranov

Ioffe Institute, 194021, St. Petersburg, Russia

E-mail: rarain1345@yandex.ru

<https://ioffe.ru/labmsc/ru/main.html>

Introduction

Negatively charged NV centers ($S=1$) in diamond are intensively studied due to their importance for quantum cryptography, computing, optics and spintronics [1,2]. For these same practical applications, it is proposed to use controlled interaction of NV⁻ centers with other defects, as well as NV⁰ centers, since they do not require additional N donors. Active research is being conducted on optical registration of cross-resonances and level anticrossings (LACs) in diamonds grown by HPHT and CVD, including measurements without applying microwave power [3,4], due to the importance of the results obtained for applications of sensors based on the registration of resonant transitions between spin levels without microwave power (for example all-optical vector magnetometry on SiC [5]), and quantum information processing. The methods of high-frequency EPR and optically detected magnetic resonance were previously used to study the properties of NV defects in diamond in strong magnetic fields (see for example [6]).

Results

The results of a study of the NV⁻ centers interaction with nitrogen and nickel spin centers in HPHT grown diamond by recording changes in the photoluminescence (PL) signal during magnetic field sweep without applying microwave power are presented. The lock-in measurements were carried out with magnetic field modulation at a temperature of 150 K with a 532 nm laser to excite PL and photodiode to collect.

The signals of the PL dependences on the magnetic field correspond to the fields at which cross-resonances are observed, i.e., the coincidence of the energy gap between the spin levels of NV⁻ centers and Ni levels, as well as the levels of N-N pairs (a pair of P1 centers, $S_{1,2}=1/2$) [7] (figure 1). The characteristics of Ni, N and NV⁻ impurity spin centers are confirmed by the results of high-frequency EPR measurements at different temperatures. For the magnetic field orientation parallel to the [111] crystal axis, several groups of lines are observed. The signal in a magnetic field of 26 mT corresponds to the coincidence of the energy gap $|0\rangle \leftrightarrow |-1\rangle$ in the NV⁻ center, directed along the [111] axis of the crystal, and the gap between the levels with $\Delta M_s = 3$ for Ni. In fields of 32–38 mT, corresponding to the second group of signals, coincidences of transition energies are observed between the levels $|0\rangle$ and $|-1\rangle$ for NV⁻ and levels with $\Delta M_s = 2$ for Ni, between the levels $|0\rangle$ and $|-1\rangle$ for NV⁻, directed along the [111] crystal axis, and the levels $|1, -1\rangle \leftrightarrow |1, 1\rangle$ for the N-N pair, as well as between different levels of NV⁻ centers directed along the axes equivalent to [111]. Cross-resonance signals between levels of directed along four equivalent axes NV⁻, Ni levels, and levels of N-N pairs are also within the range of 54–67 mT. The observed line splittings for signals in the fields of 32–38 mT and 54–67 mT are associated both with the occurrence of several cross-resonances in these regions and with the presence of hyperfine splitting of the N–N pair levels due to interaction with the ^{14}N nucleus. Also, at the corresponding orientations of the magnetic field, LAC signals for NV⁻ centers are observed, they are resolved when the field coincides with the [111] axis of the crystal.

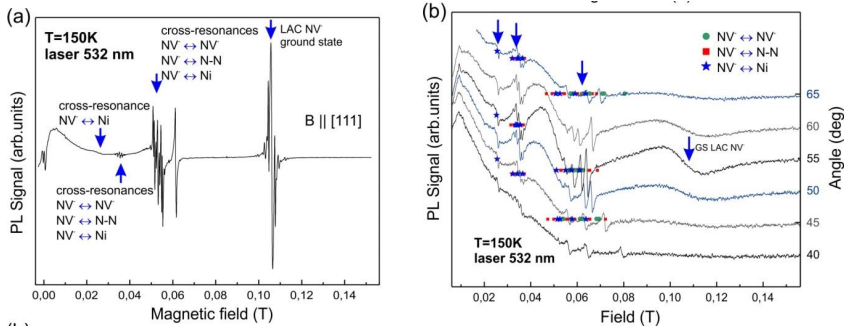


Figure 1. PL dependence on a magnetic field in diamond at a temperature of 150 K with a 532 nm laser excitation. The (a) image correspond to the direction of the magnetic field along the [111] axis of the crystal while the (b) image presents PL dependences in the angle range of 40 to 65 degrees. Signals from cross-resonances and LAC are shown with blue arrows.

Acknowledgements

The research was carried out with the support of the Ministry of Science and Higher Education of the Russian Federation (FFUG-2024-0046).

References

- Atatüre, M. et al. Material platforms for spin-based photonic quantum technologies. *Nat Rev Mater* 3, 38–51 (2018). <https://doi.org/10.1038/s41578-018-0008-9>
- Marcus W. Doherty et al., The nitrogen-vacancy colour centre in diamond. *Phys. Rep.* 528:1–45 (2013) <https://doi.org/10.1016/j.physrep.2013.02.001>
- Pellet-Mary, C. et al., Optical detection of paramagnetic defects in diamond grown by chemical vapor deposition. *Phys. Rev. B* 103, L100411. (2021) <https://link.aps.org/doi/10.1103/PhysRevB.103.L100411>
- Lazda, Reinis et al., Cross-relaxation studies with optically detected magnetic resonances in nitrogen-vacancy centers in diamond in external magnetic field. *Phys. Rev. B* 103, 134104. (2021) <https://doi.org/10.1103/PhysRevB.103.134104>
- Kirill V. Likhachev et al.; All-optical vector magnetometry based on fine and hyperfine interactions in spin-3/2 centers in silicon carbide. *J. Appl. Phys.* 7 January 2025; 137 (1): 015701. <https://doi.org/10.1063/5.0238078>
- Babunts, R.A. et al., Features of High-Frequency EPR/ESE/ODMR Spectroscopy of NV-Defects in Diamond. *Phys. Solid State* 62, 2024–2032 (2020). <https://doi.org/10.1134/S1063783420110062>
- C.A.J. Ammerlaan, Paramagnetic centers in diamond, in: M. Schulz (Ed.), *Landolt-Boernstein New Series, Vol. III/41A2a*, Springer, Berlin, 2001, pp. 6–76

Quantum entanglement in quasi-equilibrium states in NMR multi-pulse spin locking

Georgii A. Bochkin¹, Sergey G. Vasil'ev¹, Elena I. Kuznetsova¹, Edward B. Fel'dman¹

¹Federal Research Center of Problems of Chemical Physics and Medicinal Chemistry RAS, Chernogolovka, Moscow region, 142432, Russia

E-mail: bochkin.g@yandex.ru

Introduction

Multi-pulse NMR spin locking [1,2] is one of the effective methods for an investigation of spin-lattice relaxation in solids. In NMR spin-locking experiments the spin system with the dipole-dipole interactions (DDI) evolves from the initial state, which is determined by the spin polarization, to quasi-equilibrium states reached after time on the order of the inverse of dipolar frequency, ω_{loc}^{-1} . The structure of the quasi-equilibrium state depends on the relationship between the effective pulse frequency $\omega_1 = \varphi/(2\tau)$ and ω_{loc} , where φ is the pulse flip angle in the rotating reference frame (RRF) [3] and 2τ is a delay between sequential pulses. When $\omega_1 \lesssim \omega_{loc}$ the quasi-equilibrium state is described by one temperature, and when $\omega_1 \gg \omega_{loc}$, it can be described by two temperatures, Zeeman and dipolar [4]. The time dependence of these temperatures for $t \gg \omega_{loc}^{-1}$ is determined by Provotorov equations [5]; the temperatures eventually equalize.

It should be noted that the initial state of the system, which is determined by polarization alone, is separable [6]. However, the quantum correlations (quantum entanglement, quantum discord [7]) emerge while the quasi-equilibrium is forming. Thus we find a new method to study quantum correlations.

Entanglement in quasi-equilibrium state when $\omega_1 \lesssim \omega_{loc}$

We consider the simplest multi-pulse experiment [1,2] in which the system of spins ($s=1/2$) connected by the DDI is irradiated by a pulse sequence $90_y - \tau - (\varphi - 2\tau)^N$, where φ denotes a resonance pulse rotating spins by an angle φ about the x -axis of RRF [3]. The equation for the density matrix of the system reads

$$i \frac{d\rho}{dt} = [-f(t)I_x + H_{dz}, \rho(t)] \quad (1)$$

where $f(t)$ is

$$f(t) = \varphi \sum_{k=0}^{\infty} \delta(\tau + 2k\tau - t), \quad (2)$$

and H_{dz} is the secular part of the DDI relative to the z -axis. It is convenient to express H_{dz} as the sum of the secular part H_{dx} and non-secular parts $H_d^{(2)}$ and $H_d^{(-2)}$ relative to the x -axis of the RRF. This x -axis is considered the new quantization axis from now on [8]:

$$H_{dz} = -\frac{1}{2}H_{dx} + H_d^{(2)} + H_d^{(-2)}, \quad (3)$$

where

$$H_{dx} = \sum_{k < j} d_{kj} \left[2I_{kx}I_{jx} - \frac{1}{2}(I_k^+ I_j^- + I_k^- I_j^+) \right], H_D^{(\pm 2)} = -\frac{3}{4} \sum_{k < j} d_{kj} I_k^{\pm} I_j^{\pm}, \quad (4)$$

where $I_{k\alpha}$ is the spin angular momentum projection operator on the α axis ($\alpha=x,y,z$), $I_k^{\pm} = I_{zk} \pm iI_{yk}$, $I_x = \sum_k I_{kx}$, and d_{kj} is the dipolar interaction constant between spins i and j .

Switching to the interaction representation in pulses (1) [4,8]

$$\rho^*(t) = \exp \left\{ -i \left(\int_0^t f(t') dt' - \omega_1 t \right) I_x \right\} \rho(t) \exp \left\{ i \left(\int_0^t f(t') dt' - \omega_1 t \right) I_x \right\}, \quad (5)$$

and neglecting the rapidly oscillating terms with frequencies $\frac{\pi n}{\tau}$ ($n = \pm 1, \pm 2, \dots$), we obtain the following equation for the density matrix $\rho^*(t)$:

$$i \frac{d\rho^*(t)}{dt} = [H_{qe}, \rho^*(t)], \quad (6)$$

where

$$H_{qe} = -\omega_1 I_x - \frac{1}{2} H_{dx} + \frac{\sin\varphi}{\varphi} (H_d^{(2)} + H_d^{(-2)}). \quad (7)$$

When $\omega_1 \approx \omega_{loc}$, where ω_{loc} is the local dipolar interaction frequency, on the time scale $t \sim 1/\omega_{loc}$ a quasi-equilibrium is established, and the system has the density matrix

$$\rho_{qe} = \frac{1}{Z} e^{-\alpha_{qe} H_{qe}}, Z = \text{Tr}\{e^{-\alpha_{qe} H_{qe}}\}, \quad (8)$$

where α_{qe} is a parameter which will be found below.

The initial density matrix is determined solely by the Zeeman interaction and is separable [8]. Quantum correlations, including entanglement, are absent from the system at that moment. They appear while the quasi-equilibrium state forms at time $t \sim \omega_{loc}^{-1}$.

To investigate quantum correlations in the quasi-equilibrium state (8), we reduce [9] the density matrix (8) over all spins except the first two. Quantum entanglement in the two-qubit matrix $\bar{\rho}_{qe}$ can be investigated with standard methods [7]. The eigenvalues of two-qubit Hamiltonian H_{qe} obtained by reducing (7) can be easily found to be

$$\lambda_1 = -a + \sqrt{\omega_1^2 + a^2 b^2}, \lambda_2 = -a - \sqrt{\omega_1^2 + a^2 b^2}, \lambda_3 = 2a, \lambda_4 = 0, \quad (9)$$

where $a = \frac{1}{4} d_{12} = \frac{1}{4} d$, $b = 3 \frac{\sin\varphi}{\varphi}$.

To determine the concurrence [10,11], which describes quantum entanglement, for the state (8), the eigenvalues of the following operator need to be found:

$$R = (\sigma_{1y} \otimes \sigma_{2y}) \bar{\rho}_{qe} (\sigma_{1y} \otimes \sigma_{2y}) \bar{\rho}_{qe}, \quad (10)$$

where σ_{ky} ($k = 1, 2$) are the Pauli matrices acting on spins 1 and 2. The formula (10) takes into account that $\bar{\rho}_{qe}$ is real. Using the Wootters formula [11] for the concurrence, we obtain

$$C = \begin{cases} 2a_2 - e^{-2\alpha_{qe}a} - 1, & \text{if } \sqrt{a_1 a_3} + a_2 > 1 \text{ and } \sqrt{a_1 a_3} > a_2, \\ 2\sqrt{a_1 a_3} - e^{-2\alpha_{qe}a} - 1, & \text{if } \sqrt{a_1 a_3} + a_2 > 1 \text{ and } a_2 > \sqrt{a_1 a_3}, \\ 1 - 2\sqrt{a_1 a_3} - e^{-2\alpha_{qe}a}, & \text{if } 1 > \sqrt{a_1 a_3} + a_2 \text{ and } \sqrt{a_1 a_3} > a_2, \\ 1 - 2a_2 - e^{-2\alpha_{qe}a}, & \text{if } 1 > \sqrt{a_1 a_3} + a_2 \text{ and } a_2 > \sqrt{a_1 a_3}, \end{cases} \quad (11)$$

where $a_1 = x_1^2 e^{-\alpha_{qe}\lambda_1} + y_1^2 e^{-\alpha_{qe}\lambda_2}$, $a_2 = x_1 x_2 e^{-\alpha_{qe}\lambda_1} + y_1 y_2 e^{-\alpha_{qe}\lambda_2}$, $a_3 = x_2^2 e^{-\alpha_{qe}\lambda_1} + y_2^2 e^{-\alpha_{qe}\lambda_2}$, and x_i, y_i are components of eigenvectors of \bar{H}_{qe} corresponding to eigenvalues λ_i .

In the problem under consideration, the Hamiltonian (7) is an integral of motion:

$$\text{Tr}\{H_{qe}\rho_0\} = \text{Tr}\{H_{qe}\rho_{qe}\} \quad (12)$$

where ρ_0 is the initial density matrix:

$$\rho_0 = \frac{1}{Z_0} e^{-\alpha_0 \omega_0 I_x}, \quad Z_0 = \text{Tr}\{e^{-\alpha_0 \omega_0 I_x}\} \quad (13)$$

Solving the equation (13) numerically for a system of 14 spins, given φ , ω_0 and ω_1 , allows one to find α_{qe} and then the concurrence C . Fig.1 shows the temperature dependence of concurrence for $\omega_0 = 2\pi \cdot 500 \cdot 10^6 \text{ s}^{-1}$ and various values of ω_1 and φ . The most important conclusion which can be drawn from it is the existence of a critical temperature, above which concurrence (and entanglement) is absent. The critical temperature weakly depends on ω_1 and φ and is approximately 40 mK.

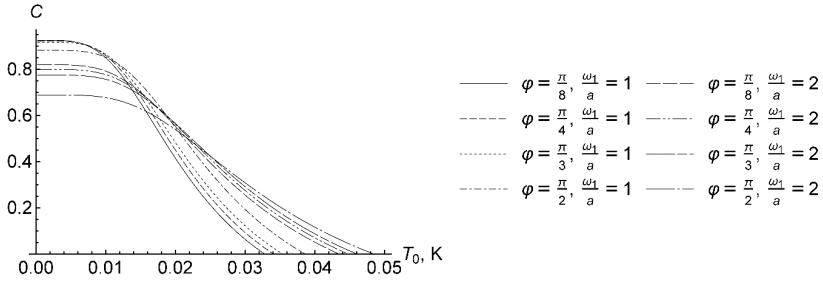


Figure 1. Temperature dependence of the concurrence in the $\omega_1 \lesssim \omega_{loc}$ case

Entanglement in quasi-equilibrium state when $\omega_1 \gg \omega_{loc}$

When $\omega_1 \gg \omega_{loc}$, at time scales about $T_2 \sim 1/\omega_{loc}$ a two-temperature quasi-equilibrium is established:

$$\rho_{qe} = \frac{1}{Z} e^{-[\alpha_{qe}(t)\omega_1 I_x - \frac{1}{2}\beta_{qe}(t)H_{dx}]}, \quad (14)$$

where evolution of the Zeeman reservoir $\alpha_{qe}(t)$ and the dipolar reservoir $\beta_{qe}(t)$ is determined by Provotorov equations when $t \gg T_2$ and leads to equalization of Zeeman and dipolar temperatures.

Calculation of concurrence in this case shows that it is always zero, i.e. the entanglement is absent in this case (the system is separable). This is caused by the strong Zeeman field, as the dipolar subsystem can be entangled in its absence.

Conclusion

Quantum entanglement in quasiequilibrium states has been theoretically studied in the multi-pulse NMR spin-locking. It has been shown that when $\omega_1 \lesssim \omega_{loc}$, the quasi-equilibrium state is entangled when the temperature does not exceed the critical temperature $T_{cr} \approx 40$ mK. In the case $\omega_1 \gg \omega_{loc}$, the resulting two-temperature quasi-equilibrium state is separable. The absence of entanglement in the case $\omega_1 \gg \omega_{loc}$ is due to a strong Zeeman field.

Acknowledgements

The work was performed as a part of a state task, State registration No. 124013000760-0.

References

1. E. D. Ostroff, J. S. Waugh. – Phys.Rev.Lett., 16, 1097 (1966).
2. W.-K. Rhim, D. P. Burum, D.D. Elleman. – Phys.Rev.Lett., 37, 1764 (1976).
3. M. Goldman. Spin Temperature and Nuclear Magnetic Resonance in Solids. – Oxford University Press, 1970.
4. Yu. N. Ivanov, B. N. Provotorov, E. B. Fel'dman. – JETP Letters, 27, 153 (1978).
5. B. N. Provotorov. – Zh.Exp.Theor.Phys., 41, 1582 (1961).
6. M. A. Nielsen, I. L. Chuang. Quantum Computation and Quantum Information. – Cambridge University Press, 2001.
7. S. M. Aldoshin, E. B. Fel'dman, M. A. Yurishchev. Low Temp.Phys., 40, 3 (2014).
8. Yu. N. Ivanov, B. N. Provotorov, E. B. Fel'dman. – Zh.Exp.Theor.Phys., 75, 1847 (1978).
9. S. I. Doronin, A. N. Pyrkov, E. B. Fel'dman. – JETP Letters, 85, 519 (2007).
10. S. Hill, W. K. Wootters. – Phys.Rev.Lett., 78, 5022 (1997).
11. W. K. Wootters. – Phys.Rev.Lett., 80, 2245 (1998).

The hydrothermal treatment effect on the relaxivity of DyF₃ nanoparticles colloidal solution

E.I. Boltenkova¹, A.V. Bogaychuk¹, M.Yu. Volkov², A.M. Garaeva¹, E.M. Alakshin¹

¹*Institute of Physics, Kazan Federal University*

²*Zavoisky Physical-Technical Institute FRC Kazan Scientific Center of RAS Kazan, Sibirsky tract, 10/7, 420029, Russia*

E-mail: katarina.kondratyeva@gmail.com

Introduction

A lot of nanoparticles research has been focused on their use in biomedical applications. In this case the nanoparticles can be used for targeted drug delivery, as a magnetic resonance imaging (MRI) and computer tomography (CT) contrast agents (CA), as nanoscale temperature sensors [1-3]. It is known that CA for MRI based on gadolinium (Gd) compounds were created for low-field MRI scanners. The r_1 relaxivities values of gadolinium-based (Gd) compounds are typically around $20 \text{ Mm}^{-1} \text{ s}^{-1}$ in magnetic fields around 1 T and are almost unchanged with magnetic field [4]. However, there is a shift towards higher-field tomographs for medical applications, which significantly improves the quality of the images obtained and the accuracy of medical diagnoses [5]. Thus, the creation of more efficient CA for high-field MRI is an actual task. The main candidates for high-field MRI CAs are substances with a high magnetic moment and not saturated at strong magnetic fields. A large number of studies show the potential of using superparamagnetic nanoparticles based on iron group elements as high-field MRI CA [6]. The next of the promising groups are compounds with an unfilled 4f shell that have these properties [7]. All Ln^{3+} ions, except La^{3+} and Lu^{3+} , have unpaired electrons and are thus paramagnetic. However, unlike their chemical behavior, their magnetic properties are determined by their electron configurations and vary sharply along the series. Unpaired electrons in paramagnetic Ln^{3+} ions other than Gd^{3+} inevitably populate f orbitals anisotropically, resulting in strong magnetic anisotropy and very short electron relaxation times (on the order of 10^{-13} s) [8]. This, in turn, leads to a significant shortening in the T_2 relaxation time compared to T_1 [9].

It is known that magnetic nanoparticles have a tendency to agglomerate and self-assemble [10]. For CAs based on nanoparticles, it is also important to pay attention to the processes that occur within the system during synthesis such as the agglomeration processes of nanoparticles because they will affect on relaxivity value.

In this work the effect of hydrothermal (classical autoclave and microwave irradiation) treatment on the r_2 transverse relaxivity value of DyF₃ nanoparticles colloidal solutions was studied. The colloidal solutions of the DyF₃ nanoparticles with different concentrations at magnetic field of 0.6, 3.65 and 9.4 T were studied by ¹H NMR to measure the T_2 relaxation times. It has been shown that the sample with treatment in a classic autoclave has the maximum relaxation rate in contrast to the sample without treatment and treatment in a microwave oven. The optimal sizes of DyF₃ nanoparticles for their use as contrast agent for MRI for different magnetic fields were determined.

Acknowledgements

This work was supported by the Russian Science Foundation (Project No. 23-72-01084).

References

1. A.E. Kianfar. – Journal of Superconductivity and Novel Magnetism, 34, 1709 (2021).
2. S. Caspani, R. Magalhães, J.P. Araújo, C.T. Sousa. – Materials, 13, 2586 (2020).
3. Y. Hou, X. Yang, R. Liu, D. Zhao, C. Guo, A. Zhu, M. Wen, Z. Liu, G. Qu, H. Meng. – International Journal of Nanomedicine, 15, 6827 (2020).

4. F.L. Giesel, A. Mehndiratta, M. Essig. – *Eur Radiol*, 20, 2461–2474 (2010).
5. A. Banerjee, B. Blasiak, A. Dash, B. Tomanek, F.C.J.M. van Veggel. Trude S. – *Chem. Phys. Rev.*, 3, 011304 (2022).
6. R. Jin, B. Lin, D. Li, H. Ai. – *Current Opinion in Pharmacology*, 18, 18 (2014).
7. H. Dong, S.-R. Du, X.-Y. Zheng, G.-M. Lyu, L.-D. Sun, L.-D. Li, P.-Z. Zhang, C. Zhang, C.-H. Yan. – *Chem Rev*, 115, 10725 (2015).
8. B.M. Alsaadi, F.J.C. Rossotti, R.J.P. Williams. – *J. Chem. Soc., Dalton Trans.* 2147, (1980).
9. S. Viswanathan, Z. Kovacs, K.N. Green, S.J. Ratnakar, A.D. Sherry. – *Chem. Rev.*, 110, 2960 (2010).
10. S. Singamaneni, V.N. Bliznyuk, C. Binek, E.Y. Tsymbal. – *J. Mater. Chem.*, 21, 16819 (2011).

Unified NMR: towards universally accessible NMR workflow with TqT “Nuclei”

Bystrov S. S.^{1,2}, *Kirilenko V. D.*^{2,3}, *Zolotov D. R.*^{2,4}, *Khrustalev A.A.*^{2,5}, *Bystrov E.S.*^{2,6}

¹*Dept. of Nuclear-Physics Research Methods, St. Petersburg State University, Russia*

²*TerraQuantTech LLC (VAT Number: 400372342), Tbilisi, Georgia*

³*Wydział Matematyki i Informatyki, Uniwersytet Łódzki, Łódź, Poland*

⁴*TRASSIR GLOBAL FZC, LLC “DSSL” (Digital Security Systems Lab), Moscow, Russia*

⁵*Bachelor of Engineering in Mechatronics and Robotics, ITMO University*

⁶*Postgraduate student of Art Criticism, St. Petersburg University of Humanities and Social Sciences, Saint-Petersburg, Russia*

E-mail: info@terraquant.tech

https://terraquant.tech

Introduction

Over the past several decades, nuclear magnetic resonance (NMR) has established itself as a fundamental analytical technique in chemical and structural investigations. Its capacity to provide critical insights—ranging from clinical diagnostics to the detailed characterization of complex biological molecules—underscores its unique value in research.

Nevertheless, extending the application of NMR beyond specialized laboratories into routine industrial settings remains challenging. The significant financial investment required for both the acquisition and upkeep of NMR systems, coupled with the demand for highly trained personnel, restricts its broader adoption in the industry.

Yet, there is considerable potential for integrating NMR methodologies into various stages of industrial processes, spanning sectors such as food production and oil refining [1–3]. Although often overlooked, this approach promises to lower production costs and improve quality control, thereby offering manufacturers a means to reduce ongoing expenses. The principal difficulty lies in reconciling the substantial costs associated with NMR technology with its prospective practical benefits.

In response to these challenges, researchers and industrial innovators have increasingly turned their attention to niche applications of NMR, leading to the development of benchtop systems. Companies like Magritek, Nanalysis, Oxford Instruments, Resonance Systems and Bruker have launched compact devices — examples being Magritek’s Spinsolve and Bruker’s Fourier 80 — that employ robust electromagnetic coils or permanent magnets operating at resonant frequencies between 20 and 90 MHz (equivalent to magnetic field strengths of 0.3–1.5 Tesla). Despite their reduced size and lower cost relative to traditional superconducting spectrometers, these systems still require operators with substantial expertise in both the instrument’s functionality and the underlying principles of physics and chemistry, which can be a significant barrier for industrial users.

Furthermore, a critical shortcoming in the current generation of benchtop NMR devices is the lack of dedicated software solutions tailored to industrial applications—an advancement that could markedly improve their utility and impact in practical settings.

Addressing this critical gap, the TqT “Nuclei” platform has been developed as a comprehensive software solution tailored specifically for industrial applications. TqT “Nuclei” bridges the disconnect between advanced NMR hardware and the practical needs of non-specialist users by offering a modular, highly customizable framework. It simplifies data acquisition, analysis, and interpretation through seamless integration of modern technologies such as machine learning, open database connectivity, and multi-vendor compatibility. By doing so, TqT “Nuclei” transforms NMR from a niche, research-intensive tool into an accessible and efficient technology for routine industrial problem-solving.

The Unified NMR

Having collected feedback from the industry leaders of the NMR analysis branch, the following software features were highlighted as lacking in the currently available software solutions of various vendors, represented on the market:

- Extensive data analysis capabilities. Among others, PCA analysis, multivariate analysis, automated and semi-automated physical properties extraction;
- Support of the modern machine learning (ML)-based analysis and automation;
- Integration with the open knowledge- and databases;
- Industry-tailored quality-of-life features, such as customizable report generation and experiments automation, multi-lingual support;
- Support of devices and data formats from multiple vendors, eliminating the need for employees to (re-)learn the device-specific software.

The above points have been made the priority of the current development of the *TerraQuantTech “Nuclei” platform*. The software has been developed following the modular component-based paradigm, tightly integrated with modern scripting languages, allowing for a significant degree and ease of consumer-side customization. The software includes a diverse range of industry-standard scientific packages, as well as built-in solutions for the common challenges posed by the analysis of NMR data.

Besides the integration with the open databases of NMR signals, which has long been the standard in the market of analytical programs for high-resolution NMR - *TerraQuantTech* offers the opportunity to create a fully custom machine-learning solution for any of the User problems, following the consent to the anonymized collection of the experimental data.



Figure 1. Screenshot of TqT “Nuclei” Acquisition page demonstrating various presets.

```

29 def wobble(tau_2: float) -> NMRspectrum:
30     p_90 = DeviceSettings.p90_us
31     p_180 = DeviceSettings.p180_us
32     tau_1 = DeviceSettings.ring_us
33     seq_null = p_90 + p_180 + tau_1 + tau_2 + 120
34
35     sequence = [
36         Silence(120),
37         Pulse("w", 180),
38         Silence(tau_2),
39         Pulse("w", 90),
40         Silence(tau_1),
41         ADC(ACQ),
42         Silence(tau_1),
43     ]
44     sig, spec = run_sequence(sequence, seq_null=seq_null)
45
46     amps = np.abs(sig.amplitudes)
47     return np.mean(amps[2:16])
48
49
50 def fit_exp_model(x, a, b, c):
51     return a + np.exp(-x / b) + c
52
53 curve = record()
54 plot(curve)
55
56 [scale, T1, y0, err = FIT_fit_model(curve, fit_exp_model)]
57 print(f"[scale], (y0), (T1), (err)"]
58
59 annotater:
60     signal:
61         time_points=curve.time_points,
62         amplitudes=fit_exp_model(curve.time_points, scale, T1, y0)
63     },
64     name="T1 fit"
65 }

```

Figure 2. Screenshot of Sequence page demonstrating T1 inversion-recovery experiment.

Conclusion

In conclusion, the TqT “Nuclei” platform marks a significant advancement in making NMR spectroscopy broadly accessible for industrial applications. By overcoming the traditional challenges of high costs, complex maintenance, and the need for specialized expertise, this modular and customizable software solution streamlines data acquisition, analysis, and interpretation through the integration of machine learning, open database connectivity, and multi-vendor support. As such, it effectively bridges the gap between advanced NMR hardware and practical, everyday industrial use, fostering enhanced quality control and cost efficiency. This work lays the groundwork for the evolution of NMR from a niche research tool into a universally deployable technology, setting a clear direction for future developments aimed at further expanding its industrial utility.

Acknowledgments

The author would like to thank every team member of TerraQuantTech company and express my deepest gratitude for all the hard work that each of you put into our project, and for your desire to create and strive for the best despite any external circumstances. N.B. I would also like to thank my dear mom and dad for their unquenchable faith in our deed.

References

1. “A Review of Applications of NMR Spectroscopy in Petroleum Chemistry” John C. Edwards, ASTM Books, 2011.
2. “Process and Quality control in food and agroindustry using TD-NMR”, D. Consalter, Proceedings of the conference “BENCHTOP NMR: FROM ACADEMIA TO INDUSTRY”
3. NMR to Industry: Development of modern universal control software for TD-NMR spectrometers, Proceedings of the conference “Spinus-2024”, St. Petersburg, Russia

NMR Diffusometry for Studying Ionic Association in Plasticized Polymers

Alexandr V. Ievlev¹, Daria A. Chetverikova², Nadezhda V. Pokhvishcheva²,
Maria A. Peshkova²

¹Department of Nuclear Physics Research Methods, Saint Petersburg State University,
1 Ulyanovskaya st., 198504, Petergof, Saint Petersburg, Russia

²Institute of Chemistry, Saint Petersburg State University, 26 Universitetskiy prospect,
198504, Petergof, St. Petersburg, Russia

E-mail: d4verikova@gmail.com

Introduction

NMR diffusometry has been developed as a powerful method to study translational diffusion [1]. Recently, it has been applied to the study of plasticized polymeric membranes of ion-selective potentiometric and optical sensors [2]. The authors determined the diffusion coefficients of ionic liquids in the polymeric phase and showed that PFG NMR is suitable for the study of such complex media. In this paper, we focus more on the potential of employing NMR diffusometry to determine the concentration ratios of components with different mobility. These data can be useful in studying the association of ions in ion-selective sensor membranes.

Ion-selective sensors are composed of a hydrophobic matrix based on a plasticized polymer and active components, which are responsible for interaction with the analyte (ion or neutral molecule) and formation of the analytical response. It is well known that ionic association can have a significant effect on the sensor response, and complex models have been developed to explain and predict this effect [3]. These models utilize the association constants between polymeric membrane components as one of the parameters. Despite the high importance of these quantities, few data on them are available in the literature. The study of equilibrium in the polymeric phase can be problematic. The estimation of concentrations (or activities) of species in a plasticized polymer is a challenging task, so indirect measurements are used to estimate important thermodynamic properties. Most works utilize potentiometric studies to determine the association constants in such systems. The developed techniques are laborious, time-consuming, and not very accurate if the association is sufficiently small [4]. Indirect measurements can also lead to systematic errors in the obtained values due to unaccounted unknown factors.

To circumvent serious errors, it is important to approach the problem from multiple perspectives and utilize a range of approaches based on unrelated fundamental principles. The present work aims to introduce NMR diffusometry into the study of ionic association to ascertain the feasibility of this method being used in further studies to determine properties of interest.

Experimental results

We have chosen some of the lipophilic organic electrolytes widely used in the field of ion-selective sensors to study their ionic properties in polyvinyl chloride (PVC) membranes plasticized with bis(2-ethylhexyl)sebacate (DOS): bromides of tetrabutylammonium (TBABr), tetrahexylammonium (THexABr), tetraheptylammonium (THepABr), tetraoctylammonium (TOctABr), and tetradecylammonium (TDecABr); tetraoctylammonium tetrakis[3,5-bis(trifluoromethyl)phenyl]borate (TOctABArF), tetrabutylammonium tetrabutylborate (TBATBB) and potassium tetrakis(4-chlorophenyl)borate (KTPClPB) (Fig. 1). Noteworthy, the plasticizer DOS serves simultaneously as a liquid solvent for the ionic components in the polymeric phase. This type of matrix is commonly used in the area of ion-selective sensors.

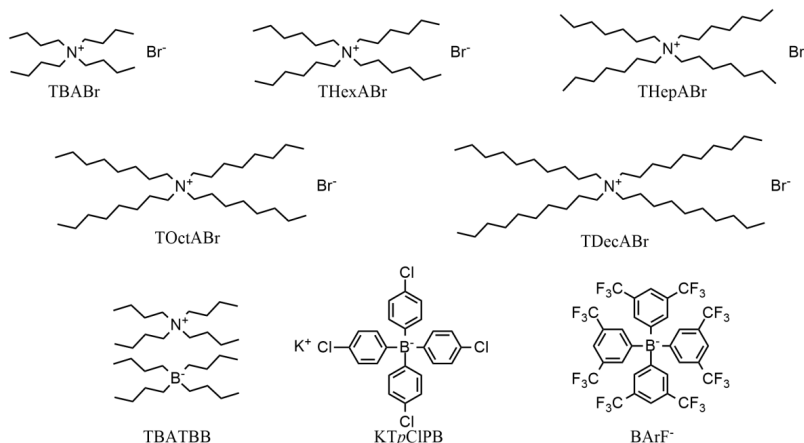


Figure 1. Lipophilic cations and anions under study.

High molecular weight PVC, DOS and volatile solvents tetrahydrofuran (THF) and cyclohexanone (CH) were Selectophore grade reagents from Fluka (Switzerland). Liquid membrane compositions were prepared by dissolving a weighted portion of PVC and an aliquot of DOS (1:2 mass ratio) in the volatile solvent THF. Then a weighted portion of the organic salt or an appropriate aliquot of its solution in CH were added to the mixture. Liquid compositions were stirred with a roller-mixer (RS-TR 5, Phoenix Instrument, Germany) for 10 min, and then poured into Petri dishes 32 mm in diameter and covered with filter paper to slow down the evaporation of THF. The dishes were left for 2 days until complete evaporation of the solvent. The salt concentration in the final membrane was varied in a range from 0 to 0.1–0.2 mole per kilogram of DOS.

To obtain NMR spectra, the membranes were placed into NMR vials. ^{79}Br (for quaternary ammonium salts), ^{19}F NMR (for TOctABArF), ^1H and ^{13}C measurements with organic salts in THF solution and in PVC-based membranes were carried out at 25 °C using a Bruker Avance III 400 WB NMR spectrometer equipped with diffusion probe DIFF/50 with gradient controller GREAT MASTER UNIT E with gradient amplifiers.

As a general tendency, all the lines in the spectra registered in polymeric matrix are broadened as compared to the spectra obtained in solutions (see an example in Fig. 2 for the spectrum of DOS). This complicates to some extent the analysis of the spectra, but meanwhile the spectrum contour is preserved in terms of the number and location of peaks.

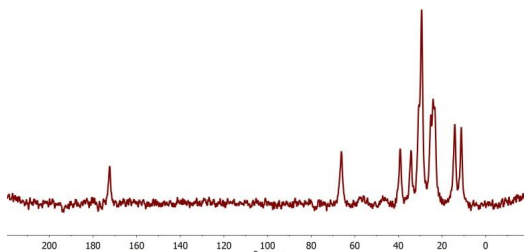


Figure 2. ^{13}C NMR spectra of the plasticizer in the polymer.

The diffusion of the species was investigated by means of pulsed field gradient-stimulated echo with a bipolar gradient (PFG STEbp technique) where the echo signal, I , is given by the well-known Stejskal-Tanner Eq. (1) [1]:

$$I(G) = I_0 e^{-D\gamma^2 G^2 \delta^2 \left(\Delta - \frac{\delta}{3}\right)} \quad (1)$$

with D : the diffusion coefficient, I_0 : the integral intensity, γ : the gyromagnetic ratio, G : the gradient amplitude, δ : the equivalent duration of the gradient pulses, and Δ : the time interval between the gradient pulses. OriginPro 2015 (OriginLab Corporation, Northampton, MA, USA), MestReNova 14.2.1 (Mestrelab Research S.L., Santiago de Compostela, Spain) were used for data processing.

The NMR spectra were recorded for all membrane compositions at different values of the gradient amplitude. It turned out that even though the obtained dependencies $I(G)$ decay exponentially, it was not always possible to approximate them by a single exponential as in Eq. (1). This situation occurs when the particle involved in transport phenomena exists in more than one form in the studied medium, e. g. in the form of a free ion and an ion pair. In this case, the corresponding dependencies are usually fitted with more than one decaying exponential [1, 2]. In our case, approximation of the $I(G)$ dependencies by a superposition of two exponentials typically gave the optimal fitting output in terms of the adjusted correlation coefficient (r^2) and the χ^2 criterion (modified Stejskal-Tanner equation):

$$I(x) = I_1 \exp(-D_1 x) + I_2 \exp(-D_2 x); \text{ with } x = \gamma^2 G^2 \delta^2 \left(\Delta - \frac{\delta}{3}\right) \quad (2)$$

The higher values of diffusion coefficients obtained after fitting the dependences of the intensity on the gradient amplitude were attributed to single ions. Lower diffusion coefficients are assigned to ion pairs, which are considered to be less mobile. The ionization (dissociation) degree of the salts can be obtained from the fraction of “fast” component of the exponential dependence $I(x)$.

In the present work, we report on the obtained values of the diffusion coefficients of the individual ionic species and on their ion pairs in the plasticized polymeric matrix. The estimated values of ionization degree and corresponding electrolyte dissociation constants will be compared with available from the literature and the applicability of PFG NMR diffusometry for direct studies of electrolytic properties in polymeric phase will be discussed.

Acknowledgements

This work was funded by the Russian Science Foundation, project number 20-73-10033. The research was partly carried out at the "Center for Magnetic Resonance Research" of the Science Park of St. Petersburg State University.

References

1. W. S. Price. – Concepts in Magnetic Resonance: An Educational Journal, 9(5), 299-336 (1997)
2. N. V. Pokhvisheva, A. A. Vanin, M. A. Vovk, M. A. Peshkova, A. V. Ievlev – Journal of Molecular Liquids, 403, 124874-124881 (2024)
3. K. N. Mikhelson. –Electroanalysis, 15, 1236-1243 (2003)
4. M. A. Peshkova, A. I. Korobeynikov, K. N. Mikhelson. – Electrochimica Acta, 53, 5819-5826 (2008)

Low field setup for DNP studies in stray field of superconducting magnet

G.A. Dolgorukov¹, V.V. Kuzmin¹, A.S. Makarchenko¹

¹Kazan Federal University, Kazan, Russia

E-mail: Sasha_chayan@mail.ru

Introduction

Nanodiamonds (ND) and other non-toxic nanoparticles are extensively used in biomedical applications, including drug delivery, imaging, and subcellular tracking. Recent studies have shown that paramagnetic centers on the surface of nanodiamonds can enable dynamic nuclear polarization (DNP) of surrounding water solutions, enhancing MRI capabilities at ultra-low magnetic fields and room temperature [1].

This study aims to validate and expand the applicability of this method to nanodiamonds and other nanoparticles with surface defects. For this purpose, a custom experimental setup capable of operating across a broad range of magnetic fields has been developed.

DNP/NMR part of the setup

This work includes the testing of this setup for ultra-low field DNP in aqueous solutions of TEMPOL DNP agent and ND nanoparticles within the 1–20 mT range. The magnetic field is achieved by using the stray field of an unshielded superconducting NMR magnet 3.6 T. The setup includes active shim coils, an NMR coil, a loop-gap EPR resonator, a low-frequency NMR preamplifier, and a passive RF switch to route microwave and radiofrequency power from a single broadband amplifier (Rohde & Schwarz, BBA100, 500 W continuous wave, 9 kHz–250 MHz) to the resonator and NMR coil, correspondingly. The NMR transmit/receive system of our custom-built broadband NMR spectrometer has been described in our prior work [2].

The preamplifier was constructed using a low-cost INA-02186 MMIC amplifier (1.8 dB noise figure and 31 dB gain) and an AD797 operational amplifier, achieving a total gain of 68 dB, a bandwidth of 0.05–1.2 MHz, and a dead time of 180 μ s.

Shim coils design

The magnetic field gradients produced by magnet alone were measured in three directions at a radial distance of 52 to 104 cm from the center of the superconducting magnet in the plane perpendicular to its axis, using a Hall sensor from Infineon (3D Magnetic Sensor 2Go TLE493D A2B6). The relative gradient values at a distance of 90 cm from the center of the magnet were found to be $G_y = 3.2$ %/cm, $G_z = 0.23$ %/cm, and $G_x = 0.34$ %/cm. The shim coils generate linear gradients in three directions (0.5 mT/cm/A for the most critical direction) to improve magnetic field homogeneity in samples with diameters up to 40 mm. The gradient coil dimensions and geometry were optimized for linearity using a Python script based on Magpylib library for magnetic field calculations. The gradient coil holders, with external dimensions of ~17 cm, were 3D-printed using PETG plastic. A 50-fold improvement in magnetic field homogeneity (the ratio of the full width at half maximum (FWHM) in echo signals) was achieved in water sample with diameter of 1 cm. The optimal NMR line width experimentally obtained is 650 ppm, which is much larger than the calculated value (15 ppm) for the developed shimming coils if the external gradients are perfectly linear, but also much less than in unshimmed case (32000 ppm).

Results

A DNP enhancement factor of 300 was successfully achieved in a test sample containing 0.7 mL of an aqueous TEMPOL solution at a concentration of 30.5 mmol/L at a microwave power of 79.6 W and magnetic field of 4.1 mT. Also, a DNP enhancement factor of 1.91 for a

detonation nanodiamonds (DND) aqueous solution (46.4 mg/ml) was achieved at a mw power of 38 W and magnetic field of 9 mT. DND powder of 98.3% purity produced by US Research Nanomaterials, Inc. (USA) was used as a sample. The declared by manufacturer particle size of the powder is 3–10 nm.

This setup is suitable for ultra-low field NMR/DNP studies, hyperpolarization experiments with noble gases, and, potentially, low-field MRI applications due to its integrated gradient system. A photograph of our assembly of the DNP setup is shown in Fig. 1. NMR tank circuit, EPR resonator, shim coils, preamplifier and $\lambda/4$ are placed inside shielding box that stands near the superconducting magnet.

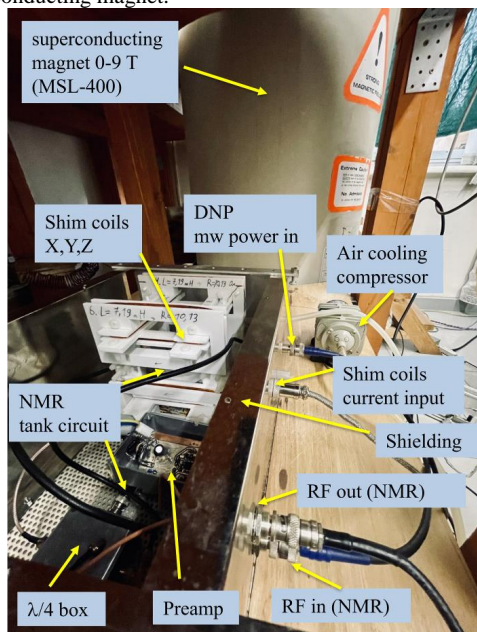


Figure 1. Photograph of the DNP box with all elements located near the superconducting magnet.

Acknowledgements

This work was financially supported by the Russian Science Foundation (project no. 24-22-00336).

References

1. Waddington A. et al.: Nature Communications. 8, 15118 (2017)
2. Kuzmin V.V. et al.: Magnetic Resonance in Solids. 21, Is.1, 19104 (2019)

Ion dynamics in liquid crystal-electrolyte mixtures

Sergey V. Dvinskikh

KTH Royal Institute of Technology, Stockholm, Sweden.

E-mail: sergeid@kth.se

Liquid-crystalline additives to liquid electrolytes in electrochemical devices may lead to enhanced performances, such as favorable changes in ionic conductivity and suppression of self-discharge [1,2]. To understand the molecular level mechanisms leading to such effects, the ionic and molecular dynamics and intermolecular interactions in liquid crystals/electrolyte mixtures were studied over a wide concentration range. The results of investigations of anisotropic diffusion using pulsed field gradient NMR methods [3] and intermolecular cross-relaxation processes by heteronuclear NOE technique [4] will be discussed.

1. X. Su, W. Jia, H. Ji, Y. Zhu. – J. Energy Storage, 41 102830 (2021)
2. J. Li et al. – Nano Energy, 115 108754 (2023)
3. S. V. Dvinskikh. – Liq. Cryst., 47, 1975 (2020)
4. M. E. Di Pietro, F. Castiglione, A. Mele. – J. Phys. Chem. B, 124, 2879 (2020)

Zero-field cross-relaxation resonances in ensembles of NV centers in diamond and fully optical magnetic field detection

Dmitry S. Filimonenko, Alexander P. Nizovtsev, Sergei Ya. Kilin, B. I. Stepanov

Institute of Physics, National Academy of Sciences of Belarus, 220072 Minsk, Belarus

E-mail: demonr@tut.by

https://master.basnet.by/lqo/

Introduction

Nitrogen-vacancy (NV) centers in diamond are a leading platform for quantum technologies, with applications in quantum cryptography, computing, and sensing. Both single NV centers and NV ensembles can act as magnetic sensors using optically detected magnetic resonance (ODMR). However, ODMR requires microwave radiation, increasing setup complexity and cost. Recent studies [1-2] proposed fully optical magnetometry methods based on photoluminescence changes near the ground-state level anticrossing line (GSLAC). These methods, though, demand precise crystal orientation and strong magnetic fields (0,1 T), limiting their practicality. The use of the zero-field cross relaxation line (ZFCRL) [3-5] makes it possible to eliminate the above-mentioned disadvantages and improve the performance of all-optical magnetometric systems. Here we investigate ZFCRL focusing on its dependence on the sample type, NV center density and temperature. We also explore cross-relaxation phenomena under different transverse magnetic fields. Furthermore, we demonstrate the fully optical implementation of a magnetic sensor based on ZFCRL in an ensemble of NV centers.

Experimental

The observation of ZFCRL was conducted using an experimental setup, the schematic of which is shown in Fig. 2(a). Nd:YAG laser beam (532 nm, 20 mW) was focused onto a diamond sample using an objective lens. Photoluminescence was collected via an optical fiber and directed to a PIN photodiode, preceded by a notch filter to block pump light. A local magnetic field was generated by two pairs of Helmholtz coils. One of the coils was supplied with a slowly varying sweep voltage at 0.01 Hz from a signal generator through a power supply (PS1). Simultaneously, a higher-frequency sinusoidal voltage ($\omega=560$ Hz) was applied, inducing a slight modulation of the magnetic field B_1 applied to the sample. This modulation resulted in a weak modulation of the optical signal, which was detected by a photodetector and a lock-in amplifier (LIA).

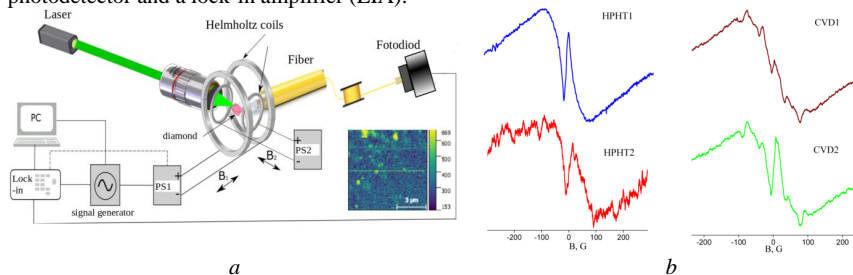


Figure 1. Experimental setup (a), dependencies of the lock-in amplifier output signal on the magnetic field strength for different samples of diamond with NV centers.

During the measurements, the modulation signal of the photodetector current at frequency ω was recorded as the magnetic field B_1 was smoothly varied. Thus, the output

signal of the LIA was proportional to the derivative of the sample fluorescence intensity as a function of the magnetic field. The second pair of Helmholtz coils was used to generate an additional magnetic field B_2 . Depending on the experiment, the coils were positioned to create a field either axially or orthogonally aligned with the primary magnetic field B_1 .

As diamond samples, we primarily used 1 mm³ monocrystalline diamonds (HPHT1), synthesized using the high-pressure high-temperature (HPHT) method, with a high concentration of NV centers (around 7 ppm). Other diamond samples included polycrystalline diamond powder (HPHT2), as well as isotopically pure diamond samples (99.9999% ¹²C) grown by chemical vapor deposition (CVD1 and CVD2). The concentration of NV centers in the CVD1 and CVD2 samples was found to be 1,5 ppm and 4 ppm, respectively. Fig. 1(b) shows the experimental dependencies of the LIA output signal on the magnetic field strength for different diamond samples. The ZFCRL width (peak-to-peak) for the HPHT1 and CVD2 samples was approximately 11 G. For the CVD2 sample with the lowest NV center concentration, a significant reduction in both the amplitude and width of ZFCRL (down to 6 G) was observed. For polycrystalline material (HPHT2 sample) the ZFCRL width increased up to 15 G. We investigated the dependence of the ZFCRL width on temperature. As the temperature decreased from 25 to -5 °C, the linewidth narrowed from 11.1 to 10.4 G.

Fig. 2 present dependencies obtained under different orientations and magnitudes of an additional magnetic field, applied axially and orthogonally relative to the sweep magnetic field. Parallel orientation of the fields results in a shift of the ZFCRL position, proportional to the magnitude of the additional field. For mutually orthogonal orientations, the evolution of the ZFCRL shape exhibits a more complex behavior. In a weak magnetic field (<10 G), the position of the dispersion curve remains unchanged, while its contour broadens and the amplitude slightly decreases. A further increase in the magnetic field leads to the emergence of two additional resonances, which gradually separate as the field strength increases.

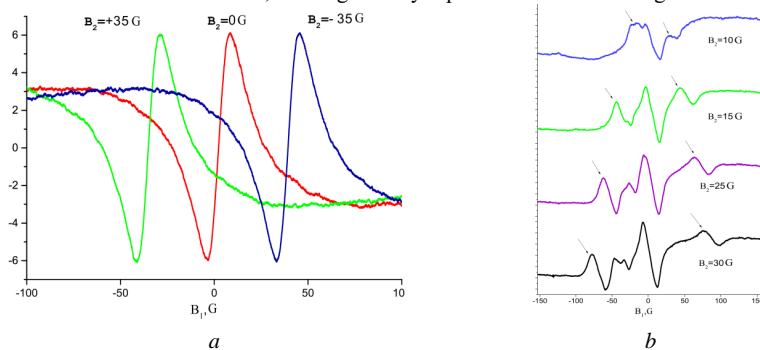


Figure 2. LIA signal dependence on the magnetic field strength when additional axial (a) and perpendicular (b) magnetic field are applied. Arrows indicate additional resonances.

ZFLAC-magnetometry

The presence of a linear region ($B < 5$ G) in the dispersion curve, which relates the applied magnetic field to the LIA output signal, makes it possible to use this signal for magnetic measurements. At the center of the curve, the LIA signal is zero. The following approaches can be used for magnetic measurements:

Measurement of Weak Magnetic Fields

No magnetic field sweep is applied. Only a slight modulation of the magnetic field is applied (approximately 0.1 G). When the measured magnetic field deviates from zero, its

magnitude is directly recorded by the change in the LIA output signal. Fig. 3(a) shows the temporal response of the magnetometer to a weak calibration magnetic field (0.5 G) varying over time as a square wave. The standard deviation of the signal from its mean value during one half-period, averaged over the entire measurement period, was 0.04 G.

Measurement of Strong Magnetic Fields

The LIA signal is fed through a power amplifier to one pair of the coils. Simultaneously, an alternating voltage at the modulation frequency (560 Hz) is applied to the same coils. A second pair of coils is aligned coaxially with the first and is used to generate the measured magnetic field. In this setup, the measured magnetic field is compensated using proportional control with negative feedback. The LIA output voltage (error signal) is converted into a control signal for the compensating magnetic field. The fields of the coils precisely cancel each other out, resulting in a net field of zero acting on the sample. Fig. 3(b) shows the temporal response of the LIA output signal to a smooth change in the measured magnetic field in the range of 0–60 G.

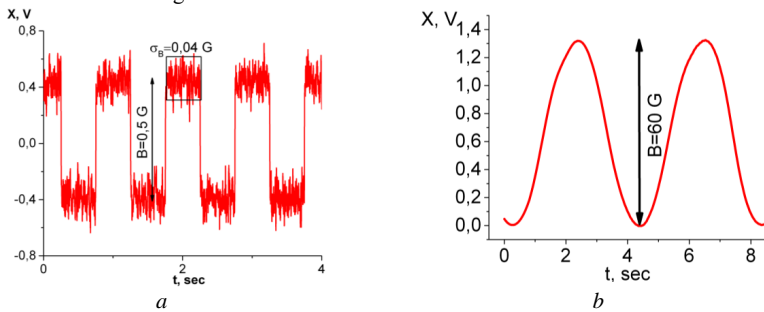


Figure 3. Temporal response of magnetometer in weak (a) strong (b) magnetic field modes

Conclusions

Magnetic spectra of NV center ensembles in diamond samples were obtained, showing pronounced zero-field resonances whose amplitude and width depend on sample type, NV center density and temperature. The effects of axial and transverse magnetic fields on these resonances were studied, demonstrating their potential for fully optical magnetometry without microwave fields. Simplified designs for NV-based optical magnetic sensors were proposed, enabling measurements in broad range of magnetic fields.

References

1. A. Wickenbrock, H. Zheng, L. Bougas [et al]. – App. Phys. Lett., 109, 053505 (2016).
2. H. Zheng, Z. Sun, G. Chatzidrosos [et al]. – Phys. Rev. Appl., 13, 044023 (2020).
3. D. S. Filimonenko, V. M. Yasinskii, A. P. Nizovtsev, S. Ya. Kilin. – Semiconductors, 52 (14), 1865-1867 (2018).
4. D. S. Filimonenko, V. M. Yasinskii, A. P. Nizovtsev, S. Ya. Kilin, F. Jelezko. – Semiconductors, 54(12), 1730-1733 (2020).
5. D. S. Filimonenko, V. M. Yasinskii, A. P. Nizovtsev, S. Ya. Kilin, F. Jelezko. – J. Appl. Spectrosc. 88(4) 1131-1143(2022).

Theory of two-stage quantum transduction based on use of magnetic material coupled to erbium-doped crystal

Aliya Galimova^{1,2}, Hasan Pişkin³, Rustem Khusnutdinov¹, Faik Mikailzade², Sergey A. Moiseev^{4,5}, Bulat Rameev^{1,2,5}

¹Kazan State Power Engineering University, Kazan/Tatarstan, 420066, Russian Federation

²Physics Department, Gebze Technical University, Gebze, Kocaeli 41400, Türkiye

³Department of Fundamental Sciences, Faculty of Engineering, Alanya Alaaddin Keykubat University, 07450 Antalya, Turkey

⁴Kazan Quantum Center, Kazan National Research Technical University, Kazan, 420111, Russian Federation

⁵Zavoisky Physical-Technical Institute – Subdivision of the Federal Research Center “Kazan Scientific Center of Russian Academy of Sciences”, Kazan/Tatarstan, 420029, Russian Federation

Approaches based on using hybrid structures based on a combination of a low-damping magnetically ordered (magnon) material with an Er-doped crystal to realize efficient quantum transduction have been theoretically studied. The application of magnon material (e.g. YIG) has the advantage of its strong coupling to microwave resonator modes, while Er-doped crystal provides a possibility of obtaining an effectively large magneto-optical interaction due to a single ion coherence transfer between magnetic and optic levels. Furthermore, the spin-wave oscillations can increase the coupling of microwave photons to Er^{3+} spin-flip transitions for two orders of magnitude. The basic parameters of two-stage microwave-to-optic transduction in the proposed hybrid system have been theoretically analyzed. The conditions needed for efficient coupling between magnetic resonance levels of Er^{3+} ions and spin wave modes have also been considered.

Introduction

The most of qubit realizations used for quantum information processing is based on the platforms operating at microwave frequencies, while long-distance transmission of quantum information is feasible only in the optical (and IR) frequency range. Therefore, quantum systems which can serve as units for the conversion (transduction) of quantum information from the MW to optical and reverse directions are needed. The work on quantum transduction requests the joining efforts of researchers working in various areas (e.g. material science, optics and microwave physics) and involves an essentially novel physics having profound importance for many other applications [1]. Microwave-to-optical (M-O) quantum conversion using rare-earth (RE) doped crystals relies on coherent transfer of quantum states between spin-flip MW transitions and optical transitions of the 4f shell of RE ions. There is however an issue in RE-based transduction related to a rather moderate strength of coupling between Er^{3+} spin-flip transitions in a diluted crystal and the MW resonator modes. The use of magnon material as a mediator has been proposed recently to overcome this issue and, in this manner, to increase the efficiency of quantum transduction [2,3].

In this work, we consider the use of the magnons in YIG as a possible efficient solution for increasing the coupling of microwave photons to Er^{3+} spin-flip transitions. Firstly, the basic parameters of two-stage MW-optic transduction in the proposed Erbium-YIG-based HQS have been theoretically analyzed. The conditions which provide the strongest interaction of the spin-wave oscillations of YIG with the magnetic resonance levels of Er^{3+} ions and spin-wave modes have been also considered. This comprehensive analysis aims to provide a deeper understanding of how to achieve optimal and efficient quantum transduction.

Basic theory of the two-stage quantum transduction

The standard input-output formalism has been used to analyze the dynamics of a two-stage quantum transductor. In this approach, the intermediate and output modes are expressed as functions of the input modes [4]. If intra-cavity fields of all the modes denoted as $\mathbf{a}(t) = (a, m_1, \dots, m_N, b)^T$ where a and b represent the input and output modes, and m_i ($i = 1, 2, \dots, N$) indicates intermediate modes, the Heisenberg equation of motion for the N -stage conversion system can be expressed in a compact matrix form:

$$\dot{\mathbf{a}}(t) = \mathbf{A}\mathbf{a}(t) + \mathbf{B}\mathbf{a}_{\text{in}}(t) \quad (1),$$

where $\mathbf{a}_{\text{in}}(t) = (a_{\text{in,ext}}, a_{\text{in,int}}, m_{1\text{in,int}}, \dots, m_{N\text{in,int}}, b_{\text{in,ext}}, b_{\text{in,int}})^T$ is the input field, matrices \mathbf{A} and \mathbf{B} can be found in the Appendix of the article [4]. The “ext” and “int” in the second subscript index denote the external coupling and the intrinsic loss of the ports, respectively, and we have assumed that each intermediate mode has only an intrinsic port. Besides, the input-output relation is given by:

$$\mathbf{a}_{\text{out}}(t) = \mathbf{B}^T \mathbf{a}(t) - \mathbf{a}_{\text{in}}(t) \quad (2)$$

When combined with the input-output relation, Eq. (1) can be solved in the frequency domain and the scattering matrix $\mathbf{S}[\omega]$ (defined by $\mathbf{a}_{\text{out}}[\omega] = \mathbf{S}[\omega]\mathbf{a}_{\text{in}}[\omega]$) can be obtained as:

$$\mathbf{S}[\omega] = \mathbf{B}^T [-i\omega \mathbf{I}_{N+2} - \mathbf{A}]^{-1} \mathbf{B} - \mathbf{I}_{N+4} \quad (3)$$

where \mathbf{I}_j is the identity matrix. The elements of the scattering matrix can be used to calculate the efficiency of quantum transduction. For the N -stage case, the efficiency is given by:

$$\eta[\omega] = |\mathbf{S}_{1,(N+3)}|^2 = |\mathbf{S}_{(N+3),1}|^2 \quad (4)$$

In our case, since we investigated the efficiency of two-stage ($N = 2$) system, we interested only in $\mathbf{S}_{1,5}$ or $\mathbf{S}_{5,1}$ matrix elements.

Using this formalism, we have calculated the efficiency of two-stage quantum transduction. The result is given below:

$$|\mathbf{S}_{1,5}|^2 = \left| \frac{i g_{12} g_{em} g_{om} \sqrt{k_{e,ext}} \sqrt{k_{o,ext}}}{k_o \left(\frac{k_{m1} \left(\frac{k_e k_{m2}}{4} + g_{em}^2 \right)}{2} + \frac{g_{12}^2 k_e}{2} \right) + \left(\frac{k_e k_{m2}}{4} + g_{em}^2 \right) g_{om}^2 + \frac{g_{om}^2}{2}} \right|^2 \quad (5)$$

where g_{ij} is the coupling rate, $k_{e,ext}$ and $k_{o,ext}$ represent external coupling rates, k_o , k_e , k_{m1} , and k_{m2} represent total dissipation rates.

Analysis of requirements for coupling of single ion ESR and collective spin-wave resonance modes

The conditions of the hybrid system at which the interaction of a hybrid system consisting of a magnetic material and rare earth (RE) ions is essentially enhanced have been established as given below. Below we consider a specific case of Er^{3+} ions as RE spin centers and yttrium iron garnet (YIG) as magnon material. In this case, the realization of the following two basic conditions is required: 1) the spin-wave resonant frequency excited in the YIG should nearly coincide with the spin transition resonance frequency of the Er^{3+} ions, 2) the magnitude of RF stray field due to spin wave oscillating should be maximal.

Following the analysis given in [6], at a fixed magnetic field, spin wave excitations are limited to a fixed range of frequencies between the limiting cases $k_x = 0$ and $k_x \rightarrow \infty$ as given below:

$$\sqrt{\omega_0(\omega_0 + \omega_M)} \leq \omega \leq \omega_0 + \omega_M/2 \quad (6)$$

The lower bound at $k_x = 0$ corresponds to the uniform precession (Kittel) mode, where all the spins inside the material precess in phase, while the short wavelength spin waves excited close to the upper limit $\omega_{sw}^{max} = \omega_0 + \frac{\omega_M}{2}$ reveal highly non-uniform precession. As a result of the non-uniform spin waves, locally highly intense stray RF magnetic fields are formed near the magnetic material. The calculations of work [6] have revealed that exactly near the boundary of “maximal” spin-wave angular frequency ω_{sw}^{max} the RF magnetic field acting on Er^{3+} centers is largely enhanced (100 times and even more). To find the conditions where we have strong interaction between two subsystems of the two-stage hybrid system (Er^{3+} ions and spin waves in YIG), the dispersion curves of the “maximal” spin waves ($\omega_{sw}^{max}(H) = \omega_0 + \frac{\omega_M}{2}$, where $\omega_0 = \gamma\mu_0 H$ and $\omega_M = \gamma\mu_0 M$ are the Larmor and demagnetization anisotropy angular frequencies) and the ESR transitions of Er^{3+} ions ($h\nu_{ESR} = g\mu_B H$, where g-factor value is anisotropic) have to be compared. Taking into account the fact that the g-factor of Er^{3+} ions in various hosts can vary in a broad range (typically from 0.5 to 15, depending on crystal symmetry and magnetic field orientation), we obtain a requirement for the hybrid system operation. Figure 1 reveals that the dispersion curve of “maximal” spin waves in YIG will cross with the dispersion curve of the erbium ESR transition only for the case of Er^{3+} g-factor values essentially higher than 2.

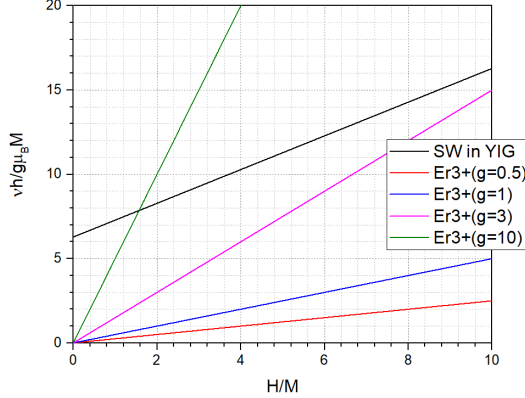


Fig. 1. The dispersion curves of “maximal” frequency for spin waves in YIG and erbium ESR transitions for various values of Er^{3+} g-factors.

Thus, the proper alignment of the crystal doped with Er^{3+} ions with respect to the thin film magnetic material (e.g. YIG shaped as a microstrip) is required. Furthermore, our analysis reveals that the Er^{3+} doped crystals of low symmetry may be advantageous because of the possibility of obtaining higher effective g-factor values needed to match the Er^{3+} and YIG microwave transitions

Conclusion

A two-stage hybrid system to increase the efficiency of MW-optic quantum transduction has been proposed. For solving the issue of weak coupling between rare earth (e.g. Er^{3+}) spin transitions and MW resonator modes, an approach based on the use of magnetic material (yttrium iron garnet, YIG) close to the rare-earth (RE) doped crystal has been theoretically considered. A theory and the basic parameters of two-stage quantum transduction based on a combination of RE dopants in various crystal hosts and a thin film magnetic material have been outlined. It has been demonstrated that it is possible to use the

spin-wave oscillations of magnon material to increase essentially a coupling MW resonator to RE spin-flip transitions. The conditions needed for efficient coupling between magnetic resonance levels of RE ions and spin wave modes have been also evaluated.

Acknowledgements

The work was supported by the TÜBİTAK project No. 121F274 and the project Otan G5859. The authors also acknowledge the support of the Technology Transfer Office (TTO) of Gebze Technical University (GTU). A.G. also thanks a grant from the Government of the Republic of Tatarstan "Algarysh" for the support of her training and internship visit to GTU.

References

1. C. Bonizzoni, M. Maksutoglu, A. Ghirri, J. van Tol, B. Rameev & M. Affronte. Coupling Sub-nanoliter BDPA Organic Radical Spin Ensembles with YBCO Inverse Anapole Resonators. *Appl. Magn. Reson.* 54, 143–164 (2023).
2. T. Puel, A. Turflinger, S. Horvath, J. Thompson, & M. Flatté. Enhancement via the Kittel mode of a magnet of the microwave to optical quantum transduction in a rare-earth-doped crystal. In: *APS March Meeting Abstracts*, vol. 68(3), 2023, Y67-003 (Las Vegas, Nevada, USA, March 5-10, 2023).
3. T. O. Puel, A.T. Turflinger, S. P. Horvath, J. Thompson, & M.E. Flatté. Enhancement of microwave to optical spin-based quantum transduction via a magnon mode, *Proc. SPIE PC12911*, Quantum Computing, Communication, and Simulation IV, PC129110H (13 March 2024); <https://doi.org/10.1117/12.2692534>.
4. X. Han, W. Fu, C.-L. Zou, L. Jiang, and H. X. Tang, “Microwave-optical quantum frequency conversion,” *Optica* 8, 1050–1064 (2021).
5. Engelhardt F., Bittencourt V. A. S. V., Huebl H., Klein O. and Kusminskiy S. V. Optimal broadband frequency conversion via a magnetomechanical transducer *Phys. Rev. Appl.* 18, 044059 (2022).
6. C. Mühlherr, V. O. Shkolnikov, and G. Burkard, Magnetic resonance in defect spins mediated by spin waves, *Phys. Rev. B* 99, 195413 (2019).

Cell size dependence of diffusion properties of PAMAM dendrimers by MD simulations

*Naira R. Gromova,^{1,2} Andrei V. Komolkin,¹ Amina D. Muratova,¹ Denis A. Markelov,¹
¹St Petersburg University, 7-9 Universitetskaya Emb., St Petersburg 199034, Russia
²Kazan State Power Engineering University, 51 Krasnoselskaya st., 42006 Kazan, Russia
 E-mail: nai.khus@yandex.ru*

Introduction

Dendron-type macromolecules called dendrimers are multifunctional structures with unique characteristics that distinguish them from other polymer systems. Their structure includes a central part (core), from which branches of various lengths extend radially, ending with functional groups. Due to such features as controlled size and shape through generations, high functionality and the possibility of modification, such molecules are becoming promising materials for the creation of innovative drugs, new composites and biotechnological solutions. Due to their large size and the complexity of the branched structure, even the computer simulation faces several difficulties [1]. These include the need to collect a large amount of data and a significant increase in calculation time (microseconds with a step in femtoseconds). We studied methanol solutions of PAMAM dendrimers (generations $G = 2-6$) at 300 K using the molecular dynamics (MD) method.

Computer simulation details and results

Simulation cell with single dendrimer and different number of molecules of solvent (i.e. different linear size of cubic simulation box, L) were simulated for each generation. Periodic boundary conditions and the force field OPLSAA [2] were used in the Gromacs 2021.4 package [3]. The equilibration of dendrimer was carried out for 200ns. And after the MD simulations were continued for 3 ms to collect data to calculate system performance. Main simulations were performed in the NPT ensemble using Berendsen barostat [4] and V-rescale thermostat [5] (B/V pair). From simulation data we calculate diffusion coefficient from mean square displacement, MSD using Einstein equation:

$$MSD(t) = 6Dt, \quad (1)$$

where D is the diffusion coefficient, t is time.

As we expected for each dendrimer a diffusion coefficient grows with increasing simulation cell. In order to eliminate this modelling artefact, we correct diffusion coefficient by using standard approach [6].

$$D_L \approx D_{MD} + 2.837 \frac{k_B T}{6\pi\eta_{sol}vL}, \quad (2)$$

where D_L and D_{MD} are rescaled and MD-derived diffusion coefficients, η_{sol} is the solvent viscosity, $\xi = 2.837$ is hydrodynamic constant, T is temperature.

After that we obtain hydrodynamic radius of dendrimers by Stokes equation:

$$R_h = \frac{k_B T}{6\pi\eta_{sol}vD}, \quad (3)$$

Unfortunately, this standard approach Eq. (1)-(3) gives results which do not correlate with experimental data. For instance R_g/R_h ratio practically does not changes with dendrimer generation number in contrast to experimental data. Thus, in order to simulation box size we utilized other method which was developed in work [7]. In this method R_h is the value calculated from the diffusion coefficient corresponding to an infinitely diluted solution approximated using all the values obtained for a specific generation. This method gives R_h values which are in agreement with experimental data.

Additionally, we calculate R_h from rotational diffusion of dendrimer. This approach gives similar results as approach from work [7]. Moreover, the obtained R_h from rotational diffusion practically do not depend on L . Thus, we believe that this method are suitable to estimate diffusion properties of dendrimers macromolecules.

Conclusions

Thus, in this work we investigated the diffusion properties of PAMAM dendrimers in methanol solutions using molecular dynamics simulations. Initially, we calculated the hydrodynamic radius (R_h) using a standard approach, but the results did not align with experimental data. To improve accuracy, we applied an alternative method which considers an infinitely diluted solution and found better agreement with experiments. Additionally, R_h values derived from rotational diffusion showed consistency and independence from simulation cell size. The findings emphasize the importance of addressing finite-size effects in MD simulations and demonstrate the reliability of alternative methods for estimating R_h .

Acknowledgements

This work is supported by the Russian Science Foundation (grants no. 23-13-00144). The simulations were performed at the Computer Resource Center of Saint Petersburg State University.

References

1. Khusnutdinova N.R., Markelov D.A. Hydrodynamic radius of dendrimers in solvents // Phys. Chem. Chem. Phys. The Royal Society of Chemistry, 2023. Vol. 25, № 41. P. 28220–28229.
2. Kaminski G.A. et al. Evaluation and reparametrization of the OPLS-AA force field for proteins via comparison with accurate quantum chemical calculations on peptides // J. Phys. Chem. B. 2001.
3. Hess B. et al. GRGMACS 4: Algorithms for highly efficient, load-balanced, and scalable molecular simulation // J. Chem. Theory Comput. 2008.
4. Berendsen H.J.C. et al. Molecular dynamics with coupling to an external bath // J. Chem. Phys. 1984.
5. Bussi G., Donadio D., Parrinello M. Canonical sampling through velocity rescaling // J. Chem. Phys. 2007.
6. Yeh I.-C., Hummer G. System-size dependence of diffusion coefficients and viscosities from molecular dynamics simulations with periodic boundary conditions // J. Phys. Chem. B. ACS Publications, 2004. Vol. 108, № 40. P. 15873–15879.
7. Lebedenko O.O. et al. Using NMR diffusion data to validate MD models of disordered proteins: Test case of N-terminal tail of histone H4 // Biophys. J. 2024.

NMR Transverse Relaxation as the Tool for Structure and Thermodynamics Analysis

Leonid Grunin^{1,2}, Yurii Grunin¹, Mariia Ivanova^{1,2}

¹ Volga State University of Technology, Lenin sq. 3, Yoshkar-Ola, Russia

² Resonance Systems Corporation, www.nmr-design.com

E-mail: mobilenmr@hotmail.com

Using the classical approach of Bloembergen–Purcell–Pound for relaxation times calculation is not really the uniform method for those types of samples that contains phases with constrained translational molecular mobility, so it has been suggested [1] the Second Moment Approximation way to utilize the *observed* T_2^* assuming that the initial part of fast falling Free Induction Decay can be fitted with the Gaussian function even if the rest of the signal might have oscillations. In other words, the T_2^* is derived from the second moment M_2 of the substituted Gaussian spectrum:

$$T_2^* = \sqrt{\frac{2}{M_2}} \quad (1)$$

This way allows for quite elegant characterization of solids structures apart from ambiguous multiple parametric fitting of time-domain FID signals.

As it was found in previous researches [2], while analyzing the NMR relaxation behavior of water molecules adsorbed on cellulose fibers, many thermodynamic potentials can be expressed in terms of T_2 , because for various types of motions it is inversely proportional to the correlation time. One of the remarkable findings there deals with the entropy that follows linearly the logarithm of changing T_2 from one adsorption layer to another. This very fact can be further expanded to *dynamical entropy* by assuming ergodicity for translational motions unfrozen samples to their structure: the number of microstates would grow with the decrease of correlation times. And while $T_2 \sim 1/\tau_c$:

$$\Delta S_{1 \rightarrow 2} \propto \ln \frac{T_{22}}{T_{21}} \quad (2)$$

This expression can be also derived by several other ways, for example from the definition of heat capacities. However, the straight implementing of (2) to any systems might meet distortions by paramagnetic impurities and restriction of molecular motions closer to crystallization or glassy states, where ergodicity does not take place. The last issue leads to consideration of structural *entropy*. So, for rigids, by taking the relaxation times from (1) and assuming the motional contribution only from constrained vibrations, the expression (2) should be reconsidered with much less proportional coefficient. Nonetheless, the general trend is already observed experimentally as it is shown in the Figure:

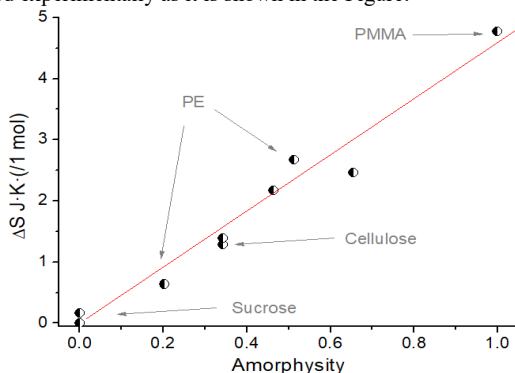


Figure 1. Entropy change calculated by (1) and (2) for some polycrystalline solids

The range of possible applications coming out of NMR Transverse Relaxation measurements varies from science fundamentals to updates of analytical methods like calorimetry or crystallography.

References

1. J. van Rooyen, L. Grunin, M. Oztop, D. Kruk, M. Manley. Unravelling temperature-dependent molecular changes in hydrated wheat and maize starches using ^1H time-domain NMR. – *Journal of Food Engineering* 375, 112041 (2024).
2. Yu. Grunin, M. Ivanova, D. Masas, and L. Grunin. Thermodynamics of Adsorption in a Cellulose–Water System. – *Russian Journal of Physical Chemistry A*, vol 94, No. 4, pp. 704–708 (2020)

Study of complex ionic liquids according to NMR relaxation and diffusion measurements.

Alexandr V. Ievlev¹, Konstantin V. Tyutyukin¹, Oscar Cabeza², Luis M. Varela³

¹*Department of Nuclear Physics Research Methods, Saint Petersburg State University, St. Petersburg 198504 Russia*

²*Departamento de Física y Ciencias de la Tierra, Facultade de Ciencias, Universidade da Coruña, Campus de A Zapateira s/n, E-15071 A Coruña. Spain*

³*Grupo de Nanomateriales, Fotónica y Materia Blanda, Departamento de Física de Partículas, Facultade de Física, Institute of Materials (iMATUS) Universidade de Santiago de Compostela, Campus Vida s/n, E-15782 Santiago de Compostela, Spain*

E-mail: a.ievlev@spbu.ru

Introduction

This work is a continuation of a series of studies [1–3] providing a comparison of ionic mobility in several complex ionic liquids based on 1-butyl-, 3-methyl-, imidazole thiocyanate [BmimSCN]. In particular, we consider novel ionic liquids in which different metals were used as the basis of the complex anion (for the details of the synthesis of compounds, see [4]). The resulting ILs differ from BmimSCN in physicochemical properties, such as color, viscosity, conductivity, operating temperature range, molecular mobility, etc.

Results and discussions

Spectra

Figure 1 show on the left the full ^{13}C spectrum of pure BmimSCN, and on the right the stack of spectra of thiocyanate complexes with Hg, Al, Cu, Zn, Cd, in comparison with the base IL. It is clearly seen that the carbon line of the SCN anion shifts depending on the complexing metal, but remains localized in the region of the imidazole ring lines from 120 to 140 ppm.

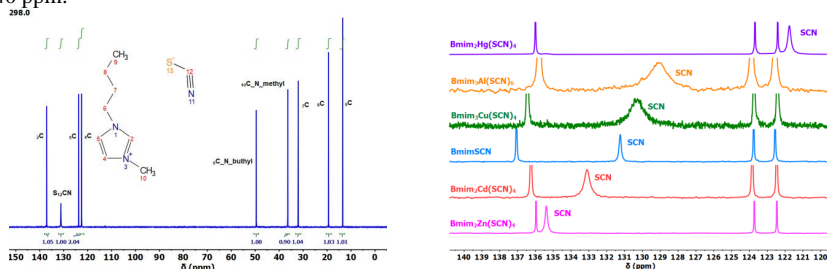


Figure 1. (left) Full spectrum ^{13}C at 298K, for pure BmimSCN, (right) A stack of ^{13}C spectra of metal complexes of 1-butyl-, 3-methyl imidazole thiocyanates.

For the complex with aluminum and copper, a broadening of the thiocyanate line is observed. This can be explained by stronger bonds with the metal, because the width of the spectral line depends on the length of the metal-ligand bond and is determined by the spin-spin relaxation time.

Diffusion

All measurements of diffusion coefficients were carried out in the resource center of the MRMI on a Bruker Avance III 400 spectrometer (100.65 MHz for carbon). The diffusion coefficients were calculated from the dependence of the attenuation of the integral intensities of the spectral lines recorded in the experiment on the square of the amplitude of the gradient pulses. The maximum strength of the gradient pulses of the magnetic field used in the

experiment was 3000 G/cm. The duration of these pulses and the interval between them were chosen as 0.001 s and 0.1 s, respectively. The temperature range in which the diffusion coefficients measurements were carried out was from 273 K to 363 K. For both cation and anion the information was obtained in experiments on the ^{13}C nucleus, while for Bmim^+ the diffusion coefficient was averaged over all spectral lines related to cation.

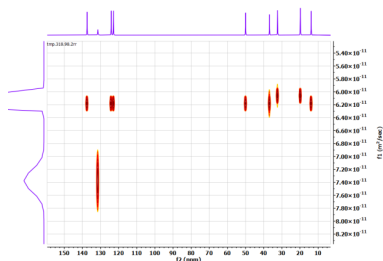


Figure 2. ^{13}C DOSY spectrum of the base BmimSCN at 318 K.

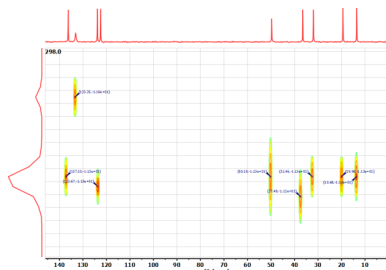


Figure 3. ^{13}C DOSY spectrum of the complex with cadmium at a temperature of 298 K.

Figures 2 and 3 show two-dimensional diffusion-weighted spectra of both the base BmimSCN and the complex ionic liquid with cadmium. It is clearly seen that in the base IL the thiocyanate anion has a higher mobility, and in the complex it is lower, compared to the mobility of the cation.

Table 1. Summary data on diffusion coefficients at a temperature of 298 K, measurements at ^{13}C are given.

Sample	δ_{SCN} , ppm	$D_{\text{Bmim}}/D_{\text{SCN}}$	$D \times 10^{12}$, $\text{m}^2 \text{s}^{-1}$	
			Bmim^+ average	SCN^-
$\text{Bmim}_3 \text{ Al}(\text{SCN})_6$	129.11	4.9	0.93	0.19
$\text{Bmim}_2 \text{ Zn}(\text{SCN})_4$	133.11	2.6	11.93	4.52
$\text{Bmim}_2 \text{ Cd}(\text{SCN})_4$	135.39	2.1	4.63	2.21
$\text{Bmim}_2 \text{ Hg}(\text{SCN})_4$	121.76	1.5	15.01	10.08
$\text{Bmim}_3 \text{ Cu}(\text{SCN})_4$	130.28	1.3	7.52	5.86
Bmim SCN	131.25	0.8	20.31	24.34

Table 1 shows the data on the mobility of anions and cations in the ionic liquids studied. The highest ratio of anion and cation mobilities was observed for the complex with aluminium, which can be explained by the size of the complex anion. The data presented in the table confirm the fact of the formation of very stable anionic complexes from thiocyanate and metal ions, the mobility of which slows down compared to the Bmim^+ cation from 1.3 to 5 times for different complexes.

Relaxation

To measure the spin-lattice relaxation rates, a standard inversion-recovery pulse sequence was used. All measurements were also performed at the MRMI resource center on a Bruker Avance III 500 MHz spectrometer (500 MHz for protons and 125.7 MHz for carbon). To analyze the temperature dependences of the relaxation rates for both nuclei, the BPP theory was used, as in Refs. [5,6]. Here we decided to present the reorientation times of the carbon nucleus belonging to the anion, calculated from the experimental values of the spin-lattice relaxation rates. Figure 4 shows the temperature dependences of the reorientation time of

carbon nuclei structurally included in the thiocyanate anion SCN^- for all the ionic liquids considered.

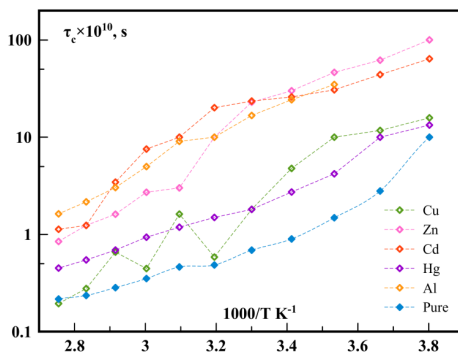


Figure 4. Temperature dependence of the reorientation time of the carbon nucleus in thiocyanate in complexes with metals: Cu, Zn, Cd, Hg, Al.

For all the studied complexes, a slowdown in mobility is observed, and this concerns not only intramolecular mobility (data on reorientation times), but also translational mobility (data on diffusion coefficients). In the studied temperature range, the change in the reorientation times of molecular groups was no more than two orders of magnitude, from units to hundreds of nanoseconds.

Acknowledgements

This work is supported by Russian Science Foundation (RSF): grant № 23-23-00430. Thanks to the staff the Resource Centre for Magnetic Resonance of Research Park at SPBU for carrying out NMR experiments.

References

- O. Cabeza, L. Segade, M. Domínguez-Pérez, E. Rilo, D. Ausín, J.A. Seijas, M.P. Vazquez-Tato, V. Matleev, A. Ievlev, J. Salgado, L.M. Varela, Strange behaviour of transport properties in novel metal thiocyanate based ionic liquids, *J. Mol. Liq.* 340 (2021) 117164. <https://doi.org/10.1016/j.molliq.2021.117164>.
- A.V. Ievlev, A.V. Koroleva, K.V. Tyutyukin, V.V. Matveev, O. Cabeza, L.M. Varela, NMR and X-ray photoelectron spectroscopy possibilities for study complex ionic liquids, in: *Magn. Reson. ITS Appl.*, St. Petersburg University Publishing House, Saint-Petersburg, 2020: pp. 89–91.
- A. V. Ievlev, K. V. Tyutyukin, N. V. Pokhvishcheva, Molecular and ionic mobility of ionic liquids with complex anions containing metals, in: *Magn. Reson. ITS Appl.*, St. Petersburg University Publishing House, Saint-Petersburg, 2024: pp. 91–93. <https://elibrary.ru/item.asp?id=67226989&pf=1>.
- O. Cabeza, L.M. Varela, E. Rilo, L. Segade, M. Domínguez-Pérez, D. Ausín, I. de Pedro, J.R. Fernández, J. González, M.P. Vazquez-Tato, Y. Arosa, E. López-Lago, R. de la Fuente, J.J. Parajó, J. Salgado, M. Villanueva, V. Matveev, A. Ievlev, J.A. Seijas, Synthesis, microstructure and volumetry of novel metal thiocyanate ionic liquids with [BMIM] cation, *J. Mol. Liq.* 283 (2019) 638–651. <https://doi.org/10.1016/j.molliq.2019.03.088>.
- V. V. Matveev, D.A. Markelov, E.A. Brui, V.I. Chizhik, P. Ingman, E. Lähderanta, ¹³C NMR relaxation and reorientation dynamics in imidazolium-based ionic liquids: Revising interpretation, *Phys. Chem. Chem. Phys.* (2014). <https://doi.org/10.1039/c4cp00637b>.
- V. V. Matveev, D.A. Markelov, A. V. Ievlev, E.A. Brui, K. V. Tyutyukin, E. Lähderanta, Molecular mobility in several imidazolium-based ionic liquids according to data of ¹H and ¹³C NMR relaxation, *Magn. Reson. Chem.* 56 (2018) 140–143. <https://doi.org/10.1002/mrc.4681>.

^2H NMR study of $[\text{P}_{444}\text{-D}][\text{OMs}]$ and $[\text{N}_{444}\text{-D}][\text{OMs}]$ ionic liquids

Alexander E. Khudozhnikov¹, Daniil I. Kolokolov¹

¹ Boreskov Institute of Catalysis, Siberian Branch of Russian Academy of Sciences, Prospekt Akademika Lavrentieva 5, Novosibirsk 630090, Russia

E-mail: alexandr.khudozhnikov@gmail.com

Close interest to ionic liquids (IL) has led to the tremendous number of new compounds that have been synthesized. Among them phosphonium-based ILs (PILs) become more popular particularly over the past decade. Compared to the ammonium-based ILs, they are considered to have superior thermal stability and conductivity [1] as well as lower viscosity [2, 3].

Several studies took interest in the reasons of better performance of PILs compared to their ammonium analogues. However, these studies are mostly limited to the tetraalkylphosphonium based IL, i.e. aprotic ionic liquids. To the best of our knowledge, the protic variant of the phosphonium ILs, such as ILs based on the trialkylphosphonium cation was studied only by Luo et al.[4]: by use of IR spectroscopy the authors have shown that N-H group of $[\text{Oct}_3\text{NH}][\text{OTf}]$ is involved in the strong hydrogen bonding network, whereas hydrogen bonds in $[\text{Oct}_3\text{PH}][\text{OTf}]$ are too weak to impact the P-H vibrations.

In this contribution we compare tributylammonium and tributylphosphonium mesylate ILs ($[\text{N}_{444}\text{-D}][\text{OMs}]$ and $[\text{P}_{444}\text{-D}][\text{OMs}]$). We investigate the dynamics of cations by ^2H NMR spectroscopy both in the solid and liquid state. The ^2H NMR spectral line shape and spin relaxation provides insight on the interaction between ions: hydrogen bonding strength and arrangement, as well as the phase transition phenomena in these ILs. The ^2H NMR spin relaxation in the liquid state characterizes the cation dynamics and allows to probe the microscopic viscosities of ILs. We focus on the mesylate as a model strong hydrogen bond acceptor anion. We support our experimental observation by quantum chemical calculation of the ionic pair structure. The optimization of the cluster containing 4 ion pairs is performed on the density function theory level. The hydrogen bond is characterized with natural bond orbital analysis.

Acknowledgements

This work has been supported by the Russian Science Foundation (grant № 24-73-00032, <https://rscf.ru/en/project/24-73-00032/>).

References

1. O. Palumbo, A. Paolone, F. Philippi, D. Rauber, T. Welton, – Int. J. Mol. Sci., 24(13), 11046 (2023).
2. C. Maton, N. De Vos, C. V. Stevens, – Chem. Soc. Rev., 42, 5963-5977 (2013).
3. S. M. Vahdat, M. A. Zolfigol, S. Baghery, – Appl. Organomet. Chem., 30, 311-317 (2-16).
4. J. Luo, O. Conrad, I. F. J. Vankelecom, – J. Mater. Chem., 22, 20574-20579 (2012).

Determination of anti-peroxyl radical capacity of flavonoids (quercetin, morin and rutin) by the kinetic EPR method with pulse reactant injection.

Gaspar Kocharyan, Makich Musaelyan

A.B. Nalbandyan Institute of Chemical Physics NAS RA, Yerevan, Armenia

E-mail: kocharyangg@ichph.sci.am

http:// https://www.ichph.am/

Introduction

Flavonoids are polyphenolic compounds with a general structure of C₆-C₃-C₆. In plants, they act as secondary metabolites and exhibit a wide range of protective functions [1].

The relevance of studying flavonoids is due to their broad spectrum of biological activities. These compounds exhibit anti-inflammatory, antifungal, and antiviral properties and play a significant role in preventing the development of neurodegenerative diseases. In most cases, the development of oncological, cardiovascular, and neurodegenerative diseases is associated with the effects of free radicals. Free radicals cause damage to cell membranes and macromolecules, leading to the emergence of various pathologies [2].

The most important property of flavonoids is their antioxidant activity, which is determined by the structure and number of functional groups. The primary mechanisms of radical scavenging include the direct neutralization of free radicals and the chelation of transition metals, which catalyze the formation of free radicals. In the process of scavenging radicals, the hydroxyl groups of ring B and A play a key role [3].

The aim of the study is to determine the antioxidant capacity of flavonoids—quercetin, morin, and rutin (Fig. 1)— and establish the relationship between the anti-peroxyl radical capacity and the structure of the flavonoid.

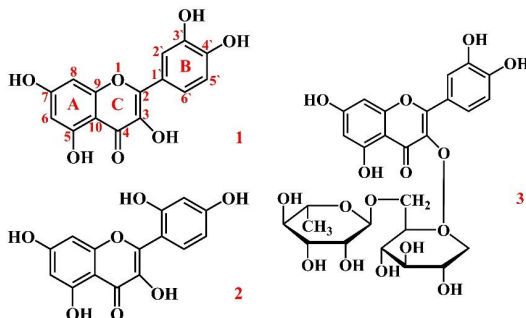


Figure 1. Molecular structures of the studied flavonoids: quercetin (1), morin (2), rutin (3).

Method

Using the kinetic-EPR method with pulse reactant injection [4], the reactions of *tert*-butylperoxyl radicals with quercetin, rutin, and morin were studied. This method offers advantages over other by direct measuring antioxidant activity and allows monitoring changes in the concentration of peroxyl radicals during their interaction with the antioxidant.

Results

The anti-peroxyl radical capacities of the studied flavonoids were measured by titration with an excess of *tert*-butylperoxyl radicals. As a reference antioxidant, the water-soluble analog of α -tocopherol, Trolox, was used, for which the anti-peroxyl radical activity

is $f = 2$. Based on the titration curves (Fig. 2) and using equation (1), the antiperoxy radical capacities were calculated and are presented in Table 1.

$$f = \frac{\Delta[\text{RO}_2^\bullet]}{[\text{AO}]_0} \quad (1)$$

where $\Delta[\text{RO}_2^\bullet]$ – the amount of the $[\text{RO}_2^\bullet]$ radicals consumed during the reaction, $[\text{AO}]_0$ – initial concentration of flavonoids.

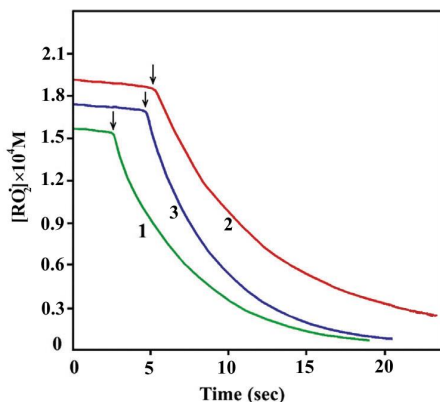


Figure 2. Kinetic decay of tert-butylperoxy radical due to reaction with the injected antioxidants quercetin (1), morin (2), rutin (3).

Table 1. Anti-peroxy radical capacities of the selected flavonoids.

Antioxidant capacity	Quercetin	Rutin	Morin	Trolox
f	3,55	2,3	1,3	2

Acknowledgements

This work is supported by the supported by the Science Committee of the Republic of Armenia, in the frames of the research project No. 21AG-1D034.

References

1. S. K. Pawar, S. Jaldappagari. – Journal of Molecular Recognition, 33.1 e2812 (2020).
2. A. Roy, A. Khan, I. Ahmad, S. Alghamdi, B. S. Rajab, A. O. Babalghith, M. R. Islam. – BioMed research international, 1, 5445291 (2022)
3. M. M. Kasprzak, A. Erxleben, J. Ochocki. – Rsc Advances, 5(57), 45853-45877 (2015).
4. L.A. Tavadyan, M.V. Musaelyan, A.B. Stepanyan, S.H. Minasyan. – Appl Magn Reson., 51, 1049-1069 (2020).

RFI suppression in the absence of magnetic resonance sensor shielding

P. Kupriyanov¹, G. Mozhukhin¹, N.G. Sarıbaş³, B. Rameev^{1,3,4}

¹*Department of Physics, Gebze Technical University, Gebze, Kocaeli 41400, Türkiye*

²*Institute of Nanotechnology, Gebze Technical University, Gebze, Kocaeli 41400, Türkiye*

³*Kazan State Power Engineering University, Kazan, Tatarstan 420066, Russian Federation*

⁴*Zavoisky Physical-Technical Institute, FRC Kazan Scientific Center of RAS, Kazan, Tatarstan 420029, Russian Federation*

Introduction

The magnetic resonance study that can't be carried out with sensor shielding is a particular problem. Especially, this situation takes place in the case of nuclear quadrupole resonance (NQR) for explosives detection [1]. One of the most famous applications for improvised explosives is using of ammonium nitrate (AN) in fertilizers. In comparison with military explosives the quantities of AN compounds need higher values [2]. The sample mass may be near 150-200 kg to reach a significant effect. The detection may be if the sensor volume is a few cubic meters. Effective shielding is very difficult for NQR sensor. The only way to compensate for interferences is by using unique geometry for the sensor and designing an electronic compensation system. In this report, we consider the second one in detail. We have a task to suppress induced interference on a sizeable toroidal sensor with an open space for a sample measuring 1.4x1.4x2 meters. It is a nitrogen-containing fertilizer. Signal detection is carried out by the NQR method with a frequency of 423 kHz. This low-frequency task requires complex shielding from significant magnetic components, mainly if registration occurs in an area with industrial electromagnetic pollution.

Phase shifting compensate system

The principle of operation of a compensated system is to obtain the same type of interference from the sensor and coils of the system and shift their phase so that the signals are in the antiphase and cancel each other out.

We already had a positive experience [3] with one compensation cylindrical coil and a phase-shifting circuit for an NQR device with a gradiometer coil as a sensor. However, there are problems with compensating RF noise from the sensor as a toroid with a gap (fig. 1)

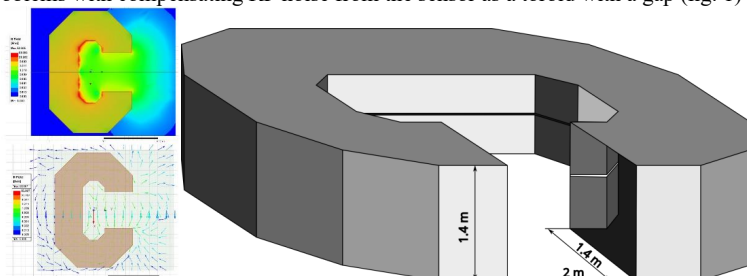


Fig.1. Image of receiver toroid coil with a gap for sample (right), model of its magnetic field (left).

Trying to compensate for interference with a simple solenoid coil had failed. This is due to the different radiation patterns of coils with various geometries. The solenoid has a broader radiation pattern. Under the same conditions, cylindrical coils gain more noise than toroidal coils with a geometry that considerably compensates for interference. Using a coil of the same geometry as the sensor for compensation is reasonable.

Experiment

The system we want to use to compensate for interference consists of two channels with consoles. Every console contains an amplifier and resonance circuit. The terminal represents the aluminum box with a coil on the plastic leg's top (fig. 2).

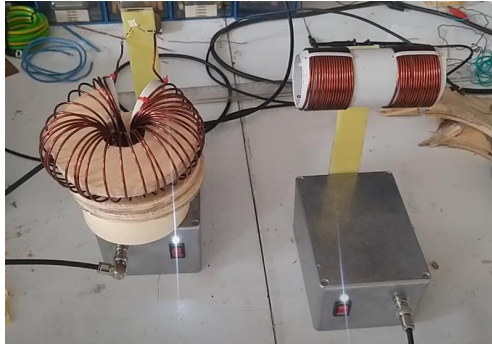


Fig.2. Two console variants with different receiver coils: solenoid on the right and toroid on the left.

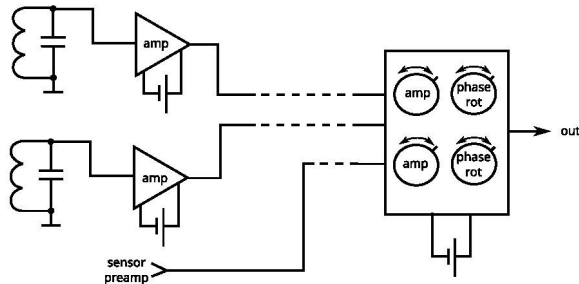


Fig.3. Compensation system diagram

Despite identical radiation patterns, specters of noise in signals from the sensor and the compensating coil did not match. We found only one reason for the problem. Sensors and compensation coils have different Q-factors. Indeed, a sizeable single-turn copper foil coil has a very high Q of about 200, while a compensation coil, on the contrary, has about 20. The only option to increase the quality factor of the coil is to take a thicker wire. But in our case, it will make the coil bulky. But there is another way. We can use an electronic filter with a narrow bandwidth. We are at this stage now.

For electronic design, we chose the affordable chip component AD862. It has two operational amplifiers in the housing and a wide bandwidth of 8 MHz. The console box contains one of these chip components. The first element of the chip is used as an amplifier, and the second element is the basis of the active filter.

Signals from consoles enter the control device via coaxial cables. The control device comprises phase shifters and potentiometers for controlling amplitudes of signals and summer.

We are not sure that a compensation system will completely eliminate interference. It may be necessary to use particular shielding for the gap of the toroidal coil. However, shielding will not require much material or incur many costs if the compensation system works effectively.

Conclusion

Thus, we designed three channel sensor systems for attenuation of outside interference. Use every additional channel allows decreasing one frequency interference signal at least 20-30 db. Summary attenuation may reach 40-50 db. However, in the case of multiple frequencies interference signals, we need to tune every channel for individual frequencies. Experimental estimations produce near 30 db attenuation.

References

1. J.B. Miller, G.A. Barrall, "Explosives Detection with Nuclear Quadrupole Resonance", *American scientist*, Vol. 93 (1), 50 (2005)
2. G.V. Mozzhukhin, S.V. Molchanov, G.S. Kupriyanova, A.V. Bodnya, V.V. Fedotov, Guoxin Hao, Yanbo Jin, Tianliang Ren, Guojin Zhang. The Detection of Industrial Explosives by the Quadrupole Resonance Method: Some Aspects of the Detection of Ammonium Nitrate and Trinitrotoluene; In: *Explosives Detection using Magnetic and Nuclear Resonance Techniques*, NATO Science for Peace and Security Series B: Physics and Biophysics, (Eds: Fraissard, Jacques; Lapina, Olga), Springer 2009, pp. 231-244.
3. E. Doğan, K. Çinar, P. Kupriyanov, G. Mozzhukhin and B. Rameev. "Development of Method for Suppression of Transient Processes in Large Power NQR Sensor," 2023 Photonics & Electromagnetics Research Symposium (PIERS), Prague, Czech Republic, 2023, pp. 917-920, doi: 10.1109/PIERS59004.2023.10221332.

Study of the influence of Au nanoparticles of various shapes on the dynamics and structure of tyrosine using ^1H NMR methods

Galina Kupriyanova, Mark Smirnov, Andrey Zyubin, A. Zozulya, Ivan Lyatun

¹Immanuel Kant Baltic Federal University, 236041 Kaliningrad, Russian Federation

E-mail: GKupriyanova@kantiana.ru

Introduction

The use of nanoparticles (NPs) and nanomaterials in medicine has significantly expanded their potential for the treatment of diseases and opened up new opportunities in the development of new pharmaceuticals, drug delivery systems, and tissue regeneration [1]. Amino acid-functionalized (AA) metal nanoparticles (NPs) have significant prospects. However, to improve the methods of molecular design and further study of the AA-NPs system, a comprehensive understanding of the interaction mechanisms, dynamic properties, and structural changes that occur in organic molecules under the influence of metal NPs is required. Various analytical methods, including electron absorption spectroscopy, Raman spectroscopy, Fourier transform infrared spectroscopy (FTIR), and high-resolution ^1H NMR spectroscopy have been used to study the effect of metal NPs on some amino acids. It was found that amino acid molecules are adsorbed on the surface of NPs, forming a "protein crown" - a soluble dynamic complex. The geometry and adsorption rate of 20 amino acids near the surface of Au NPs were modeled. [2] NMR spectroscopy was also successfully used to study samples containing metal nanoparticles. We used diffusion-ordered NMR spectroscopy (DOSY) to study the dynamics of aqueous tyrosine solution samples (AST) in the presence of Au NPs and platinum nanoparticles (Pt NPs) [3]. In [3], the effect of metal nanoparticles on the translational mobility of AST was studied, and changes in the hydrodynamic radius of AA molecules were found during adsorption near the surfaces of nanoparticles. However, it should be noted that there are some difficulties in determining internuclear distances and structural changes in the presence of nanoparticles using NOESY methods due to the presence of spin-spin interaction between the protons of the CH_2 group and the CH side chain of L-tyrosine, which cannot be completely suppressed. This paper presents the results of studies of AST in the presence of Au NPs of different shapes (spherical, rod-shaped and star-shaped) and Pt NPs, performed using ^1H NMR spectroscopy.

Samples.

In this work, aqueous solutions of the amino acid L-tyrosine (AST) in combination with three types of gold nanoparticles (Au NPs) differing in their geometric shape and platinum nanoparticle (Pt NPs) were studied. Gold NPs of three geometric shapes were used: spherical, star-shaped and rod-shaped. To 120 μl of AST, 48 μl of a solution containing Au NPs of each of the shapes described above were added. 60 μl of deuterated water were added to the samples to stabilize the resonance conditions and DSS as an internal standard. Also, 370 μl of water were added to all samples. The concentration of the amino acid L-tyrosine in all samples was 10^{-2} mol/l.

^1H NMR Experiments

All ^1H NMR experiments such as DEPT, COSY and NOESY were performed on a Varian 400 MHz NMR spectrometer with a constant magnetic field of $B_0 = 9$ T. The spectral width was chosen to be 16.1 ppm, the number of accumulations was 512, and the relaxation delay was 1 second. The intense water signal was suppressed using the pulse sequence «Water ES». MestReNova software was used to process the NMR spectra. NOESY experiments were performed at different mixing times of 300, 500 and 700 ms.

Results and discussion

The results of the DEPT and COSY experiments allowed us to identify the spin-spin coupling scheme and assign signals in the ^1H NMR spectra of AST with nanoparticles. The presence of spin-spin interaction was found not only between the spins of the protons of the CH_2 group and the H- in the side chain, but also between the protons of the benzene ring and the protons of the side chain in samples of AST in the presence of star-shaped Au NPs. To clarify the optimal mixing parameters and determine the errors affecting the determination of the cross-relaxation coefficients, the dynamics of magnetizations in the scalar coupled spin system $\text{ABC}_1\text{C}_2\text{D}$ was studied. Two cases were considered. The first case was the dynamics of magnetizations of independent spins, caused only by cross-relaxation processes, specified by a system of differential equations in the form:

$$\begin{bmatrix} \dot{A} \\ \dot{B} \\ \dot{C}_1 \\ \dot{C}_2 \\ \dot{D} \end{bmatrix} = \begin{bmatrix} -\rho_A & \sigma_{AB} & \sigma_{AC1} & \sigma_{AC2} & 0 \\ \sigma_{BA} & -\rho_B & \sigma_{BC1} & \sigma_{BC2} & 0 \\ \sigma_{C1A} & \sigma_{C1B} & -\rho_{C1} & \sigma_{C1C2} & \sigma_{C1D} \\ \sigma_{C2A} & \sigma_{C2B} & \sigma_{C2C1} & -\rho_{C2} & \sigma_{C2D} \\ 0 & 0 & \sigma_{DC1} & \sigma_{DC2} & -\rho_D \end{bmatrix} \begin{bmatrix} A - A_0 \\ B - B_0 \\ C_1 - C_{10} \\ C_2 - C_{20} \\ D - D_0 \end{bmatrix}$$

where A,B,C₁,C₂ and D are z- magnetizations of a,b,c₁,c₂ and d spins in tyrosine [3]. The second case was the dynamics of magnetization of scalar-coupled spins. The differential system of equations for the scalar-coupled spin system ABDC_1C_2 of protons (a, b, d, c₁, c₂) for the second case was obtained taking into account the works [4]. Solutions of the system of equations revealed the presence of a negative NOE effect. The intensities of cross-relaxation peaks such as I_{ac2} , I_{bc1} , I_{dc2} , I_{dc1} exhibit a nonlinear dependence on time. Moreover, the linear section for I_{ac2} , I_{bc1} was observed up to 300 ms, whereas for I_{dc2} , I_{dc1} the minimum values were observed at 1000 ms. The optimal value in the experiments was chosen to be 500 ms. In order to minimize errors in the correct determination of cross-relaxation rates and determination of internuclear distances from the data of cross-relaxation peak intensities, the experiments were carried out at mixing times of 300 ms, 500 ms, and 700 ms. In the approximation of a linear increase in the cross-peak intensities, the relationships between the internuclear distances of two pairs of protons i j and kl are given by the approximate relationship: $r_{kl} = r_{ij} [I_{ij}(t)/I_{kl}(t)]^{1/6}$ [4].

The NMR analysis of experimental data of AST in the presence of NPs showed that the conformation and mobility of tyrosine changes near the nanoparticles. This is indicated by two factors: the oppositely directed shift of the chemical shifts of the protons of the benzene ring and side chain, Hd and Hc1, Hc2 in the CH_2 group and the change in the normalized cross-relaxation rates of AST in the presence of NPs. Thus, in the presence of Pt NP, the chemical shifts of protons a and b shift by 0.06 ppm toward the weak field, and in the presence of star-shaped Au NP, they shift by 0.07 ppm. (b proton) This fact indicates a decrease in the electron charge density in the benzene ring. The greatest changes in chemical shifts were observed in the presence of star-shaped gold NPs. If the signals of aromatic protons and the CH_2 group shifted to the weak field region, then the signal of the proton in the side chain shifted to the strong field region. Comparison of the obtained ^1H NMR spectral parameters of the studied samples with the data presented in science-intensive databases indicates that such conformations of tyrosine are not described in the literature. The spectral databases describe 5 different conformers of tyrosine, distinguished by different positions of the side chain relative to the benzene ring [5]. But none of them coincide with our data. To estimate the relative internuclear distances in tyrazine, the relative values of the cross-relaxation coefficients were calculated using the formula [3]:

$$\sigma_{is\tau_m} = \left(\frac{I_{is}(t_m)}{n_i I_{ii}(t_m)} + \frac{I_{si}(t_m)}{n_s I_{ss}(t_m)} \right) / 2$$

Here I_{ii} , I_{ss} , I_{ij} are the intensities of diagonal (ii, jj) and cross-relaxation peaks (ij), respectively, τ_m is the mixing time.

Conclusions

Based on ^1H NMR spectral and cross-peak intensity data in NOESY, we can draw conclusions about the multidirectional effect of Au NPs of different shapes and platinum on AST, causing conformational changes. In the presence of star-shaped Au NPs, the side chain rotates toward the benzene ring, moving apart the *a* and *b* protons of the benzene ring, while the protons in the CH_2 group move closer, while being symmetrically located relative to the *a* protons of the benzene ring. One of the proofs of the side chain rotation toward the benzene ring is the appearance of a cross peak between the *a* and *d* protons in NOESY. Whereas in the presence of Au NPs in the form of rods, the *a* and *b* protons move closer and away from the side chain, while the cross-peak between the *a* and *d* protons disappears, and the protons of the CH_2 group move away from each other.

References

1. Baig, N., Kammakam, I., & Falath, W. (2021). Nanomaterials: a review of synthesis methods, properties, recent progress, and challenges. *Materials Advances*, 2(6), 1821–1871. doi:10.1039/d0ma00807a
2. F.Ramezani, M. Amanlou , H.Rafii-Tabar Amino acids interaction with gold nanoparticle. *Amino Acids*. 46(4) 2013 p. 911-920 DOI 10.1007/s00726-013-1642-6
3. M. Smirnov, G. Gamov, A. Zyubin, A. Zozulya, I. Lyatun, E. Demishkevich, G. Kupriyanova, I. Khodov. Interaction of gold and platinum nanoparticles with L-tyrosine in aqueous solution: Conformational and dynamic changes. *Journal of Molecular Liquids*. 2024 420(19):126822 DOI: 10.1016/j.molliq.2024.126822 (Q1)
4. Boelens,R., Koning,M.G., van der Marel,G.A., van Boom,J.H., & Kaptein,R. (1989) Iterative Procedure for Structure Determination from Proton-Proton NOEs Using a Full Relaxation Matrix Approach. Application to a DNA Octamer. *J. Magn. Reson.* 82, 290-380
5. <https://pubchem.ncbi.nlm.nih.gov/compound/Tyrosine#section=1H-NMR-Spectra>

Proton MRD profile analysis in Human Serum Albumin solutions: a two site exchange model approach

Néstor Juan Rodríguez de la Cruz¹, Carlos Alberto Cabal Mirabal^{2,3}, Robert N. Muller⁴, Sophie Laurent⁴, Fabian Tamayo Delgado², Juan Carlos García Naranjo^{2,3} and Manuel Arsenio Lores Guevara^{2,3}

¹Escuela de Física, Facultad de Ciencias, Universidad Autónoma de Santo Domingo, Zona Universitaria, Distrito Nacional, Santo Domingo, República Dominicana.

²Centro de Biofísica Médica. Universidad de Oriente. Patricio Lumumba S/N. CP: 90500. Santiago de Cuba, Cuba.

³Centro de Neurociencias de Cuba. La Habana, Cuba.

⁴Laboratoire de RMN et d'Imagerie Moléculaire. Service de Chimie Générale, Organique et Biomédicale. Faculté de Médecine et de Pharmacie. Université de Mons. Belgique.

Introduction

Proton (¹H) Magnetic Relaxation studies of protein solutions have been successfully used to develop medical applications [1-3]. To improve these medical applications or to create new applications a proper understanding of proton magnetic relaxation (PMR) in protein solutions is needed.

In this work we present and discuss the results obtained in Human Serum Albumin (HSA) using a two sites water exchange model (2SWEM) under the consideration of spherical and ellipsoidal geometries. On the other hand, we compare the obtained results with those previously obtained for Hb [4].

Materials and Methods

Lyophilized HSA were obtained from SIGMA Aldrich and diluted in Buffer Saline Phosphate (PBS, pH 7.4) to obtain samples of 50 mg/ml. A Fast Field Cycling NMR Relaxometer (Stelar FFC 2000 Spinmaster) was used, in the range from 20 KHz to 10 MHz, to obtain the PMR dispersion (¹HMRD) profiles at 310 K. Additional points at 20 MHz and 60 MHz were added after measuring the samples in the Mq20 and Mq60 NMR analyzers (Minispec) from Bruker [4].

Results and discussion

Figure 1 shows the typical ¹HMRD profile obtained in HSA solutions at 310 K. The parameters resulting from the fit of the experimental ¹HMRD profiles to 2SWEM were summarized in Table 1. Despite the 2SWEM with ellipsoidal geometry fits the ¹HMRD profiles better than the same model considering spherical geometry; the uncertainties in the physical parameters obtained from the fit is bigger for the consideration of ellipsoidal geometry than for spherical geometry.

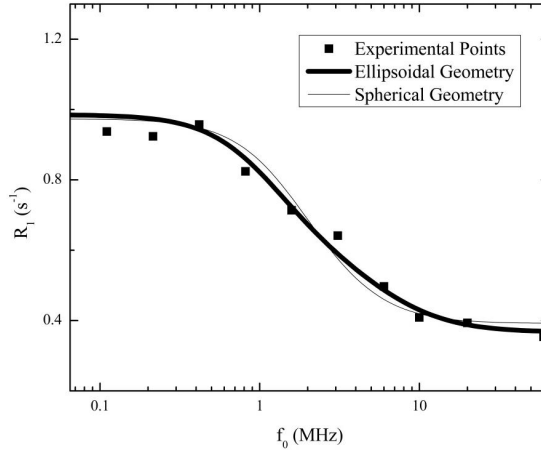


Figure 1. Typical $^1\text{HMRD}$ profile in HSA solutions at 310 K. The profile has been fitted using the two sites water exchange model with spherical and ellipsoidal geometries.

Table 1. Parameters obtained from the fit of the experimental $^1\text{H MRD}$ profiles (310 K) to the 2SWEM in samples of HSA considering spherical and ellipsoidal geometries.

Parameters	2SWEM Sphere	2SWEM Ellipsoid
$R_{1w}^{\text{bulk}} (\text{s}^{-1})$	0.405 ± 0.021	0.383 ± 0.027
$\delta_1 \times 10^7 (\text{s}^{-2})$	1.18 ± 0.161	0.518 ± 0.346
$t_R \times 10^{-8} (\text{s})$	4.26 ± 0.377	
$t_{R1} \times 10^{-8} (\text{s})$		5.11 ± 4.12
$t_{R2} \times 10^{-8} (\text{s})$		1.15 ± 1.25
$t_{R3} \times 10^{-8} (\text{s})$		1.09 ± 1.26

The values of t_R obtained for the HSA ($C=50\text{mg/ml}$) samples, using 2SWEM, are significantly lower than those obtained in previous works for intracellular Hb concentrated ($C=322 \text{ mg/ml}$) solutions [4]. This result is completely in agreement with the predictions of the models of Mooney (Eq. (1)) and Debye (Eq.(2)) for the values of the absolute dynamic viscosity of the protein solution (η_P) and t_R respectively [5].

$$\eta_P = \eta_0 \exp\left(\frac{AC}{1-BC}\right) \quad (1)$$

$$\tau_R = \frac{4\pi r_P^3}{3kT} \eta_P \quad (2)$$

where η_0 is the absolute dynamic viscosity of the solvent and the constants A and B are related with the geometry of the protein and the intermolecular interactions respectively [6]. Moreover, r_P is the radius of the protein molecule, k the Boltzmann's constant and T the absolute temperature [5]. From Eqs. (1) and (2) is clear that the increased value of C in concentrated Hb justifies the increasing in t_R for Hb with respect to the HSA. The values of r_P are 27 Amstrong for HSA and 32 Amstrong for Hb, which also supports the differences of t_R between HSA and Hb. The η_0 and T values are the same for both proteins. A similar result is obtained for the value of the major correlation time of the HSA molecule described as an

ellipsoid (t_{R1}), which is lower than the values of the corresponding correlation time for the protein molecule at the Hb concentrated solution considering an ellipsoidal geometry for the macromolecule (tdata not shown).

Conclusions

Despite the 2SWEM with ellipsoidal geometry fits the ^1H MRD profiles better than the same model considering spherical geometry; the uncertainties in the physical parameters obtained from the fit is bigger for the consideration of ellipsoidal geometry than for spherical geometry. The values of the correlation times for the HSA rotational movement obtained from the fit, for both geometries, are lower than those values obtained for concentrated hemoglobin solutions, which is in agreement with the models of Mooney and Debye.

Acknowledgements

This work has been supported by the Belgian FNRS.

References:

1. M. A. Lores-Guevara, J. C. García-Naranjo, C. A. Cabal-Mirabal, Appl. Magn. Reson. A50, 541 (2019) “<https://doi.org/10.1007/s00723-018-1104-0>”
2. Y. Mengana Torres, M. A. Lores Guevara, J. C. García Naranjo, B. T. Ricardo Ferro, L.C. Suárez Beyries, I. C. Rodríguez Reyes and J. Philippé. . International Journal of Biochemistry, Biophysics & Molecular Biology; A4 (2), 25 (2019)
3. M. A. Lores-Guevara, C. A. Cabal, R. N. Muller, S. Laurent, F. Tamayo, J. C. García. Appl. Magn. Reson. A53, 387 (2022)
4. M. A. Lores-Guevara, Y. Mengana-Torres, J.C. García-Naranjo, N. Rodríguez-Suárez, L.C. Suárez-Beyries, M.A. Marichal-Feliu, T. Simón-Boada, I. Rodríguez-Reyes, J. Phillipé. Plasma Dynamic Viscosity Determined by NMR. Appl. Magn. Reson. A49 (10), 1075 (2018) <https://doi.org/10.1007/s00723-018-1026>.
5. M. A. Lores-Guevara, C.A. Cabal-Mirabal, O. Nascimento, A. M. Gennaro, Appl. Magn. Reson. A30, 121 (2006) “<https://doi.org/10.1007/BF03166986>”
6. Monkos K. Int. J. Biol. Macromol. A16 (1) (1994)

Spin Hyperpolarization Of ^{77}Se Nuclei Using Signal Amplification By Reversible Exchange (SABRE) At Microtesla Fields

Kiryutin A. S.¹, Markelov D. A.^{1,2}, Kosenko I. D.³, Osmanov V. K.⁴, Godovikov I. A.³, Yurkovskaya A. V.¹

¹International Tomography Center SB RAS, Novosibirsk, Russia

²Novosibirsk State University, Novosibirsk, Russia

³A.N. Nesmeyanov Institute of Organoelement Compounds RAS, Moscow, Russia

⁴Nizhny Novgorod State Technical University, Nizhniy Novgorod, Russia

E-mail: d.markelov@tomo.nsc.ru

Nuclear magnetic resonance (NMR) and magnetic resonance imaging (MRI) are both characterized by a low level of sensitivity which is attributed to the low thermal polarization of nuclear spins. Nuclear spin hyperpolarization provides a highly effective solution for improving the sensitivity of NMR and MRI up to several orders of magnitude, which is based on the preparation of the non-equilibrium nuclear magnetization. Parahydrogen Induced Polarization (PHIP) [1] is a hyperpolarization technique that uses parahydrogen, a non-magnetic spin isomer of molecular hydrogen, as a means to enhance NMR signals. Despite being NMR-silent, parahydrogen possesses nuclear spin order that can be transferred to the nuclear magnetization of the target molecule. This, in turn, requires parahydrogen to be involved in a symmetry-breaking chemical process. In hydrogenative PHIP, the substrate with unsaturated bonds is hydrogenated by parahydrogen in the presence of a homogeneous or heterogenous catalyst. This gives rise to strong enhancement of the ^1H NMR signals of the hydrogenation product. In signal amplification by reversible exchange (SABRE) [2], which is also termed as non-hydrogenative PHIP, a parahydrogen and substrate molecule participate in reversible interactions with an Ir-based catalytic complex, as demonstrated in Fig. 1 a.

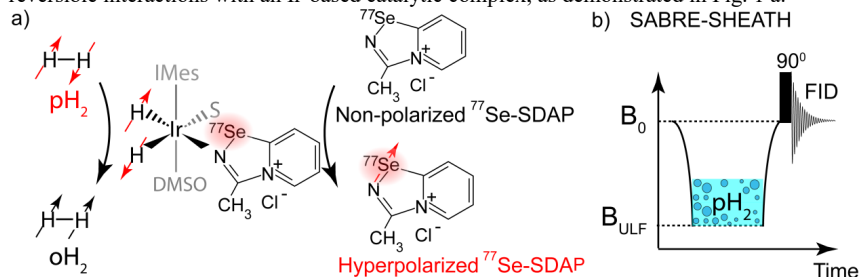


Figure 2. a) Schematics of SABRE hyperpolarization of 3-methyl-[1,2,4]-selenadiazolo-[4,5-a]-pyridine-4-ium chloride (SDAP). Parahydrogen ($p\text{H}_2$) and SDAP participate in reversible interactions with Ir-based polarization transfer complex (PTC). DMSO stands for dimethyl-sulfoxide, S stands for the second equatorial ligand of the PTC ($\text{S} = \text{Cl}^-$ or DMSO), IMes stands for 1,3-bis(2,4,6-trimethylphenyl)-imidazole-2-ylidene. In the complex, ^{77}Se ($s=1/2$) nucleus of SDAP acquires polarization via spin-order transfer from $p\text{H}_2$ -nascent protons. Dissociation of hyperpolarized SDAP from the PTC results in formation of free hyperpolarized SDAP in solution. b) SABRE-SHEATH experimental protocol used for hyperpolarization of ^{77}Se nuclei of SDAP. The sample is transferred from magnetic field of the NMR spectrometer (B_0) to the ultralow magnetic field (B_{ULF}) of a microtesla range. The sample is bubbled with $p\text{H}_2$, and its spin-order is transferred to ^{77}Se nuclei. Hyperpolarized ^{77}Se NMR spectrum is acquired at high magnetic field of the NMR spectrometer using a 90° pulse.

During the transient bonding of the substrate and parahydrogen with the polarization transfer complex (PTC), the substrate acquires polarization due to the J-couplings with the hydride ^1H nuclei stemmed from a parahydrogen molecule. The following dissociation of the substrate from the PTC leads to formation of the hyperpolarized substrate in bulk. Typically, heteronuclear polarization transfer by SABRE occurs in magnetic shields. This method is termed as SABRE-SHEATH (SHield Enables Alignment Transfer to Heteronuclei) [3], which involves transferring the sample from the NMR spectrometer to a zone with an ultralow magnetic field, B_{ULF} (smaller than $1\ \mu\text{T}$), as shown in Fig 1 b. This procedure is performed to meet the strong coupling condition between the heteronuclei and protons. Ultralow magnetic fields are usually provided by magnetic shields, which compensate the magnetic field of the Earth. To the date, this is the most conventional technique for efficient ($> 10\%$ of polarization) heteronuclear SABRE hyperpolarization.

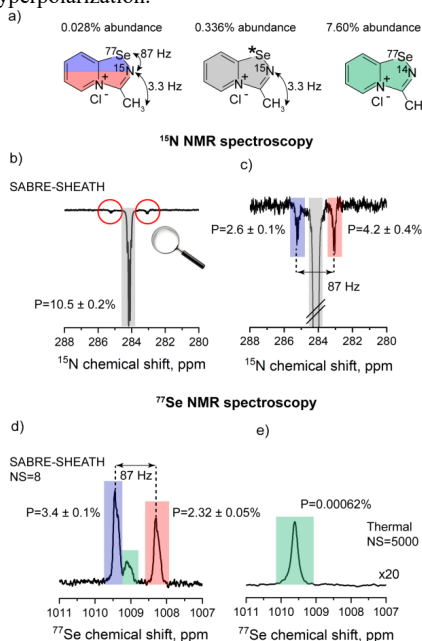


Figure 3. a) Different isotopologues of SDAP observed in the ^{15}N and ^{77}Se NMR spectra: ^{15}N - ^{77}Se SDAP (0.028% of natural abundance), ^{15}N - ^{77}Se SDAP (0.336 % of natural abundance, ^{77}Se stands for all stable non-magnetic isotopes of selenium), ^{14}N - ^{77}Se SDAP (7.60% of natural abundance). NMR signals from different isotopologues of SDAP are highlighted by the corresponding colors. b), c) SABRE-SHEATH hyperpolarized ($B_{\text{ULF}} = 0.4\ \mu\text{T}$) ^{15}N NMR spectrum of SDAP. b) The central signal belongs to hyperpolarized ^{15}N - ^{77}Se SDAP. c) Two sidebands with the splitting of $87\ \text{Hz}$ belong to hyperpolarized ^{15}N - ^{77}Se SDAP ($J_{\text{N-Se}} = 87\ \text{Hz}$). d) SABRE-SHEATH hyperpolarized ($B_{\text{ULF}} = 0.4\ \mu\text{T}$) ^{77}Se NMR spectrum of SDAP acquired with 8 signal accumulations. The central signal corresponds to ^{14}N - ^{77}Se SDAP ($P = 0.0040 \pm 0.0003\%$, not shown). The signals with the splitting of $87\ \text{Hz}$ correspond to hyperpolarized ^{15}N - ^{77}Se SDAP ($J_{\text{N-Se}} = 87\ \text{Hz}$). e) Thermal ^{77}Se NMR spectrum of SDAP acquired with 5000 signal accumulations at $B_0 = 9.4\ \text{T}$ (scaled by a factor 20). The thermal signal corresponds to ^{14}N - ^{77}Se SDAP. In panels b)-d) the temperature of the sample was equal to $15\ ^\circ\text{C}$, in panel e) the temperature was equal to $25\ ^\circ\text{C}$.

Whereas ^{13}C and ^{15}N nuclei are common targets for SABRE hyperpolarization, hyperpolarization of other heteronuclear spins is challenging. One such example is the ^{77}Se nucleus, which is a magnetic isotope of selenium ($s=1/2$). Low natural abundance (7.603 %) and small value of nuclear magnetic momentum of the ^{77}Se nucleus (which is 1.3-fold smaller than magnetic momentum of the ^{13}C nucleus) results in inherently low sensitivity of the ^{77}Se NMR spectroscopy. This significantly limits the practical applications of the ^{77}Se NMR spectroscopy, which is very informative due to ^{77}Se nuclei exhibit a large chemical shift dispersion of over 3000 ppm. This property of ^{77}Se nuclei makes them a useful probe for organic synthesis, biological studies *in vivo* and temperature sensing [4]. To the best of our knowledge, only one publication dedicated to the ^{77}Se hyperpolarization is present, where dissolution dynamic nuclear polarization (d-DNP) has been used to hyperpolarize ^{77}Se nuclei in sodium selenite and sodium sulfate [5]. Therefore, in this work, we examine the feasibility of hyperpolarization of ^{77}Se nuclei using SABRE. We demonstrate efficient hyperpolarization of ^{77}Se nuclei (7.0 ± 0.8 % of ^{77}Se polarization) using signal amplification by reversible exchange (SABRE) at ultralow magnetic fields of a microtesla range. The ^{77}Se hyperpolarization was performed for a biologically relevant molecule, 3-methyl-[1,2,4]-selenadiazolo-[4,5-a]-pyridine-4-ium chloride (SDAP). The most efficient hyperpolarization of ^{77}Se nuclei was achieved for the ^{15}N - ^{77}Se isotopologue of SDAP (0.028 % natural abundance) which contains two different types of heteronuclear spins. We show that the ^{77}Se nuclei of SDAP acquire polarization in the polarization transfer complex in a relayed manner via the J-coupling with the complex-coordinating ^{15}N nucleus. Therefore, this work paves the road for the following optimization of polarization transfer on ^{77}Se or other heteronuclei with $s=1/2$ by SABRE, especially in spin systems containing several types of heteronuclei (e.g. using RF excitation at low magnetic fields).

Acknowledgements

This work is supported by the Russian Science Foundation (Grant No. 25-23-00607).

References

1. C.R. Bowers, D.P. Weitekamp, Parahydrogen and synthesis allow dramatically enhanced nuclear alignment, *Journal of the American Chemical Society*, 109 (1987) 5541-5542.
2. R.W. Adams, J.A. Aguilar, K.D. Atkinson, M.J. Cowley, P.I.P. Elliott, S.B. Duckett, G.G.R. Green, I.G. Khazal, J. López-Serrano, D.C. Williamson, Reversible Interactions with para-Hydrogen Enhance NMR Sensitivity by Polarization Transfer, *Science* (Washington, DC, United States), 323 (2009) 1708-1711.
3. M.L. Truong, T. Theis, A.M. Coffey, R.V. Shchepin, K.W. Waddell, F. Shi, B.M. Goodson, W.S. Warren, E.Y. Chekmenev, N-15 Hyperpolarization by Reversible Exchange Using SABRE-SHEATH, *Journal of Physical Chemistry C*, 119 (2015) 8786-8797.
4. M.S. Silva, D. Alves, D. Hartwig, R.G. Jacob, G. Perin, E.J. Lenardão, Selenium-NMR Spectroscopy in Organic Synthesis: From Structural Characterization Toward New Investigations, *Asian Journal of Organic Chemistry*, 10 (2021) 91-128.
5. E.H. Suh, J. Ratnakar, J. Singh, Z. Kovacs, Dissolution Dynamic Nuclear Polarization of the ^{77}Se Nucleus, *Analysis & Sensing*, 3 (2023) e202200086.

Study of fluoride nanoparticles nucleation processes by NMR in the capillary system

B.M. Mukhamadullin, E.M. Alakshin, E.I. Boltenkova, A.M. Garaeva, A.V. Bogaychuk
 Kazan Federal University, Kazan, Russian Federation, 420008, 18 Kremlyovskaya street
 E-mail: BuMMukhamadullin@stud.kpfu.ru

Introduction

The range of practical applications for nanoparticles across various fields continues to expand each year. Advanced multifunctional nanoparticles are employed for targeted drug delivery, fluorescence imaging of body tissues, as MRI contrast agents, biological markers, disease sensors, and in the treatment of specific types of cancer [1-3]. By adjusting synthesis parameters, it is possible to modify particle size, shape, and other characteristics, which in turn significantly influence their chemical and physical properties [4].

Real-time tracking of nanoparticles growth

To obtain nanoparticles with predefined properties, it is crucial to monitor and control synthesis processes in real time. The primary techniques used for real-time analysis include TEM, FRET, DLS, XRD, NMR and UV spectroscopy. Since no single method provides a universal solution, the choice of technique depends on the specific research objectives and the compatibility of the method with the materials and experimental conditions.

NMR is recognized as a noninvasive and highly informative tool for studying synthesis kinetics. However, its application presents challenges due to the complexity of NMR probe design, where reagents are mixed. Variations in the filling volume of the NMR probe, along with initial NMR settings such as pulse parameters and homogeneity, can change during the reaction. Furthermore, many chemical reactions occur rapidly, making them difficult to track. As a result, new high-speed NMR techniques are being developed to capture fast reaction dynamics [5, 6].

Novel monitoring technique

Previous studies have predominantly focused on slow chemical reactions and nanoparticle nucleation processes. Chemical reactions are typically performed using either a reagent drip system or flow microreactors, which introduce additional challenges in NMR signal acquisition. In classical coprecipitation synthesis from colloidal solutions, reactions occur almost instantaneously. The use of NMR relaxometry to investigate nanoparticle nucleation, growth, and colloidal system evolution is limited by the extremely short relaxation times. To extend reaction durations, viscous media are often utilized.

In this study, the formation of fluoride nanoparticles in a capillary tube was investigated. Real-time measurements longitudinal magnetization recovery during the chemical reaction were performed. The dynamics of fluoride and chloride components throughout the reaction were examined.

Thus, a method for tracking nanoparticle nucleation based on the capillary effect has been proposed.

Acknowledgements

This work was financially supported by the Russian Science Foundation (Project No. 23-72-10039).

References

1. Caspani S. et al. Magnetic nanomaterials as contrast agents for MRI //Materials. – 2020. – V. 13. – P. 2586.

2. Kianfar E. Magnetic nanoparticles in targeted drug delivery: a review //Journal of Superconductivity and Novel Magnetism. – 2021. – V. 34. – P. 1709-1735.
3. Hou Y. et al. Pathological mechanism of photodynamic therapy and photothermal therapy based on nanoparticles //International journal of nanomedicine. – 2020. – P. 6827-6838.
4. Dolai J., Mandal K., Jana N. R. Nanoparticle size effects in biomedical applications //ACS Applied Nano Materials. – 2021. – V. 4. – P. 6471-6496.
5. Gal M., Mishkovsky M., Frydman L. Real-time monitoring of chemical transformations by ultrafast 2D NMR spectroscopy //Journal of the American Chemical Society. – 2006. – V. 128. – P. 951-956.
6. Bechet D. et al. Multifunctional ultrasmall nanoplatforms for vascular-targeted interstitial photodynamic therapy of brain tumors guided by real-time MRI //Nanomedicine: Nanotechnology, Biology and Medicine. – 2015. – V. 11. – P. 657-670.

Investigation of Relaxation Times of Cotton Oil-Diesel Fuel Mixtures by TD-NMR

Cengiz Okay¹, A.Talha Demir¹, Bulat Rameev^{2,3,4}

¹*Department of Physics, Marmara University, 81040 Göztepe-Istanbul, Turkey*

²*Department of Physics, Gebze Technical University, Gebze, Kocaeli 41400, Türkiye*

³*Kazan State Power Engineering University, Kazan, Tatarstan 420066, Russian Federation*

⁴*Zavoisky Physical-Technical Institute, FRC Kazan Scientific Center of RAS, Kazan, Tatarstan 420029, Russian Federation*

E-mail: cokay@marmara.edu.tr

Abstract

Molecular dynamics of various liquids can be probed by Time-Domain Nuclear Magnetic Resonance (TD-NMR) through the measurements of the spin-lattice (T_1) and spin-spin relaxation time (T_2). In this study, the relaxation times T_1 and T_2 of the cotton oil-diesel fuel mixtures in various ratios from pure diesel fuel to pure cotton oil using Bruker Minispec mq-20 TD-NMR device. We have demonstrated that the TD-NMR can be applied as an effective method for online monitoring of the ratio of cotton oil to diesel fuel in a biofuel mixture, and, in general, to control fuel quality and its basic parameters in combustion vehicles.

Introduction

Global energy consumption from fossil fuels is rising quickly due to population growth and industrialization. This motivates researchers to search for novel “green” and sustainable alternative energy sources. One of alternative energy sources is the use of biofuels (e.g. vegetable oils, biodiesel, ethanol, etc.) in transportation and agriculture vehicles instead of petroleum-based fuels. Their impact can be significant from an economic and scientific standpoint. Many studies prove that vegetable oils can be used in diesel engines as a fuel substitute for fossil fuels [1, 2]. Researchers have shown that using vegetable oils directly in engines can lead to long-term issues because their viscosity is around ten times that of diesel fuel [3]. To lower their viscosity to make them suitable for diesel engines, a few basic chemical techniques have been proposed [4]. These techniques include dilution, creating microemulsion, bond breaking, and esterification [5]. Each kind of vegetable oil is characterized by a specific average composition of fatty acids. The most common technique for analyzing the content of fatty acids is gas chromatography (GC). On the other hand, over the past 20 years ^1H NMR approach has also gained importance in the fatty acid analysis of biofuels [6–8]. However, in many practical cases, Time-Domain Nuclear Magnetic Resonance (TD-NMR) can be also applied instead high-resolution NMR technique due to its lower cost and maintenance requirements. For biofuels, one of the easiest ways to decrease their viscosity making them suitable for use in motor engines is to make a mixture of fuel with diesel oil. In this case, however, we met an issue of controlling the ratio of mixture with some, preferably low-cost and practical technique.

In this study, spin-spin (T_2) and spin-lattice (T_1) relaxation times of cotton oil-diesel fuel mixtures have been measured by TD- NMR in a whole range of the oil/fuel concentrations.

Experimental procedures

In this study, Bruker Minispec mq-20 Time-Domain NMR (TD-NMR) device was used to measure the relaxation times of diesel fuel, cotton oil and their mixtures. All samples were maintained in the NMR apparatus for at least 10 minutes before each measurement to reach the temperature equilibrium and to minimize the effect of convection. The Carr-Purcell-Meiboom-Gill (CPMG) pulse sequence was used to probe the T_2 relaxation time, while the

inversion recovery sequence was used to measure the T_1 relaxation time. Different echo times were tested to assess the impact of self-diffusion. The echo time was finally set at 0.5 ms for the minimization diffusion term.

Experimental results and their discussion

The relaxation curves for spin-lattice (T_1) and spin-spin (T_2) for each sample are presented in Figures 1a and 1b.

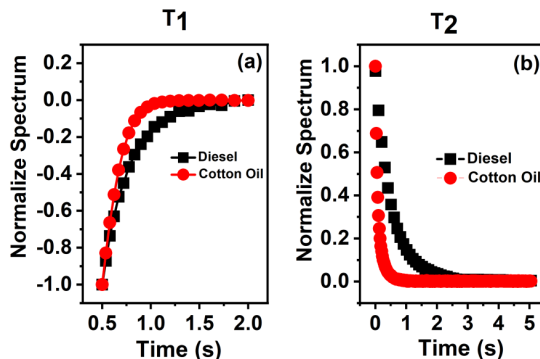


Figure 1. Spin-lattice (panel-a) and spin-spin (panel-b) relaxation curves

The T_1 and T_2 values were determined by applying exponential fitting to each sample's relaxation time curve. The dependence of T_1 and T_2 on mixture ratio is presented in Figure 2.

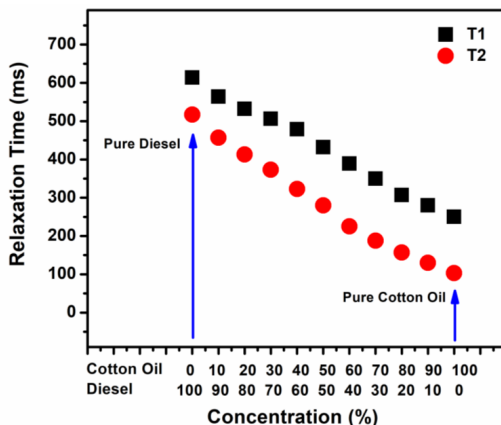


Figure 2. Spin-lattice (T_1) and spin-spin (T_2) relaxation times for various cotton oil-diesel mixtures.

As expected, the T_1 values are consistently higher than the T_2 values for all concentrations. It is well known that the relaxation times are inversely proportional to a liquid viscosity, that is the shorter relaxation times correspond to the higher viscosity. It is known that the viscosity of cotton oil is higher than diesel fuel [9], therefore the relaxation time of oil

is expected to be shorter than that of diesel fuel. The steady decrease in the relaxation times reflects the increase in the viscosity value of the mixture with the amount of cotton oil. This means that the oil/fuel ratio in a specific biofuel at some preset temperature can be accurately established by TD NMR measurements.

Thus, we demonstrated that the TD NMR technique can be applied to control both the oil/fuel ratio in a biofuel at some preset temperature as well as to probe the biofuel mixture viscosity. Taking into account recent enormous progress in the development of mobile and low-cost TD NMR devices, the TD NMR control devices can be implemented for online monitoring of biofuels (in general, any kind of fuels) both at gas stations and in the concept of smart cars.

References

1. Meher, L. C.; Vidya Sagar, D.; Naik, S. N. (2006, June). Technical aspects of biodiesel production by transesterification - A review, *Renewable and Sustainable Energy Reviews*, 248–268. doi:10.1016/j.rser.2004.09.002
2. Dmytryshyn, S. L.; Dalai, A. K.; Chaudhari, S. T.; Mishra, H. K.; Reaney, M. J. (2004). Synthesis and characterization of vegetable oil derived esters: Evaluation for their diesel additive properties, *Bioresource Technology*, Vol. 92, No. 1, 55–64. doi:10.1016/j.biortech.2003.07.009
3. Çetin, M.; Yüksel, F. (2007). The use of hazelnut oil as a fuel in pre-chamber diesel engine, *Applied Thermal Engineering*, Vol. 27, No. 1, 63–67. doi:10.1016/j.applthermaleng.2006.04.025
4. Karaosmanoğlu, F. (1999). Vegetable Oil Fuels: A Review, *Energy Sources*, Vol. 21, No. 3, 221–231. doi:10.1080/00908319950014858
5. Schwab, A. W.; Bagby, M. O.; Freedman, B. (1987). Preparation and properties of diesel fuels from vegetable oils, *Fuel*, Vol. 66, No. 10, 1372–1378. doi:10.1016/0016-2361(87)90184-0
6. Babu, A. K.; Devaradjane, G. (2003). Vegetable Oils And Their Derivatives As Fuels For CI Engines: An Overview, *JOURNAL OF FUELS AND LUBRICANTS* (Vol. 112)
7. Monteiro, M. R.; Ambrozin, A. R. P.; da Silva Santos, M.; Boffo, E. F.; Pereira-Filho, E. R.; Lião, L. M.; Ferreira, A. G. (2009). Evaluation of biodiesel-diesel blends quality using ¹H NMR and chemometrics, *Talanta*, Vol. 78, No. 3, 660–664. doi:10.1016/j.talanta.2008.12.026
8. Siudem, P.; Zielińska, A.; Paradowska, K. (2022). Application of ¹H NMR in the study of fatty acids composition of vegetable oils, *Journal of Pharmaceutical and Biomedical Analysis*, Vol. 212. doi:10.1016/j.jpba.2022.114658
9. Alptekin, E.; Canakci, M. (2008). Determination of the density and the viscosities of biodiesel-diesel fuel blends, *Renewable Energy*, Vol. 33, No. 12, 2623–2630. doi:10.1016/j.renene.2008.02.020

Electron Spin Resonance of Fe-doped TiO₂ nanoparticles

Daria A. Pomogailo^{1,2}, Anastasiya S. Kovalenko³, Anton M. Nikolaev³, Leonid M. Kustov^{2,4}, Olga A. Shilova³

¹*D. I. Mendeleev University of Chemical Technology, Miusskaya Ploshchad, 9/1, Moscow, Russian Federation*

²*N. D. Zelinsky Institute of Organic Chemistry Russian Academy of Sciences, Leninsky Prospect, 47, Moscow, Russian Federation*

³*Branch of Petersburg Institute of Nuclear Physics named by B.P. Konstantinov of National Research Centre "Kurchatov Institute" – I. V. Grebenshchikov Institute of Silicate Chemistry, Saint-Petersburg, Makarov embankment, 2, Russian Federation*

⁴*Department of Chemistry, M. V. Lomonosov Moscow State University, Leninskie Gory 1/3, Russian Federation*

E-mail: texafirin@ya.ru

Introduction

Titanium dioxide (TiO₂) is a semiconductor material with a band gap of 3.2 eV (for anatase), due to which it is widely used in photocatalysis under ultraviolet irradiation. Expanding the spectral range of TiO₂ to visible light is possible by reducing the width of the gap. It is known that doping TiO₂ with Fe atoms can lead to a decrease in band gap and contribute to an increase in photocatalytic activity in the both ultraviolet and visible regions.

Synthesis and Structure

Nanoparticles of TiO₂ were prepared by coprecipitation from aqueous solutions of TiCl₄ and FeCl₃, varying the Fe/Ti ratio in the initial solution from 0 to 4 at.%. An aqueous solution of ammonia was used as a precipitant. To obtain anatase, the sediments were heat treated at 500°C.

The resulting nanoparticles were studied by X-ray phase analysis (XRD), Fourier transform infrared spectroscopy (FTIR) and scanning electron microscopy with local energy-dispersive X-ray spectroscopy (EDX). The XRD results showed that the nanoparticles of TiO₂ corresponded to the anatase phase. The presence of iron oxides was not detected by XRD. Absorption bands corresponding to vibrations of both Ti-O-Ti bonds (470 and 1150 cm⁻¹) and Fe-O (range 580-620 cm⁻¹) were detected in the FTIR spectra. This data may indicate that Fe was incorporated into the anatase structure rather than crystallizing as a separate phase (FeO_x). The results of EDX analysis showed an increase in the iron content in nanoparticles with an increase of the amount of Fe introduced into the initial solution during synthesis.

However these research methods do not allow us to fully understand in which form exactly iron is present in the studied powders. It was decided to use the Electron Paramagnetic Resonance (EPR) method to solve this problem. So the purpose of this work was to study the effect of iron doping on the EPR spectra of Fe-doped nanoparticles of TiO₂.

The interpretation of EPR/FMR spectra

EPR spectra were recorded using «Bruker EMX Plus» X-band spectrometer with a modulation frequency of 100 kHz in thin 4 mm quartz ampoules. To calculate the number of paramagnetic centers we used the crystal CuCl₂·2H₂O with a known number of paramagnetic centers.

A comparison of the areas under the spectra for TiO₂-Fe(2%)-anatase and TiO₂-Fe(4%)-anatase samples (Fig. 1) showed that with increasing iron content the number of paramagnetic particles decreases. In the spectra of these samples, two resonance lines are observed with g-factors of 4.21 and 1.98, corresponding to Fe³⁺ [1]. They are usually attributed to a high-spin state with a distorted orthorhombic environment localized in the anatase phase or to iron cations in an orthorhombic structure such as brookite [2].

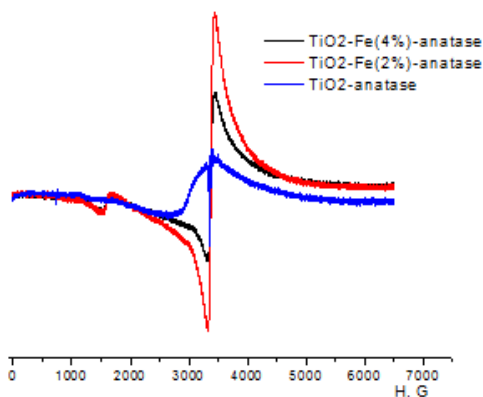


Figure 1. Electron Paramagnetic Resonance spectra of TiO_2 -anatase samples with different content of Fe.

Conclusion

The number of paramagnetic centers increases with addition of 2 at. % of Fe to anatase, and further increasing in the proportion of Fe in anatase leads, on the contrary, to decrease in the number of paramagnetic centers. This may be due to the fact that at small amounts (2 at. %) iron atoms are incorporated into the anatase structure, and at 4 at. % iron forms the separate phase (iron oxide), increasing the proportion of non-paramagnetic centers in the sample.

Acknowledgements

This work is carried out within the framework of the research topic of the state task of the NRC "Kurchatov Institute" – PNPI – IchS No. 1023033000122-7-1.4.3 "Physico-chemical foundations of the inorganic synthesis of micro- and nanostructured inorganic, organo-inorganic and ceramic materials and coatings for bio-, energy- and resource-saving technologies". The authors (D.A.P. and L.M.K.) are grateful for the financial support of the Russian Scientific Foundation (grant No. 23-73-30007).

References

1. Kokorin, A.I., Amal, R., Teoh, W.Y. – Appl. Magn. Reson., 48, 447-459 (2017).
2. R. Arroyo, G. Cyrdoba, J. Padilla, V.H. Lara. – Mater. Lett., 54, 397 (2002).

Further development of the theory of spin exchange in dilute solutions of paramagnetic particles

Salikhov K.M.

Zavoisky Physical-Technical Institute of the Federal Research Center "Kazan Scientific Center of the Russian Academy of Sciences".

Address: Russia, Tatarstan, 420043 Kazan, Sibirsky Trakt Str. 10/7

Phone: +78432720503 E-mail: salikhov@kfti.knc.ru

The great interest in studying spin exchange is explained by the fact that EPR spectroscopy makes it possible to determine the frequency of bimolecular collisions in complex environments, including biological ones.

Based on 50 years of research, I have formulated a new paradigm of spin exchange [1-3]. The formulation of a new paradigm of spin exchange in solutions has given a new impetus to the development of this scientific discipline. Some theoretical predictions have already been confirmed [4-7].

In this report, a number of new experiments are formulated to confirm the fundamental provisions of the new paradigm of spin exchange in solutions and its manifestations in EPR spectroscopy.

The results obtained in the study of spin exchange in solutions of paramagnetic particles can be used in other scientific fields. In particular, a new protocol for determining the frequency of bimolecular collisions in solutions has been formulated, taking into account the mixed shape of the EPR spectrum lines, which has traditionally been neglected. In spin exchange, the mixed shape of the lines arises as a result of the return of quantum coherence to the spin from the interaction partner in a collision. The new protocol increases the reliability and accuracy of determining the frequency of bimolecular collisions in solutions, including in biological media, using spin exchange as a model process.

Spin exchange, namely the effect of the so-called exchange narrowing of spectra, may be useful for creating a Bose-Einstein condensate of spin excited states (spin excitons or spin polaritons) at room temperatures [8].

A new protocol developed for analyzing the shape of spectra in the presence of spin exchange can be used in other situations when the mechanism of paramagnetic relaxation is a spectral diffusion, for example, during chemical exchange [9]. This is possible because the kinetic equations for spin magnetization in the cases of chemical exchange and spin exchange coincide.

1. K.M. Salikhov, Current state of the theory of spin exchange in dilute solutions of paramagnetic particles. New paradigm of spin exchange and its manifestations in EPR spectroscopy. UFN (Physics Uspekhi), 189, 1017-1043 (2019).
2. K.M. Salikhov, Fundamentals of spin exchange. Story of a paradigm shift. Springer (2019) Springer, International Publishing.
3. K.V. Salikhov, Manifestation of coherence transfer in spectroscopy. New paradigm of spin exchange and its manifestations in EPR spectra. Bull. Russian Acad. Sci. Phys. 84, 659–663 (2020).
4. B.L. Bales, M. Peric, I. Dagutan, M.K. Bowman, M.M. Bakirov, R.N. Schwartz. Experimental Observation of a Peculiar Effect in Saturated Electron Paramagnetic Resonance Spectra Undergoing Spin Exchange. Magnetic Polariton? J. Phys. Chem. Letters 13, 10952-1057 (2022).
5. K. M. Salikhov, M. M. Bakirov, R. B. Zaripov and I. T. Khairutdinov. Experimental confirmation of the formation of a spin polariton in dilute solutions of paramagnetic particles. Phys.Chem. Chem.Phys. 25, 17966 (2023).

6. B.L. Bales, M. Peric, R.N. Schwartz. Experimental Observation of a Peculiar Effect in Electron Paramagnetic Resonance Spectra for Nitroxides Undergoing Fast Spin Exchange: Emission. *J. Phys. Chem. Letters* (2024).
7. K.M. Salikhov, M.M. Bakirov, I.T. Khairutdinov, R.B. Zaripov, Experimental confirmation of the formation of collective modes of the magnetization motion of paramagnetic particles in solutions due to spin exchange. *J. Magn. Reson.* 363, 107703 (2024).
8. K.M. Salikhov. New Approach to the Formation of Bose-Einstein Condensate. *Appl. Magn. Reson.* 56, issue 1 (2025); doi.org/10.1007/s00723-024-01723-2
9. R. Ernst, G. Bodenhausen, A. Wokaun. Principles of nuclear magnetic resonance in one and two dimensions. (1987) pp. 215-217. Clarendon Press, Oxford.

Competitive ion transport in polymer gel electrolytes studied by NMR

Nikita A. Slesarenko¹, Alexander V. Chernyak^{1,2}, Kyunsylu G. Khatmullina,^{1,3} Anna A. Slesarenko,¹ Olga V. Yarmolenko¹.

¹ Federal Research Center of Problems of Chemical Physics and Medicinal Chemistry RAS, 142432 Chernogolovka, Russia

² Osipyan Institute of Solid State Physics RAS, 142432 Chernogolovka, Russia

³ National Research University "Moscow Power Engineering Institute", Krasnokazarmennaya street 14, Moscow, 111250 Russia

E-mail: n.slasarenko@icp.ac.ru

<https://www.icp.ac.ru>

Introduction

Previously, a polymer gel electrolyte was synthesized based on polyethylene glycol diacrylate, LiBF₄ salt in ethylene carbonate, and 1-ethyl-3-methylimidazolium tetrafluoroborate (EMIBF₄) – ionic liquid (IL). It exhibited thermal stability up to 350 °C [1], but the lithium diffusion coefficients in this system were low [2]. The aim of this work was to investigate the influence of the solvate environment of the Li⁺ cation on the ion transport properties in a polymer gel electrolyte with the introduction of an ionic liquid. 1,3-Dioxolane (DOL), diglyme (G2), tetraglyme (G4), and ethylene carbonate (EC) were chosen as solvent molecules solvating the Li⁺ cation.

The pulsed field gradient NMR (PFG NMR) enables the determination of the partial contribution of each charge type (cation or anion) to the total ionic mobility [3]. Comparison of the results of different methods will provide information on molecular and ionic transport, as well as translational mobility at different spatial scales. This will provide a deeper understanding of the cationic transport processes in the polymer gel-electrolyte system.

Materials

The polymer electrolytes were synthesized via radical polymerization of PEGDA in the presence of the initiator benzoyl peroxide (PB). The composition of the polymerizable mixture was as follows: PEGDA, LiBF₄, DOL/G2/G4/EC, EMIBF₄, and 1 wt.% PB for the entire sample. The curing of this mixture was performed using a stepwise mechanism: 60°C – 3 h, 70°C – 1 h, 80°C – 1 h [2]. PE compositions:

- **PE1:** PEGDA-LiBF₄-IL-DOL (1:1:6:4)
- **PE2:** PEGDA-LiBF₄-IL-G2 (1:1:6:2)
- **PE3:** PEGDA-LiBF₄-IL-G4 (1:1:6:1)
- **PE4:** PEGDA-LiBF₄-IL-EC (1:1:6:4)

Methods

High resolution NMR

High-resolution NMR spectra of the polymer electrolyte (¹H, ⁷Li, ¹¹B, ¹³C, ¹⁹F) were recorded on the AVANCE-III-500 Bruker NMR spectrometer (proton Larmor frequency of 500 MHz). The measurement frequencies were 500, 194, 160, 126, and 471 MHz for ¹H, ⁷Li, ¹¹B, ¹³C, and ¹⁹F, respectively, and the measurements were performed at room temperature (22 ± 1 °C). The chemical shift scale was calibrated using the DMSO-d₆ signal in the capillary as an external standard (2.50 ppm for ¹H).

Pulsed field gradient NMR

The self-diffusion coefficients were measured on ¹H, ⁷Li, and ¹⁹F nuclei by the pulsed field gradient technique at the frequencies 400, 155.5, and 376.5 MHz, respectively. The

measurements were carried out on Bruker AVANCE-III-400 NMR spectrometer, equipped with the diff60 gradient unit. The pulsed field gradient stimulated echo sequence was used.

Results and discussion

The diffusion coefficients (D_s) on ^1H , ^7Li , and ^{19}F nuclei for all PE compositions were measured by PFG NMR. All obtained diffusion decays exhibited an exponential dependence. Measurements of D_s on different nuclei provide information on the mobility of the following ions and molecules: on ^1H nuclei — EMI⁺ cations and solvent molecules, on ^7Li nuclei — lithium cations, and on ^{19}F — BF_4^- anions.

Table 1. Diffusion coefficients of ^1H (EMI⁺, solvent), ^7Li (Li⁺), ^{19}F (BF_4^-) at 22.5 °C

Compositions	$D_{^7\text{Li}}, \text{m}^2/\text{s}$	$D_{^{19}\text{F}}, \text{m}^2/\text{s}$	$D_{\text{IH(EMI}^+), \text{m}^2/\text{s}}$	$D_{\text{IH(Sol)}, \text{m}^2/\text{s}}$
PE1 (DOL)	4.09×10^{-12}	1.36×10^{-11}	1.93×10^{-11}	4.46×10^{-11}
PE2 (G2)	6.64×10^{-12}	1.34×10^{-11}	1.72×10^{-11}	2.05×10^{-11}
PE3 (G4)	4.53×10^{-12}	8.41×10^{-12}	1.18×10^{-11}	6.78×10^{-12}
PE4 (EC)	1.81×10^{-12}	1.32×10^{-11}	1.83×10^{-11}	3.08×10^{-11}

The highest diffusion mobility of Li⁺ cations was observed for the PE2 composition containing G2. In general, the mobility of the Li⁺ cation decreases in the PE series: 2>3~1>4. It is worth noting that for PE3, where the lowest mobility of EMI⁺ and BF_4^- ions was observed compared to other compositions, the diffusion of lithium cations was only slightly lower than that in the PE2 composition.

Temperature experiments were also carried out to measure the diffusion coefficients D_s on the nuclei ^1H , ^7Li and ^{19}F in the temperature range from 0 to 60 °C. The dependencies follow Arrhenius behavior. The activation energies of diffusion were calculated.

The activation energy of EMI⁺ diffusion in pure IL was 21 kJ/mol, and in cross-linked PEGDA, this value was higher for all the studied polymer electrolytes PE1-4, since the diffusion of IL in the cross-linked polymer matrix is hindered.

For compositions containing diglyme or tetraglyme as a solvent ($E_a = 26.7$ and 22.4 kJ/mol, respectively), significantly lower activation energies for the diffusion of lithium cations were observed compared to compositions with DOL and EC ($E_a = 30.6$ and 35.5 kJ/mol). At the same time, the E_a of diffusion of solvent molecules was higher for PE2 and PE3 ($E_a = 28.8$ and 27.5 kJ/mol) than for PE1 and PE4 ($E_a = 24.1$ and 23.6 kJ/mol).

To understand the processes of competitive ion transport, the hydrodynamic radius of all ions and molecules was calculated from the diffusion coefficients on all nuclei using the Stokes-Einstein equation:

$$D = \frac{kT}{c\pi\eta r_s} \quad (1)$$

where c is a constant, η is the viscosity, and r_s is the Stokes radius for diffusing particles.

Figure 1a shows the dependence of the relative hydrodynamic radius of the lithium cation on temperature for four solvents.

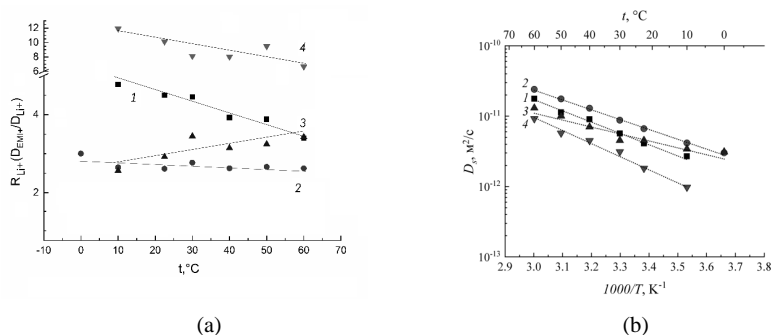


Figure 1. Temperature dependence of a) the relative hydrodynamic radius of the lithium cation, b) the diffusion coefficients of 7Li for PE compositions 1-4. The numbers correspond to the PE compositions.

As can be seen from Fig. 1a, the relative hydrodynamic radius of the lithium cation for systems with small molecules (EC, DOL, and diglyme) decreases with increasing temperature. This is consistent with the existence of both the first and second coordination spheres of the solvent molecules around the lithium cation. The effective solvation radius decreases with increasing temperature due to the increased lability of the second coordination sphere. The largest slope was observed in the case of cyclic molecules, whereas for diglyme, it was practically absent.

In the case of tetraglyme, this dependence is reversed, i.e., with increasing temperature, the solvation shell increases. This is probably due to the re-solvation of the lithium cation from the polymer matrix to tetraglyme. The anomalous slope angles of the temperature dependence of the hydrodynamic radius, as well as the diffusion coefficients for lithium (Fig. 1b), can be attributed to the different solvation environment of the lithium cation in the polymer-tetraglyme system at different temperatures. Thus, at low temperatures, R_{Li^+} in this system, as calculations have shown, decreases. This can be explained by the coordination of the lithium cation along the polymer matrix, then Li^+ passes into the $Li^+(G4)$ complex and, with increasing temperature, into its more stable complex $(G4)Li^+(G4)$, as was shown in [4].

Acknowledgements

NMR measurements were performed using equipment of the Multi-User Analytical Center of the Institute of Problems of Chemical Physics RAS and Science Center in Chernogolovka RAS with the support of State Assignment of the Institute of Problems of Chemical Physics RAS (state registration number 124013000743-3 (FFSG-2024-0008)).

References

- O.V. Yarmolenko, K.G. Khatmullina, G.R. Baymuratova, N.A. Emelianov, R.K. Baimuratova, A.V. Yudina. – High Energy Chemistry, 57, 375-382 (2023).
- K.G. Khatmullina, N.A. Slesarenko, A.V. Chernyak, G.R. Baymuratova, A.V. Yudina, M.P. Berezin, G.Z. Tulibaeva, A.A. Slesarenko, A.F. Shestakov, O.V. Yarmolenko – Membranes, 13, 548 (2023).
- V.I. Volkov, O.V. Yarmolenko, A.V. Chernyak, N.A. Slesarenko, I.A. Avilova, G.R. Baymuratova, A.V. Yudina. – Membranes, 12, 416 (2022)
- G.R. Baymuratova, K.G. Khatmullina, G.Z. Tulibaeva, I.K. Yakushenko, P.A. Troshin, O.V. Yarmolenko, – Russ. Chem. Bulletin, 71, 2108 (2022)

Influence of the shape of gold nanoparticles on the structural and dynamical properties of L-tyrosine

M. Smirnov, A. Zozulya, I. Lyatun, G. Kupriyanova

Institute of Physics, Mathematics and Information Technology, Immanuel Kant Baltic Federal University, 236041, Kaliningrad, Russia

E-mail: smirnov.mark2015@yandex.ru

http://kantiana.ru

Introduction

This work is devoted to the study of NMR parameters of the aromatic amino acid L-tyrosine in the presence of noble metal NPs of different shapes by high-resolution NMR spectroscopy and NMR relaxometry methods [1, 2].

The results obtained will be useful for the development of biocompatible materials based on metal nanoparticles for medicine. A stable and long-lived «amino acid-nanoparticle» system is required for medical applications, including fluorescent tag delivery, theranostics, etc.

Experiment

High-resolution ^1H NMR spectra of aqueous solution of L-tyrosine (AST) were obtained on a Varian 400 MHz NMR spectrometer with a constant magnetic field $B_0=9.4$ T. The spectral width was chosen to be 16.1 ppm, the number of scans was 512, and the relaxation delay was 1 second. The intense water signal was suppressed using the pulse sequence «Water ES».

The Inversion-Recovery pulse sequence was used to measure T_1 relaxation times. The following experiment parameters were used: the relaxation delay was 10 seconds, the number of scans was 256. The time of the experiment was 15 hours and 20 minutes. The «Presat» pulse sequence was used to suppress the water signal in the relaxation experiment.

Samples

In the study, AST was studied in combination with three types of gold nanoparticles differing in their geometrical shape. Gold nanoparticles of three geometric shapes were used:

1. Spherical;
2. Star-shaped;
3. Rod-shaped.

Gold nanoparticles were visualised by electron microscopy on a Zeiss Crossbeam 540 dual-beam station. A star-shaped image of gold nanoparticles is presented in Fig.1 (a), and a similar image of rod-shaped NPs is presented in Fig.1 (b).

To 120 μl of AST was added 48 μl of a solution containing gold NPs of each of the forms described above. 60 μl of deuterated water was added to the samples. Sodium trimethylsilylpropanesulfonate (DSS) was used as an internal NMR standard. Also, 370 μl of water was added to all samples. The concentration of the amino acid L-tyrosine in all samples was 10^{-2} mol/L.

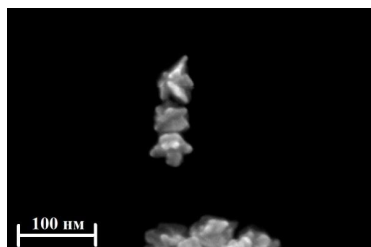


Figure 1 (a). Scanning electron microscope image of star-shaped gold nanoparticles

Results

The high-resolution ^1H NMR spectra of both AST alone and with the addition of three different types of gold nanoparticles are presented in Figure 2. The assignment of signals in the ^1H NMR spectrum to individual molecular fragments of the tyrosine molecule was performed on the basis of COSY and TOCSY experiments according to [3]. The structural formula of L-tyrosine is also presented in Fig. 2.

Analysis of ^1H NMR spectra (see Fig.2) reveals multidirectional changes of chemical shifts of tyrosine signals in the presence of gold NPs of different shapes.

The chemical shifts of AST signals in the presence of star-shaped gold NPs shift to the strong-field region by 0.01 ppm. This trend is observed for all molecular fragments without exception.

When adding a solution containing gold NPs in the form of rods, a much more complicated situation is observed. The proton doublet of the benzene ring a is shifted by 0.07 ppm to the strong field region, while b has a shift of 0.09 to 0.10 ppm. The quartet of the CH group shows a shift to the strong-field region by 0.09 ppm. The proton C1 quartet of the CH_2 group is shifted by 0.07 ppm, and the C2 quartet shows a similar shift to the strong field region of 0.08 ppm.

Fig.3 shows the distribution diagram of longitudinal relaxation times T_1 of four tyrosine samples.



Figure1 (b). Scanning electron microscope image of rod-shaped gold nanoparticles.

Based on the presented data, the tendency that the addition of gold NPs first of all affects the relaxation time of the protons of the benzene ring a and b of the tyrosine molecule is clearly visible. The addition of spherically shaped gold particles leads to an increase in the relaxation time of the proton of the benzene ring a by 0.13 - 0.16 s, and that of the proton b by 0.26 - 0.31 s.

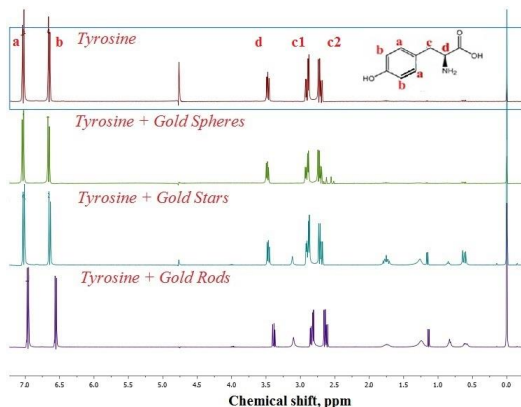


Figure 2. ^1H NMR spectra of AST and AST with the addition of spherical, star-shaped and rod-shaped gold nanoparticles.

When rod-shaped gold NPs are added, a diametrically opposite situation is observed. The T1 time of proton a is reduced by 0.05 - 0.12 s, and b by 0.13 - 0.29 s relative to tyrosine without NPs. A similar situation is observed in the tyrosine sample with the addition of star-shaped NPs. The T1 time for proton a decreases by 0.04 - 0.11 s, and for b by 0.14 - 0.34 s.

It is worth noting that the addition of any type of NPs has an extremely weak effect on the relaxation time of the protons of the CH₂ group, and this tendency is especially noticeable for the proton of C2.

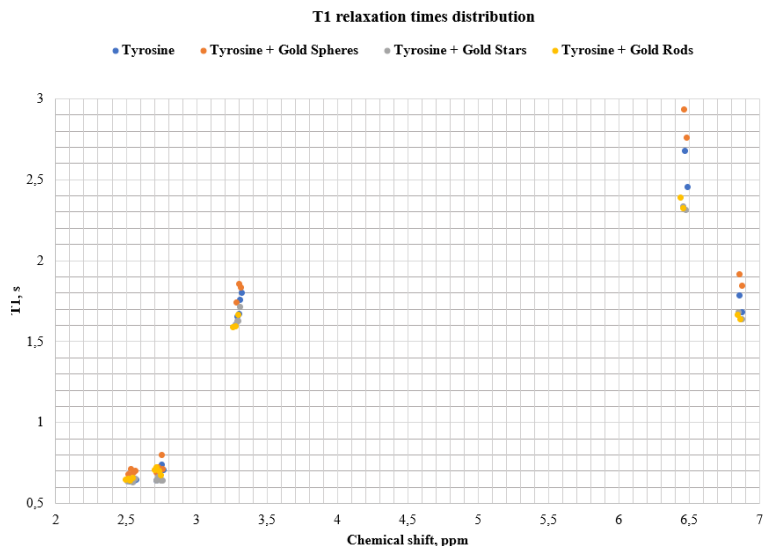


Figure 3. Distribution of T1 relaxation times of four investigated tyrosine samples

References

1. Mark Smirnov, George Gamov, Andrey Zyubin, Alexander Zozulya, Ivan Lyatun, Elizaveta Demishkevich, Galina Kupriyanova, Ilya Khodov. Interaction of gold and platinum nanoparticles with L-tyrosine in aqueous solution: Conformational and dynamic changes. *Journal of molecular liquids (Q1)*. Volume 420 (2025), 126822 DOI:10.1016/j.molliq.2024.126822;
2. Smirnov M.L., Zyubin A.Yu., Demishkevich E.A., Kupriyanova G.S. 1H NMR Rhodamine in asin silver solution. XIX INTERNATIONAL SCIENTIFIC CONFERENCE "INNOVATION IN SCIENCE, EDUCATION AND ENTREPRENEURSHIP – 2021", SECTION "PHYSICS OF CONDENSED STATE". Proceedings. Kaliningrad State Technical University, 2022. 667 pp. ISBN 978-5-7481-0485-2
3. PubChem [Internet]. Bethesda (MD): National Library of Medicine (US), National Center for Biotechnology Information; 2004-. PubChem Compound Summary for CID 16213583, L-Tyrosine-13C9; [cited 2025 Feb. 24]. Available from: <https://pubchem.ncbi.nlm.nih.gov/compound/L-Tyrosine-13C9>

Development of a new class of adiabatic inverting MCA pulses combining constant and offset-independent adiabaticity

Alexander V. Snadin^{1,2}, Alexey S. Kiryutin², Natalya N. Fishman², Nikita N. Lukzen^{1,2},

¹Department of Physics, Novosibirsk State University, Novosibirsk, Russia

²International Tomography Center, Siberian Branch of the Russian Academy of Sciences, Novosibirsk, Russia

E-mail: a.snadin@tomo.nsc.ru

Introduction

Adiabatic techniques in NMR and EPR offer new opportunities to control and modulate spectra in magnetic resonance, which opens new doors for research in materials science, biology and chemistry. Adiabatic pulses are a class of amplitude- and frequency-modulated RF/microwave pulses that are relatively insensitive to magnetic field inhomogeneity and off-resonance effects. A notable feature of adiabatic inverting pulses is the possibility of rectangular spin inversion over a large frequency range, which allows their involvement in medical clinical MRI studies for sharper selection of spatial slices.

At present, offset-independent amplitude (OIA) [1] pulses are among the most popular, with the adiabaticity parameter fixed for all isochromats of a given spectral contour, but only for a single moment of time, when the current frequency of the pulse coincides with the frequency of the corresponding isochromat. Despite their popularity, these pulses have poor performance in some cases, requiring high peak power of the B_1 field amplitude and being sometimes completely inefficient. In a previous study [2], we proposed an alternative approach (CA) for constructing adiabatic pulses. This approach ensures constant adiabaticity for the central isochromat throughout the pulse and enhances efficiency, even in cases where the pulse duration is limited.

Methods

In this paper, we have developed inverting MCA pulses that combine CA and OIA opportunities. We derived and solved the differential equations for the time dependencies of the RF field amplitude and frequency offset, which provide these two conditions. We then studied and compared the spectral selectivity and stability of the constructed pulses by scaling the RF field amplitude with those of other popular adiabatic inverting pulses. The MCA pulses obtained exhibited notable stability and superior performance in comparison to other OIA pulses under conditions of low adiabaticity. Additionally, a script has been provided to generate a shape pulse file for the TopSpin program utilizing our adiabatic inverting pulse for incorporation into the experimental procedures [3].

The proposed MCA pulses were also verified experimentally on an NMR spectrometer, which confirms the numerical simulation results.

Acknowledgements

This work is supported by the Russian Science Foundation (Contract No. 23-73-10103).

References

1. M.Garwood, L. DelaBarre, The return of the frequency sweep: designing adiabatic pulses for contemporary NMR, *J. Magn. Reson.*, 153 (2001) 155-177.
2. K.L. Ivanov, A.V. Snadin, A.S. Kiryutin, N.N. Lukzen, Analytical solution for the inverting pulses with constant adiabaticity, *J Magn Reson*, 343 (2022) 107298.
3. <https://doi.org/10.5281/zenodo.13745124>

"Ionic Liquid EAN/ $\text{Al}(\text{NO}_3)_3/\text{H}_2\text{O}$ " System Studied by NMR and Computational Methods

Milosh Ubovich^{1,2}, Kirill A. Mukhin¹, Vladimir V. Matveev¹, Andrey V. Egorov¹,
Vladimir I. Chizhik¹

¹Faculty of Physics, Saint Petersburg State University, Saint Petersburg, Russia

²Resource center "Physical methods of surface investigation", Saint Petersburg State University Research park, Saint Petersburg, Russia

³Institute of Chemistry, Saint Petersburg State University, Saint Petersburg, Russia

E-mail: v.chizhik@spbu.ru

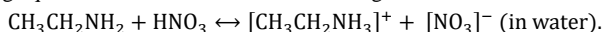
Introduction

In recent decades, ionic liquids (ILs) have attracted considerable attention of the scientific community due to their unique physical and chemical properties. It makes them as a distinct and prominent area of research [1]. Ethylammonium nitrate (EAN), the first example of a protic ionic liquid (PIL), has drawn considerable interest because of its wide-ranging potential applications across various fields.

While lithium salts have been the most effective materials for electrochemical devices to date, there is increasing interest in electrolytes that incorporate divalent and trivalent ions. These salts offer significantly higher energy density compared to lithium-based systems. Several studies have examined the physical and chemical properties of solutions containing aluminum nitrate in EAN in order to study such systems in more detail. Research using the ^1H NMR method revealed that these solutions retain water (it originates from aluminum crystallohydrates) within the first solvation shell of the Al^{3+} cation, even after standard drying processes. This bound water cannot be easily detected using conventional Karl Fischer titration. The aim of this study is to explore whether it is possible or impossible to eliminate water from the "Ionic Liquid EAN/ $\text{Al}(\text{NO}_3)_3/\text{H}_2\text{O}$ " system and to analyze how the state of water in the system changes with variations in temperature and aluminum salt concentration.

Experimental

The samples were prepared using EAN and crystalline hydrate $\text{Al}(\text{NO}_3)_3 \cdot 9\text{H}_2\text{O}$ (purity $\geq 99.9\%$). EAN was synthesized from aqueous solutions of 70 % ethylamine and 25 % nitric acid by mixing equimolar amounts of these chemical agents in an ice bath:



The solvent (EAN containing a moderate amount of water) was used to prepare mixtures with $\text{Al}(\text{NO}_3)_3 \cdot 9\text{H}_2\text{O}$: 1 kg of solvent contains 8.70 moles of EAN and 3.31 moles of H_2O .

The samples were prepared by gravimetric method. Water concentrations were verified using integral intensities of the ^1H spectral lines of EAN and water. It was determined the following molar compositions for the investigated "EAN/ $\text{Al}(\text{NO}_3)_3/\text{H}_2\text{O}$ " mixtures: $1\text{Al}^{3+} - 17.4[\text{EA}]^+ - 20.4[\text{NO}_3]^- - 15.6\text{H}_2\text{O}$ (≈ 0.5 mol of $\text{Al}(\text{NO}_3)_3 \cdot 9\text{H}_2\text{O}$ /1kg of the solvent) and $1\text{Al}^{3+} - 8.7[\text{EA}]^+ - 11.7[\text{NO}_3]^- - 12.3\text{H}_2\text{O}$ (≈ 1.0 mol of $\text{Al}(\text{NO}_3)_3 \cdot 9\text{H}_2\text{O}$ /1kg of the solvent). A drying procedure was performed under the pressure of 10^{-3} mbar and temperature of 80 °C. The aim of this procedure is to check the possibility/impossibility of removing water from samples.

NMR method was applied in the present study. The powerful capabilities of NMR to investigate of ILs are perfectly demonstrated [2]. All NMR experiments were carried out using Bruker Avance III 500 MHz Spectrometer at 500 MHz for ^1H nuclei, 130 MHz for ^{27}Al , and 36.1 MHz for ^{14}N . Spin-lattice relaxation times, T_1 , were measured using the "inversion-recovery" technique. The temperature range between 293 and 363 K in increments of 10 K were used. The accuracy of temperature stabilization was ± 0.1 K.

Results

The Al^{3+} cations predominantly exist in an octahedral aqueous environment, with 5.8 ± 0.2 water molecules in the first coordination shell at a relatively high water content and room temperature ($1\text{Al}^{3+} - 17.4[\text{EA}]^+ - 20.4[\text{NO}_3]^- - 15.6\text{H}_2\text{O}$). The hydrogen exchange time (τ_m) in this substructure is approximately 0.1 ms at 320–330 K. This time decreases significantly at higher temperatures. As the temperature rises, complexes containing 1–2 nitrate anions begin to appear, and their relative concentration at the temperature of 363 K, calculated from the integral intensities of the ^{27}Al lines, is approximately 0.15–0.20. The existence of distinct ^{27}Al NMR lines even at 363 K (see Fig. 1) indicates slow anion exchange, with exchange time more than 0.3 ms. This suggests that nitrate anions remain coordinated to Al^{3+} cations for a longer duration compared to the exchange time of hydrogen atoms in water molecules.

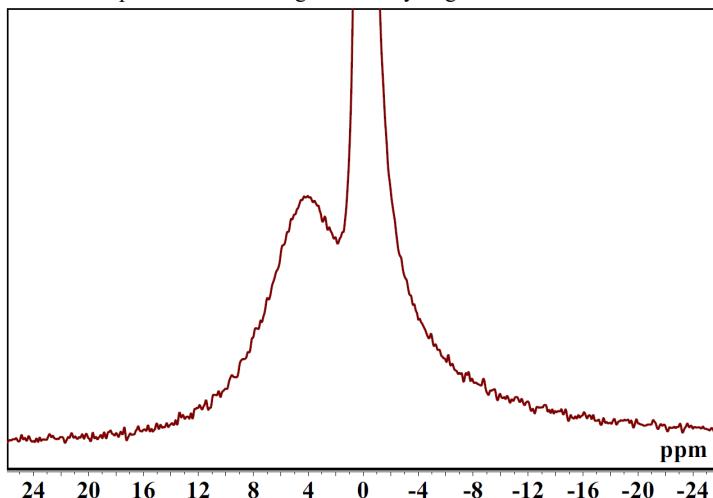


Figure. 1. The ^{27}Al spectra for the mixture ($1\text{Al}^{3+} - 17.4[\text{EA}]^+ - 20.4[\text{NO}_3]^- - 15.6\text{H}_2\text{O}$) at 363 K.

The integral calculations for the 9.5 ppm line indicate an average of 5.5 ± 0.2 water molecules in the Al^{3+} coordination sphere when the amount of water molecules per Al^{3+} cation is reduced ($1\text{Al}^{3+} - 8.7[\text{EA}]^+ - 11.7[\text{NO}_3]^- - 12.3\text{H}_2\text{O}$). This implies that, under conditions of lower water content, while the majority of complexes retain the octahedral structure $\text{Al}(\text{NO}_3)_3 \cdot 6\text{H}_2\text{O}$, some complexes form where nitrate anions partially replace water molecules.

To assess the possibility of removing water from the system, a standard drying procedure was conducted for 72 hours. The ^1H water spectra consist of the main single line (in the range of 9–10 ppm) from water molecules near the Al^{3+} cations and very weak line (around 5.5 ppm) from water in the "mosaic" of EAN ions at all temperatures. The average number of water molecules near the Al^{3+} cation can be calculated (4.1 ± 0.2) from the integral intensity of the main water line. There is a significant (not complete) displacement of water molecules by anions $[\text{NO}_3]^-$. This finding is further supported by the ^{27}Al NMR spectra (see also [3]).

To interpret the NMR spectra the quantum-chemical calculations of the electron shielding constants for the ^1H and ^{27}Al nuclei in mixed cation-anion complexes were involved. Quantum-chemical calculations were performed using Gaussian 09 Revision D.01 [4]. Structural parameters of fully optimized geometries obtained using B3LYP [5, 6] and 6-

311+G(d,p) basis set. The electron shielding constants for each substructure under consideration were calculated with the gauge-including-atomic-orbital (GIAO) formalism [7, 8] at the B3LYP/6-311+G(d,p) popular model level. The difference in the electron shielding (by the quantum-chemical calculations) of the ^{27}Al nuclei in the octahedral complex and others is in accordance with the experimental splitting.

One of the goals of this work was to analyze how the presence of the aqua complex near the aluminum cation ($[\text{Al}(\text{H}_2\text{O})_6]^{3+}$) affects the microstructure and molecular mobility in the mixture of EAN and aluminum nitrate. Molecular dynamics simulation method was chosen as the research method, since it allows one to monitor the evolution of a system at the molecular level. The simulation of the “EAN + $[\text{Al}(\text{H}_2\text{O})_6]^{3+}[(\text{NO}_3^-)_3]$ ” system was carried out using the molecular dynamics method applying the MDynaMix v5.0 software package [9] in a cubic cell with periodic boundary conditions in an NPT ensemble at the temperature of 298 K and atmospheric pressure (Nose-Hoover thermostat [10, 11] and Hoover barostat [12]). The potential proposed in the works [13, 14] was employed to describe the interaction of EA^+ cations. A model nitrate anion was treated as a 4-site planar structure with the central nitrogen atom and three oxygen atoms at the distance of 1.22 Å with all O-N-O angles of 120° [15]. The sum of Coulomb and Lennard-Jones (12-6) potentials described the interaction of the model nitrate-anion and other particles. Two potential parameter sets of nitrate-anion were considered (see Refs. [13, 16]). The potential parameters of the model Al^{3+} ion were described in Ref. [17]. Three-site SPC/E [18] water model was considered in the present study. Simulation time was 1 ns. Residual water appearing during the preparation of mixtures with aluminum salts can strongly influence the structure and properties of a system, and this effect should be taken into account in practice of designing mixtures for different applications.

Acknowledgments

This work was supported by the Russian Science Foundation (project № 23-23-00049). All NMR measurements were carried out in the Resource Center "Magnetic Resonance Research Methods" of Research Park of Saint Petersburg State University.

References

1. Welton T. – Biophys. Rev., 10, 691–706 (2018).
2. Damodaran K. – Prog. Nucl. Magn. Reson. Spectrosc., 129, 1–27 (2022).
3. Ubovich M., Mukhin K. A., Mikhailovskaya A. P., et al. – J. Phys. Chem. B, 128, 51, 12769–12774 (2024).
4. Frisch M. J., Trucks G. W., Schlegel H. B., et al., Gaussian 09, Revision D.01. Gaussian, Inc., Wallingford CT, 2013.
5. Becke A. D. – J. Chem. Phys., 98, 1372–1377 (1993).
6. Lee C., Yang W., Parr R. G. – Phys. Rev. B., 37, 785–789 (1988).
7. Ditchfield R. – Mol. Phys., 27, 789–807 (1974).
8. Wolinski K., Hinton J. F., Pulay P. – J. Am. Chem. Soc., 112, 8251–8260 (1990).
9. Lyubartsev A. P., Laaksonen A. – Comp. Phys. Comm., 128, 3, 565–589 (2000).
10. Nose S. – Mol. Phys., 52, 2, 255–268 (1984).
11. Martyna G. J., Tobias D. J., Klein M. L. – J. Chem. Phys., 101, 5, 4177–4189 (1994).
12. Martyna G. J., Tuckerman M. E., Tobias D. J., et al. – Mol. Phys., 87, 5, 1117–1157 (1995).
13. Umebayashi Y., Chung W.-L., Mitsugi T., et al. – J. Comput. Chem. Jpn., 7, 4, 125–134 (2008).
14. Choe J., Kim K., Chang S. – Bull. Korean Chem. Soc., 21, 2, 200–206 (2000).
15. Ebner C., Sansone R., Hengrasmee S., et al. – Int. J. Quant. Chem., 75, 805–814 (1999).
16. Megyes T., Balint S., Peter E., et al. – J. Phys. Chem. B., 113, 13, 4054–4064 (2009).
17. Faro T. M. C., Thim G. P., Skaf M. S. – J. Chem. Phys., 132, 114509 (2010).
18. Berendsen, H. J. C.; Grigera, J. R.; Straatsma, T. P. – J. Phys. Chem., 91, 24, 6269–6271 (1987).

Directional solidification in gallium under strong magnetic field: NMR studies

A. A. Vasilev¹, D. Yu. Nefedov¹, E. V. Charnaya¹, M. K. Lee², L.-J. Chang³

¹*Physics Department, St. Petersburg State University, St. Petersburg 198504, Russia*

²*Instrument Center of Science and Technology at National Cheng Kung University, Tainan 70101, Taiwan*

³*Department of Physics, National Cheng Kung University, Tainan 70101, Taiwan*

E-mail: allisher93529@yandex.ru

Introduction

Metals and metallic alloys with particular orientations of the crystalline axes in the grains and controllable microtextures are of exceptional importance for various technological applications [1,2]. The orientation of a single oriented crystalline phase upon solidification of tin was observed by nuclear magnetic resonance [3,4]. The latter method of proving the alignment of crystalline axes along particular directions has the advantage over other methods as it can be done within the magnet of the NMR spectrometer at different temperatures due to strong angular dependence of the resonance line position. In the present study we used the commercial NMR spectrometer supplied with a superconducting magnet to demonstrate the directional solidification of metallic gallium in the strong magnetic field.

Experiment

The sample was a gallium ball of 1 mm in diameter wrapped in a Teflon tape to prevent touching with the ceramic NMR coil insert and changing the shape upon melting. Gallium has two stable isotopes, ⁶⁹Ga and ⁷¹Ga, with rather similar abundances. Both isotopes have the spin equal to 3/2. Their gyromagnetic ratios γ and quadrupole moments Q are $\gamma_{69}=6.44\cdot 10^{-7} \text{ rad}\cdot\text{T}^{-1}\cdot\text{s}^{-1}$, $Q_{69}=0.168 \text{ barn}$ and $\gamma_{71}=8.18\cdot 10^{-7} \text{ rad}\cdot\text{T}^{-1}\cdot\text{s}^{-1}$, $Q_{71}=0.106 \text{ barn}$ for ⁶⁹Ga and ⁷¹Ga, respectively. Most measurements in the present work were carried out for both gallium isotopes.

Studies were carried out using a Bruker Avance 400 NMR pulse spectrometer at magnetic field 9.4 T within a temperature range from 150 to 350 K. We observed NMR signals for both gallium isotopes. The NMR spectra were recorded at different temperatures when gallium was in the liquid, solid, or supercooled states as Fourier transforms of the free induction signals after a 90-degree pulse. The frequency shifts of the resonance lines were referenced to NMR lines of the gallium isotopes for the GaAs single crystal at room temperature.

Results

The melting temperature of the stable α modification of gallium is 302.9 K. An example of the NMR line for ⁷¹Ga at 314 K is shown in Fig. 1,a (left panel). Gallium is easy to be supercooled. The resonance lines for the supercooled gallium are similar to those above the melting point. The integral intensity of the lines is proportional to the amount of melted gallium. Fig. 1,a (right panel) demonstrates a temperature dependence of the integral intensity of the ⁷¹Ga resonance line relevant to the gallium melt when the sample was first heated up to 314 K, then cooled down to 156 K well below the complete gallium freezing, and subsequently warmed up to the initial temperature. As can be seen in Fig. 1,a (right panel) the intensity of the NMR signal from supercooled gallium became zero at 270.9 K. At the same temperature two Gaussians emerge in the NMR spectra of ⁷¹Ga centered at 1280 and 210 ppm (Fig. 1,b).

To understand the directions of the α -Ga crystalline axes in the oriented parts with respect to the magnetic field we studied the angular dependences of the resonance line positions (Fig 2). The quadrupole shifts of the resonance lines due to the central transitions in

a strong field of 9.4 T can be calculated using the perturbation theory of the second order [5]. The quadrupole shift δ_Q for the spin 3/2 can be written as a sum of the isotropic and anisotropic contributions:

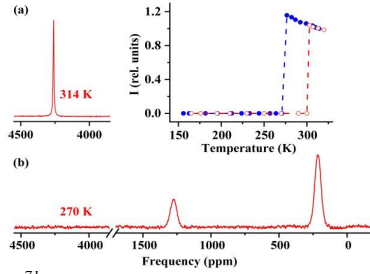


Fig. 1. (a) Left panel: ^{71}Ga NMR line for the melted gallium at 314 K, right panel: temperature dependence of the intensity of the NMR signal from melted gallium at cooling (blue solid circles) and warming (red open circles). The dashed lines are guides for the eye. (b) ^{71}Ga NMR spectrum for oriented α -Ga at 270 K

$$\delta_Q = \delta_{iso} + \delta_{an} = -\frac{\nu_Q^2}{10\nu_L} \left(1 - \frac{\eta^2}{3} \right) - \frac{\nu_Q^2}{2\nu_L} \left[A(\varphi, \eta) \cos^4 \theta + B(\varphi, \eta) \cos^2 \theta + C(\varphi, \eta) \right], \quad (1)$$

where ν_L is the Larmor frequency, ν_Q is the quadrupole frequency, η is asymmetry, θ and φ are the polar angles specifying the magnetic field direction with respect to the principle axes of the EFG tensor. The coefficients in the second term are given by:

$$\begin{aligned} A(\varphi, \eta) &= -\frac{27}{8} - \frac{9}{4} \eta \cos 2\varphi - \frac{3}{8} \eta^2 \cos^2 2\varphi, \\ B(\varphi, \eta) &= \frac{15}{4} - \frac{1}{2} \eta^2 + 2\eta \cos 2\varphi + \frac{3}{4} \eta^2 \cos^2 2\varphi, \\ C(\varphi, \eta) &= -\frac{23}{40} + \frac{14}{15} \eta^2 + \frac{1}{4} \eta \cos 2\varphi - \frac{3}{8} \eta^2 \cos^2 2\varphi. \end{aligned} \quad (2)$$

Neglecting the anisotropy of the Knight shift, we can write the expression for the total shift δ as:

$$\delta = K_{iso} + \delta_Q, \quad (3)$$

where K_{iso} is the isotropic Knight shift in α -Ga. The rotation angle γ was set to zero in the initial position of the sample.

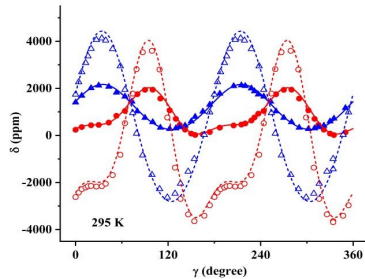


Fig. 2. Dependences of the NMR line shifts in the oriented α -Ga on the rotation angle γ . Open and closed symbols correspond to ^{69}Ga and ^{71}Ga , respectively. Solid and dashed lines are fits using Relationships 1 – 3.

According to the fit, the oriented parts of gallium have their crystalline a -axis directed along the external magnetic field. The angle γ is then the angle between the magnetic field and the crystalline a -axis. The energetically favorable orientations of the crystalline axes in magnetic field correspond to the minimization of the magnetic energy of the nuclei formed upon cooling the melt. The correlations between the orientation of the crystalline nuclei and magnetic energy are established due to anisotropy of the magnetization tensor.

In another thermal cycle we heated the gallium sample up to 340 K and started the cooling process. Gallium was frozen at 257 K in contrast to 270.9 K during the previous thermal cycles. Then the sample was cooled down to 233 K and warmed up. The whole sample was melted at 267 K, which is relevant for β -Ga. The dependence of the integral intensity of the ^{71}Ga NMR signal in the melt is shown in Fig. 3. Starting from 257 K at cooling and up to 267 K at warming, a single narrow signal was observed, which is unambiguously caused by oriented β -Ga.

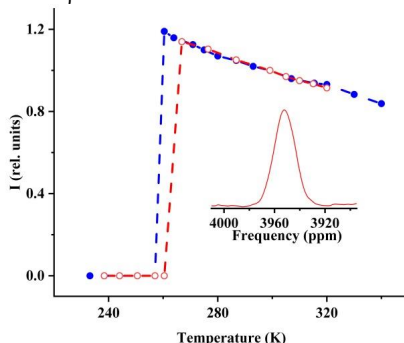


Fig. 3. Temperature dependence of the ^{71}Ga NMR signal intensity from melted gallium at cooling from 340 K (blue solid circles) and subsequent warming (red open circles). The dashed lines are guides for the eye. The inset shows the ^{71}Ga NMR line for the oriented β -Ga at 257 K.

The lines corresponded to the central $+1/2 \leftrightarrow -1/2$ transition for both α - and β -gallium were observed in different thermal cycles. The intensity of the lines and the angular dependences of the line frequency shifts suggested that more than 1/3 of the gallium volume had ordered crystalline axes. The results were quite reproducible for particular cooling-warming thermal cycles. It was found that the NMR signals from the oriented β -Ga disappeared below 230 K due to the polymorph transition into α -Ga.

Acknowledgements

Measurements were carried out in SPbGU using the equipment of "Center for Diagnostics of Functional Materials for Medicine, Pharmacology and Nanoelectronics".

References

1. X. Zhang, J. Li, Y. Liu, B. Lu, Sh. Liang, J. Zhou. *Nature Com.* 15, 2735 (2024).
2. X. Wang, X. He, T. Wang, Y. Li. *Addit. Manuf.* 35, 101174 (2020).
3. C. Tien, E. V. Charnaya, M. K. Lee. *J. Magn. Magn. Mater.* 322, 2712 (2010).
4. E. V. Charnaya, C. Tien, M. K. Lee. *Phys. Solid State* 52, 1539 (2010).
5. J. F. Baugher, P.C. Taylor, T. Oja, P. J. Bray. *J. Chem. Phys.* 50, 4914 (1969).

Lindblad dephasing relaxation and quantum entanglement in two-spin systems

*Sergey G. Vasil'ev¹, Elena I. Kuznetsova¹, Elizaveta I. Shipulya^{1,2}, Edward B. Fel'dman¹,
Alexander I. Zenchuk¹*

¹*Federal Research Center of Problems of Chemical Physics and Medicinal Chemistry RAS,
Chernogolovka, Moscow region, 142432, Russia*

²*Moscow State University, Moscow, 119991 Russia
E-mail:viesssw@mail.ru*

Introduction

The Lindblad equation [1] is widely used for solving problems of the interaction of open spin systems with the environment [2,3]. The Lindblad equation conserves all properties of the density matrix during the evolution of the systems. In particular, the positive definiteness of the density matrix [1] is conserved in the course of evolution. Although the Lindblad approach can be applied to systems with an arbitrary number of spins, analytical solutions are possible in special cases only. We consider the dephasing relaxation in a two-spin system in multiple quantum (MQ) NMR [4,5] when an exact solution of the Lindblad equation can be obtained. We show that the spectrum of MQ NMR coherences consists of the zeroth- and plus/minus second orders only in a system with dephasing relaxation. The dependencies of the intensities of MQ NMR coherences on the relaxation rate are also obtained.

On the basis of quantum dynamics in MQ NMR we investigate quantum correlations [6] (quantum entanglement) in the considered system. We obtain the dependence of quantum entanglement on the relaxation rate.

MQ NMR in a two-spin system with the dephasing relaxation

We consider the Lindblad equation [1] for a two-spin system in the conditions of multiple quantum (MQ) experiment [7] with dephasing relaxation. The equation for the density matrix for this case reads

$$\frac{d\rho(t)}{dt} = \frac{Di}{2} [I_1^+ I_2^+ + I_1^- I_2^-, \rho(t)] + g \sum_{k=1}^2 \left\{ I_{zk} \rho(t) I_{zk} - \frac{1}{2} I_{zk}^2 \rho(t) - \frac{1}{2} \rho(t) I_{zk}^2 \right\}, \quad (1)$$

where D is the coupling constant of the dipole-dipole interaction, I_{ak} ($k=1,2$) is the spin angular momentum projection operator on the a axis ($a = x, y, z$), I_k^+ , I_k^- ($k=1,2$) are the raising and lowering operators and g is the rate of the dephasing relaxation. It is possible to simplify Eq.(1) for spins $1/2$ when $I_{zk}^2 = 1/4$ performing the transformation

$$\rho(t) = e^{\frac{1}{2}gt} \bar{\rho}(t) \quad (2)$$

Then we can rewrite Eq. (1) in the following form

$$\frac{d\bar{\rho}(t)}{dt} = \frac{Di}{2} [I_1^+ I_2^+ + I_1^- I_2^-, \bar{\rho}(t)] + g \sum_{k=1}^2 I_{zk} \bar{\rho}(t) I_{zk} \quad (3)$$

At $t=0$ the system is in the thermodynamic equilibrium state and its density matrix is

$$\bar{\rho}(0) = \frac{e^{\beta I_z}}{Z}, \quad Z = \text{Tr} \{ e^{\beta I_z} \}. \quad (4)$$

It is possible to obtain an analytical solution of Eq.(3) with the initial state (4). As a result, the density matrix has the X-form [6] and can be represented as

$$\bar{\rho}(t) = \begin{pmatrix} a_{11} & 0 & 0 & a_{14} \\ 0 & a_{22} & 0 & 0 \\ 0 & 0 & a_{33} & 0 \\ a_{41} & 0 & 0 & a_{44} \end{pmatrix}, \quad (5)$$

where the matrix elements a_{11} , a_{14} , a_{22} , a_{33} , a_{41} , a_{44} are

$$\begin{aligned} a_{11} &= \frac{e^{\frac{gt}{2}} \cosh \frac{\beta}{2}}{4 \cosh^2 \frac{\beta}{2}} + \frac{1}{2} \tanh \frac{\beta}{2} \cos \sqrt{D^2 - \frac{g^2}{4}} t + \frac{g}{4} \frac{\tanh \frac{\beta}{2}}{\sqrt{D^2 - g^2/4}} \sin \sqrt{D^2 - g^2/4} t, \\ a_{14} = a_{41} &= \frac{1}{2i} \tanh \frac{\beta}{2} \frac{D}{\sqrt{D^2 - g^2/4}} \sin \sqrt{D^2 - \frac{g^2}{4}} t, \\ a_{22} = a_{33} &= \frac{e^{\frac{gt}{2}}}{4 \cosh^2 \frac{\beta}{2}}, \\ a_{44} &= \frac{e^{\frac{gt}{2}} \cosh \frac{\beta}{2}}{4 \cosh^2 \frac{\beta}{2}} - \frac{1}{2} \tanh \frac{\beta}{2} \cos \sqrt{D^2 - \frac{g^2}{4}} t - \frac{g}{4} \frac{\tanh \frac{\beta}{2}}{\sqrt{D^2 - g^2/4}} \sin \sqrt{D^2 - \frac{g^2}{4}} t. \end{aligned} \quad (6)$$

The density matrix of Eq.(5) allows us to obtain the intensities of MQ NMR coherences. The intensity of the MQ NMR coherence of the zeroth order is

$$J_0(t) = \tanh \frac{\beta}{2} \left(\cos \sqrt{D^2 - \frac{g^2}{4}} t + \frac{g}{2\sqrt{D^2 - g^2/4}} \sin \sqrt{D^2 - \frac{g^2}{4}} t \right)^2 e^{-gt}. \quad (7)$$

The intensities of the MQ NMR coherences of the plus/minus second order are

$$J_{\pm 2}(t) = \frac{1}{2} \tanh \left(\frac{\beta}{2} \right) \frac{D^2 e^{-gt}}{D^2 - g^2/4} \sin^2 \sqrt{D^2 - \frac{g^2}{4}} t \quad (8)$$

If the dephasing relaxation is absent these MQ NMR intensities are

$$J_0(t) = \tanh \frac{\beta}{2} \cos^2 Dt, \quad J_{\pm 2}(t) = \frac{1}{2} \tanh \frac{\beta}{2} \sin^2 Dt. \quad (9)$$

It is interesting to notice that the oscillations of MQ NMR coherences are determined by $\sqrt{D^2 - g^2/4}$ but not D as in the case without relaxation. The reduction of the oscillation frequency as compared with D was observed experimentally in [7].

Quantum entanglement in a two-spin system with dephasing relaxation

To determine the concurrence [8,9], which describes quantum entanglement, for the state (5), the eigenvalues of the following operator need to be found:

$$R = (\sigma_{1y} \otimes \sigma_{2y}) \bar{\rho}(t) (\sigma_{1y} \otimes \sigma_{2y}) \bar{\rho}^*(t), \quad (10)$$

where σ_{ky} ($k = 1, 2$) are the Pauli matrices acting on spins 1 and 2. The density matrix $\bar{\rho}^*(t)$ is the complex conjugate of $\bar{\rho}(t)$. Using the Wootters formula [9] for the concurrence, we obtain

$$C = \begin{cases} 2(|a_{14}| - a_{22}), & \text{if } |a_{14}| > a_{22} \\ 0, & \text{if } |a_{14}| < a_{22} \end{cases} \quad (11)$$

Fig.1 demonstrates the dependence of the concurrence on the dimensionless evolution time $\tau = Dt$ for different rates of dephasing relaxation g/D at $\beta=1.5$. Dephasing relaxation destroys the quantum correlations.

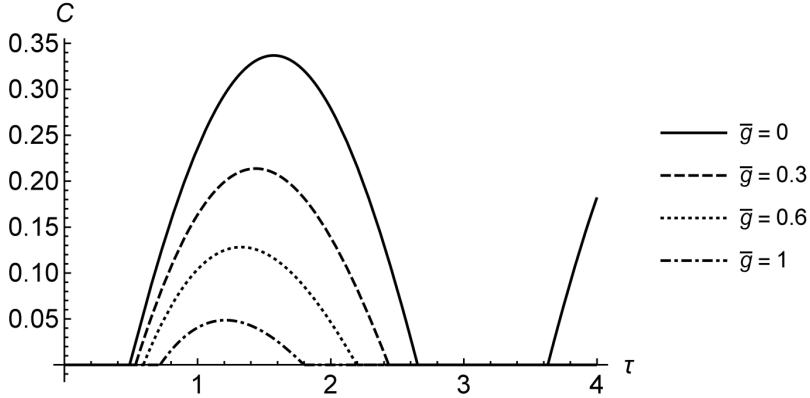


Figure 1. The dependence of the concurrence on the dimensionless evolution time at different rates of the dephasing relaxation.

Conclusion

The dependence of the intensities of MQ NMR coherences on the rate of dephasing relaxation in a two-spin system has been theoretically studied. Quantum correlations (quantum entanglement) has been investigated at different values of the rate of dephasing relaxation.

Acknowledgements

The work was performed as a part of a state task, State registration No. 124013000760-0.

References

1. J. Preskill. Lecture notes for physics 229: Quantum information and Computation. California Institute of Techology. 1998.
2. M.H.Levitt, C.Bengs J.Magn.Reson. 310, 106645 (2021)
3. D.Manzano AIP Advances 10, 025106 (2020)
4. J. Baum, M. Munowitz, A. N. Garroway, A. Pines J. Chem. Phys. 83, 2015 (1985)
5. S.I.Doronin, I.I.Maksimov, E.B.Fel'dman J. Exp. Theor. Phys. 91, 597 (2000)
6. S. M. Aldoshin, E. B. Fel'dman, M. A. Yurishchev Low Temp. Phys., 40, 3 (2014)
7. E. B. Fel'dman , E. I. Kuznetsova , K. V. Panicheva , S. G. Vasil'ev, A. I. Zenchuk J. Magn. Reson. 363, 107706 (2024).
8. S. Hill, W. K. Wootters Phys.Rev.Lett., 78, 5022 (1997).
9. W. K. Wootters Phys.Rev.Lett., 80, 2245 (1998).

Silicon-enhanced incorporation of boron into AlPO-11 framework according to ^{11}B solid-state NMR

Ilya V. Yakovlev¹, Aleksandr V. Toktarev¹, Aleksandr A. Shubin², Evgeniy S. Papulovskiy¹, Olga B. Lapina¹

¹Boreskov Institute of Catalysis, p. Lavrentieva 5, 630090 Novosibirsk, Russia

²Institute of Solid State Chemistry and Mechanochemistry, ul. Kutateladze 18, 630090 Novosibirsk, Russia

Modern heterogeneous catalysts often require flexibility in their catalytic properties. One of the notable examples of such flexible catalytic systems are the family of aluminophosphate (AlPO) molecular sieves that can be used as catalysts and catalyst supports in various industrially important processes. Various heteroatoms can be introduced into the AlPO framework in order to tune its catalytic properties. One of the most widely used substitutions is $\text{P}^{5+} \rightarrow \text{Si}^{4+}$, H^+ which creates strong Bronsted acid sites. However, an excessive amount or strength of acid sites may lead to undesirable results such as hydrocarbon cracking in the isomerization reactions or even carbonization and deactivation of the catalyst. The activity of the resulting framework can be finely tuned by introduction of another element, e.g. boron.

In our previous work [1], we have shown that the substitution of boron into the framework of aluminophosphate AlPO-11 is extremely inhibited. One of the possible reasons for such a weak interaction is the particularly ordered character of hydration of this framework [2] and the hydrolysis of the B-Al bonds. As a result, the concentration of boron in the resulting BAPO-11 material is barely detectable. In this work, we provide the ^{11}B NMR experimental evidence of introduction of boron into the AlPO-11 framework simultaneously with silicon. If both of these elements are introduced in a one-pot reaction, the concentration of boron in the resulting BSAPO-11 material is orders of magnitude higher compared to BAPO-11. This may be caused by the disruption of aluminophosphate by Si atoms, which allows for B sites to stabilize in the framework.

Acknowledgements

This work was supported by the Russian Science Foundation (RSF grant № 23-13-00151).

References

1. Yakovlev I.V., Toktarev A.V., Shubin A.A., Papulovskiy E.S., Cherepanova N.E., Lapina O.B. Incorporation of Boron into the AlPO-11 Framework According to ^{11}B and ^{27}Al Solid-State NMR Spectroscopy and First-Principles Calculations Applied Magnetic Resonance. 2023. V.54. P.957–969.
2. Yakovlev I.V., Shubin A.A., Papulovskiy E.S., Toktarev A.V., Lapina O.B. Repulsive Lateral Interaction of Water Molecules at the Initial Stages of Adsorption in Microporous AlPO₄-11 According to ^{27}Al NMR and DFT Langmuir. 2024. V.40. N12. P.6384–6393.

Magnetic relaxation properties of metal-carbon heterostructures

Natalia P. Yevlampieva¹, Vasily T. Lebedev², Maria V. Popova², Mikhail A. Vovk¹, Alexander V. Shvidchenko³, Biligma B. Tudupova³, Victor I. Kuular³

¹*St. Petersburg State University, St. Petersburg, Russia*

²*Petersburg Nuclear Physics Institute named by B.P. Konstantinov, National Research Center Kurchatov Institute, Gatchina, Leningrad region, Russia*

³*Ioffe Institute, St. Petersburg, Russia*

E-mail: n.yevlampieva@spbu.ru

Introduction

Developments of new composite nanostructures for biomedicine are aimed for expanding the diagnostic capabilities of drugs when combined with a therapeutic effect [1-3]. This involves searching for opportunities to maximize both factors (diagnostic, therapeutic) by optimally combining the beneficial properties of selected components and ensuring targeted delivery of drugs that can be placed on specially selected platforms (quantum dots, iron oxide nanoparticles, gold and its shell-type structures), capable, among other things, of stimulating the activity of drugs [1].

To solve these problems, metal oxides and metal-organic frameworks, including gold, silicon and nanoparticles with lanthanides are used [4]. Such objects are in demand for numerous applications (drug delivery, gene chemo-, photo- and photodynamic therapy, hyperthermia, photoacoustics, ultrasound imaging, bioseparation, tissue engineering) [5,6]. Among promising biomedical materials, nanodiamonds with unique chemical-mechanical properties attract attention as promising platforms for the design of therapeutic combinations in personalized medicine tasks [7]. Methods are being developed for the association of drugs with nanodiamonds and their hybrids with nanoporous silicon, carbon nanotubes and fullerenes for targeted delivery and overcoming cellular resistance to serial drugs [8].

In this work we have synthesized functional heterostructures with magnetic molecules being endofullerenols $M@C_{2n}(OH)_X$ ($2n \geq 30$, $X \sim 30$) with 4f and 3d metal atoms (M) [9,10]. These molecules were placed on the surface of detonation nanodiamonds (DND) for the applications in Magnetic Resonance Imaging (MRI), Photodynamic Therapy (PDT), and nuclear medicine also. The specific feature of endofullerenols is a strong capturing of heavy magnetic atoms inside a durable carbon cage without any risks of organism intoxication when the encapsulated atoms conserve the original useful physical and chemical properties. We aimed to reach a positive effect in the enhancement of relaxivity magnetic metal ions as a result of the attachment of fullerenols at diamond surface to provide a fine distribution of these molecules and organize their effective interaction with water surrounding to get faster proton spin relaxation and guarantee a high contrasting characteristics of novel developed preparations.

Samples and NMR experiments

Fullerenols were produced by hydroxylation of endofullerenes synthesized in electric arc [9,10]. The nanodiamonds (size 4-5 nm) were chemically purified and annealed in a hot flow of hydrogen (air), obtaining DNDZ+ and DNDZ- crystals with positive (negative) potentials in water (30-70 mV), which ensured the stability of diamond colloids with a large specific surface area of particles ($\sim 400 \text{ m}^2/\text{g}$) [11]. In aqueous media, the $M@C_{2n}(OH)_X$ molecules formed hydrogen bonds with the hydrophilic groups (H, OH, COOH) of diamonds via hydroxyls. The association of components was enhanced by hydrophobic and electrostatic interactions, which allowed the formation of complexes $M@C_{2n}(OH)_X + \text{DNDZ}^+$, $M@C_{2n}(OH)_X + \text{DNDZ}^-$. The following aqueous solutions were studied in the experiments:

1. DNDZ+(0.30 % wt.), concentration 3 mg/ml; 2. DNDZ-(0.32%), 3.2 mg/ml; 3. DNDZ-(0.32 %)+Gd@C₈₂(OH)_x (X ~ 30) (0.15 %), 4.7 mg/ml; 4. DNDZ+(0.3 %)+Gd@C₈₂(OH)_x (0.15 %), 4.5 mg/ml; 5. Gd@C₈₂(OH)_x (0.30 %), 3 mg/ml; 6. H₂O; 7. Ho@C_{2n}(OH)₄₀ (2n ~ 40), (0.30 %), 3 mg/ml; 8. DNDZ-(0.32 %) + Ho@C_{2n}(OH)₄₀ (0.15 %), 4.7 mg/ml; 9. DNDZ+(0.3 %) + Ho@C_{2n}(OH)₄₀ (0.15 %), 4.5 mg/ml; 10. Fe@C_{2n}(OH)_x (2n ~ 60, X ~ 30) (0.33 %), 3.3 mg/ml; 11. DNDZ-(0.32 %) + Fe@C_{2n}(OH)_x (2n ~ 60, X ~ 30) (0.16 %), 4.8 mg/ml; 12. DNDZ+(0.3 %) + Fe@C_{2n}(OH)_x (2n ~ 60, X ~ 30) (0.16 %), 4.6 mg/ml.

Magnetic relaxation properties of aqueous dispersions of complexes with magnetic atoms (Gd, Ho, Fe) were studied in NMR experiments at ambient temperature (297 K) with determination of longitudinal and transverse relaxation times (T₁, T₂) for protons in solutions (Bruker 500 MHz Avance III spectrometer, Magnetic Resonance Research Centre, St. Petersburg State University).

Results

To evaluate the efficiency of preparations with metals, inverse spin relaxation times (1/T₁, 1/T₂) were found in solutions. The corresponding values for water (1/T_{1w}, 1/T_{2w}) were subtracted from them, normalizing to metal concentrations (C_{mm}, mmol/L). Finally, magnetic relaxation characteristics of substances were calculated, $r_{1,2} = [1/T_{1,2} - 1/T_{1,2w}]/C_{mm}$ (Fig.1).

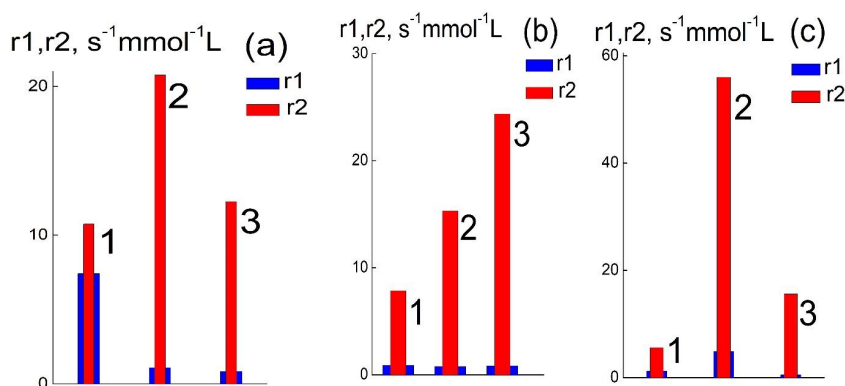


Figure 1. Longitudinal and transverse relaxivities (r_1, r_2) of fullerenols (1) with Gd, Ho, Fe (a, b, c) and their complexes with DNDZ- or DNDZ+ diamonds (2, 3) in aqueous solutions.

In the structures with Gd-fullerenols, the parameter $r_2 \sim 21 \text{ s}^{-1}mmol^{-1}L$ is the highest in the complex with DNDZ-. For MRI contrast, the difference $\Delta r = r_2 - r_1 \sim 20 \text{ s}^{-1}mmol^{-1}L$ is crucially important. For a small value of $r_1 \sim 1 \text{ s}^{-1}mmol^{-1}L$, the Δr magnitude exceeds significantly that for pure fullerenols ($\Delta r \sim 3 \text{ s}^{-1}mmol^{-1}L$) and fullerenols on DNDZ+ platform ($\Delta r \sim 11 \text{ s}^{-1}mmol^{-1}L$) (Fig.1a). Indeed, the Gd@C₈₂(OH)_x+DNDZ- complexes are more effective than pure fullerenols and can create a necessary contrast by using the dose six times lower.

In contrast to Gd-fullerenols, which provided the maximum transverse relaxation rate upon interaction with DNDZ- particles, fullerenols with Holmium give an even greater effect when they are linked with DNDZ+, $r_2 \sim 25 \text{ s}^{-1}mmol^{-1}L$, and the $\Delta r \sim 24 \text{ s}^{-1}mmol^{-1}L$ for a

reduced $r_1 \sim 0.8 \text{ s}^{-1}\text{mmol}^{-1}\text{L}$. This indicates a significant role of electrostatic forces between the components in the formation of effective magnetic complexes with Ho (Fig.1b).

However, a record result $r_2 \sim 56 \text{ s}^{-1}\text{mmol}^{-1}\text{L}$ we have achieved when associated Fe-fullerenols with DNDZ- diamonds. In this case the difference $\Delta r \sim 51 \text{ s}^{-1}\text{mmol}^{-1}\text{L}$ is ~ 12 times greater than the parameter $\Delta r \sim 4 \text{ s}^{-1}\text{mmol}^{-1}\text{L}$ for free fullerenols (Fig.1c).

Thus, $\text{Fe}@\text{C}_{2n}(\text{OH})_x + \text{DNDZ-}$ complexes demonstrate clearly a key role of diamonds as the active platforms that allows for a more than tenfold increase in relaxivity comparatively to this one for free fullerenols. In general, the proposed methodology for the creation of effective contrast agents for MRI by using nanodiamond platforms for magnetic molecules seems to be applicable for theranostics.

Acknowledgements

This work is supported by the Russian Science Foundation (grant № 25-45-01024). Authors thank the Magnetic Resonance Research Centre of Saint-Petersburg State University for the delivered ability to perform the experiments and technical help.

References

1. F. Chen, E. B. Ehlerding, W. Cai. – J. Nucl. Med., 55 (12), 1919–1922 (2014).
2. S. M. Hosseini, J. Mohammadnejad, R. Najafi-Taher, Z. Beiram Zadeh, M. Tanhaei, S. Ramakrishna. – ACS Appl. Bio Mater., 6(4), 1323–1338 (2023).
3. A. Coene, J. Leljaert J. – Appl. Phys., 131, 160902 (2022).
4. B. Carrese, G. Sanità, A. Lamberti. – Cancers, 14(19), 4654 (2022).
5. Functionalized Magnetic Nanoparticles for Theranostic Applications. M. Pandey, K. Deshmukh, C. M. Hussain (Eds.). Scrivener Publishing LLC, 2025, 564 P. Print ISBN:9781394172405, DOI:10.1002/9781394172917.
6. S. E. Sandler, B. Fellows, O. Thompson Mefford. – Anal. Chem. 91(22), 14159–14169 (2019).
7. D. Ho, C.-H. Katherine Wang, E. Kai-Hua Chow. – Science Advances, 1(7), e1500439-e1500439 (2015).
8. M. I. Kanyuk. – Biotechnologia Acta, 8(2), 1-25 (2015).
9. V. P. Sedov, A. A. Szhogina, M.V. Suyasova, V.A. Shilin, V.T. Lebedev. Method of obtaining water soluble hydroxylated endometallofullerenes of lanthanides. Patent Rus. Ru 2659972 C1. Reg. 04.07.2018. Published: 04.07.2018, Bul. No. 19. P.1-10.
10. V. P. Sedov, A. A. Szhogina, M. V. Suyasova, V. T. Lebedev. Method for obtaining endofullerenes of 3d metals. Patent Rus. Ru 2664133 C1. Reg. 15.08.2018. Published: 15.08.2018. Bull. No 23. P.1-13.
11. A.E. Aleksenskii. Technology of preparation of detonation nanodiamond. In Detonation Nanodiamonds. Science and Applications; Vul, A.Y., Shenderova, O.A. (Eds.). Pan Stanford Publishing: Danvers, MA, USA, P. 37–72 (2014).

Intra- and intermolecular transfer of parahydrogen-induced hyperpolarization via nuclear Overhauser effect induces RASER

Anna P. Yi^{1,2}, Ivan A. Trofimov³, Oleg G. Salnikov¹, Andrey N. Pravdivtsev⁴, Henri de Maissin^{3,5}, Eduard Y. Chekmenev⁶, Jan-Bernd Hövener⁴, Andreas B. Schmidt^{3,5,6}, Igor V. Koptiyug¹

¹Laboratory of Magnetic Resonance Microimaging, International Tomography Center SB RAS, Novosibirsk, Russia

²Department of Natural Sciences, Novosibirsk State University, Novosibirsk, Russia

³Division of Medical Physics, Department of Diagnostic and Interventional Radiology; University Medical Center Freiburg, Faculty of Medicine, University of Freiburg, Freiburg, Germany

⁴Section Biomedical Imaging, Molecular Imaging North Competence Center (MOIN CC), Department of Radiology and Neuroradiology; University Medical Center Schleswig-Holstein and Kiel University, Kiel, Germany

⁵German Cancer Consortium (DKTK), partner site Freiburg and German Cancer Research Center (DKFZ), Im Neuenheimer Feld 280, Heidelberg, Germany

⁶Department of Chemistry, Integrative Biosciences (Ibio), Karmanos Cancer Institute (KCI); Wayne State University, Detroit, United States

E-mail: anna.i@tomo.nsc.ru

Introduction

One of the central issues of nuclear magnetic resonance (NMR) and magnetic resonance imaging (MRI) techniques is their intrinsically low sensitivity. Hyperpolarization techniques allow to successfully overcome this problem and amplify the signal of up to several orders of magnitude [1]. ParaHydrogen-Induced Polarization (PHIP) is rapidly developing hyperpolarization method, which is based on the catalytic pairwise parahydrogen (p-H₂) addition to an unsaturated precursor. Pairwise addition of p-H₂ breaks the singlet symmetry of ¹H spins, making it possible to detect enhanced NMR signals of the resultant molecule. There are two protocols for hyperpolarization by PHIP. PASADENA protocol employs hydrogenation at a high magnetic field, where Zeeman interaction prevails over spin-spin coupling, and results in multiplet polarization of nascent p-H₂ protons. In the second protocol, ALTADENA, a precursor reacts with p-H₂ at a low field (e.g., Earth's one) and after it polarization transfer proceeds adiabatically to an NMR spectrometer probe resulting in net polarization of ¹H spins [2].

In recent years significant and rapid progress was achieved in investigation and applications of RASER effect in hyperpolarization experiments [3]. RASER phenomenon lies in an emergence of a positive feedback between the sample magnetization and an NMR spectrometer coil, provided that the sample is strongly negatively polarized and the population inversion threshold in the analyzed system is exceeded. When RASER is generated using PHIP, all emissive signals become significantly suppressed, resulting in the large positive net hyperpolarization in the system [4]. Recently it was shown that this positive hyperpolarization converts into the opposite-sign hyperpolarization of other spins through intra- and intermolecular dipolar interactions. Such approach was called Parahydrogen and RASER-Induced Nuclear Overhauser Effect (PRINOE) and may be realized in both ALTADENA and PASADENA protocols for hyperpolarization of various nuclei [4, 5].

Earlier PRINOE experiments were carried out using PHIP precursors with C=C bonds [4, 5]. However, it was demonstrated that p-H₂ addition to triple bonds catalyzed by cationic Rh complexes often produce greater hyperpolarization, indicating that this approach may be prospective in PRINOE experiments as well. Thus, herein, we study RASER and PRINOE

effects with the utilization of triple bond compounds such as propargyl alcohol (**1'**), 3-butyne-2-ol (**2'**), 2-methyl-3-butyne-2-ol (**3'**) as the PHIP precursors (Fig. 1).

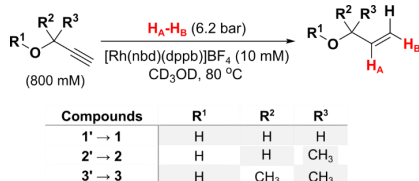


Figure 1. Reaction scheme of pairwise addition of *p*-H₂ to precursors 1'–3' to yield HP products 1–3.

Results and discussion

Both PASADENA and ALTADENA protocols were used to generate RASER. In the PASADENA protocol hydrogenation occurred in the NMR spectrometer probe via *p*-H₂ bubbling through the preheated solution. In the ALTADENA protocol *p*-H₂ addition was performed at the Earth's field followed by transfer of the sample into the NMR probe.

PASADENA protocol resulted in RASER of all three protons of allylic fragment in each of three substrates **1–3** (Fig. 2). Hyperpolarization of the proton **1c** (which does not originate from *p*-H₂) at PASADENA conditions indicates the occurrence of intramolecular PRINOE, which was effective enough to create negative hyperpolarization beyond the RASER threshold (Fig. 2). In the case of ALTADENA experiments the RASER effects for protons which did not originate from *p*-H₂ were observed as well. For **1** and **2** polarization is efficiently transferred at low field via J-coupling network, while for **3** RASER of methyl protons was again induced by means of intramolecular dipolar interactions within the molecule, as there is no J coupling between the corresponding spins and nascent *p*-H₂ protons. Moreover, simulations were conducted and it was proved that one may produce RASER effect on the spin, which was pumped by PRINOE.

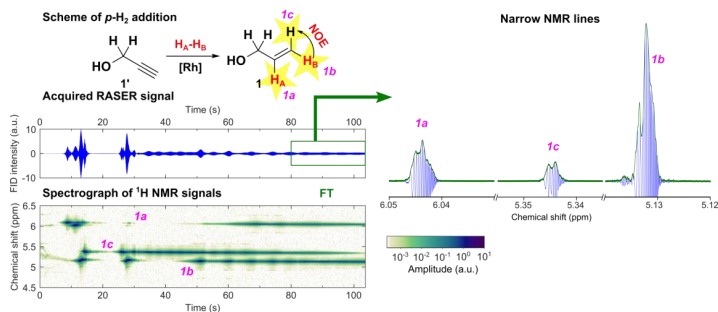


Figure 2. PASADENA experiment with **1** demonstrates RASER activity of the **1c** proton induced by intramolecular NOE.

Next benzene was added to the solution, which functioned as an inert analyte which can be hyperpolarized by PRINOE. ALTADENA protocol was exploited to initiate RASER. The PRINOE buildup and decay kinetics was followed by recording the set of spectra with a small flip angle. It was found that anomalous oscillations in benzene signal phase and intensity are observed in the middle of the kinetic curve (Fig. 3a). We proposed that these effects resulted from RASER induction on benzene. Although it was not possible to detect benzene RASER without the application of an RF pulse, the emergence of RASER was

demonstrated after application of a single 3° pulse at the anticipated maximum of the PRINOE kinetics (Fig. 3b). Thus, the feasibility of RASER induction by intermolecular PRINOE was revealed for the first time.

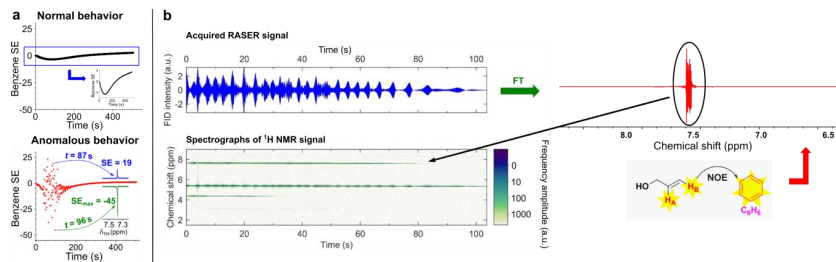


Figure 3. (a) PRINOE kinetic curves of benzene; (b) PRINOE-induced RASER on benzene analyte revealed after triggering with a single 3° pulse.

The effect of the RF pulsing parameters on the benzene RASER induction was further investigated via variation of the pulse flip angle and interpulse delay. As a result, the 2D map of signal enhancement (SE) dependence on these two parameters was plotted (Fig. 4). It was found experimentally and confirmed by simulations that signal enhancement increases while both the pulse flip angle and the interpulse delay were diminished.

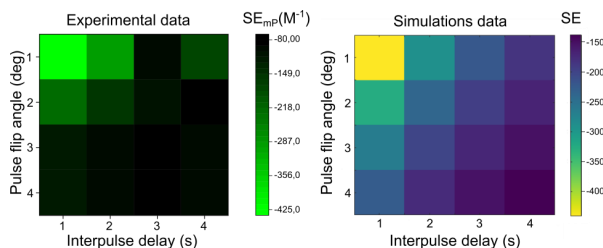


Figure 4. 2D map of signal enhancement dependence on the pulse flip angle and the interpulse delay: experiments (left) and simulations (right).

Acknowledgements

This work was supported by the Russian Science Foundation (grant 24-73-10093).

References

1. K. V. Kovtunov et al. Hyperpolarized NMR Spectroscopy: d-DNP, PHIP, and SABRE Techniques. – *Chem. Asian J.*, 13, 1857–1871 (2018).
2. R. A. Green et al. The theory and practice of hyperpolarization in magnetic resonance using parahydrogen. – *Prog. Nucl. Magne. Reson. Spectrosc.*, 67, 1–48 (2012).
3. S. Appelt et al. From LASER physics to the para-hydrogen pumped RASER. – *Prog. Nucl. Magn. Reson. Spectrosc.*, 114–115, 1–32 (2019).
4. S. Korchak et al. Spontaneous Enhancement of Magnetic Resonance Signals Using a RASER. – *Angew. Chem. Int. Ed.*, 60, 20984–20990 (2021).
5. O. G. Salnikov et al. Through-Space Multinuclear Magnetic Resonance Signal Enhancement Induced by Parahydrogen and Radiofrequency Amplification by Stimulated Emission of Radiation. – *Anal. Chem.*, 94, 15010–15017 (2022).

Electrophoretic NMR and its application in studying the electro kinetic transport of water and methanol in Nafion membranes

Pavel Yushmanov

P&L Scientific, Stockholm, Sweden

E-mail: pavel@plscientific.se

Electrophoretic NMR (eNMR), having been introduced more than 30 years ago, is a useful yet not very widespread methodology. It is based upon applying a voltage and thereby an electric field across the NMR sample volume. When done so, ionic species are set into motion that can be detected by experiments exploiting pulses of magnetic field gradients that are parallel to the direction of the applied electric field. Hence, pulse sequences of typical eNMR experiments are often similar to those of diffusion NMR experiments, with the major differences being (i) the need for electric field pulses and (ii) the information in the form of electrophoretic mobilities is extracted from the signal phase instead of signal attenuation [1–3].

Moreover, the eNMR approach can be employed to study electroosmotic migration in porous polymer electrolyte membranes. In this application, the component-resolved electroosmotic drag of water and methanol in fully hydrated Nafion membranes with different methanol concentrations can be characterized.

The typical experimental setup and eNMR pulse sequence for that application are shown below in Fig. 2 and 1, respectively [4]. The first shaped RF pulse is applied parallel to a gradient pulse (g) to select the sensitive slice from which the signal is recorded. The polarity of the current pulse (I) is alternated between subsequent scans while its amplitude is varied during the experiment. The small gradient pulse applied during the big delta time eliminates unwanted coherence transfer phenomena.

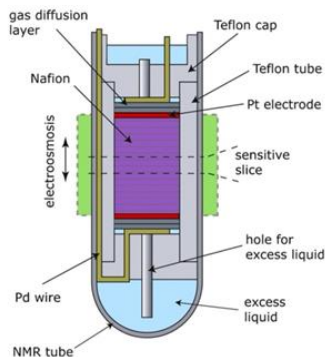


Fig. 1. Sample cell for electrokinetic NMR experiments [4]

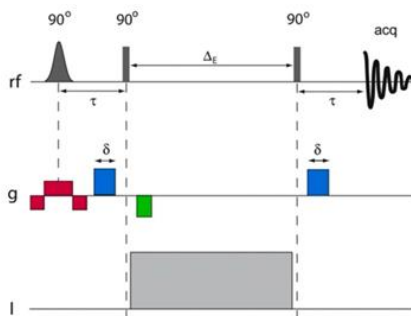


Fig. 2. The NMR pulse program for measuring the electro-osmotic drift velocity [4]

Typical ^1H NMR spectra recorded at zero current and the observed variation of the phase shifts of NMR signals arising from all exchangeable hydrogens (Δ) and from methanol CH_3 hydrogens (solid Δ) on prepared Nafion membranes sample equilibrated in a 0.1 mole fraction methanol solution is shown in Fig. 3 and 4, respectively. A phase shift of 10° corresponds to a velocity of 9×10^{-5} m/s under the current experimental conditions

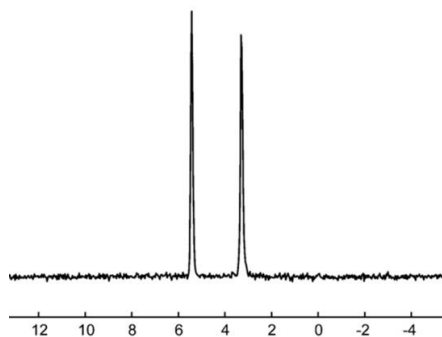


Fig. 3. ^1H NMR spectra obtained from Nafion membrane sample swollen in aqueous solution with 0.10 mole fraction methanol [4]

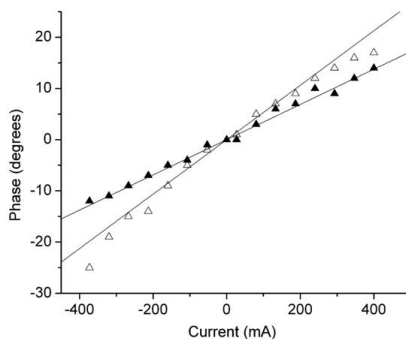


Fig. 4. The NMR pulse program for measuring the electro-osmotic drift velocity [4]

The processed data from the result of eNMR measurements (Fig. 4) and supplementary diffusion data for the water—methanol mixture shows that the drag coefficient is lower for methanol than for water.

References

1. Y. Fang, P. V. Yushmanov, I. Furó, Improved accuracy and precision in electrophoretic NMR experiments. Current control and sample cell design, *J. Magn. Reson.* 318 (2020) 106796. <https://doi.org/10.1016/j.jmr.2020.106796>.
2. P. Stilbs, Diffusion and Electrophoretic NMR, De Gruyter, 2019. <https://doi.org/10.1515/9783110551532>.
3. P&L Scientific, Overview, (2022). www.plscientific.se/?eNMR/Overview.
4. F. Hallberg, T. Vernersson, E.T. Pettersson, S. V. Dvinskikh, G. Lindbergh, I. Furó, Electrokinetic transport of water and methanol in Nafion membranes as observed by NMR spectroscopy, *Electrochim. Acta.* 55 (2010) 3542–3549. <https://doi.org/10.1016/j.electacta.2010.01.064>.

¹H NMR spectroscopy application for assessment catalytic behavior of comb-like polyelectrolytes in Suzuki reaction

Zefirova P.M.¹, Kadnikov M.V.¹, Fetin P.A.¹, Zorin I.M.¹

¹*Institute of Chemistry, Saint Petersburg State University, Saint Petersburg, Russia*

E-mail: zef.p.m002@gmail.com

Introduction

Micellar catalysis is one of the most intensive developing field of modern ecofriendly chemistry. Different surfactants as micellar catalytic systems enable to perform organic reactions, for example, Suzuki cross coupling reaction, using only water as a solvent. Catalytic effect of such systems is achieved by increasing of the local concentration of reagents solubilized in micelles and catalyst bonded to micelle surface due to ionic interactions. This approach allows to reduce usage of toxic organic solvents during the synthesis, obviously it corresponds Green Chemistry principals. It was shown [1] that comb-like polyelectrolytes are effective surfactants for micellar catalysis. Their pros are low threshold aggregation concentrations, high solubilization capacity and reusability. The synthesis of novel comb-like polyelectrolytes, their characterization and behavior as surfactants in water performed Suzuki reaction are goal of this work. The ¹H NMR spectroscopy method was used to confirm the structure of the synthesized monomers, as well as to determine their polymers catalytic activity. The report will show how routine one-dimensional proton NMR spectra can be used for micellar catalytic purposes.

Synthesis and catalysis

Monomers were synthesized in 3 stages (Fig. 1). The polymerization was carried out in water, so series of polymers with different concentrations of dipicolinic acid units was obtained. The real percentage of dipicolinic units was determined by UV spectroscopy. Suzuki reaction of phenylboronic acid and 1-bromo-4-nitrobenzene with PdCl₂ as catalyst was performed in water with different concentrations of polyelectrolytes. The conversion of the functional groups was measured using ¹H NMR spectroscopy.

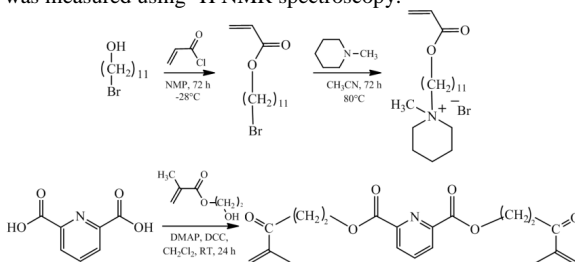


Figure 1. Scheme of monomers synthesis

Acknowledgements

This work was supported by a grant RSF № 24-73-00193. Authors are grateful the research park of St. Petersburg State University: RC of Magnetic resonance and cryogenic department.

References

1. Fetin P.A., Fetina V.I., Kadnikov M.V., Orlova V.V., Ermolenko E.I., Lezov A.A., Zorin I.M. Comb-like polyelectrolytes with pyridinium and trimethylammonium cations: Micellar catalytic and antibacterial properties // Colloids. Surf. A. Physicochem. Eng. Asp. 2024, 690, 133696

NMR-related services

Repair and upgrade of NMR spectrometer; repair of NMR hardware

- Upgrade of AVANCE I to AVANCE III or HD generations
- Upgrade of PC workstation with Windows and Linux-based system (AlmaLinux) with the most modern Topspin version that fits the present Bruker system
- Repair of AVANCE I – HD hardware (SGU boards, HPPR units, power supplies, amplifiers, and MAS and temperature controllers)

Repair, upgrade, and modification of the NMR probes:

- Repair of the gradient coil for high-resolution liquid probes
- Replacing broken glassware
- Repair of the ATMA system's floating and permanent faults
- Repair of MAS probes; supply of MAS consumables
- Upgrade of NMR probes to different bore sizes and (or) NMR frequency
- Production of the exchangeable insert for the DIFF family gradient probe



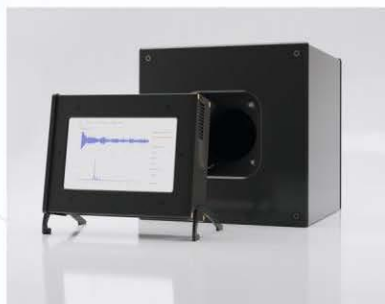
TerraQuantTech

Innovative solutions in NMR

«By combining scientific excellence and practical capabilities, TerraQuantTech delivers revolutionary products for nuclear magnetic resonance»

TerraQuantTech combines scientific research and practical experience to offer solutions that increase competitiveness and optimize manufacturing processes.

We offer two innovative products that change the approach to nuclear magnetic resonance (NMR):



Nu-Resonance – NMR spectrometer based on the earth's magnetic field



TQT Nuclei – Unified platform for analysis and management ЯМР-данными

Find out how our technologies can help you optimize your research and production processes!



More information on our website: ru.terraquant.tech

Poster Session

Generator of arbitrary sequences of commands/pulses

Artem S. Alexandrov, Daria L. Melnikova, Vladimir D. Skirda

Molecular physics department, Institute of Physics, Kazan Federal University

E-mail: artem.s.alexandrov@yandex.ru

Modern nuclear magnetic resonance (NMR) instruments represent complexes of relatively high complexity and usually contain: high frequency generators, power amplifiers, heterodyne and superheterodyne receiving amplifiers, RF switches, gradient pulse amplifiers, current sources of shimming coils, various kinds of controllers - sample temperature, sample rotation speed, etc. A modern NMR experiment requires phase coherence of all devices involved in the formation and registration of the NMR signal, in other words, synchronous control of frequency, phase, shape of RF pulses, amplitude and shape of gradient pulses, gain of the receiving path, phase of the registered signal, sampling frequency of the ADC and so on. This coherence is provided by a special device - an interval programmer of arbitrary sequences of commands and/or pulses. At present, of the available and satisfactory interval programmer implementations for NMR, only PulseBlaster by SpinCore Technologies [1], OpenCORE NMR developed by K. Takeda [2] and STEMLab by Red Pitaya [3] can be distinguished. However, each of the systems has its own disadvantages that limit their application in the development of new NMR devices: PulseBlaster and STEMLab have a closed hardware specification, OpenCORE - has only a fixed number of plug-in devices.

In this work, we propose an implementation of an interval programmer of arbitrary sequences of pulses and/or command words based on the programmable logic integrated circuit Xilinx XC6SLX9. The programmer is clocked at 50 MHz, has an internal memory of 2048 command words. The duration of the time interval set by one command can take values from 20 ns to 0.334 seconds with multiplicity of 20 ns, the programmer has the ability to form nested cyclic sequences with the number of repetitions up to 2^{16} and the number of nested cycles up to 16. Thus, the total duration of the generated sequences can reach 10^{80} seconds. The programmer allows synchronization of up to 245 devices via parallel synchronous bus with 8-bit addressing and up to 24 devices via gating pulses. The scope of the programmer is not limited to NMR only, it can be applied to any task requiring real-time synchronization of devices.

Acknowledgements

This work was funded by the subsidy allocated to Kazan Federal University for the state assignment in the sphere of scientific activities number FZSM-2023-0016.

References

1. Programmable TTL Pulse Generator, Delay Generator, Digital Word Generator and Timing Engine, <https://www.spincore.com/products/PulseBlaster> (2025).
2. K. Takeda. In Annual Reports on NMR Spectroscopy, 74, 355-393 (2011).
3. STEMLab 125-14, <https://redpitaya.com/stemlab-125-14> (2025).

Exploring the Ability of the P=O Group to Form Multiple Hydrogen Bonds

Omar Alkhuder¹, Mikhail A. Kostin¹, Peter M. Tolstoy¹

¹Institute of Chemistry, St. Petersburg State University, St. Petersburg, Russia

E-mail: omar.alkhuder2016@gmail.com

Introduction

The formation and strengthening of hydrogen bonds lead to changes in the geometric and spectral characteristics of complexes [1]. These interactions are best described by their electronic structure, with other parameters like energy and geometry being consequences. Due to difficulties in extracting detailed electronic information, spectroscopic parameters (e.g., NMR and IR) become essential probes and markers for the properties of complexes, such as those involving a P=O functional group acting as a proton or halogen acceptor [2].

Phosphine oxides as probes

Recent studies have shown that the spectral characteristics of the P=O group can act as probes, providing valuable information for diagnosing the main hydrogen bond characteristics in complexes. The P=O group is highly useful in NMR spectroscopy due to the presence of the ³¹P, which confers high sensitivity and effectiveness for chemical shift to the P=O group in forming and studying non-covalent interactions. Previously, the P=O group has been used in numerous studies for characterizing the acceptor properties of solvents and other compounds exhibiting Lewis acidity (known as the Gutmann-Beckett scale of acceptor numbers, AN), Brønsted acidity, or combined Lewis and Brønsted acidity [3].

In all previous works, complexes with a single hydrogen bond were studied despite experimental and theoretical evidence of multiple hydrogen bonds forming with the same P=O group, whether in solutions or in the crystalline state [4, 5].

Mechanisms of Hydrogen Bond Formation by the P=O Group

In this work, we present experimental and theoretical evidence demonstrating the ability of the P=O group to form multiple hydrogen bonds in solution. This study elucidates the relationship between hydrogen bond strength and the chemical shift of the ³¹P for Ph₃PO (Fig. 1a) complexes with substituted phenols (Fig. 1b).

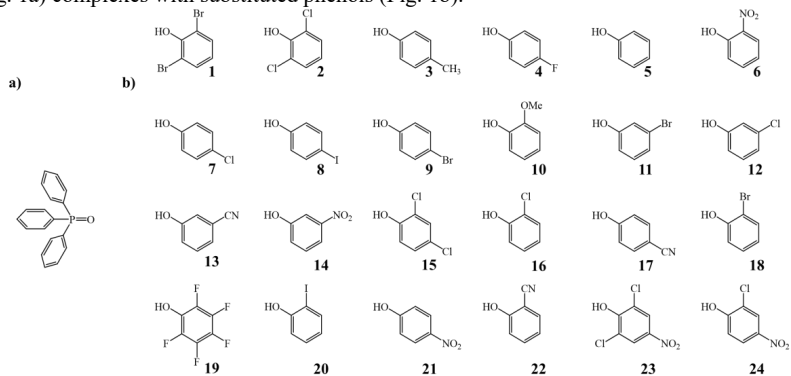


Figure 1. **a)** Triphenylphosphine oxide (Ph_3PO). **b)** Substituted phenols.

In the experimental section, the complexes were studied in a polar aprotic solvent (liquefied freonic mixture $\text{CDF}_3/\text{CDF}_2\text{Cl}$), which is characterized by chemical inertness, low

freezing point (<100 K), and low viscosity at low temperatures. The experiments were conducted using a Bruker Avance III 500 NMR spectrometer.

Two kinds of complexes were identified in low-temperature (100 K) ^1H and ^{31}P NMR spectra: 1:1 complexes (Fig. 2a), and 1:2 complexes (Fig. 2b). For example, Fig. 2c,d shows the signals of 1:1 and 1:2 complexes of Ph_3PO and 4-chlorophenol in ^1H and ^{31}P NMR spectra, while Fig. 3 shows a series of spectra recorded for solutions of Ph_3PO with various substituted phenols.

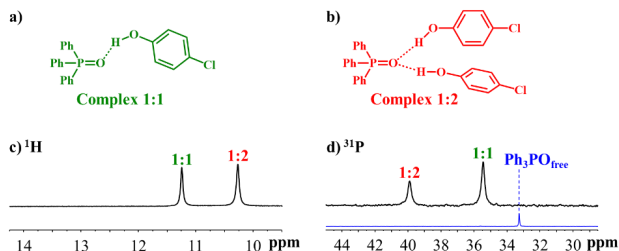


Figure 2. Structures of complexes formed in solution a) complex 1:1 b) complex 1:2. c) and d) ^1H and ^{31}P NMR spectra recorded for solution of Ph_3PO and 4-chlorophenol and solution of Ph_3PO in $\text{CDF}_3/\text{CDF}_2\text{Cl}$ solvent at 100 K.

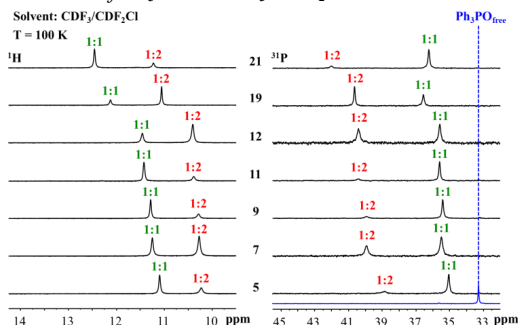


Figure 3. The series of ^1H and ^{31}P NMR spectra of Ph_3PO complexes with substituted phenols in $\text{CDF}_3/\text{CDF}_2\text{Cl}$ solvent at 100 K.

Using previously established correlation linking the ^1H NMR chemical shift changes upon complexation, $\Delta\delta\text{H}$, with the enthalpy of complexation, ΔH , given by the expression [6]

$$-\Delta H(\text{in kJ} \cdot \text{mol}^{-1}) = 4.18 \cdot \Delta\delta\text{H}(\text{in ppm}) + 1.67 \quad (1)$$

we were able to propose a new correlation, this time with ^{31}P NMR chemical shift changes:

$$-\Delta H(\text{in kJ} \cdot \text{mol}^{-1}) = 20.73 \cdot \Delta\delta\text{P}^{0.44}(\text{in ppm}) \quad (2)$$

Fig. 4a shows the resulting relationship between hydrogen bond enthalpy and the change in ^{31}P NMR chemical shift, both in the 1:1 and 1:2 complexes. From Fig. 4a, we can see that some complexes deviate from the general correlation, and to explain these deviations, we used quantum chemistry. For complexes Ph_3PO with with proton donors 1–24 and/or explicit solvent molecules, the calculations of optimized geometries and harmonic vibration frequencies were performed using Gaussian 16 software package at the pw6b95/def2–TZVPD with GD3 level of theory, without BSSE. The set of NMR parameters was calculated using the GIAO approach at the WPO4/pcseg–2 level of theory, polarizable continuum model (PCM, $\epsilon = 40$) was used for implicit solvent effects.

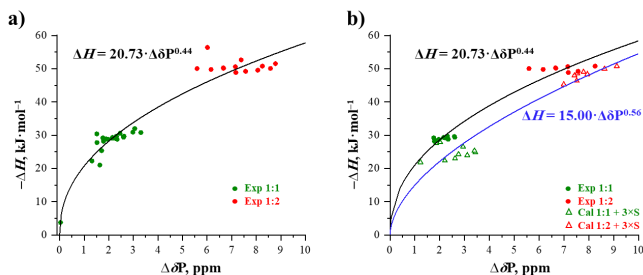


Figure 4. a) Correlation $\Delta H(\Delta\delta P)$ for Ph_3PO complexes with substituted phenols. b) A comparison between experimental and computational results for some complexes.

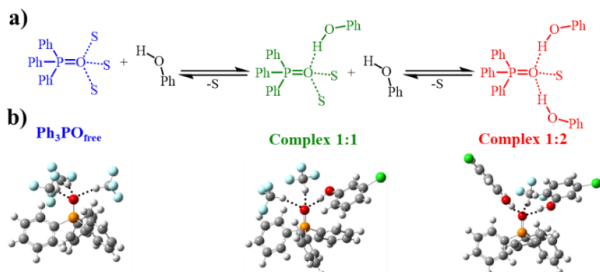


Figure 5. a) The hydrogen bond formation reaction of Ph_3PO complexes with substituted phenols, which we have achieved. b) Examples of calculated structures.

We conducted a wide range of chemical calculations in an attempt to deduce the reason for the deviation from the general correlation, and we ultimately concluded that Ph_3PO forms three hydrogen bonds with the solvent molecules. When a hydrogen bond is formed between Ph_3PO and the phenol molecule, a substitution process occurs, with some solvent molecules remaining as shown in Fig. 5a. This leads to the deviation of the complexes from the general correlation. Examples of the calculated structures are shown in Fig. 5b. A comparison of the experimental results and quantum computational results for some 1:1 and 1:2 complexes is shown in Fig. 4b.

Acknowledgements

This work is supported by the RSF grant 23-13-00095. The NMR spectra were recorded at the Center for Magnetic Resonance of SPbU Research Park. Quantum-chemical calculations were performed at the Computing Center of St. Petersburg State University Research Park.

References

1. E. Y. Tupikina, M. V. Sigalov, O. Alkhuder, and P. M. Tolstoy, *ChemPhysChem.*, 2024, e202300970.
2. M. A. Kostin, O. Alkhuder, L. Xu, D. V. Krutin, R. E. Asfin and P. M. Tolstoy, *Phys Chem Chem Phys.*, 2024, 26, 10234–10242.
3. J. A. McCune et al., *Phys. Chem. Chem. Phys.*, 2014, 16, 23233–23243.
4. E. Y. Tupikina., et al., *J Phys Chem C.*, 2018, 122, 1711–1720.
5. M.A. Kostin, O. Alkhuder, L. R. E. Asfin and P. M. Tolstoy, *Phys. Chem. Chem. Phys.*, 2025, 27, 1143–1154.
6. J. Reuben, *Journal of the American Chemical Society.*, 1986, 108, 1735–1738.

Physicochemical characterization of carbon-coated magnetic cobalt nanoparticles

Alonso-Geli, Yamirka^{1}; López-Alexander, Rosmery²; Lores-Guevara, Manuel A.¹*

¹ Centro de Biofísica Médica, Patricio Lumumba 507, Altos de Quintero, Santiago de Cuba, Cuba

² Hospital Oncológico "Conrado Benítez", avenida de Los Libertadores, Santiago de Cuba, Cuba

*E-mail: yamirka.alonso@uo.edu.cu

Introduction

Cobalt and cobalt oxide nanoparticles (NPs) show properties such as antimicrobial, anticancer, catalytic, antioxidant, antifungal, and capable of inhibiting enzymes; this versatility has led to a growing number of biomedical applications. The study of the new properties of NP allows the development of various applications in various spheres, particularly in biomedicine [1]. We plan to use commercial carbon-coated cobalt NPs (TurboBeads™ Carboxy) in biomedical applications, but, these particles are not adequately characterized, so we propose to develop the physicochemical characterization of these coated NPs by spectrophotometric and magnetic relaxation techniques.

Materials and Methods

Preparation of carbon-coated cobalt magnetic NP suspension stabilized with sodium citrate

A stock solution (10 mg/mL) of carbon-coated cobalt NPs (TurboBeads™ Carboxy, Aldrich) was prepared in 1M PBS, pH 7.4, plus 3 mM sodium citrate to stabilize the NPs suspension. The suspension was sonicated in an ultrasonic bath (400 W, 15 minutes).

UV-visible absorption spectrum of carbon-coated cobalt NPs

The UV-Vis spectrum of carbon-coated cobalt NPs suspension (0.1 mg/mL) was detected by measuring the absorbance at different wavelengths between 200 and 900 nm in a spectrophotometer. The absorbance value of the solvent is used as a reference.

Calibration curve of absorbance as a function of carbon-coated cobalt NPs concentration

A calibration curve of absorbance was made at the wavelength of maximum absorption, as a function of NP concentration (0.02 - 0.40 mg/mL).

Calibration curve of transverse relaxation time (T₂) as a function of carbon-coated cobalt nanoparticles concentration

A T₂ calibration curve was performed as a function of NP concentration (concentration range: 1.0 to 50.0 mg/mL) at 20 °C, using a LapNMR magnetic resonance console (Tecmag, Houston, USA), coupled with a permanent magnet (B₀ = 0.1 T, ν₀ = 4.03 MHz). The Carr-Purcell-Meiboom-Gill pulse sequence (90° and 180° radiofrequency pulses of 6 and 12 μs respectively, 8000 echoes and echo time of 500 μs) was used for T₂ measurement.

Data processing and statistical analysis

T₂ was calculated by determination of the echoes maximum amplitude on magnetic resonance signal using the proprietary Matlab line code. Data processing and statistical analysis were performed using Microsoft Excel 2019.

Results and Discussion

Preparation of stabilized carbon-coated cobalt NPs suspension

The stock solution of carbon-coated cobalt NPs (10 mg/mL) in 1M PBS, pH 7.4, was sonicated at 400 W during 15 minutes. It was obtained a very unstable NPs suspension, whose particles remained suspended for about 10 minutes.

Carbon coated cobalt NPs have greater stability in some physical and chemical conditions [2], however, carbon layer decreases the solubility of the NPs in polar solvents, which favors precipitation. We chose 3 mM sodium citrate as the stabilizing agent for the NP suspension used, as can be observed in Fig. 1. The suspension with 3 mM sodium citrate (B) is more homogeneous than suspension without sodium citrate (A). The effect of stabilization of NP suspensions by sodium citrate is due to the citrate anions cover the surface of each NP; the electrostatic repulsion of the anionic layer prevents the agglomeration of the NPs [3].

UV-visible absorption spectrum of carbon-coated cobalt NPs

Ultraviolet-visible spectroscopy is a powerful technique for various applications. When a substance absorbs maximum light at a given wavelength, a unique relationship is created between the substance and its characteristic spectrum that allows qualitative analysis to determine the presence of certain substances and quantitative analysis to determine the quantities of said substance.

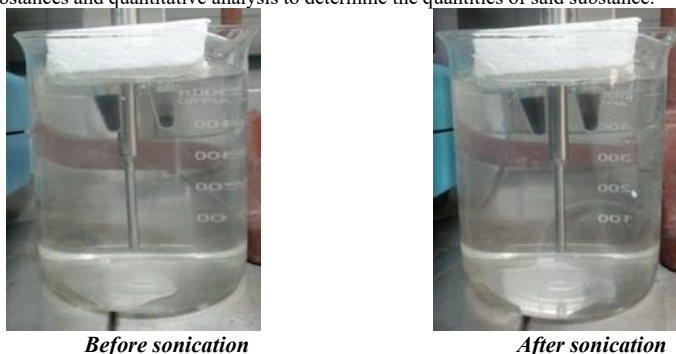


Fig. 1 Preparation and stabilization of NP suspensions without sodium citrate (tube A, left) and with 3 mM sodium citrate (tube B, right), before and after sonication.

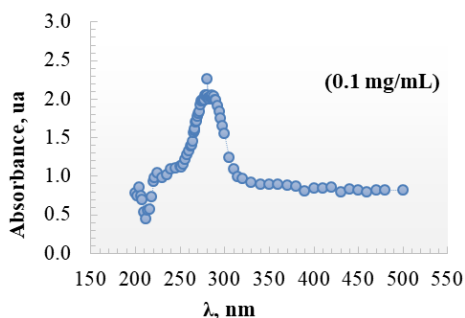


Fig. 2. UV-visible absorption spectrum of a suspension of NPs stabilized with sodium citrate at 0.1 mg/mL (wavelength between 200 and 900 nm).

Ultraviolet-visible absorption spectrum of a suspension of NPs stabilized with sodium citrate at of 0.1 mg/mL, results in a maximum absorption peak was at 281 nm, as can be seen in Fig. 2.

The peak of maximum absorption of the carbon coated cobalt NPs is very close to the peak of maximum absorption of proteins (280 nm due of the aromatic aminoacids residues), which would be an important controversial issue for the conjugation of NPs to these macromolecules.

The external carbon layer not only shields the inner nanometallic element from agglomeration, oxidation and degradation, but also improves the impedance match between magnetic and dielectric characteristics of the core-shell configuration [4].

Electronic interactions between cobalt NPs and coating material can lead to changes in the density of electronic states, modifying absorption characteristics and how they absorb light [5].

Calibration curve absorbance vs. concentration

In the calibration curve of absorbance at 281 nm (wavelength of maximum absorption) *versus* NP concentration (0.02 to 0.40 mg/mL) was observed a direct relationship between the absorbance at 281 nm and the NPs concentration was obtained (see Fig. 3).

Linear regression analysis showed a correlation coefficient (R^2) of 0.9933 to the equation of a straight line $y=mx$, where m is the slope and reaches an average value of 6.6 ± 0.3 mL/mg. This result shows a good correlation of the data to a linear behavior in the range of concentrations studied.

With these results it is possible to calculate the concentration of cobalt NPs in an unknown sample by interpolation, with the equation:

$$c(\text{mg/mL}) = \frac{A_{281\text{nm}}}{m(\text{mL/mg})} \quad (2)$$

The calibration curve plot shows the limit of detection (LOD) and the limit of quantification (LOQ) are about 0.02 mg/mL; the dynamic range is the entire used NP concentration range.

The obtained LOD indicates the method can detect concentrations as low as 0.02 mg/mL of the NP; this is a relatively low value, suggesting that the method has a good ability to detect the NP at low concentrations. The slope is quite high, for every unit of NP concentration (g/L), the T_2 increases by 6.6 units. A high slope indicates that the method is sensitive, as small variations in NP concentration result in significant changes in response. The intercept of 0 suggests that when there is no NP present, the method response is also zero. This is desirable characteristic and it indicates there is no background noise or interference affecting the absorbance measurement. The combination of a low LOD (0.1 g/L) and a high slope (6.6) suggests that the method is highly sensitive and reliable for the detection of the NP at low concentrations, making it suitable for applications where accurate and sensitive detection is required.

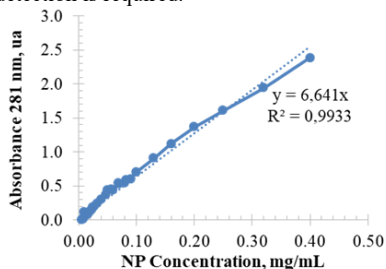


Fig. 3. Calibration curve of absorbance at 281 nm in NP concentration range

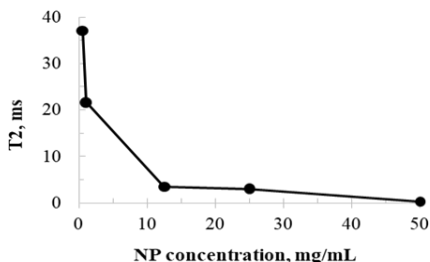


Fig.4 Calibration curve of T_2 in NP concentration range between 0.5 and 50.0 mg/mL.

between 0.02 and 0.40 mg/mL.

Calibration curve of transverse relaxation time (T_2) as a function of carbon-coated cobalt nanoparticles concentration

A calibration curve of T_2 versus concentration (50.0, 25.0, 12.5, 1.0; and 0.5 mg/mL) was obtained, it is useful for indirectly measurement of carbon coated cobalt NPs concentration from T_2 values in unknown samples.

The calibration curve plot in Fig. 4 shows LOD and LOQ are about 0.5 mg/mL; the dynamic range is between 1.0 and 10.0 mg/mL; and limit of linearity (LOL) is about 12.0 mg/mL.

T_2 versus concentration shows a linear relationship in the dynamic range; at concentrations away from this range in both directions, an asymptotic trend is observed; in case of values below the linear range, T_2 tend to free water value, and in case of concentrations above the dynamic range, it is shown a tendency to decrease T_2 until parameter's measurement is not possible due to the detection limit of the equipment. The calibration curve should look linear and have a section that is non-linear (LOL), a sign that instrumental detection is nearing saturation.

We performed a new calibration curve of limiting the concentration to the range 1.0-10.0 mg/mL. It was observed a fit of the data to a straight line of the form $y=mx+n$ (Fig. 5), where $m=-25.8$ s mL/mg and the intercept $n=326.7$ ms. The negative slope means that these two variables are negatively related; T_2 showed a significantly negative correlation with NP concentration at 4 MHz, suggesting a T_2 -shortening effect of cobalt.

The obtained LOD indicates the method can detect concentrations as low as 0.5 mg/mL of the NP; this is a very low value, suggesting that the method has a good ability to detect the NP at low concentrations. The slope module is quite high, for every unit of NPs concentration (g/L), the T_2 decreases by 25.8 units. A high slope indicates the method is sensitive, as small variations in NP concentration result in significant changes in response. A high intercept indicates that, even in the absence of the NP, there is a significant response. This may be a sign of background noise, due to proton density of the solvent. A high intercept can mask the NP signal, but it is not possible to avoid.

R^2 shows a good fit and the regression model is able to adequately explain the variation in the response variable.

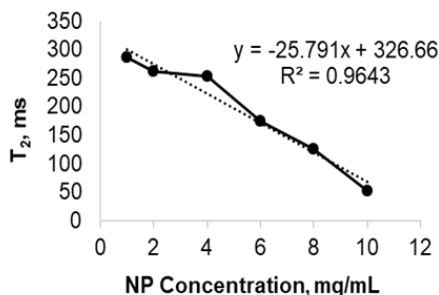


Fig. 5 Calibration curve of T_2 in NP concentration range between 1.0 and 10.0 mg/mL.

Comparison of spectrophotometric and NMR methods for determining NP concentration

Both calibration curves can be used as a methods to determine the NP unknown concentration by interpolation, but with different performances. The spectrophotometric method is more reliable due to its intercept of zero; however, it has a lower sensitivity to changes in concentration.

Another important disadvantage is that the peak of maximum absorption is at 281 nm, very close to the peak of maximum absorption of proteins, which would be an important limitation for the conjugation of NPs to these macromolecules. NMR method offers greater sensitivity and a lower LOD, but the high intercept can be a drawback that affects the precision of the measurements. The choice between the two methods will depend on the specific needs of each study.

Conclusions

A maximum absorption peak of the carbon-coated cobalt NPs was detected at 281 nm; two calibration curves as a function of concentration were obtained, one for the spectrophotometric method at 281 nm in the concentration range 0.02 to 0.40 g/L, and the other for the NMR method in the concentration range between 1.0 to 10.0 mg/mL. Both calibration curves can be used to determine the unknown NPs concentration by interpolation.

Acknowledgements

This work is supported by the Belgian Development Cooperation through VLIR-UOS, MRI Centre of the University of New Brunswick in Canada.

References

1. Materón, E. M., Miyazaki, C. M., Carr, O., et al. (2021). Applied Surface Science Advances, 6, 100163.
2. Malhotra, N., Audira, G., Chen, J. R., et al. (2020). Molecules, 25(9), 2256.
3. Ranošzek, K., Tomaszewska, E., Socha, E., et al. J Nanopart Res. 2017; 19(8):273.
4. Zhang, D., Xu, F., Lin, J., et al. (2014). Carbon, 80, 103–111.
5. Yimyai, T., Thiramanas, R., Phakkeeree, et al. (2021). Advanced Functional Materials, 31(37), 2102568.

The FMR/EPR studies of magnetite/maghemite nanoparticles, synthesized by different methods

Andronenko S.I.¹, Nikolaev A.M.^{2,3}, Suharzhovsky S.M.⁴, Sinelnikov A.A.⁵, Kovalenko A.S.², Abiev R.Sh.^{2,6}, Ivanova A.G.^{2,3}, Shilova O.A.^{2,3,6}

¹Kazan Federal University, Kazan, Russia

²Branch of Petersburg Institute of Nuclear Physics named by B.P. Konstantinov of National Research Centre "Kurchatov Institute" – I.V. Grebenshchikov Institute of Silicate Chemistry, Saint-Petersburg, Russia

³Saint-Petersburg Electrotechnical University "LETI", Saint-Petersburg, Russia

⁴Saint-Petersburg State University, Saint-Petersburg, Russia

⁵Voronezh State University, Voronezh, Russia

⁶Saint-Petersburg State Institute of Technology, Saint-Petersburg, Russia

E-mail: sergey.andronenko@gmail.com

Introduction

Iron oxides have been known for a long time but they still attract definite attention. Magnetic iron oxides (magnetite Fe_3O_4 and maghemite $\gamma\text{-Fe}_2\text{O}_3$) possess a wide range of useful properties. Their nanoparticles can be used as magnetic agents in medicine and biology for marking biomaterials, for penetrating cells of living organisms, or for local heating. Electron paramagnetic resonance (EPR) study was applied to investigate magnetic properties of these magnetite/maghemite nanoparticles. The EPR spectrometer Bruker Eleksys E580 (X-band, 9.46 GHz) was used to study the nanoparticles of magnetite/ maghemite at various temperature from 100 to 350 K.

Synthesis and Structure

Magnetic magnetite/maghemite nanoparticles has been obtained by co-precipitation using 0,5 M solutions of iron chlorides (II) and (III). 12.5% aqueous solution of ammonia was used as precipitator. Precipitation was carried out either by dripping (samples #2 [1] and #3 [2-4]) or in the microreactor with intensively swirling flows (sample #1 [1]). Sample №1: Synthesis in the microreactor MRISF-1, drying in the vacuum; Sample №2: Bubbling with Ar at the 60°C, drying in the vacuum; Sample №3: 16-hour aging of the precipitate in the mother liquor, drying in the air. Experimental results obtained by X-ray powder diffraction and scanning electron microscopy are given in the Table 1.

Table 1. Data from X-ray phase analysis and scanning electron microscopy of magnetic nanopowders [1-4].

Sample	SEM	XRD		
	Particle size, nm	Unit cell parameter, Å	Cation vacancies per unit cell	$\text{Fe}^{2+}/\text{Fe}^{3+}$ ratio
# 1	~5 – 10	8.362 (3)	0.18	0.46/2.36
# 2	~10 – 20	8.369 (3)	0,15	0.55/2.30
# 3	~10 – 25	8.367 (3)	0.16	0.52/2.32

Note: all the powders were extracted from the solution with magnet and dried at 100 °C.

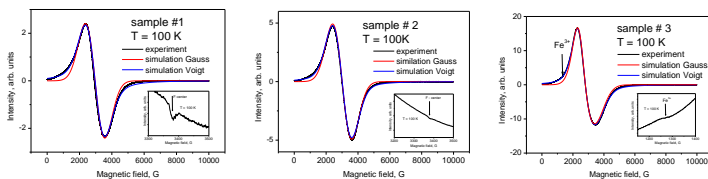


Figure 1. EPR/FMR signals of the samples 1, 2 and 3, at 100 K. The insets show additional EPR signals.

The interpretation of EPR/FMR spectra

The EPR/FMR spectrum can be represented as a broad asymmetric line which is typical for the paramagnetic centers with axial symmetry. According to the previously mentioned assumptions, spin Hamiltonian (SH) with axial symmetry and effective spin $S = 1/2$ was used for the interpretation. I. e., each magnetic nanoparticle is assigned an effective spin $S = 1/2$, and then this magnetic nanoparticle is considered as an analog of a paramagnetic ion. The following spin-Hamiltonian (SH) was used:

$$\mathcal{H}_S = g_x \mu_B B_x S_x + g_y \mu_B B_y S_y + g_z \mu_B B_z S_z \quad (1)$$

where: μ_B – Bohr magneton, $i = x, y, z$, g_i – principal matrix values g , S_i – electron spin components of S ($S = 1/2$), B_i – components of the external magnetic field vector B ; $g_x = g_y < g_z$. The SH parameters are presented in Table 2. The additional EPR spectrum observed in the samples #1 and 2 was described by the same SH with $S = 1/2$, it was assumed that $g_x = g_y = g_z$, and this spectrum assigned to oxygen vacancies with trapped electron (F-centers).

Table 2. SH parameters for the samples of Fe_3O_4 at $T = 100 \text{ K}$ and $T = 300 \text{ K}$. The lineshapes are Voigt for all samples.

Sample	T, K	g_x	g_y	g_z	$(\Delta B_{pp})_x/2$ [G]	$(\Delta B_{pp})_y/2$ [G]	$(\Delta B_{pp})_z/2$ [G]	Gs/Lz %
#1	300	2.17	2.17	2.17	500	500	500	70/30
	100	2.28	2.28	2.28	590	590	590	60/40
#2	300	2.19	2.19	2.19	480	480	480	80/20
	100	2.24	2.24	2.24	600	600	600	75/25
#3	300	2.07	2.07	2.55	550	550	230	80/20
	100	2.15	2.15	2.65	650	650	280	70/30

$(\Delta B_{pp})_i$ – c Corresponding components of EPR linewidth (peak-to-peak), used for simulation of EPR lineshape, G_s -Gaussian lineshape and L_z – Lorentzian lineshape

The additional EPR signals were observed at 100 K in the sample #3: 1275 G and (very low intercity) 1850 G. These signals can be ascribed to Fe^{3+} ion, which is not involved in magnetically ordered network. It may belong to paramagnetic centers in rhombohedral environment, located in some diamagnetic inclusions or on surface. The additional signals, observed also in the sample #1 and #2, could be assigned to oxygen defects with $g = 2.0$. During the precipitation of nanoparticles from the solution, structural defects, such as oxygen

vacancies, can form in their crystal structure. Such a vacancy becomes paramagnetic by electron trapping. They are characterized by narrow EPR lines with $g = 2.0$, and their observation is possible only at temperatures close to the temperature of liquid nitrogen. However, these signals were not stable and if oxygen vacancy lost the electron, the EPR signal disappears, even if the number of vacancies does not change. Therefore, the signal at 3375 G ($g = 2.0$) was not observed in the samples #3. This could happen probably to the aging for 16 h in mother liquid

EPR/FMR lineshape

In superparamagnets, there must be some kind of mixture of homogeneous and inhomogeneous broadening, reflected in Voigt shape. Voigt lineshape is a convolution of Gaussian and Lorentzian shape. At low temperatures, ferromagnetic properties are manifested as a result of "freezing" of magnetic moments and, accordingly, EPR line has large contribution of the Lorentz lineshape. At room temperature, paramagnetic behavior is manifested, which reflected in preferable Gaussian lineshape. The lineshape of the samples #1 and #2 is isotropic, which implies very narrow distribution of nanoparticle sizes and their spherical shape. The lineshape of the sample #3 is similar to that, observed in the previously studied [5] and highly anisotropic. It could mean very broad distribution of particle size for this sample and their nonsphericity, that could be caused by the aging for 16 h in mother liquid. The aging allowed the growth and partial oxidation of some particles, while fast synthesis of the samples 1 and 2 prevented the forming of different-sized particles. The shift of g -value to lower resonance fields for low temperatures is due to the increase in magnetic moment of nanoparticles. Temperature dependencies of integrated intensity of FMR line for all three samples are similar and roughly correspond to ZFC (zero field cooling) magnetization of magnetite samples with maximum at about 200–250 K.

Acknowledgements

This work is carried out within the framework of the research topic of the state task of the NRC "Kurchatov Institute" – PNPI – IchS No. 1023033000122-7-1.4.3 "Physico-chemical foundations of the inorganic synthesis of micro- and nanostructured inorganic, organo-inorganic and ceramic materials and coatings for bio-, energy- and resource-saving technologies".

References

1. R. Sh, Abiev, A.M. Nikolaev, A.S. Kovalenko, Yu.E. Gorshkova, N.V. Tsvigun, A.E. Baranchikov, G.P. Kopitsa, O.A. Shilova, –Chem. Eng. Res. Des., 205, 335–342 (2024).
2. O.A. Shilova, A.S. Kovalenko, A.M. Nikolaev, T.V. Khamova, I.Yu. Kruchinina, G.P. Kopitsa. –Russ. J. Inorg. Chem., 69, 329–342 (2024).
3. O.A. Shilova, A.M. Nikolaev, A.S. Kovalenko, A. A. Sinel'nikov, G. P. Kopitsa, A. E. Baranchikov, –Russ. J. Inorg. Chem., 65, 426–430 (2020).
4. A. S. Kovalenko, O.A. Shilova, A.M. Nikolaev, S. V. Myakin, –Colloid Journal, 85, 389–397 (2023).
5. S.I. Andronenko, A.M. Nikolaev, S.M. Suhartzhevsky, A.A. Sinelnikov, A.S. Kovalenko, A.G. Ivanova, O.A. Shilova, –Ceramics, 6, 1623–1631 (2023).

Construction of sensitivity maps for wireless coils using ^{19}F MRI

Nikolay V. Anisimov¹, Pavel Tikhonov², Anna Hurshkainen²

¹Faculty of Fundamental Medicine, Lomonosov Moscow State University, Moscow, Russia

²School of Physics and Engineering, ITMO University, St. Petersburg, Russian Federation

E-mail: anisimovnv@mail.ru

Introduction/Purpose

Calculating sensitivity maps for coils used in MRI is complicated when they interact with others. This relates to wireless coils, the task of which is to amplify the NMR signal in its sensitivity zone and transmit it via inductive coupling to a wired coil connected to the receiver. However, it is difficult to conduct an experimental verification of the calculations. The aim of the work is to experimentally obtain sensitivity maps of wireless coils.

Material and Methods

For the experimental construction of sensitivity maps of wireless coils, the approach described in [1] was used, where it was applied to wire coils. Namely, immersion of the coil in a visualizing medium and obtaining a volumetric image from this medium. Fluorine-containing liquid (Novec 1230, $\text{C}_6\text{F}_{12}\text{O}$) is used as a visualizing medium. Therefore, its image is obtained by the ^{19}F MRI. It is important that the liquid is chemically inert - non-toxic and does not damage objects immersed in it. It also does not conduct electricity and has a low permittivity ($\epsilon=2.3$), therefore it has little effect on the tuning of the coil under study and does not affect its quality factor.

Several types of wireless coils were investigated: those made using conventional technology, namely, solenoid and 4-turn loop, as well as coils based on transmission line resonator (TLR) and metamaterial-inspired (MMI) technologies. A 8-leg (20 cm) surface MMI coil has seven hybrid modes, and for this study the third mode was chosen. Capacitors were connected to the coils (except for TLR coils) to tune them to resonance at a frequency approximately equal to the NMR of fluorine (19.83 MHz). All coils are shown in Fig. 2. The coils were inductively coupled to wire coils. These coils created using traditional technology – 2-turn loop in experiments with a 10-turn solenoid and 4-turn loop, and a 1-turn loop in other cases. In both cases, the wire coil was also immersed in a fluorine-containing liquid, while it was connected to a transmit-receive switch, due to which it was transceiver.

The experiments were conducted on a 0.5T clinical scanner Bruker Tomikon S50. Scanning was performed using the 3D GRE method with the parameters: TR/TE=50/7 ms, FA=10°. Depending on the coil size, the isotropic resolution was set within the range from 1 mm to 3 mm. The MMI and TLR coils were made from $20 \times 20 \text{ cm}^2$ plates with conductors obtained by etching foil-clad textolite. They were placed in a plastic basin filled with 9 liters of fluorine-containing liquid – Fig. 1B. The solenoid and frame coils were immersed in a plastic container measuring $12 \times 12 \times 6 \text{ cm}^3$ – Fig. 1A.

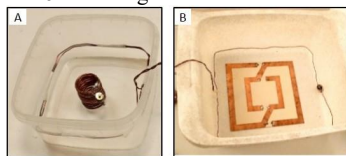


Figure 1. Wired and wireless coils in containers with fluorinated liquid. Left: 2-turn loop and solenoid in a small plastic container; Right: 1-turn loop and TLR coil in a plastic basin

Results

^{19}F MR images were obtained of a fluorinated liquid containing wireless coils – Fig. 2. They clearly show an increase in signal near (inside) the wireless coils, which correlates well with their calculated sensitivity maps.

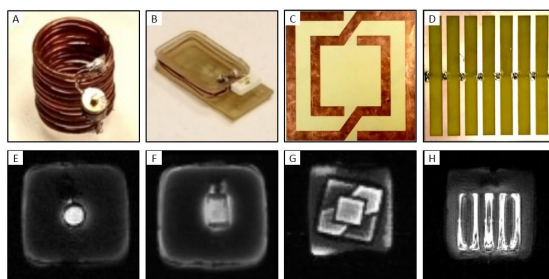


Figure 2. Wireless coils – photos (top row) and their ^{19}F MR images in coronal projection (bottom row). A, D – solenoid, B, F – 4-turn loop, C, G – TLR coil, D, H – MMI coil

The axial projection images show a decrease in sensitivity as one moves away from the center and plane of the coil – Fig. 3A-C. The sensitivity map can be presented not only in the form of graphs, but also in the form of a three-dimensional image - Fig. 3D.

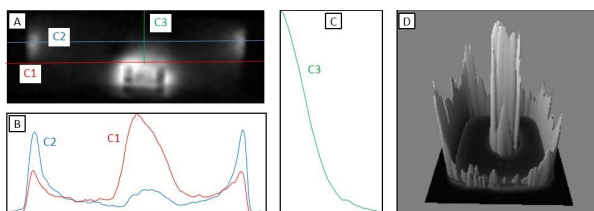


Figure 3. A – ^{19}F MRI of 4-turn loop in axial projection. B and C are graphs of the MR signal along the lines C1, C2, C3 indicated in panel A. On panel C, the graph is stretched along the horizontal axis by 2 times. D - the image of the coil in the coronal projection is presented as a volumetric image

Discussion/Conclusion

The method of visualizing MRI coils works well for both conventional wire coils and wireless coils of various types. Note that in our case, the signal from the wire coils is also presented in the images. The wire coils did not need to be placed in a fluorine-containing liquid. We did this only to minimize the size of their turns.

Although the sensitivity maps are constructed for coils tuned to the NMR frequency of fluorine, they may be applicable to coils of similar geometric proportions tuned to other frequencies.

Acknowledgment

The study was conducted under the State Assignment of Lomonosov Moscow State University

References

1. N. V. Anisimov, et al. - Appl. Magn. Reson., 55, 753-765 (2024).

Simultaneous detection of nuclei ^{13}C , ^{23}Na , ^{27}Al and ^{55}Mn at 0.5 Tesla

Nikolay V. Anisimov¹, Arina A. Tarasova²

¹*Faculty of Fundamental Medicine, Lomonosov Moscow State University, Russian Federation*

²*Faculty of Physics, Lomonosov Moscow State University Russian Federation*

E-mail: anisimovny@mail.ru

Introduction/Purpose

In a weak field, the Larmor frequencies of a number of magnetic isotopes are very close, which gives the possibility of simultaneous detection of signals from them. For this, it is necessary that the receiver bandwidth (analog part) be greater than the difference in Larmor frequencies. Beside this, it is desirable that the speed of the analog-digital converter (ADC) be appropriate - it determines the sampling rate R and the spectrum width (SW), which are related by the ratio: $R=2SW$. The spectra are simply interpreted if the value of SW is less than the difference in Larmor frequencies. Otherwise, it is necessary to take into account the undersampling effect - the appearance of signals at frequencies that are separated from the true ones by a frequency multiple of SW . The location of the subspectra on it, related to different nuclei, depends on the SW value and can be calculated in advance. In our work [1], we showed how this is done for a field of 0.5 T as applied to pairs of nuclei ($^1\text{H}/^{19}\text{F}$, $^{13}\text{C}/^{23}\text{Na}$). In this work, we demonstrate the possibility of simultaneous detection of signals from 4 nuclei (^{13}C , ^{23}Na , ^{27}Al , ^{55}Mn).

Materials and Methods

The experiments were conducted on a clinical 0.5 T MR scanner Bruker Tomikon S50. It is built using the AVANCE technology. The main components of the receiver are the preamplifier HPPR and the main amplifier RX-22. The latter is built using a heterodyne circuit, in which the frequency spectrum of the received signal is transferred to the 22 MHz range, in which the main amplification occurs. The 22 MHz bandwidth of the amplifier is 1 MHz. The amplified signal is fed to two phase detectors, which differ in that for one of them the phase of the reference frequency is shifted by 90° , which allows quadrature detection. The signals from the outputs of the phase detectors are fed to the ADC HADC, which is capable of digitizing the signal with a maximum frequency of 400 kHz, which in turn allows obtaining routine spectra up to 200 kHz wide.

Taking into account our technical capabilities, for simultaneous detection of signals with different gyromagnetic ratios, the maximum difference in their Larmor frequencies should not exceed 1 MHz. For a field of 0.5 T, this applies to some heavy nuclei. For example, ^{13}C (5.3 MHz), ^{23}Na (5.6 MHz), ^{27}Al (5.4 MHz), ^{55}Mn (5.2 MHz). They they give acceptable signals from relatively accessible compounds. There are other nuclei whose Larmor frequencies meet the requirements - ^{63}Cu (5.8 MHz), ^{65}Cu (5.9 MHz), ^{129}Xe (5.8 MHz). But at the time of the measurements, we did not have samples that gave an acceptable signal.

The difference between the Larmor frequencies of ^{23}Na and ^{55}Mn exceeds 200 kHz, which exceeds the capabilities of our ADC. Therefore, their simultaneous detection is possible only using the undersampling effect.

The samples used were: ^{13}C -enriched (95%) sodium bicarbonate (NaHCO_3), 1 g of which was dissolved in 11 ml of water, as well as aqueous solutions of aluminum chloride AlCl_3 (1 g) and potassium permanganate KMnO_4 (2 g), both in 24 ml.

A 6-turn loop with a diameter of 9.5 cm was used as a transmit/receive coil, inside which 3 glass vials with samples were placed. RF excitation was carried out by 4 pulses, following without intervals. The pulse filling frequencies corresponded to the Larmor frequencies of the simultaneously detected nuclei.

Preliminarily, the pulse duration at which the maximum NMR signal is obtained was determined for each nucleus. For this purpose, by varying the pulse duration, we obtained a spectrum from a single-pulse sequence in which the same 1-s delay was set between pulses (for signal accumulation) as for the planned 4-pulse sequence. As a result, for the nuclei ^{13}C , ^{23}Na , ^{27}Al and ^{55}Mn , the optimal pulse durations were determined - 2 ms, 2.4 ms, 2.4 ms and 1.2 ms, respectively. A significant spread in durations with relatively small differences in γ is explained by the unevenness of the frequency response of the receive-transmit switch, as well as the detuning between the coil frequency and the Larmor frequency of the nucleus. The long pulse durations and uneven frequency response are due to the fact that the receive-transmit switch used is a proprietary one, which is optimized only for protons.

The receiver frequency (the reference frequency of its phase detector) F_0 was set so that during quadrature detection the central frequency of the spectrum corresponded to the half-average value between the maximum (F_A) and minimum (F_B) Larmor frequencies of the detected nuclei: $F_0 = (F_A + F_B)/2$. In our case $F_A = 5.6$ MHz, $F_B = 5.2$ MHz, so $F_0 = 5.4$ MHz.

We set the SW values to 127 kHz, 40 kHz, 10 kHz and 2.7 kHz. With these values, the difference between the true precession frequency $F_{A,B}$ and the receiver frequency F_0 was $\pm N$ SW, where maximum N was 1, 4, 16 and 64, respectively.

Result/Discussion

Fig. 1 shows the spectra obtained at two digitization rates, and therefore different SW - 127 kHz and 2.7 kHz. The number of accumulations was 8K and 32K, respectively, and the scanning time was 8 hours and 32 hours. For each peak, the isotopes are indicated, as well as the N values characterizing the undersampling effect.

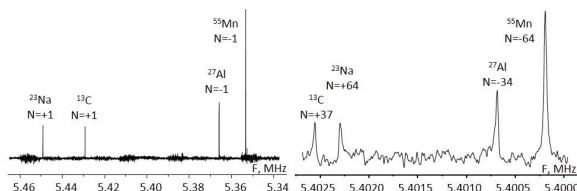


Figure 1. Spectra obtained with simultaneous detection of nuclei ^{13}C , ^{23}Na , ^{27}Al and ^{55}Mn . the peak frequencies differ from the Larmor ones in the $N \cdot SW$, the N values are indicated

The noise distribution on the spectrum differs from the normal one - there are individual bursts, the intensity of which is 1-2 orders of magnitude greater than for thermal noise. They are caused by RF interference, which is typical for low Larmor frequencies. In this case, conventional shielding is ineffective, and special methods are used to suppress them [2].

Simultaneous detection of signals from different isotopes may be of interest for synchronous monitoring of dynamic changes in the characteristics of the studied substances or individual samples as a result of chemical reactions or technological processes.

Acknowledgment

The study was conducted under the State Assignment of Lomonosov Moscow State University.

References

1. N. V. Anisimov, O.S. Pavlova. - Appl. Magn. Reson., 49, 523–532 (2018).
2. Y. Zhao, et al. - NMR in Biomed., e4956:1-13 (2023). doi:10.1002/nbm.4956

¹²⁵Te NMR spectra in *Td*-phase WTe₂

Antonenko A.O.¹, Charnaya E.V.¹, Marchenkov V.V.^{2,3}, Naumov S.V.², Lee M.K.⁴, Chang L.J.⁴

¹Faculty of Physics, Saint Petersburg State University, Saint Petersburg 199034, Russia

²Mikheev Institute of Metal Physics, Ural Branch of the Russian Academy of Sciences,

Yekaterinburg, Russia

³Ural Federal University, Yekaterinburg, Russia

⁴Department of Physics, National Cheng Kung University, Tainan 70101, Taiwan

E-mail: a.antonenko@spbu.ru

Introduction

Topological properties in materials open a new world in condensed matter physics. The best-known types of topological materials are topological insulators and topological semimetals, the latter include Dirac and Weyl semimetals [1,2]. Weyl semimetals are realized in systems without spatial-inversion or time-reversal symmetry.

Theoretical calculations predicted that layered tungsten ditelluride belongs to Weyl type II semimetal [3]. However, the results obtained so far [4-6] are not sufficient to confirm the topological nature of WTe₂. The results in [7] do not demonstrate a clear influence of topological features of the WTe₂ zone structure on the nuclear magnetic resonance (NMR) spectra, nevertheless deviations from the Korringa's law were observed. The latter was explained by the probable contribution of the topological features of the WTe₂ zone structure to the spin-lattice relaxation times. In [8] the results for nuclear spin-lattice relaxation at two single crystal orientations in magnetic field were obtained, which evidence in favor of the topological nontriviality of WTe₂.

The present work reveals features of ¹²⁵Te NMR spectra for both monocrystalline WTe₂, depending on its orientation relative to the external magnetic field **B**₀, and powdered WTe₂.

Experiment

The layered single crystal WTe₂ has been growing by the chemical transport method with Br₂ as the transport agent for three weeks in a sealed quartz ampoule under vacuum conditions. There were obtained a thin plate with dimensions of 0.2x3x4 mm and a WTe₂ crystal. The latter was ground to powder in an agate mortar. We call this powdered sample as #1. Two WTe₂ single crystals were grown by the self-flux method and ground in an agate mortar for further measurements. We call these powders as #2 and #3.

WTe₂ crystallizes in the *Td*-phase with an orthorhombic lattice structure (non-centrosymmetric space group *Pmn*2₁) [9]. The structure of WTe₂ remains stable with changing temperature [10,11]. The X-ray diffraction method was used to verify the phase homogeneity as well as to determine the crystal structure and directions of crystallographic axes in the single crystal. X-ray phase analysis confirmed the formation of *Td*-phase WTe₂ with an orthorhombic lattice structure.

The ¹²⁵Te NMR spectra for WTe₂ single crystal and powders were obtained at room temperature using Bruker Avance 400 and Bruker Avance 500 pulsed NMR spectrometers with the operating frequencies for ¹²⁵Te nuclei of 126.24 and 157.79 MHz, respectively. The ¹²⁵Te NMR frequency shifts were calculated using the universal $\bar{\nu}$ scale [12]. The orientation of the WTe₂ single crystal plate was changed manually: the angle (φ) between the direction of the crystallographic axis *c* and the external magnetic field **B**₀ was set with a protractor with the accuracy that can be provided by the human eye. The angle φ varied from 0 to 140°. The

spin-echo pulse sequence ($\pi/2-\tau-\pi$) with $\pi/2$ pulse duration from 2.5 to 5.8 μs was used in different series of measurements.

Results and discussion

Two types of spectra were obtained: cumulative spectra and envelope. The cumulative spectra are the sum of the spin echo signals at different frequency offsets. The spectra of the second type were obtained by plotting the envelopes by points corresponding to the integral intensities of the echo signals at various excitation frequencies.

A set of ^{125}Te NMR spectra was obtained for the WTe_2 single crystal in magnetic field 9.4 T at different values of the angle φ between the c -axis and the magnetic field \mathbf{B}_0 . Differences in the ^{125}Te NMR spectra for WTe_2 powders grown by different methods (#1, #2 and #3) (fig. 1) have been revealed. It is shown that the spectra for single crystal and powder WTe_2 grown by the same method are in a good agreement with each other.

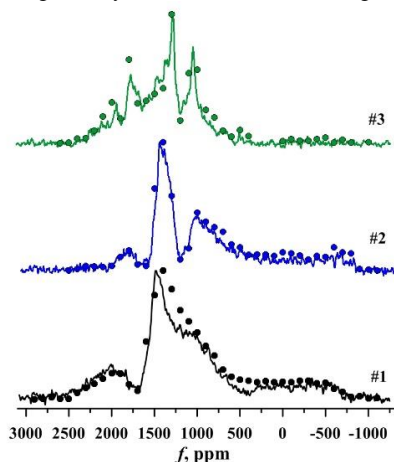


Figure 1. ^{125}Te NMR spectra for WTe_2 powders grown by different methods (#1, #2 and #3). The data were obtained at magnetic fields of 9.4 T (#1) and 11.75 T (#2, #3) at room temperature. The solid lines correspond to the cumulative spectra, dots – to the intensities of the spin echo signals obtained by varying the excitation frequency.

The presence of several lines in the ^{125}Te NMR spectra has been demonstrated both for powders and for single crystal at different orientations. Not all of the lines in the spectra can be explained in terms of the crystal structure of WTe_2 , which has four non-equivalent tellurium crystallographic positions. The nature of the low frequency lines in the single crystal and powder spectra remains unclear.

Varying the angle φ in the range of 15° – 50° , it was shown that the shape of the ^{125}Te NMR spectrum did not undergo pronounced changes: at any angle between the c -axis and the magnetic field \mathbf{B}_0 the spectrum was a superposition of eight lines. Thus, at $\varphi = 15^\circ$ – 50° , the spectra consisted of four lines centered around 1500 ppm and overlapping each other (call this group of lines L_3), and of four lines L_1, L_2, L_4, L_5 symmetrically separated from L_3 by 700–900 ppm depending on the orientation of the single crystal. The lines L_1 and L_2, L_4 and L_5 merged in pairs in the frequency regions 2300–2500 ppm and 600–800 ppm, respectively, and the shift δ of these lines was observed to change.

It is shown that the behavior of the line shift in the ^{125}Te NMR spectrum for the WTe_2 single crystal does not follow the well-known angular dependence [13]:

$$\nu' = \nu \left(\frac{3\cos^2\beta - 1}{2} + \frac{\eta}{2} \sin^2\beta \cos 2\alpha \right), \quad (1)$$

where α, β – Euler angles, η – asymmetry factor.

Nuclear spin-lattice relaxation times were measured using the saturation recovery technique. The recovery of the longitudinal nuclear magnetization after pulse saturation by a

series of $\pi/2$ -degree pulses followed an exponential law (fig. 2). The found values of the spin-lattice relaxation time were in a good agreement with the times previously obtained for the WTe_2 single crystal in the orientations $c \parallel \mathbf{B}_0$ and $c \perp \mathbf{B}_0$ [7].

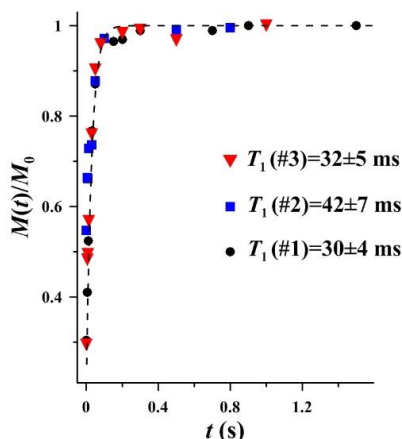


Figure 2. Recovery of the longitudinal nuclear magnetization of ^{125}Te with time t to the equilibrium value M_0 after saturation for WTe_2 powders grown by different methods (#1, #2 and #3) for a line centered around 1450 ppm. The data were obtained at magnetic fields of 9.4 T (#1) and 11.75 T (#2, #3) at room temperature.

Acknowledgements

The measurements were performed with the use of the equipment of the centers of the Research Park of St. Petersburg State University "Center for diagnostics of functional materials for medicine, pharmacology, and nanoelectronics" and "X-ray diffraction studies."

References

1. T.O. Wehling, A.M. Black-Schaffer, A.V. Balatsky. – Adv. Phys., 63, 1-76 (2014).
2. N.P. Armitage, E.J. Mele, A. Vishwanath. – Rev. Mod. Phys., 90, 015001 (2018).
3. A.A. Soluyanov, D. Gresch, Z. Wang, Q. Wu, M. Troyer, X. Dai, X. Dai, B.A. Bernevig. – Nature, 527, 495-498 (2015).
4. P. Li, Y. Wen, X. He, Q. Zhang, Ch. Xia, Zh.-M. Yu, Sh.A. Yang, Zh. Zhu, H.N. Ishareef, Xi-X. Zhang. – Nat. Commun., 8, 2150 (2017).
5. Y.J. Wang, J.X. Gong, D.D. Liang, M. Ge, J.R. Wang, W.K. Zhu, C.J. Zhang. arXiv: 1801.05929 (2018).
6. C.-L. Lin, N. Kawakami, R. Arafune, E. Minamitani, N. Takagi. – J. Phys: Condens. Matter, 32, 243001 (2020).
7. A.O. Antonenko, E.V. Charnaya, M.K. Lee, L.J. Chang, J. Haase, S.V. Naumov, A.N. Domozhirova, V.V. Marchenkov. – Phys. Solid State, 61, 1979-1984 (2019).
8. A.O. Antonenko, E.V. Charnaya, A.L. Pirozerskii, D.Yu. Nefedov, M.K. Lee, L.J. Chang, J. Haase, S.V. Naumov, A.N. Domozhirova, V.V. Marchenkov. – Results in Phys., 21, 103793 (2021).
9. B.E. Brown. – Acta Crystallogr., 20, 268-274 (1966).
10. D. Kang, Y. Zhou, W. Yi, C. Yang, J. Gou, Y. Shi, S. Zhang, Z. Wang, C. Zhang, S. Jiang, A. Li, K. Yang, Q. Wu, G. Zhang, L. Sun, Z. Zhao. – Nature Commun., 6, 7804 (2015).
11. X.-C. Pan, X. Chen, H. Liu, Y. Feng, Z. Wei, Y. Zhou, Z. Chi, L. Pi, F. Yen, F. Song, X. Wan, Z. Yang, B. Wang, G. Wang, Y. Zhang. – Nature Commun., 6, 7805 (2015).
12. R.K. Harris, E.D. Becker, S.M.C. De Menezes, R. Goodfellow, P. Granger. – Pure Appl. Chem., 73, 1795-1818 (2001).
13. D. Freude. Encyclopedia of Analytical Chemistry. John Wiley & Sons, Ltd, 2006.

Multifunctional Heptanuclear Iron Complex: Magnetic Properties and Potential Applications in MRI

E.E. Batueva¹, A.R. Sharipova², E.N. Frolova², A.A. Sukhanov², O.A. Turanova^{1,2},
A.N. Turanov^{1,2}

¹*Institute of Physics, Kazan Federal University, Kazan, Russia*

²*Zavoisky Physical-Technical Institute, FRC Kazan Scientific Center of RAS, Kazan, Russia*

E-mail: kathrin200001@gmail.com

Introduction

Multinuclear complexes are promising compounds for creating multifunctional materials. The combination of physicochemical properties, as well as the possibility of switching these properties under external influence, increases the potential scope of these compounds. One example of such a compound is the heptanuclear iron complex Fe(II)-Fe(III) with the general structural formula $[\text{Fe(II)(CN)}_6\{\text{Fe(III)(L)}\}_6]\text{NCS}_2$, where L = dianion N,N-bis(1-hydroxy-2-benzyliden)-1,7-diamino-4-azageptane, which has been synthesized.

Results

The effective magnetic moment of the complex, determined by magnetometry, was $\mu_{eff} \approx 14.5\mu_B$ at $T = 300$ K. Due to its large magnetic moment, Fe(II)-Fe(III) heptanuclear complex has potential applications in medicine as a contrast agent in diagnostic studies using magnetic resonance imaging (MRI). The spin-spin and spin-lattice relaxation time of HDO in a colloidal solution for this complex of has been measured in a colloidal solution of this molecular magnet with sodium dodecyl sulfate was measured by ¹H NMR spectroscopy at various concentrations, and its relaxivity were also calculated. The measurements have been carried out using Bruker AVANCE III spectrometer (500.13 MHz) at a temperature of 300 K.

It has been shown through magnetometry and EPR methods that the heptanuclear complex exhibits spin-crossover properties ($S = 1/2 \leftrightarrow 5/2$) at temperatures between 4 and 150 K. This work also presents results of the influence of laser radiation at wavelengths of 355 and 580 nm on the properties of this complex up to a temperature of 40K. It was found that the intensity of the lines in EPR spectra of the high-spin and low-spin states of the iron ion decreases equally by about 35% upon irradiation at $T = 20$ K. This may be due to the ligand-metal electron transfer and the formation of a metastable state, which is not recorded in the spectra due to the short lifetime. The polarized signal in the form of emission was observed in TR EPR spectra after a laser pulse at $T = 25$ K. The shape of the spectrum changed, and both emission and absorption signals were observed at $T = 40$ K.

Molecular dynamics simulation of C₆₀/C₇₀ fullerene complexes with peptide dendrimer containing histidine spacers

Valeriy V. Bezrodnyi¹, Sofia E. Mikhianiuk², Oleg V. Shavykin^{1,3}, Igor M. Neelov^{1,2},
Nadezhda N. Sheveleva¹ and Denis A. Markelov¹

¹St. Petersburg State University, 7/9 Universitetskaya nab., 199034 St. Petersburg, Russia

²St. Petersburg National Research University of Information Technologies, Mechanics and Optics (ITMO University), Kronverkskiy pr. 49, 197101 St. Petersburg, Russia

³Tver State University, Zhelyabova St., 33, 170100 Tver, Russia

⁴Institute of Macromolecular Compounds RAS, Bolshoi pr.31, 199004, St.Petersburg, Russia

E-mail: v.v.bezrodniy@mail.ru

Introduction

Fullerene is the bioactive molecules whose biomedical application is limited by its low solubility in water¹. Since the discovery of fullerenes², their potential for use in biomedicine has been explored. Fullerenes are considered as promising drug delivery systems; however, their clinical trials have only just begun³.

Dendrimers can be effectively used as nanoscale containers for the delivery of hydrophobic fullerenes. Dendrimers are currently used in many industrial, biomedical, and pharmaceutical applications due to their unique properties⁴. From the earliest research on dendrimers, their potential as nanocontainers for drug and gene delivery has been recognized, as they are capable of forming complexes with a variety of bioactive molecules⁵. Novel lysine-based peptide dendrimers with additional dipeptide (2Gly, 2Lys, 2Arg, and 2His) spacers between lysine branch points were previously studied by our team using molecular dynamics simulations⁶⁻⁸. Also, we and our colleagues studied the possibility of using these dendrimers for siRNA delivery^{9,10}.

The aim of this work is to study the formation and structure of the complex between a lysine dendrimer with double histidine amino acid residues in the spacers (i.e., with a repeating element consisting of three amino acid residues Lys-2His) and fullerene (C₆₀ or C₇₀), as well as to study the influence of the pairing effect between imidazole groups on the complex formation and the structure of the resulting complex.

Formation of a stable dendrimer-fullerene complex at normal pH

The process of complex formation for the dendrimer-fullerene system can be studied using the time dependence of R_g . As can be seen from Fig. 1a and Fig. 1b, the initial value of R_g for the Lys-2His-C₆₀ complex is high for all three curves corresponding to different initial positions of the fullerene (var1, var2, and var3) relative to the dendrimer, since the fullerene is located far from the dendrimer. Then, after some decline, it reaches a plateau and fluctuates around the equilibrium value, characterizing the formation of the Lys-2His+C₆₀ complex.

For the C₇₀ fullerene, the process of complex formation with the Lys-2His dendrimer has a similar character (Fig. 1b) to C₆₀, but the fluctuations of R_g during the complex formation with the initial conditions var1 and var2 are somewhat smaller. At the same time, in the third variant of the initial conditions (Fig. 1b, for the initial conditions var3, blue curve), more pronounced fluctuations are observed in the first part of the trajectory (from 0 to 250 ns) of R_g compared to the calculation variants var1 and var2 for C₇₀. However, at the beginning of the second equilibrium part of the trajectory (from 250 ns to 500 ns), the differences in the R_g values decrease. In this case, the average R_g value for the time from 250 ns to 500 ns becomes close to the results of other calculations. The results obtained for R_g confirm the fact of the formation of a stable dendrimer-fullerene complex, as well as the fact that the “Lys-

2His+C₇₀” complex has, on average, greater compactness and, accordingly, density compared to the Lys-2His+ C₆₀ complex.

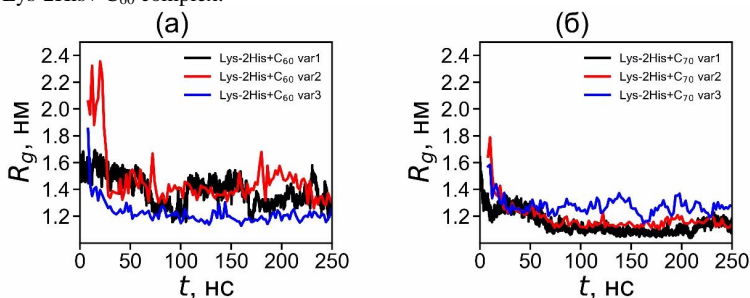


Figure 1. Time dependence of R_g for complexes a) Lys-2His+C₆₀, b) Lys-2His+C₇₀ with uncharged histidines for the first 250 ns at the stage of fullerene encapsulation in the dendrimer). Initial conditions var1, var2, var3 correspond to three different initial variants of the fullerene arrangement (see materials and methods).

Analysis of the structure and properties of a dendrimer-fullerene complex at normal pH

The internal structure of the complexes (averaged over three trajectories with different initial locations of fullerenes relative to the center of inertia of the dendrimer) at normal pH can be clearly demonstrated using the radial distribution function of the density of dendrimer and fullerene atoms in the resulting complexes.

$$\rho(r) = \frac{M(r)}{V(r)}, \quad (1)$$

where $\rho(r)$ is the average density in a spherical layer at a distance r from the center of mass of the dendrimer, $V(r)$ is the volume of the spherical layer.

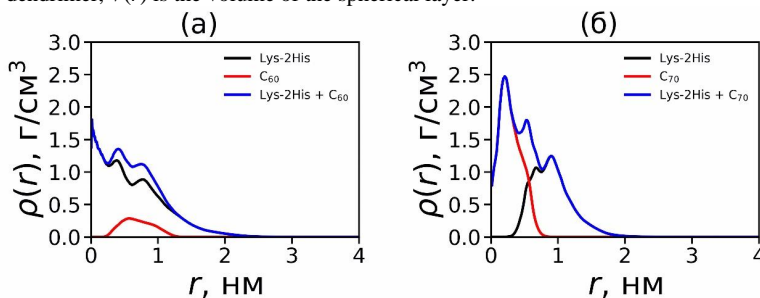


Figure 2. Density distribution for dendrimer (black curve), fullerene (red curve) and dendrimer-fullerene complex (blue curve) for a) Lys-2His+C₆₀, b) Lys-2His+C₇₀. The results are averaged over three different MD simulations corresponding to three different initial arrangements of fullerene (var1, var2 and var3).

As can be seen from Fig. 2b, in the Lys-2His+C₇₀ complex, fullerene places into the center of the dendrimer (red curve), and it is located at distances from $r=0$ nm to $r=0.8$ nm, with a maximum at $r=0$ nm. At the same time, in the Lys-2His+C₆₀ complex, after equilibrium is established, Fig. 2a, fullerene does not place into the center of the dendrimer and is located between its center and the outer surface of the dendrimer molecule, at distances from $r=0.3$ to

1.2 nm from its center with a maximum at 0.6 nm (Fig. 2a, red curve).

Thus, it can be concluded that both fullerenes, C₆₀ and C₇₀, are encapsulated by the Lys-2His dendrimer, however, fullerene C₇₀ is located practically at the center of gyration of the dendrimer, while fullerene C₆₀ is shifted relative to the center of gyration of the dendrimer and is located somewhere in the middle between the center and the outer surface of the dendrimers.

The work was carried out with financial support from the Russian Science Foundation (grant No. 24-13-00158). The simulations were performed at the Computer Resources Center of Saint Petersburg State University

References

1. Chawla, P.; Chawla, V.; Maheshwari, R.; A. Saraf, S.; K. Saraf, S. Fullerenes: From Carbon to Nanomedicine. *Mini-Reviews Med. Chem.* 2010, 10 (8), 662–677. <https://doi.org/10.2174/138955710791572497>.
2. Kroto, H. W.; Heath, J. R.; O'Brien, S. C.; Curl, R. F.; Smalley, R. E. C₆₀: Buckminsterfullerene. *Nature* 1985, 318 (6042), 162–163. <https://doi.org/10.1038/318162a0>.
3. Kazemzadeh, H.; Mozafari, M. Fullerene-Based Delivery Systems. *Drug Discov. Today* 2019, 24 (3), 898–905. <https://doi.org/10.1016/j.drudis.2019.01.013>.
4. González Corrales, D.; Fernández Rojas, N.; Solís Vindas, G.; Santamaría Muñoz, M.; Chavarria Rojas, M.; Matarrita Brenes, D.; Rojas Salas, M. F.; Madrigal Redondo, G. Dendrimers and Their Applications. *J. Drug Deliv. Ther.* 2022, 12(1-s), 151–158. <https://doi.org/10.22270/jddt.v12i1-s.5307>.
5. Ziemba, B.; Borowiec, M.; Franiak-Pietryga, I. There and Back Again: A Dendrimer's Tale. *Drug Chem. Toxicol.* 2022, 45 (5), 2169–2184. <https://doi.org/10.1080/01480545.2021.1915327>.
6. Mikhtaniuk, S.; Bezrodnyi, V.; Shavykin, O.; Neelov, I.; Sheveleva, N.; Penkova, A.; Markelov, D. Comparison of Structure and Local Dynamics of Two Peptide Dendrimers with the Same Backbone but with Different Side Groups in Their Spacers. *Polymers (Basel)*. 2020, 12 (8), 1657. <https://doi.org/10.3390/polym12081657>.
7. Bezrodnyi, V. V.; Shavykin, O. V.; Mikhtaniuk, S. E.; Neelov, I. M.; Sheveleva, N. N.; Markelov, D. A. Why the Orientational Mobility in Arginine and Lysine Spacers of Peptide Dendrimers Designed for Gene Delivery Is Different? *Int. J. Mol. Sci.* 2020, 21 (24), 9749. <https://doi.org/10.3390/ijms21249749>.
8. Bezrodnyi, V. V.; Mikhtaniuk, S. E.; Shavykin, O. V.; Neelov, I. M.; Sheveleva, N. N.; Markelov, D. A. Size and Structure of Empty and Filled Nanocontainer Based on Peptide Dendrimer with Histidine Spacers at Different PH. *Molecules* 2021, 26 (21), 6552. <https://doi.org/10.3390/molecules26216552>.
9. Gorzkiewicz, M.; Konopka, M.; Janaszewska, A.; Tarasenko, I. I.; Sheveleva, N. N.; Gajek, A.; Neelov, I. M.; Klajnert-Maculewicz, B. Application of New Lysine-Based Peptide Dendrimers D3K2 and D3G2 for Gene Delivery: Specific Cytotoxicity to Cancer Cells and Transfection in Vitro. *Bioorg. Chem.* 2020, 95, 103504. <https://doi.org/10.1016/j.bioorg.2019.103504>.
10. Gorzkiewicz, M.; Kopeć, O.; Janaszewska, A.; Konopka, M.; Pędziwiatr-Werbicka, E.; Tarasenko, I. I.; Bezrodnyi, V. V.; Neelov, I. M.; Klajnert-Maculewicz, B. Poly(Lysine) Dendrimers Form Complexes with siRNA and Provide Its Efficient Uptake by Myeloid Cells: Model Studies for Therapeutic Nucleic Acid Delivery. *Int. J. Mol. Sci.* 2020, 21 (9), 3138. <https://doi.org/10.3390/ijms21093138>.

Quantum-Chemical study of Interactions of Fe_2O_n ($n=7, 9$) Clusters with H_2 and O_2 Molecules

*K.V. Bozhenko*¹, *A.N. Utenyshev*¹, *L.G. Gutsev*¹, *S.M. Aldoshin*¹, and *G.L. Gutsev*²

¹ Federal Research Center of Problems of Chemical Physics and Medicinal Chemistry, Russian Academy of Sciences, Chernogolovka, Moscow region, 142432 Russia

² Department of Physics, Florida A&M University, Tallahassee, FL 32307, United States
bogenko@icp.ac.ru

Introduction

The electronic and geometric structure of Fe_2O_7 and Fe_2O_9 clusters, as well as the products of their interaction with H_2 and O_2 molecules in the gas phase, was calculated using the density functional method. Heats of reactions of the clusters with H_2 and O_2 have been obtained. It was demonstrated that in the case of reactions of Fe_2O_7 with an H_2 molecule, the total spin of initial reactants and final products are different, that is, spin relaxation occurs during the reactions.

Computational details

Calculations were performed by the density functional theory method in the generalized gradient approximation (DFT-GGA) with the GAUSSIAN-09 program [1] using the 6-311+G* basis set. The BPW91 functional consisting of the Becke exchange and the Perdue–Wang correlation was chosen as the exchange-correlation functional. The choice of this functional and basis set was justified by the previous estimate of their efficiency in calculations of 3d-metal monoxides MO and dioxides MO_2 ($M = \text{Sc–Zn}$), where good agreement was found between the experimental data and the results of calculations by other methods considering the electron correlation energy. The logic of the search for the ground states of Fe_2O_n ($n=7, 9$) clusters and compounds formed after their interaction with H_2 and O_2 was as follows. For each cluster, probable geometric structures were generated, and full state optimization was performed with these geometries for all calculated spin multiplicities. The state with the lowest total energy was taken as the ground one for the given cluster. Local total spin moments on atoms were calculated using the basis set of natural atomic orbitals.

Results and Discussion

It has been found that the ground state of the Fe_2O_7 and Fe_2O_9 clusters is a singlet nonmagnetic state [2]. Therefore, the reaction of the Fe_2O_7 cluster with the O_2 molecule does not lead to a change in spin multiplicity. Similarly, when the Fe_2O_9 cluster interacts with the H_2 molecule, spin multiplicity does not change. And the singlet state of Fe_2O_7 changes in the reaction with the H_2 molecule, since the ground state of $\text{Fe}_2\text{O}_7\text{H}_2$ is a triplet ($2S + 1 = 3$). Therefore, the results of our calculations allow us to state that nanoparticles based on Fe_2O_7 clusters can be used as sensors for detecting hydrogen molecules, if they retain the pattern of changing the total magnetic moment upon interaction with hydrogen molecules. The determined activation barriers for the calculated reactions are relatively small, which indicates the absence of significant obstacles in the path of these reactions.

Acknowledgements

The work was carried out in accordance with the State assignment AAAA-A19-119111390022-2 for the Federal Research Center for Problems of Chemical Physics and Medicinal Chemistry, RAS.

References

1. M. J. Frisch, G. W. Trucks, H. B. Schlegel, et al., Gaussian 09, Revision C.01. (Gaussian, Inc., Wallingford CT, 2009).
2. K.V. Bozhenko, A.N. Utenyshev, L.G. Gutsev, L.G. Gutsev, S.M. Aldoshin. Quantum-Chemical Modeling of Interactions of Fe_2O_7 and Fe_2O_9 Clusters with H_2 and O_2 Molecules. Russian Journal of Inorganic Chemistry, 2024, Vol. 69, No. 12, pp. 1877–1883. DOI: 10.1134/S0036023624602824.

Microstructure and molecular mobility in the ternary LiCl-CsCl- H₂O system. A molecular dynamics simulation study

Cheremensky S.O.¹, Egorov A.V.¹

¹*Department of Nuclear-Physics Research Methods, Faculty of Physics, Saint-Petersburg State University*

E-mail: st087373@student.spbu.ru

It has recently been shown [1] that the ternary LiCl-CsCl-H₂O system is a potentially promising electrolyte for batteries. In order to optimize the ratio of solution components, it is necessary to identify the mechanisms of microstructure formation as well as the main factors affecting the molecular mobility in such systems. In the present work, the molecular dynamics simulations were used for this purpose. At all, 13 systems were considered: 11 ternary and 2 binary solutions (see Fig. 1).

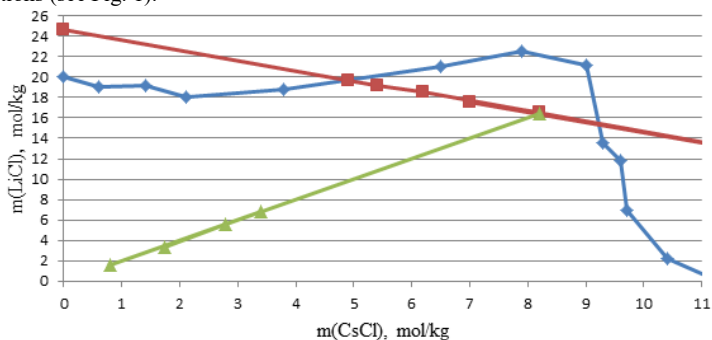


Fig. 1. Phase diagram of the LiCl–CsCl–H₂O ternary system. The studied concentrations are shown as green and brown symbols

Simulations were carried out using the MDynaMix v.5.0 software package [2]. All systems were modeled in an isothermal-isobaric ensemble (25°C, 1 atm) in a cubic cell with periodic boundary conditions. The SPC/E water model [3] was employed to describe the solvent molecules. The Li, Cs, and Cl cations were modeled using the potentials described in Refs. [4–6]. The equations of motion were solved using Verlet algorithm with a time step of 2 fs. Coulomb interactions were treated using Ewald method. The temperature and pressure were kept constant using the Nose-Hoover algorithm. For each system the equilibration time was equal to 1 ns, the following simulation run was 1 ns long.

The composition and stability of the solvation shells of the ions, self-diffusion of solution components as well as water rotational reorientation in the LiCl-CsCl-H₂O ternary system were studied in detail. A special attention was given to the effects of changes in the ratio of lithium and cesium cations on molecular mobility.

References

1. Cell Rep. Phys. Sci. 2022, 3, 10068
2. Comp. Phys. Comm. 2000, 128, 565
3. J. Phys. Chem. 1987, 91, 6269
4. J. Chem. Phys. 1992, 96, 6970
5. Chem. Phys. Lett. 1994, 227, 211
6. J. Chem. Phys. 1994, 100, 3757

Proton attached to nitrogen in porphyrins and tetrapyrroles

Nina Djapic¹

¹University of Novi Sad, Technical Faculty "Mihajlo Pupin", Zrenjanin, Serbia

E-mail: nina.djapic@tfzr.rs

Introduction

In the solution-state ^1H NMR spectrum, the chemical shift of proton attached to nitrogen in porphyrins and tetrapyrroles, occurs downfield. The chemical shift value of proton attached to nitrogen depends on molecular structure of a porphyrin and tetrapyrrole, on the solvent used, the presence of hydrogen-bonding, aromaticity, the concentration and many others. Proton attached to nitrogen is exchanged with deuterium, in a protic deuterated solvent, inducing the peak disappearance.

Solution-state ^1H NMR spectra of porphyrins and tetrapyrroles

Find the signals of proton attached to nitrogen in porphyrins and tetrapyrroles in the solution-state ^1H NMR spectra (Fig. 1, Fig. 2 and Fig. 3).

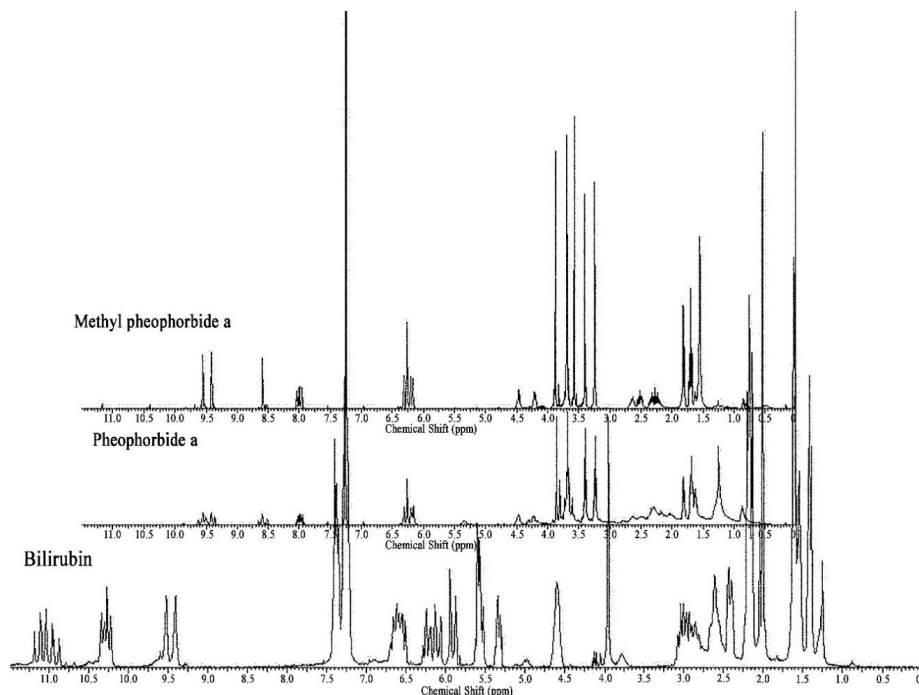


Figure 1. The solution-state ^1H NMR spectra of bilirubin, pheophorbide a and methyl pheophorbide a recorded on a 360 MHz spectrometer, solvent used CDCl_3

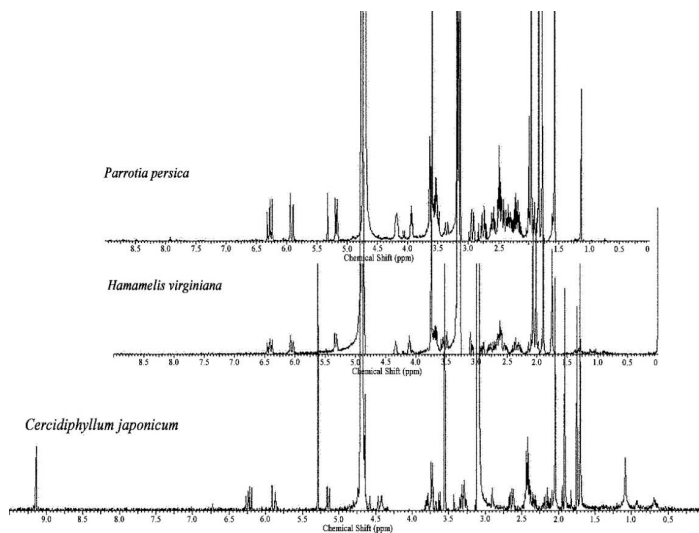


Figure 2. The solution-state ^1H NMR spectra of tetrapyrroles isolated from *Cercidiphyllum japonicum*, *Hamamelis virginiana* and *Parrotia persica* leaves, recorded on a 360 MHz spectrometer, solvent used CD_3OD

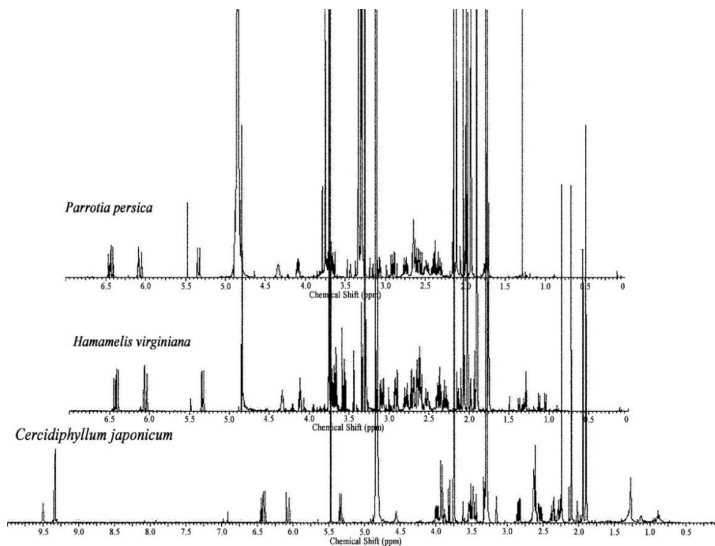


Figure 3. The solution-state ^1H NMR spectra of tetrapyrroles isolated from *Cercidiphyllum japonicum*, *Hamamelis virginiana* and *Parrotia persica* leaves, recorded on a 500.13 MHz spectrometer, solvent used CD_3OD

Potential of NMR spectroscopy for assessing the hydrophobicity of microsphere cellulose carriers for spiking cancer cells

Anastasia S. Dmitriyeva¹, Boris P. Nikolaev,^{2,3} Ludmila Yu. Yakovleva², Viacheslav S. Fedorov^{2,4}, Maxim Shevtsov^{2,4}

¹ Saint-Petersburg State Institute of Technology, St. Petersburg, Russian Federation

² Institute of Cytology of the Russian Academy of Sciences (RAS), St. Petersburg, Russian Federation

³ Saint-Petersburg Technopark, Engineering Centre API, Saint-Petersburg, Russian Federation

⁴ Personalized Medicine Centre, Almazov National Medical Research Centre, Akkuratova Str. 2, 197341 Saint Petersburg, Russia

E-mail: dmitriyeva03@bk.ru

Introduction

Methods of diagnostics and therapeutic courses of oncological diseases based on the isolation of circulating tumor cells (CTC) from biological fluids are a valuable tool of modern medicine. This approach can be implemented through specific interaction of an oncomarker with a molecule containing a region capable of binding to its epitope. Solid malignant tumors, as well as CTC, are characterized by increased expression of the membrane-associated protein HSP70. The peptide TKDNNLLGRFELSG (TKD), consisting of 14 amino acids, is able to specifically interact with HSP70, since it follows the residue sequence of its oligomerization domain [1]. The ¹³C NMR spectra confirm the composition of TKD in synthesis. It is also necessary to immobilize the peptide on a heterophase carrier for affine separation. A good candidate for CTC capture is magnetic microspherical cellulose. The cellulose microcarrier has a developed porous surface represented by a network of micro- and macropores, is inert, is characterized by high strength, contains functional hydroxyl groups in the structure that have the potential for activation. Inclusion of MNPs into pores ensures convenient and efficient separation of the extracted material from the total analyzed volume under the action of an external magnetic field. The morphology and structure of microsphere cellulose and ¹³C spectra of TKD was measured by MRI, NMR at a spectrometer with microscale tomographic accessory Bruker AvanceIII 400 MHz (Bruker, FRG).

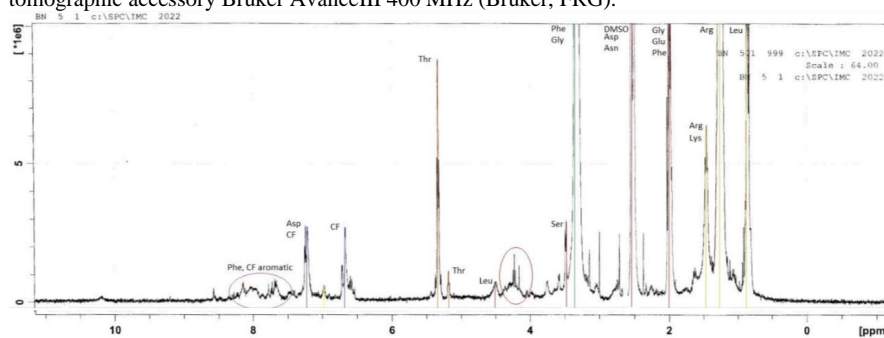


Figure 1 – ¹³C NMR spectrum of TKD

Results and discussion

For reliable analytical data, an important aspect is sorption caused by non-specific hydrophobic interactions. The assessment of the magnitude of hydrophobic interactions between the sorbate and the matrix is usually made based on the distribution coefficient P of the neutral molecule between the aqueous phase and the stationary phase the chromatographic carrier and subsequent comparison of the coefficient P with the octanol/water comparison system [2]. Redistribution of the hydrophobic probe can be measured by chromatographic methods with a change in the polarity of the eluent, the type of sorbate (alkylated alcohols, amines, etc.) and spectral methods. In this work, the ^1H -NMR method, a spectrally unlimited method of the optical range in turbid media, was used. The CHCl_3 molecule was chosen as a radio spectral probe, the coefficient of which according to the Hahn criterion is $\text{Log}P = 1,97$. The convenience of chloroform for probing sorbents consists in the small size of the molecule, which facilitates penetration into microgel areas, the singlet structure of the NMR line, high polarity ($\epsilon = 4.8$) and poor solubility in water provide spectral tracking of the molecule in the hydrophobic sites of the sorbent.

The shape of the NMR line of a liquid in the pores of a spheroidal form of a biphasic composite material is determined primarily by the difference in magnetic susceptibility $\Delta\chi$, the demagnetizing factor N , and the magnitude of the resonance frequency ν . The degree of porosity of the medium, i.e. the number of spheroidal pore inclusions per unit volume of the sample, does not affect the shape of the line, as follows from the relation [3].

$$H_{in} = H_0(1 + N\Delta\chi) + \sum_i H_i(r)$$

where $H_i(r)$ is the field strength created by the i -th spheroid pore at point r inside the selected spheroid, H_0 - external magnetic field

In the case of nanosized pores, rapid molecular motion causes the second term $H_i(r)$ to be averaged to zero and, thus, to the complete leveling of all possible types of dependence on the degree of porosity of the medium. Thus, the width of the NMR line of such a nanoporous medium turns out to be dependent on sorption characteristics

^1H -NMR spectra were measured by Fourier spectroscopy on a Spinsolve 60 Carbon Ultra spectrometer (Margitek) in standard 5 mm ampoules. Sorbent samples were placed in ampoules to which CHCl_3 was added, after equilibrium was established, the spectra were recorded with preliminary withdrawal excess solvent. The signal position was counted relative to the TMS solution. The ^1H NMR spectrum of CHCl_3 in water and cellulose sorbent is shown in Fig. 2.

To stabilize chloroform during storage, alcohol is added to commercial reagent (~ 0.6 w/w%), which corresponds to the presence of a triplet (1.97-1.74 ppm) and quartet (4.50-4.26 ppm) spectral lines Fig. 2 (a). The spectral line attributed to chloroform has a chemical shift of 8.35 Fig. 2 (a).

Conclusion

When CHCl_3 was added to the cellulose microcarrier, it turned out that the molecules of the hydrophobic probe are capable of being sorbed equally with the ethanol molecule, as evidenced by the broadening of the spectral lines of both substances Fig. 2 (b). The ratio of the integral intensities of CHCl_3 and EtOH, proportional to the molar content of nuclei giving a signal, for a sample of CHCl_3 in water was 1:9. However, for CHCl_3 in a microcellulose carrier, this ratio was equal to 1:2, which indicates greater sorption of the hydrophobic molecule of CHCl_3 than EtOH. The last fact is significant for biosensing since discovered some rate hydrophobicity of microporous cellulose matrix can appreciably affect the nonspecific interaction of TKD conjugate with CTC.

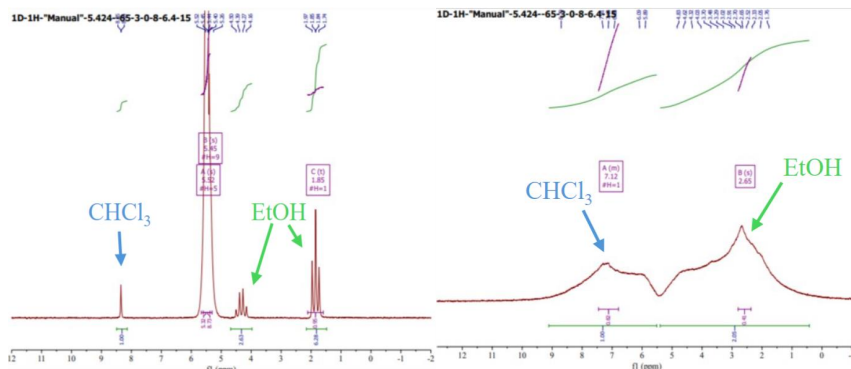


Figure 2. ^1H NMR spectrum of CHCl_3 in water (a) and in the cellulose microsphere sorbent (b)

Acknowledgments

The work was supported by the Ministry of Science and Higher Education of the Russian Federation (Agreement No. 075-15-2022-301). The authors are grateful for aid in organizing experiments to A. Mazur, A. Dobrodumov, I. Voevodina.

References

1. Meng Y. et al. TKD peptide as a ligand targeting drug delivery systems to memHsp70-positive breast cancer//International journal of pharmaceutics. – 2016. – V. 498. – №. 1-2. – P. 40-48.
2. Supriyo Saha, Log P in Encyclopedia of Physical Organic Chemistry. Chapter in book: Encyclopedia of Physical Organic Chemistry, 6 Volume, 2017, WILEY INTER SCIENCE NEWYORK
3. Luk'yanov A.E., Bulygin A.N., Nikolaev B.P., Petrov L.N. Calculation of inhomogeneous broadening of nuclear magnetic resonance lines in dispersions of spherical particles / Colloid. journal (russian). - 1982. - V. 44. - No. 1. - P. 35 - 40.

Analysis of hyperfine and quadrupole interactions in the first coordination sphere of ^{14}N in hexagonal boron nitride

E.V. Dmitrieva¹, G.V. Mamin¹, F.F. Murzakanov¹, I.N. Gracheva¹, M.R. Gafurov¹, V.A. Soltamov²

¹*Institute of Physics, Kazan Federal University, Kremlyovskaya 18, Kazan 420008, Russia*

²*Ioffe Institute, Polytekhnicheskaya, 26, St. Petersburg 194021, Russia*

E-mail: dev600@mail.ru

Introduction

The vacancy centers present significant interest for quantum technologies due to spin optical properties. A notable advantage of the hexagonal boron nitride (hBN) vacancy defects compared to analogous materials is the presence of magnetic moments associated with the nuclei surrounding the vacancies, as illustrated in Figure 1A. This characteristic is particularly valuable for quantum operations, where the existence of two qubits is essential. The interaction between the magnetic moments and the electronic states of the vacancies could facilitate coherent control and manipulation of qubit states. Particularly promising is the use of hBN in quantum sensing, where it can be utilized to develop highly sensitive sensors capable of detecting subtle variations in parameters such as temperature, magnetic fields, etc [1].

Materials

Hexagonal boron nitride is a material characterized by crystalline structure, which consists of two-dimensional atomic layers. These layers are held together by weak van der Waals forces, allowing for unique properties such as high thermal conductivity. The hexagonal boron nitride crystal exhibits a symmetry space group of $P6_3/mmc$. One of the most interesting types of defects in hBN is the boron vacancy, which is shown in Figure 1B. A boron vacancy is the absence of a boron atom in the crystal lattice, there is an electron density in place of the boron vacancy in hexagonal boron nitride. To induce these vacancy defects, the hBN crystal was subjected to electron irradiation at an energy of 2 MeV at room temperature. The crystal dimensions were $0.90 \text{ mm} \times 0.54 \text{ mm} \times 0.05 \text{ mm}$.

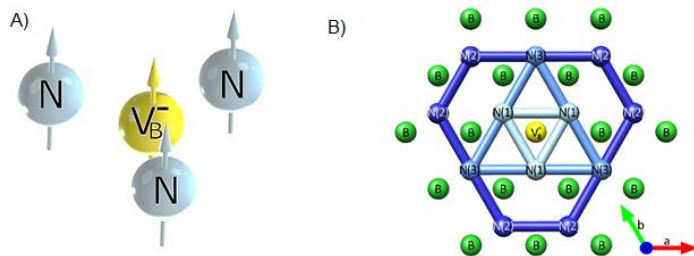


Figure 1. A) Schematic illustration of a boron vacancy V_B^- surrounded by three nearest nitrogen nuclei (coordination sphere №1). B) Crystal lattice of hexagonal boron nitride with demonstration of coordination spheres of nitrogen atoms.

Methods

Magnetic resonance experiments were conducted using a W-band (94 GHz) Bruker Elexsys E680 spectrometer. Figure 2A illustrates the Electron Spin Resonance (ESR) spectrum with optical excitation achieved through a laser operating at a wavelength of 532 nm. The spectrum was recorded utilizing a pulse sequence:

$\frac{\pi}{2}(MW) - \tau - \pi(MW) - \tau - ESE$, where $\pi(MW) = 72 \text{ ns}$, $\tau = 260 \text{ ns}$, ESE – electron spin echo.

ENDOR experiments were also conducted using a laser with a wavelength of 532 nm. The chosen pulse sequence was the Mims sequence:

$$\frac{\pi}{2}(MW) - \tau - \frac{\pi}{2}(MW) - t_1 - \pi(RF) - t_2 - \frac{\pi}{2}(MW) - \tau - ESE, \quad \text{where } \pi(RF) = 160 \mu\text{s}.$$

Results and discussion

Measurements were performed for two orientations: when the magnetic field was aligned both parallel and perpendicular to the hexagonal symmetry axis of the crystal. From the experimental results, values for the g-factor and the zero-field splitting (ZFS) parameter D were extracted. For a comprehensive analysis, simulations of the spectra were carried out for the aforementioned orientations, along with an orientation-dependent simulation. The observed vacancy center is characterized by a triplet ground state exhibiting a zero-field splitting of approximately $D = 3.55 \text{ GHz}$ and g-factor = 2.004. The signal corresponding to the transition from 0 to -1 was detected as radiation, which can be elucidated by the transitions depicted in Figure 2B [2].

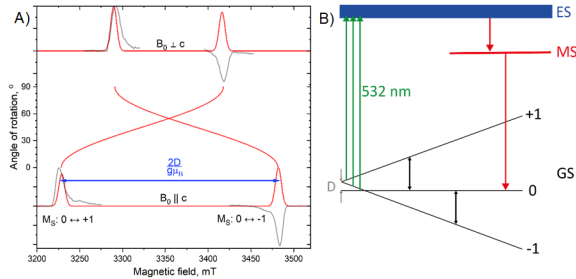


Figure 2. A) ESR spectrum (black line) and the spectrum simulation (red line) and angular dependence simulation for vacancy center (W-band, $T = 25 \text{ K}$). B) Schematic representation of the energy levels for the vacancy center with optical excitation at a wavelength of 532 nm. ES – excited state, MS – metastable state, GS – ground state.

The spin Hamiltonian encompasses five distinct types of interactions, namely the electronic Zeeman interaction, ZFS, nuclear Zeeman interaction, hyperfine interaction, and nuclear quadrupole interaction. In the case of parallel alignment ($c \parallel \mathbf{B}_0$), it can be expressed as:

$$\hat{H} = g\mu_B \mathbf{B}_0 S_z + D \left(S_z^2 - \frac{S(S+1)}{3} \right) - \gamma \hbar \mathbf{B}_0 I_z + \sum_{i=1}^3 \left(A_{xx} S_x I_{x(i)} + A_{yy} S_y I_{y(i)} + A_{zz} S_z I_{z(i)} + \frac{C_q}{4I(2I-1)} \left(3I_{z(i)}^2 - I(I+1) + \frac{\eta}{2} (I_{x(i)}^2 - I_{y(i)}^2) \right) \right). \quad (1)$$

Simulations of ENDOR spectra (Fig. 3), which took into account ^{14}N ($I = 1$, 99.6 %) from the first coordination sphere for orientations parallel and perpendicular to the magnetic field, resulted in the determination of the principal components of tensor A . The values obtained were $A_{xx} = 45.0 \text{ MHz}$, $A_{yy} = 46.5 \text{ MHz}$ and $A_{zz} = 87 \text{ MHz}$. Based on this, the values of the Fermi contact interaction constant $A_{iso} = 59.5 \text{ MHz}$ and the dipole-dipole interaction constant $A_{dd} = 13.75 \text{ MHz}$ were calculated. The magnitude of the quadrupole interaction

$C_q = 1.96$ MHz was determined, as well as the asymmetry parameter $\eta = -0.07$ [3].

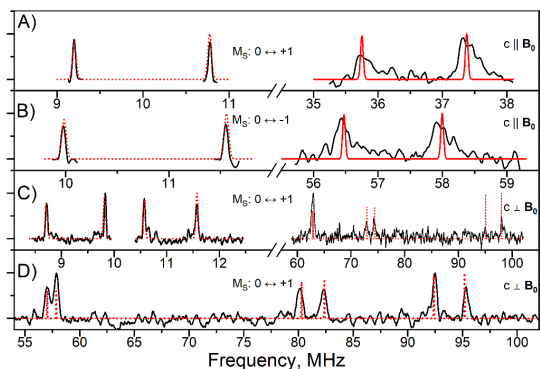


Figure 3. The ENDOR spectrum of ^{14}N displays two electronic transitions: one corresponding to the $M_S = 0 \leftrightarrow +1$ transition at a magnetic field of $B_0 = 3223.1$ mT, and the other for the $M_S = 0 \leftrightarrow -1$ transition at $B_0 = 3480.5$ mT. A, B, C) $\varphi = 7.7^\circ$, $T = 50\text{K}$. D) $\varphi = 18.4^\circ$, $T = 25\text{K}$, where φ – angle of deviation in the plane of dangling bond.

Summary

Magnetic resonance experiments, including ESR and ENDOR, were performed to analyze the electron-nuclear interactions of vacancies. The color center exhibited a triplet ground state with zero-field splitting $D = 3550$ MHz and g-factor = 2.004. Simulations revealed the principal components of tensor A : $A_{xx} = 45.0$ MHz, $A_{yy} = 46.5$ MHz and $A_{zz} = 87$ MHz. Quadrupole interaction magnitudes and the asymmetry parameter were also determined: $C_q = 1.96$ MHz, $\eta = -0.07$. The studied hyperfine and quadrupole interactions between spins unveil new horizons in the creation of complex entangled states, which serve as the foundation for quantum computing. The entangled states arising from these interactions can be harnessed to execute quantum algorithms with high efficiency, significantly enhancing the computational capabilities of contemporary quantum systems. This knowledge will enable researchers to predict the behavior of quantum systems more accurately, optimize qubit manipulation processes.

Acknowledgments

Financial support of the Russian Science Foundation under Grant RSF 24-12-00151 is acknowledged.

References

1. Sumukh Vaidya, Xingyu Gao, Saakshi Dikshit, Igor Aharonovich & Tongcang Li Quantum sensing and imaging with spin defects in hexagonal boron nitride. – *Advances in Physics*: X, 8:1, 2206049 (2023).
2. F.F. Murzakhanov, G.V. Mamin, S.B. Orlinskii, U. Gerstmann, W.G. Schmidt, T. Biktagirov, I. Aharonovich, A. Gottscholl, A. Sperlich, V. Dyakonov, V.A. Soltamov. – *Nano Letters*, 22, 2718 – 2724 (2022).
3. I.N. Gracheva, F.F. Murzakhanov, G.V. Mamin, M.A. Sadovnikova, B.F. Gabbasov, E. N. Mokhov, M. R. Gafurov. – *The Journal of Physical Chemistry C*, 127, 3634 – 3639 (2023).

Study of conformation of mechanically activated calcium gluconate irradiated with gamma quanta

A.R. Gafarova¹, G.G. Gumarov¹, R.B. Zaripov¹, D.S. Rybin²

¹ Zavoisky Physical-Technical Institute, FRC Kazan Scientific Center of RAS, Kazan 420029, Russian Federation

² UdmFRC Ural Branch of RAS, Izhevsk, 426067, Russia

E-mail: albina-gafarova@mail.ru

The study of the stereochemical structure of biologically active substances plays a key role in various aspects of pharmaceutical activity, from the development and production of drugs to the control of their quality and safety. However, there are substances for which it is not possible to study classical methods for determining the spatial structure. In particular, such substances include mechanically activated nanodispersed amorphous form of calcium gluconate (MACG), demonstrating increased therapeutic efficacy compared to other calcium-containing drugs. This effect may be associated with stereochemical changes induced by mechanical activation. In this regard, the approach to research proposed in the work using the electron paramagnetic resonance method, quantum chemical methods, and gamma irradiation allows us to obtain data on the structure of MACG.

The EPR spectra of mechanically activated calcium gluconate are shown in Fig. 1. (MACG). A narrow single line is observed in the W-band spectrum designated by us as the R radical [1]. To obtain information on the structural changes of gluconic acid anions, SA MA was irradiated. The EPR spectra of MACG irradiated with a dose of 400 Gy are shown in Fig. 1.

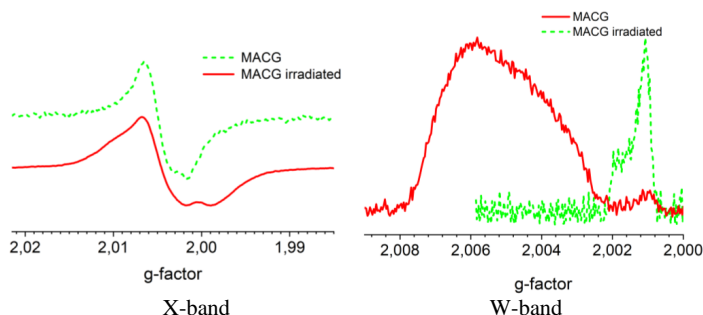


Figure 1 – EPR spectra of mechanically activated calcium gluconate (MACG) and irradiated mechanically activated calcium gluconate.

Analysis of the X- and W-band EPR spectra using quantum chemistry methods showed that stable carbon-centered radicals localized mainly on C2 atoms, as well as an unidentified radical R, are formed when irradiated with MACG. The hyperfine interaction tensor obtained as a result of quantum chemical calculations was $A = [6.8 \ 3.0 \ 35.1]$, the isotropic part of which is 15 MHz. According to the McConnell relation, this value of the hyperfine interaction corresponds to a torsion angle of 68 degrees. The value of this torsion angle coincided with the X-ray diffraction data for crystalline calcium gluconate [2]. Based on this observation, it can be concluded that part of the gluconic acid anion near the calcium atom does not change its structure during mechanical activation. Unfortunately, the absence of stable radicals localized on other carbon atoms did not allow us to calculate the torsion angles for the C3-C5 fragment. However, it can be assumed that the impossibility of stabilizing radicals on carbon atoms C3-C5 may be associated with a change in the geometry

of the molecule. It is known that in gluconic acid, as a result of turning the C3-C5 fragment by 120° , a transition from a linear to a curved conformation occurs (1P в 3G+) [3]. Presumably, this process occurs during the mechanical activation of calcium gluconate. Therefore, radicals accumulate only on the C2 atoms since the central part of the molecule is “closed” by curved gluconic acid anions. (Fig. 2, 6)).

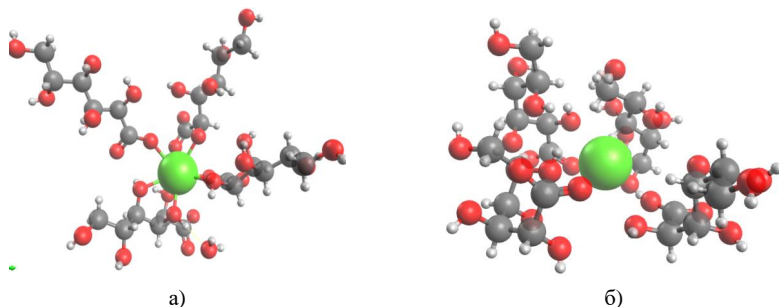


Figure 2 – a) The structure of crystalline calcium gluconate according to X-ray structural analysis [2]; b) – the same structure with the C3-C5 fragment rotated by 120 degrees.

References

1. Multifrequency EPR study of radicals formed under the action of γ -irradiation and mechanical activation in calcium gluconate / A.R. Gafarova, G.G. Gumarov, R.B. Zaripov, D.S. Rybin, G.N. Konygin // Chemical Physics and Mesoscopy. - 2024. Vol. 26, No. 3. P. 299-305
2. Crystal and solution structures of calcium complexes relevant to problematic waste disposal: calcium gluconate and calcium isosaccharinate / V. Bugris, Cs. Dudas, B. Kutus, [et al.] // Acta Crystallographica - 74(6) - 2018 - P. 598-609.
3. Horton, D. Conformations of D-gluconic, D-mannonic, and D-galactonic acids in solution, as determined by n.m.r. spectroscopy / D. Horton, Z. Walaszek, I. Ekiel // Carbohydrate Research. – 1983. –Vol. 119. – P.263-268.

Influence of substitutes and chalcogen atom nature on the alkylation of phosphine chalcogenides

Galiakhmetov S.A.¹, Mulloyarova V.V.¹, Antonov A.S.^{2,3}

¹*St. Petersburg State University, St. Petersburg, Russia*

²*University of Regensburg, Regensburg, Germany*

³*Ludwig Maximilian University of Munich, Munich, Germany*

E-mail: *st117534@student.spbu.ru*

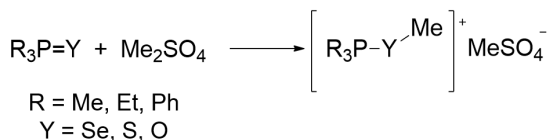
Introduction

Phosphine chalcogenides $R_3P=Y$, (where Y: O, S, Se) have a number of practically useful properties and are valuable for many scientific fields. Thus, for example, disubstituted salts of the phosphine selenides and sulfides are used in organocatalysis as catalysts and in crystalline or molecular design to obtain substances with desired properties [1, 2]. The particular interest of the phosphine chalcogenide molecules is associated with the peculiarity of the electronic structure of the chalcogen atom. There is a negative electrostatic potential region on the chalcogen atom, which allows it to act as an electron donor in various non-covalent interactions; and there is a positive electrostatic potential region (at the continuation of the covalent bond; the so-called σ -hole), due to which these molecules can form a chalcogen bond [3, 4]. This dual nature of molecules is used in the development of correlation methods for non-covalent interactions studying in a number of works. [5] Another important feature of phosphine chalcogenides is the presence of phosphorus nucleus with a 100% natural abundance of the magnetically active isotope ^{31}P , with a high gyromagnetic ratio and spin 1/2, which makes it possible to carry out research by the simple NMR experiment.

In this work the influence of substitutes and chalcogen atom nature on the alkylation reaction rate of phosphine chalcogenides $R_3P=Y$ is devoted by ^{31}P NMR spectroscopy in solution.

Methods and Objects of research

Alkylation reactions of the phosphine chalcogenides were carried out with dimethyl sulfate (Me_2SO_4) in solution in $CDCl_3$ according to the following scheme:



Scheme 1. Alkylation reaction of phosphine chalcogenides $R_3P=Y$.

The influence of substituents and a chalcogen atom on the reaction rate was studied by ^{31}P NMR spectroscopy. The overall concentration of the phosphine chalcogenides in samples was in the range of 0.1–1M, and the concentration of dimethyl sulfate was 1M.

Experimental details

NMR spectra were recorded on a Bruker 300 MHz DPX spectrometer (7.05 T, 121.49 MHz for ^{31}P) at $T = 300.2K$ with time intervals of 15, 30 and 60 minutes. The 1D sequence with power-gated decoupling scheme and 30° -pulses with the delay of 5 s for ^{31}P were used for measurements of $^{31}P\{^1H\}$ NMR spectra. Spectra were recorded as the sum of 64 scans for ^{31}P . Based on the obtained NMR data, kinetic curves of phosphine selenides with various substitutes (Fig. 1) and phosphine chalcogenides (Fig. 2) were constructed and the rate constants for each reaction were determined.

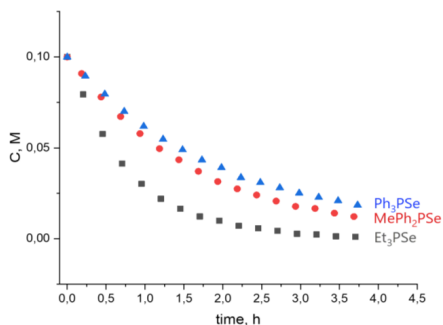


Figure 1. Kinetic curves of phosphine selenides

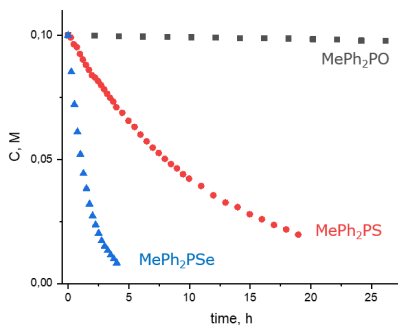


Figure 2. Kinetic curves of phosphine chalcogenides

Acknowledgements

This work was supported by the Russian Science Foundation (project No 23-13-00095). All NMR spectra were recorded at the Center for Magnetic Resonance at the St. Petersburg State University Research Park.

References

1. Y. Pang, Z. Zhao, P. P. Zhou, Y. Wang. – Nat. Commun., 14, 2041-1723 (2023).
2. Chand A, Sahoo DK, Rana A, Jena S, Biswal HS. – Acc. Chem. Res., 53, 1580–1592 (2020).
3. D. V. Krutin, A. S. Zakharov, E. Y. Tupikina, V. V. Mulloyarova. – PCCP., 26(30), 20450–20461 (2024).
4. Andrew J. Peloquin, Dr. Colin D. McMillen, Dr. Scott T. Iacono, Dr. William T. Pennington. – ChemPlusChem., 86, 2192-6506 (2021).
5. Mariusz Michalczyk, Wiktor Zierkiewicz, and Steve Scheiner. – J.Phys.Chem.A., 129(2), 545–554 (2025).

NMR assignment of eucaryotic initiation translation factor 5A of *Candida albicans*

Vyacheslav E. Gonvalin¹, Polina V. Egorova¹, Natalia S. Garaeva^{1,3}, Marat M. Yusupov^{1,4}
and Konstantin S. Usachev^{1,2,3}

¹Federal Research Center «Kazan Scientific Center of Russian Academy of Sciences» Russia, 420008 Kazan, Lobachevskogo, 2/31, Russian Federation

²Kazan Federal University, 18 Kremlevskaya, Kazan 420008, Russian Federation

³National Research Centre 'Kurchatov Institute', Russian Federation, 123182, Moscow, 1, Akademika Kurchatova Square, Moscow.

⁴Institut de Génétique et de Biologie Moléculaire et Cellulaire, CNRS UMR7104, INSERM U964, Université de Strasbourg, 1 rue Laurent Fries, F-67400 Illkirch, France

E-mail: Gonaylinslava@gmail.com

Introduction

Candida albicans (*C. albicans*) is a yeast-like microscopic fungus that can normally be found in the human body on the mucous membranes of the intestines, oral cavity and urogenital tract. However, when the immune system is weakened, *C. albicans* begins to exhibit pathogenic properties. This can manifest as a disease known as candidiasis.

The eukaryotic translation initiation factor 5A (eIF5A) is a highly conserved ribosomal factor that also plays an important role in translation elongation and termination [1].

The role of eIF5A in translation elongation is to stabilize tRNA at the P-site during the synthesis of complex polyproline motifs. A unique feature of eIF5A is that its activity is critically dependent on hypusination, a post-translational modification of a highly specific lysine residue to a hypusine residue [2]. This residue is located in one of the flexible loops of eIF5A, which stabilizes tRNA in the P-site during the synthesis of complex polyproline motifs. The majority of studies indicate that eIF5A-dependent proteins comprise amino acid sequences consisting of three proline residues or two consecutive proline and glycine residues (Pro-Pro-Pro or Pro-Pro-Gly). This is attributed to the inefficient nature of glycine and proline as acceptors of the growing polypeptide chain [3].

The involvement of eIF5A in translation termination is associated with its interaction with the factors eRF1 and eRF3. This interaction leads to the release of the synthesised polypeptide chain [4].

Methods

The object of the study was the eIF5A-GB1 protein from *Candida albicans*. The protein consists of 219 amino acid residues, with a molecular weight of 23.9 kDa, an isoelectric point of pI = 5.64, and an extinction coefficient of 14440 (absorbance 0.6 = 1 g/L).

NMR spectra were recorded on an Avance III HD™ Bruker 700 MHz spectrometer equipped with a QCI cryoprobe (¹H/¹F, ¹³C, ¹N, ³¹P). The NMR sample contained 0.5 mM eIF5A-GB1 in phosphate buffer solution (see Appendix), 2% sodium azide (NaN₃), and 5% D₂O. To determine the positions of secondary structure elements in eIF5A-GB1, the following NMR experiments were previously conducted: HSQC, HNCA, HN(CO)CA, HNCACB, CBCA(CO)NH, HNCO, HN(CA)CO, ¹N-TOCSY HSQC, ¹N-NOESY HSQC, and ¹³C-NOESY-HSQC. High-resolution NMR spectra were processed using the CcpNMR Analysis software [5]

Results

The assignment of ¹H, ¹³C, and ¹N nuclear signals was performed for 127 out of 219 amino acid residues (58.3%) of the protein.

Chemical shift indices were calculated and used in the DANGLE software package [6] to predict the positions of secondary structure elements in eIF5A-GB1, revealing two α-

helices and nine β -strands with the topology (β_1 - β_2 - α_1 - β_3 - β_4 -...- β - β - α - β - β). The (β_1 - β_2 - α_1 - β_3 - β_4) region belongs to the stabilizing GB1 domain, while the (...- β - β - α - β - β) region corresponds to the C-terminal domain of eIF5A.

Acknowledgements

The research was carried out under Agreement No. 075-15-2025-012 dated 27 February 2025 on granting a grant from the federal budget in the form of a subsidy for the implementation of a scientific project under the supervision of an engaged leading scientist.

References

1. Laura K.M., Michael D.M., Leah M.A., et al. – Methods Enzymol., № 430, 397-408 (2007)
2. Turpaev K.T. – Biochemistry (Moscow), v. 83 №8, 1099-1110 (2018)
3. Spirin A.S. – Soros Educ J., №11, 65-70 (1998)
4. Finkelstein A.V. – Moscow: KDU, 456 p. (2012)
5. Vranken W.F., Boucher W., Stevens T.J., et al. – Proteins., v.59, 687-696 (2005)
6. Cheung M.S., Maguire M.L., Stevens T.J., Broadhurst R.W. – Journal of Magnetic Resonance 202(2), 223-233 (2010)

NMR control of the synthesis of pharmaceutical intermediates

Kristina S. Gorkovaia, Victoria V. Abzianidze, Alexander S. Bogachenkov, Denis V. Krivorotov, Leonid S. Chisty, Diana S. Suponina

Research Institute of Hygiene, Occupational Pathology and Human Ecology of Federal Bio-Medical Agency, St.Petersburg, Russian Federation

E-mail: kristinagork@gmail.com

Introduction

In our country, growing relevance of rare (orphan) diseases problem is associated with the expansion of opportunities for early diagnosis of this group of diseases and with the emergence of effective methods of treating patients. Therefore, there is an increase need to develop our own production of orphan drugs.

Pulmonary Arterial Hypertension (PAH) is a subgroup of pulmonary hypertension in which the blood pressure in the pulmonary arteries and arterioles (the blood vessels located proximal to the capillary bed, the site of oxygen exchange in the lungs) is elevated [1]. It leads to the increased pulmonary vascular resistance which will eventually lead to the right heart failure and the death without necessary treating.

Selexipag is the first in Russia and the only globally approved representative of a new class of oral medicines, prostacyclin IP-receptor agonists for treatment of PAH [2]. According to one of the strategies for the synthesis of selexipag, a halogen derivative of methylsulfamide is used as an intermediate. Its acylation is difficult, since protons of the NH₂-group of the initial sulfamide have pronounced acidic properties.

The reaction was monitored using the Nuclear magnetic resonance (NMR) method. The choice of this method is due to the inability to detect the desired compound in the MS-spectrum, which is caused by its relatively low ionizing ability under electrospray conditions. In addition, high-performance liquid chromatography (HPLC) method doesn't also allow to control the reaction due to the absence of groups glowing in ultraviolet light.

Methods

A chloroacetyl chloride was selected as the halogen derivative of methylsulfamide, the synthesis method of which was reproduced according to patent WO2017029594A1 [3] (Fig. 1). ¹H NMR spectra were recorded in DMSO-d₆ on a Bruker Avance III 400 UltraShield Plus NMR spectrometer (400 MHz ¹H operating frequency). The signals of residual protons of the solvent were used as a standard. Sample preparation: 2 mg of reaction mass were diluted with 0.5 ml of DMSO-d₆.

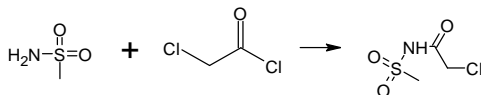


Figure 1. Synthesis of 2-chloro-N-(methylsulfonyl)acetamide

Results and discussion

The approbation of these methodics showed a low yield of the desired product. That's why new synthesis conditions were selected. The NMR control method allowed us to select 2-chloro-N-(methylsulfonyl)acetamide as an intermediate of the reaction and to develop an optimal method for its synthesis. (Fig. 2).

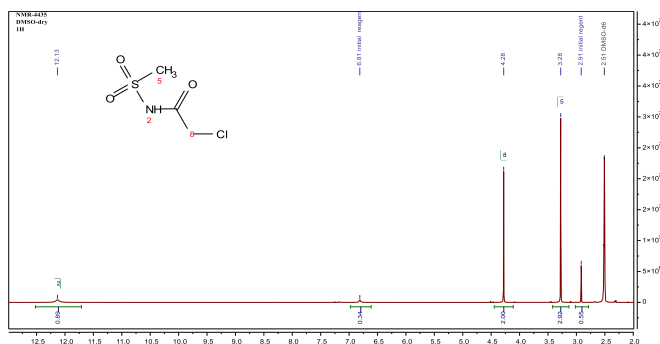


Figure 2. ^1H NMR-spectrum reaction mass

2-chloro-N-(methylsulfonyl)acetamide was detected in the ^1H NMR spectrum as signals: δ 12.13 (s, 1H), 4.28 (s, 2H), 3.28 (s, 3H) (Fig. 2).

Based on the ratio of the areas of the signal peaks in the NMR-spectrum of the reaction mass, a preliminary assessment of the conversion of the initial methylsulfamide was carried out, which was 84%. The unreacted methylsulfamide (16%) was detected in the ^1H NMR spectrum as two different signals: δ 6.81 (s) and δ 2.91 (s) (Fig. 2). The attribution of these signals to the unreacted methylsulfamide was confirmed by comparing the NMR spectra of the reaction mass and of the initial methylsulfamide (Fig 3).

Thus, 2-chloro-N-(methylsulfonyl)acetamide, an intermediate of selexipag synthesis, was obtained with a purity of 84% using the NMR method control.

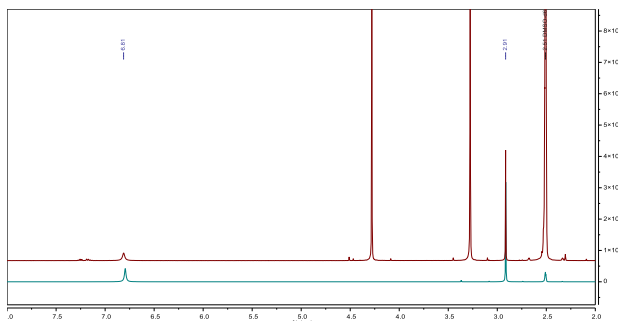


Figure 3. Stack of ^1H NMR-spectra of reaction mass (upper spectrum) and initial methylsulfamide (lower spectrum)

References

1. Boucly A, Gerges C, Savale L, Jaïs X, Jevnikar M, Montani D, Sitbon O, Humbert M. Pulmonary arterial hypertension. *Presse Med.* 2023 Sep;52(3):104168. doi: 10.1016/j.lpm.2023.104168. Epub 2023 Jul 28. PMID: 37516248.
2. Ilyin N. V., Ivanov K. I., Martynyuk T. V. New treatment options for pulmonary arterial hypertension-the first selective prostacyclin receptor agonist Selexipag //Cardiovascular therapy and prevention. – 2019. – Vol. 18. – No. 6. – P. 80-87.
3. S. Oruganti, B. Kandagatla, V. Hareshwar Dahanukar et al. Patent WO no. WO2017029594A1, 2017.

The optimization of the conditions of 2D NMR spectra registration for the analysis of thermoplastic organic compounds in molten state

Ilya A. Grishanovich, Semyon L. Shestakov, Alexander Yu. Kozhevnikov

Core facility center "Arktika", Northern (Arctic) federal university named after M.V. Lomonosov, Arkhangelsk city, Russian Federation

E-mail: i.grishanovich@narfu.ru

The data of one-dimensional NMR spectroscopy (^1H , ^{13}C) are often not enough for the certain identification of the chemical structure of thermoplastic organic compounds [1], in addition, the prolonged time of ^{13}C spectra registration lowers the method efficiency. Two-dimensional experiments (HSQC, HMBC) can complement the obtained data, but their use for insoluble samples or systems with low concentration of new-formed bonds is also limited, because the signals are either absent or with extremely low intensity. The application of two-dimensional spectroscopy for solid-state samples, usually studied with CP/MAS method, are complicated with technical issues, caused by necessity of sample spinning and low resolution of solid-state NMR spectra [2].

In this work, we offer the approach, based on the transition of sample into molten state directly in NMR sample tube. In case of model systems with simple structures (L-lactide), method allowed to register HSQC spectra successfully at 25 °C. However, the signals in HSQC spectra were not observed for more complex systems (polylactide), which can be related to appearance of cavities in the sample volume during the melt stiffening.

The setting of temperature mode, matching with melting point of the sample, which was obtained during co-polymerization of lactide in presence of phenol and maleic anhydride (84 °C), allowed to significantly reduce the contribution of anisotropic interactions (dipole and quadruple) due to increase of molecules mobility, which led to lines narrowing and improve of spectrum resolution (fig. 1).

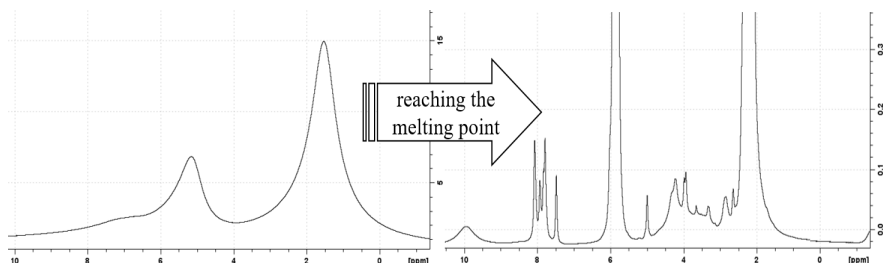


Figure 1. The change of ^1H spectrum after reaching of the sample melting point.

After the registration of ^1H -NMR spectrum at the melting temperature of the lactide copolymer sample we managed to obtain the perceptible signals in HSQC spectrum, which is presented at fig. 2.

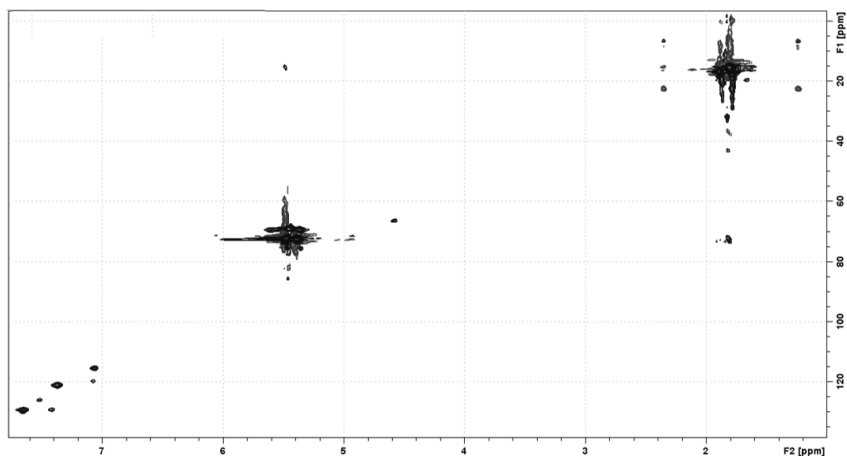


Figure 2. HSQC spectrum of sample of lactide copolymer at 84 °C.

The proposed method can allow to analyze the structure of complex organic systems, where the application of usual approaches to the 2D NMR spectra registration is limited because of, for example, technical issues or necessity to keep the initial structure without solvent influence.

References

1. Brandolini A. J. Nuclear Magnetic Resonance of Polymeric Materials //Handbook of Plastics Analysis. – CRC Press, 2003. – C. 385-488.
2. Zhang R., Chen W., Miyoshi T. Elucidations of Structure and Molecular Dynamics of Complex Polymers by State-of-the-Art Solid-State NMR Spectroscopy //Macromolecules. – 2024. – T. 57. – №. 5. – C. 1893-1918.

Investigation of the magnonic nonlinear phase shifter based on forward volume spin waves

Roman V. Haponchik, Alexey B. Ustinov

Department of Physical Electronics and Technology, St.Petersburg Electrotechnical University, St.Petersburg, -197376 Russia

E-mail: rvgaonchik@etu.ru

Introduction

Recent years, interest in studying of the nonlinear properties of spin waves (SW) propagating in magnonic crystals (MC) has increased. Such nonlinear phenomena as envelope solitons [1] and nonlinear frequency shift of intense SW [2] have been investigated. However, a number of important issues remain unexplored. These include the problems of investigating of the nonlinear phase shift of a small-amplitude SW induced by a large-amplitude pump SW propagating in MC at different frequencies, taking into account the nonlinear damping of the pump SW. The interest in the study of such effect is due to the need to develop magnonic logic circuits in which the output SW signal of the previous logic element would control the SW signal of the subsequent logic element [3].

Theoretical model

The purpose of this work is to develop a theoretical model and an experimental prototype of a nonlinear phase shifter (NPS), the operating principle of which is based on the effect of an induced nonlinear phase shift of forward volume SW propagating in a one-dimensional MC.

To do this we developed original theoretical model. Since the nonlinear phase shift of small-amplitude SW depends on the evolution of the amplitude of large-amplitude pump SW during their simultaneous propagation in the MC, we first derived formulas for the nonlinear damping of SW in a regular magnetic film waveguide. To describe the propagation of two nonlinearly coupled waves, the system of modified nonlinear Ginzburg-Landau equations was used:

$$\begin{cases} i \frac{dU_1}{dt} + iV_{g1} \frac{dU_1}{dz} - N_{11}|U_1|^2 U_1 - N_{12}|U_2|^2 U_1 = \\ = -i(\eta_1 + v_{11}|U_1|^2 + v_{12}|U_1|^4)U_1; \\ i \frac{dU_2}{dt} + iV_{g2} \frac{dU_2}{dz} - N_{21}|U_1|^2 U_2 - N_{22}|U_2|^2 U_2 = \\ = -i(\eta_2 + v_{21}|U_2|^2 + v_{22}|U_2|^4)U_2. \end{cases} \quad (1)$$

here v_{11} and v_{21} – third order decrements of nonlinear damping, v_{12} and v_{22} – fifth order decrements of nonlinear damping for the first and second SW respectively, N_{11} and N_{22} – nonlinear self-interaction coefficients describing the effect of the amplitude of the first and second SW on its nonlinear frequency shift, N_{11} and N_{21} – nonlinear coefficients describing the effect of the amplitude of the second and first SW on the nonlinear frequency shift of the first and second SW respectively.

Solving the system of nonlinear Ginzburg-Landau equations (1) will give us an expression describing the dependence of the Fourier-amplitude of the first (operating) and second (pump) spin waves $U_{\omega 1,2}(z)$ on the coordinate. The solution is very cumbersome, so we will not present it here. Detailed expressions are given in the paper [4]. An expression that allows one to calculate the induced nonlinear phase shift of the operating SW taking into account nonlinear damping of the pump SW written as follow:

$$\varphi_{1NL} = -\frac{1}{V_{g1}} \int_0^z (N_{11}U_{\omega 1}^2(z) + N_{12}U_{\omega 2}^2(z)) dz, \quad (2)$$

here V_{g1} – group velocity of the operating SW. Note, that $\varphi_{1NL} = \varphi_{SNL} + \varphi_{INL}$, here φ_{SNL} – intrinsic nonlinear phase shift, φ_{INL} – nonlinear phase shift induced by the pump SW. The phase shift φ_{SNL} determines the first term in (2), and φ_{INL} determines the second term.

At the last stage, additional attenuation of the pump wave due to Bragg reflection during its propagation at the frequencies of the band gaps of the MC was taken into account. The transmission coefficient describing reflection of SW from a periodic structure was derived using the coupled wave method [5]. For this purpose, the MC transmission coefficient was rewritten as a product of several terms describing the nonlinear damping of SW and the attenuation associated with their reflection:

$$H_{MC}(\omega) = H_{NLSW}(\omega)H_R(\omega), \quad (3)$$

here $H_{NLSW}(\omega)$ and $H_R(\omega)$ – transmission coefficients describing the nonlinear damping of SW and the attenuation of SW associated with Bragg reflection in MC respectively. Afterwards, having written down the overall transmission coefficient $H_{MC}(\omega)$, we will be able to express the amplitude of the operating signal as $U_1^2(z) = H_{MC}(\omega)U_{01}$. The coefficient $H_R(\omega)$ is equal to “1” outside the frequencies of the MC band gaps, therefore the propagation of SW outside these zones is described using the usual model. In the case of SW propagation at bandgap frequencies, the transmission coefficient becomes less than “1” due to its reflection from the periodic structure.

Experimental setup

An experimental prototype of a magnonic NPS (Fig. 1) was fabricated with using a MC made of 5.7 μm thick yttrium-iron-garnet (YIG) film (1). The 10 grooves (2) with a depth of 0.1 μm and a period of $\Lambda = 300 \mu\text{m}$ were etched on the surface of the film. The width of the grooves was 100 μm . Microstrip antennas (3) with a length of 2 mm and a width of 50 μm were used to excite and receive forward volume SW. The antennas were positioned directly on the MC surface, and the distance between them was $d = 3 \text{ mm}$. Microstrip lines (4) with a characteristic impedance of 50 Ohm were used to supply a microwave signal to the input antenna and receive the transmitted microwave signal from the output antenna. The saturation magnetization of the selected YIG-film was 1400 Oe, and the magnitude of the external magnetic field was 2500 Oe. The half-width of the ferromagnetic resonance curve was 0.6 Oe.

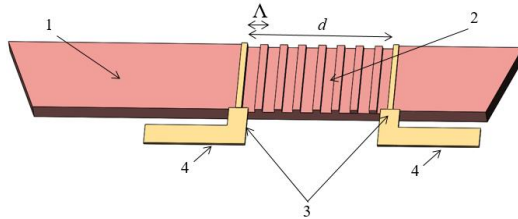


Fig. 1. Experimental prototype of the magnonic NPS

The measurements were carried out in two stages. At the first stage, the input and output microstrip lines of the experimental prototype were connected directly to a vector network analyzer (VNA). The frequency response and the phase-frequency characteristic of the studied prototype were measured. At the second stage, measurements of the induced nonlinear phase shift of SW in MC were carried out. To do this, the experimental prototype was included in the experimental setup. The VNA was switched to the phase versus time measurement mode. In this mode, the VNA generated a continuous low-power microwave signal. At the same time, the microwave generator generated a pulsed microwave signal, further amplified by an amplifier. Thus, the continuous operating and relatively intense pump

pulses were simultaneously excited in the YIG-film. As a result, the dependence of the phase of the operating microwave signal on time was observed on the screen of the VNA.

Figure 2 (a) shows the frequency response of the NPS prototype. Figures 2 (b, c) shows the induced nonlinear phase shift of the operating SW measured for two frequencies of the operating signal located between the band gaps of the MC versus pump signal power. Arrows in Figure 2 (a) shows operating signal frequencies f_s , as well as pump signal frequencies f_{BG} . The operating signal power was $10 \mu\text{W}$.

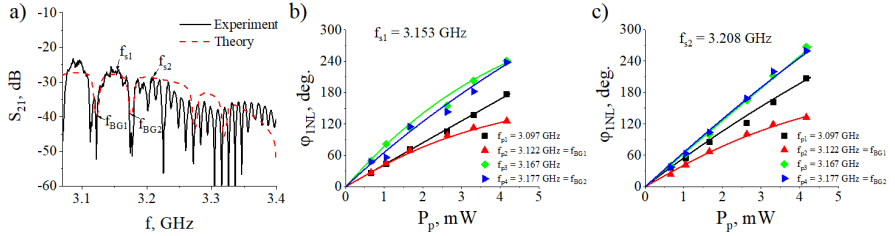


Fig. 2. Frequency response of the NPS based on forward volume SW (a), theoretical (curves) and experimental (symbols) characteristics of the induced nonlinear phase shifts of the operating SW versus pump SW power for two operating SW frequencies f_s and four pump SW frequencies f_p (b) and (c).

Conclusion

The results of the investigation showed that our model is in the good agreement with the experimental data. The model can be used to describe the characteristics of the magnonic NPS's based on the forward volume SW for their further use in magnonic logic circuits.

Acknowledgements

The work was supported in part by the Ministry of Science and Higher Education of Russian (Grant № FSEE-2025-0008).

References

1. M.A. Morozova, et. al. – Phys. Rev. B, 110, 104408 (2024).
2. A.V. Bagautdinov, A.B. Ustinov. – Tech. Phys. Lett. 13, 16-20 (in Russian) (2023).
3. A. Mahmoud, F.Vanderveken, C. Adelman. – AIP Adv. 96, 035119 (2020).
4. A.B. Ustinov, N.A. Kuznetsov, R.V. Haponchyk. – Appl. Phys. Lett. 119, 192405 (2021).
5. A. Yariv. – IEEE J. Quant. El. QE-9, 919-933 (1973).

Effect of palladium(II) on NMR spectra of coordinated semicarbazones

Artem S. Igonin¹, Ekaterina I. Isaeva¹, Ivan A. Godovikov², Ruslan I. Baichurin¹

¹Faculty of Chemistry, Herzen State Pedagogical University, Saint-Petersburg, Russian Federation

²A. N. Nesmeyanov Institute of Organoelement Compounds of Russian Academy of Sciences, Moscow, Russian Federation

E-mail: as@igonin-02.ru

Introduction

Palladium(II) (¹⁰⁵Pd) complexes are widely used in a variety of fields, including catalysis and the pharmaceutical industry, among others [1]. Due to this, the challenge of identifying and characterizing these compounds using NMR spectroscopy, as well as understanding the effect of the ¹⁰⁵Pd core on the nature of the spectra of these systems, remains relevant.

The experimental basis of the study

We have synthesized several dimeric coordination complexes of palladium (II) with semicarbazone ligands [(PdL¹⁻⁴)₂Cl]. The synthesis involved the reaction of a palladium precursor, K₂PdCl₄, with L¹-L⁴ semicarbazones followed by formation of a palladacycle (L¹-L³) or additional coordination of the phenolic hydroxyl group (L⁴), as shown in Figure 1.

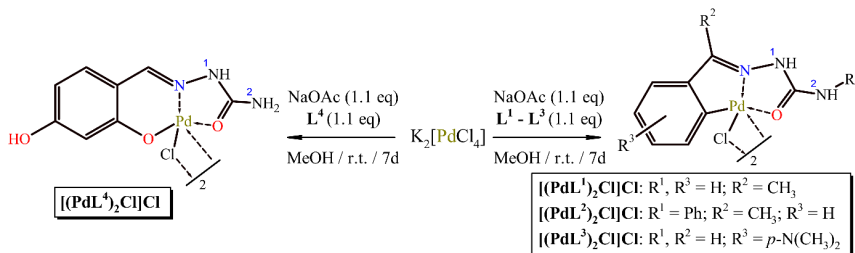


Figure 1. General scheme of synthesis and structure of the obtained complexes

The compounds were studied using NMR spectroscopy using Jeol ECX400A spectrometer with an operating frequency of 399.78 (¹H) and 100.53 (¹³C) MHz ($[(\text{PdL}^1)_2\text{Cl}]\text{Cl}$, $[(\text{PdL}^2)_2\text{Cl}]\text{Cl}$) and on Bruker Avance IIIITM HD 500 MHz with an operating frequency of 500.13 (¹H) and 125.77 (¹³C) MHz ($[(\text{PdL}^3)_2\text{Cl}]\text{Cl}$, $[(\text{PdL}^4)_2\text{Cl}]\text{Cl}$) in DMSO-*d*₆ at 25°C.

The influence of palladium(II)

The origins of the challenging interpretation

As is well known, the primary challenges in analyzing the ¹H and ¹³C NMR spectra of ¹⁰⁵Pd compounds stem not only from the frequent presence of various paramagnetic impurities in samples, which can sometimes lead to significant line broadening of the spectra, but also from spin-spin interactions between the ¹H and ¹³C nuclei in the product structure and the quadrupole moment of the palladium nuclei ($Q = 66 \text{ fm}^2$, $I = 5/2$, $\gamma = -1.23 \cdot 10^7 \text{ rad s}^{-1} \text{ T}^{-1}$) [2, 3] can also cause serious distortions in the spectral pattern.

Interpretation of the spectra of complexes $[(\text{PdL}^1)_2\text{Cl}]\text{Cl}$ & $[(\text{PdL}^2)_2\text{Cl}]\text{Cl}$

The main pattern observed in the analysis of the spectra for the synthesized compounds is a marked broadening of signals in the ^1H NMR spectrum (Table 1).

Table 1. ^1H NMR spectra of L^1 , L^2 & $[(\text{PdL}^1)_2\text{Cl}]\text{Cl}$, $[(\text{PdL}^2)_2\text{Cl}]\text{Cl}$

Compound	NMR spectra, δ , ppm., DMSO- d_6			
	CH_3	H^a (H^m) [H^p]	H^{a*} (H^m) [*] [H^p] [*]	N^1H (N^2H_2) [N^2H]
L^1	2.15 s	7.79 d (7.31 – 7.33 m) [7.31 – 7.33 m]		9.30 s (6.45 s) [-]
$[(\text{PdL}^1)_2\text{Cl}]\text{Cl}$	2.18 s	6.38 – 7.50 m		10.27 w. s (6.38 – 7.50 m) [-]
L^2	2.24 s	7.87 – 7.89 m (7.37 – 7.39 m) [7.37 – 7.39 m]	7.61 d (7.27 – 7.29 m) [7.00 t]	9.76 s (-) [8.82 s]
$[(\text{PdL}^2)_2\text{Cl}]\text{Cl}$	2.28 s	6.99 m 7.24 – 7.28 m 7.43 – 7.44 m 7.9 m	6.99 m 7.24 – 7.28 m 7.43 – 7.44 m 7.9 m	9.31 w. s 9.75 w. s (-) [8.95 s]

In particular, in the compound $[(\text{PdL}^1)_2\text{Cl}]\text{Cl}$ signals of the amino group N^2H_2 and the benzene ring are so broadened that they "merge" into one composite multiplet at 6.38 – 7.50 ppm. This fact may also be facilitated by some weak-field shift in the signal of the protons of this amino group caused by the deshielding of the electron density of the metal center during complex formation.

However, it is worth noting that, for coordination compounds of ^{105}Pd , spectra with normal, non-broadened signals have been observed, despite the significant quadrupole moment of ^{105}Pd . The investigation of complex compounds $(\text{PdL}^{1-2})_2\text{Cl}$ by mass-spectrometry has revealed their dimeric nature. This suggests that the broadened signals in the spectra of the complexes we obtained are due to their binuclear structure, as well as possibly the paramagnetism of palladium compounds that may be present as impurities due to partial intramolecular reduction in DMSO. On the dimeric nature of $[(\text{PdL}^2)_2\text{Cl}]\text{Cl}$ also indicates the presence of two signals at 9.31 and 9.75 ppm in the ^1H NMR spectra, corresponding to protons of the N^1H amino groups in different dimeric fragments. This can be explained by one of the amino groups acting as a hydrogen bond donor in a dimeric molecule, with a chloride ion coordinating to its proton [5], thus making the amino groups non-equivalent and manifesting as two signals in the spectrum.

The increase in the number of signals in the ^{13}C NMR spectrum is largely due to the removal of the magnetic equivalence of carbon atoms in the benzene ring of the semicarbazone during palladium coordination, as well as spin-spin interaction with the ^{105}Pd nucleus. In this case, a characteristic shift occurs in the region of the weak field for signals C^1 and C^2 of the carbon atoms of the benzene ring of the semicarbazone, due to the formation of a metallocycle. It is also worth noting that the formation of a metallocycle is pronounced in the ^1H - ^{13}C -HMQC spectrum $[(\text{PdL}^1)_2\text{Cl}]\text{Cl}$, where the fourth cross-peak appears in the region of aromatic protons and carbon atoms, due to the removal of magnetic equivalence from the atoms of the benzene ring, but the fifth cross peak does not appear due to the substitution of a proton in the second position with a ^{105}Pd atom.

Interpretation of the spectra of complexes $[(\text{PdL}^3)\text{Cl}]\text{Cl}$ & $[(\text{PdL}^4)\text{Cl}]\text{Cl}$

The effect of the inclusion of additional donor functional groups ($4\text{-N}(\text{CH}_3)_2$ (L^3), $2,4\text{-OH}$ (L^4)) in the ligand structure on the spectral features of ^{105}Pd complex compounds has been investigated. Despite evidence of a similar dimeric structure (in particular, by the integral intensities of ^1H NMR spectra and an increase in the number of signals in ^{13}C NMR spectra), the signals remain un-broadened. At the same time, the number of signals in the proton spectra of both complexes increases significantly, probably due to the spin-spin interaction of protons with ^{105}Pd , which can be demonstrated by the example of $[(\text{PdL}^3)_2\text{Cl}]\text{Cl}$ (fig. 2).

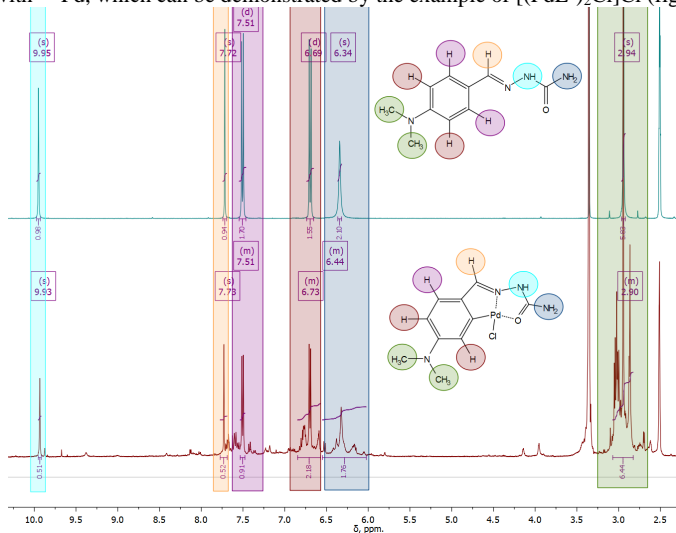


Figure 2. Spectra of compounds L^3 & $[(\text{PdL}^3)_2\text{Cl}]\text{Cl}$

Thus, it can be concluded that the introduction of additional donor functional groups into the structures of dimeric ^{105}Pd complexes with semicarbazones leads to a levelling of signal broadening in the proton spectrum, however, it contributes to a greater manifestation of the spin-spin interaction of protons with ^{105}Pd .

References

1. R. Aggarwal, J. Takkar, R. Bala, et. al. – J. Mol. Struct., 1329, 141410 (2025).
2. I. A. Mir, Q. U. Ain, T. Qadir, et. al. – J. Mol. Struct., 1295, 136216, (2024).
3. R. K. Harris, E. D. Becker, S. M. C. de Menezes, et. al. – Solid State Nucl. Magn. Reson., 22(4), 458-483 (2002).
4. Thomas J. N. Hooper, Thomas A. Partridge, Gregory J. Rees, et. al. – Phys. Chem. Chem. Phys., 41 (2018).
5. G. Kurpik, A. Walczak, M. Gołdyn, et. al. – Inorg. Chem., 61(35), 14019–14029 (2022).
6. O. V. Khromova, M. A. Emelyanov, A. F. Smol'yakov, et. al. – Inorg. Chem., 61(14), 5512–5523 (2022).

Features of the study of the pore space of the core by the method of nuclear magnetic resonance

Dmitry Ivanov¹, Vladimir Skirda¹

¹Institute of Physics, Kazan (Volga region) Federal University

E-mail: f.ma.dima@mail.ru

Introduction

Many processes of interest to industry and society are associated with the presence of liquids in a porous medium. Biopolymers, catalysts, native and artificially created membranes – most of the materials that surround us are porous. One of the areas in the study of porous materials is rocks – cores. Today, there is an extensive list of classical methods [1] that can be used to characterize the porous space of a core, however, in most cases, their use is associated with the need to violate the integrity of the sample. In this regard, the non-invasive method of nuclear magnetic resonance (NMR) has been widely used in oil field geology and geophysics in recent decades [2]. In this paper, we will demonstrate some features that need to be paid attention to when conducting studies of the porous space of a core using the NMR method.

Materials and methods

Atlantic sal NMR studies were performed on a dolomite core sample. To determine the open porosity, the core sample, previously dried to a constant mass, was saturated with a proton-containing fluid - water. According to the results of preliminary tests, the open porosity of the core is ~ 5%. For a number of tests, the core sample was saturated with an aqueous solution of copper sulfate.

To study the pore space of the core, a comprehensive approach was used based on the analysis of experimental data from a number of NMR techniques:

1. Spin-spin relaxation. Relaxation attenuation was recorded using a CPMG pulse sequence;
2. NMR cryoporometry. Based on the data obtained by the Solid-echo pulse technique, the dependence of the fraction of the solid-state component of the NMR signal (p_s) on temperature is constructed;
3. DDIF. Using internal magnetic field gradients for spatial localization of diffusing molecules.

Results

Well The non-exponential relaxation decays obtained by the KPMG method were presented in the form of a spectrum (Figure 1a) of relaxation times using the original program “Spectrum of spin-spin relaxation times” developed at the Department of Physics of Molecular Systems of the Institute of Physics of Kazan Federal University. According to [3], the obtained spectrum of spin-spin relaxation times can be formally presented as a pore size distribution (Figure 1b) by applying the following relationship:

$$\frac{3}{r} = \frac{1}{T_2\rho}$$

where ρ is the relaxivity value, which essentially determines the degree of interaction of liquid molecules with the pore surface and can depend on many, a priori unknown, factors. Based on literary sources, for example [4,5], devoted to the study of dolomite cores, $\rho \approx 1 \text{ } \mu\text{m/ms}$ was adopted as a trial value for the relaxation characteristic.

Figure 1 shows the spectrum of spin-spin relaxation times, as well as the pore size distribution.

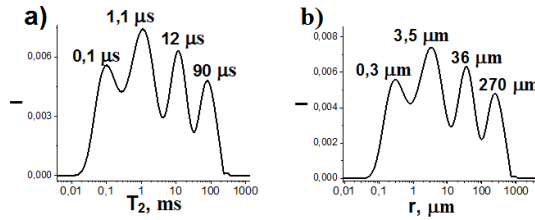


Figure 1. a) Differential spectrum of spin-spin relaxation times for a core sample saturated with water; b) Pore size distribution. Each peak is labeled with the average spin-spin relaxation time (a) and the average pore size (b)

Thus, within the framework of the accepted assumptions, at least four pore size regions with a minimum of $\sim 0.3 \mu\text{m}$ and a maximum of $\sim 270 \mu\text{m}$ were recorded in the core sample under study. Usually, in most studies based only on the analysis of relaxation time spectra, the study is completed at this stage.

Nevertheless, simple calculations indicate some inconsistencies in the obtained results. For example, the estimate of the pore size of $270 \mu\text{m}$, made for $T_{2\text{max}} \approx 90 \mu\text{s}$ at $\rho = 1 \mu\text{m/ms}$, seems implausible, since the time required to reach the corresponding boundaries of a pore with such dimensions by the diffusion method is about 4.5 sec, which is significantly more than 90 ms.

In this regard, let us consider the results of additional studies. One of the factors that significantly influences the values of relaxation times, and, consequently, the values of the calculated pore sizes, may be associated with the influence of paramagnetic impurities, which may be located not only on the pore surface, but also dissolved in the fluid itself. Therefore, let us consider the influence of the copper sulphate concentration in the saturating fluid on the recorded NMR characteristics of the fluid in the pore space, namely, on the maximum value of the relaxation time in the T_2 time spectrum (Fig. 2).

As can be seen from Figure 2, an increase in the copper sulphate concentration to 1% has virtually no effect on the $T_{2\text{max}}$ times, although for free water in the same concentration range the T_2 time decreases by about 30 times. Thus, the presented results give reason to believe that the maximum value of $T_{2\text{max}} \approx 90 \text{ ms}$ found above is indeed associated with the characteristics of the porous structure and, therefore, characterizes a certain pore size. As a reasonable estimate, we can take the value of the diffusion range of water molecules with a self-diffusion coefficient equal to $2.7 \cdot 10^{-9} \text{ m}^2/\text{s}$ for a time of $T_{2\text{max}} \approx 90 \text{ ms}$. The calculated value of the maximum pore size in the core obtained in this way turns out to be approximately equal to only $36 \mu\text{m}$. Interestingly, approximately the same value ($38 \mu\text{m}$) was recorded by us experimentally using the DDIF technique [6], which is by definition sensitive to the maximum values in the pore size distribution. Such discrepancy between the results obtained from the analysis of the relaxation time spectra and the data of other NMR techniques may be due to the fact that the accepted value of $\rho = 1 \mu\text{m/ms}$, taken from the literature as typical for dolomites, does not correspond to the sample we studied. In order to match the value of the maximum pore size determined from the relaxation time spectrum with the calculation data and experimental results of the DDIF technique, it was necessary to take $\rho = 0.14 \mu\text{m/ms}$, which is almost an order of magnitude less than the value recommended for dolomites in the literature. Then, the pore sizes determined from the relaxation time spectrum data (Fig. 1) at $\rho = 0.14 \mu\text{m/ms}$ will take the following values, respectively: 0.04; 0.49; 5 and $38 \mu\text{m}$. Note that the pore size value of $0.04 \mu\text{m}$ in this case is in good agreement with the results obtained by the NMR cryoporometry method (Fig. 3).

The differential spectrum shown in Figure 3 demonstrates the presence of two regions of different sizes: 2 and 33 nm. The size of the 2 nm limits is classified as micropores.

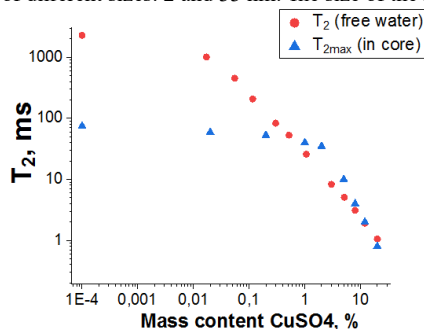


Figure 2. Dependence of spin-spin relaxation times on the concentration of copper sulfate. The behavior of the relaxation time of water with copper sulfate in the volume (T_2) is indicated by round symbols, and the value of the longest transverse relaxation time for water molecules in the core (T_{2max}) is indicated by triangular symbols

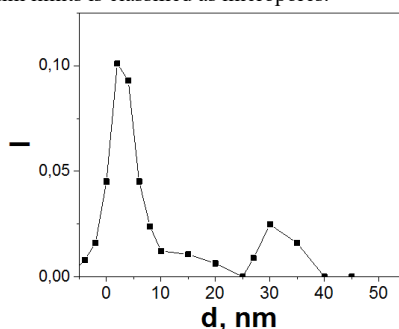


Figure 3. Pore size distribution spectrum obtained from NMR cryoporometry data

Thus, the minimum size of 0.04 μm obtained from NMR relaxometry is close to one of the sizes (33 nm) obtained in NMR cryoporometry, and the maximum size of 38 μm practically coincided with the estimate of 36 μm in the DDif method.

Thus, this work demonstrates the importance of the simultaneous use of complementary NMR methods for the correct analysis of the characteristics of the porous structure of the core. At the same time, it is shown that based on the comparison of the results, such an important characteristic of the porous material as relaxivity can be determined for each studied sample independently.

Acknowledgements

This work was funded by the subsidy allocated to Kazan Federal University for the state assignment in the sphere of scientific activities number FZSM-2023-0016.

References

1. L. M. Anovitz, D. R. Cole. Characterization and analysis of porosity and pore structures. – Rev. in Miner. and geochem., 1, 61-64 (2015).
2. M. Elsayed. A review on the applications of nuclear magnetic resonance (NMR) in the oil and gas industry: laboratory and field-scale measurements. – J. of Petr. Explor. and Prod. Techn., 12, 2747-2784 (2022).
3. J. J. Howard, W. E. Kenyon. Determination of pore size distribution in sedimentary rocks by proton nuclear magnetic resonance. – Mar. and petr. Geol., 9, 139-145 (1992).
4. R. R. Peesu. Automated Image Processing of Petrographic Thin Sections for Digital Reservoir Description: A Bridge to Correlate with Core and NMR Data. – SPE, D012S145R004 (2022).
5. H. Wang. Study on SWCC and PSD evolution of compacted loess before and after drying-wetting cycles. – Bul. of Engin. Geol. and the Envir., 5, 180-194 (2023).
6. Y. Q. Song. Determining multiple length scales in rocks. – Nature, 2406, 178-181 (2000).

Modelling localization of various statins within a POPC bilayer by molecular dynamics and metadynamics

Nataliya V. Karmanova, Aydar R. Yulmetov

Kazan Federal University, Kremlevskaya Str., 18, 420008, Kazan, Russia

E-mail: ajulmeto@kpfu.ru

Introduction

Statins are a general pharmacological group that, with the help of some of its structural parts, imitate the HMG-CoA reductase binding to HMG-CoA[1]. Statin molecules include various additional atomic groups, and the effectiveness and side effects of statins vary significantly depending on them processes occurring in the human organism are still not fully understood and there are many hypotheses about the pathway of action of statins. There are studies confirming that the depth of statin penetration into the model membrane correlates with the risk of side effects[1].

The aim of this work was to study the parameters of statins binding to a lipid bilayer based on POPC (1-palmitoyl-2-oleoyl-sn-glycero-3-phosphocholine) using the molecular dynamics (MD) and metadynamics methods. The objects of the study were two lipophilic statins — atorvastatin and pitavastatin and two hydrophilic statins — rosuvastatin and pravastatin. Studies of the binding of these statins to lipid bilayers based on POPC were previously carried out using the NMR method [2,3].

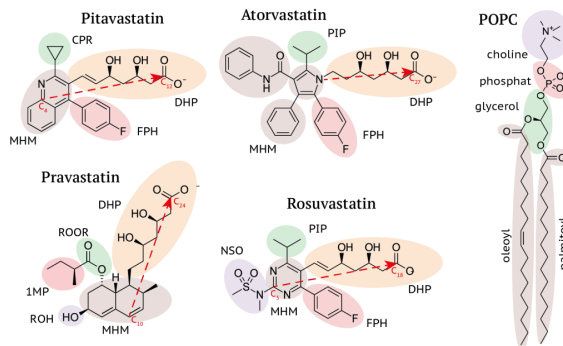


Figure 1. Chemical structures of compounds studied. Arrows in red are the directors used in the orientation analysis. Atomic groups: the dihydroxy pentanoate group (DHP), the ester group (ROOR), the 1-methylpropyl group (1MP), the fluorophenyl (FPH), the hydroxyl group (ROH), the isopropyl group (PIP), the cyclopropyl group (CPR), the sulfanamide group (NSO) and the main hydrophobic moiety (MHM).

Methods

All systems contained 100 lipids per layer and about 55 water molecules per lipid. Calculations were performed with the full-atom CHARMM36 force field after energy minimization and NPT NVT equilibration. To analyze the MD results and subsequent calculations using metadynamics, it is necessary to specify collective variables (CV). In this study, such parameters were the position of the statin relative to the bilayer center d_z and the tilt angle θ of the statin to the bilayer normal. To determine the tilt angle, it is necessary to specify a vector in the statin molecule. For example, for atorvastatin, this was the vector directed from the nitrogen in N_1 to C_{27} . The selected vectors for each statin are presented in fig. 1. The MD trajectories were used as starting points for the metadynamics calculations. The

metadynamics simulations were performed using the GROMACS program with PLUMED plugin[4]. The calculations were performed in parallel in 36 linked replicas, calculated on different processor cores, for 100 ns each. The total simulation time for each statin can be estimated at $36 \times 100 = 3600$ ns.

Results

Simulations of single statin binding to POPC bilayer

Pitavastatin is incorporated into the lipid bilayer quite rapidly. MD during the first 30 ns led to spontaneous "immersion" of the statin into the membrane (Fig. 2). The simulation was continued, but no changes occurred beyond small fluctuations, and it can be assumed that the statin is firmly fixed in the membrane.

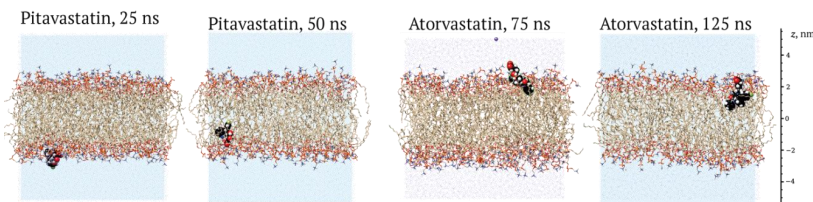


Figure 2. Penetration of statins into the POPC bilayer.

The results for pravastatin were different, this molecule was unable to penetrate the bilayer, and pravastatin was at some distance (approximately 3.25 ± 0.5 nm) from the model membrane throughout the simulation. Rosuvastatin showed similar behavior. Simulation of atorvastatin for about 70 ns did not result in binding of atorvastatin to the bilayer, it tended to be at the edges of the cell, but after 75 ns, the statin was first localized shallowly at the surface of the bilayer, slightly immersed in it, and then quickly immersed to a distance of about 1.5 nm from the center.

Modeling the interaction of statins with a bilayer using metadynamics

We obtained a one-dimensional graph for the dependence of energy on the coordinate z of the statin and a two-dimensional map of energy on the tilt angle and coordinate.

Based on the obtained free energy surface (FES) profile (Fig. 3), it can be confidently assumed that the immersion of pitavastatin into the bilayer will be a fast process (there are no barriers at the bilayer/water interface), and the presence of the molecule in the bilayer is stable. The energy profiles for rosuvastatin, atorvastatin and pravastatin have a small potential barrier (3-5 kJ/mol) at the bilayer/water interface despite the completely different atomic groups in the composition and their overall lipophilicity. Perhaps, the cyclopropyl or quinoline groups unique to pitavastatin could reduce the barriers to penetration into the bilayer.

Simulations of 40 statin binding to POPC bilayer

The MD method was used to calculate the system of statin molecules with a bilayer (20% concentration) for each statin. The number of statins was determined by the desire to obtain the same concentration values that were in the NMR experiments of Galliulina et al. [2,3]. The simulation was carried out for 500 ns for a system of 200 phospholipids and 40 statins with the addition of $\text{Na}^+ \text{Cl}^-$ ions to a concentration of 100 mM.

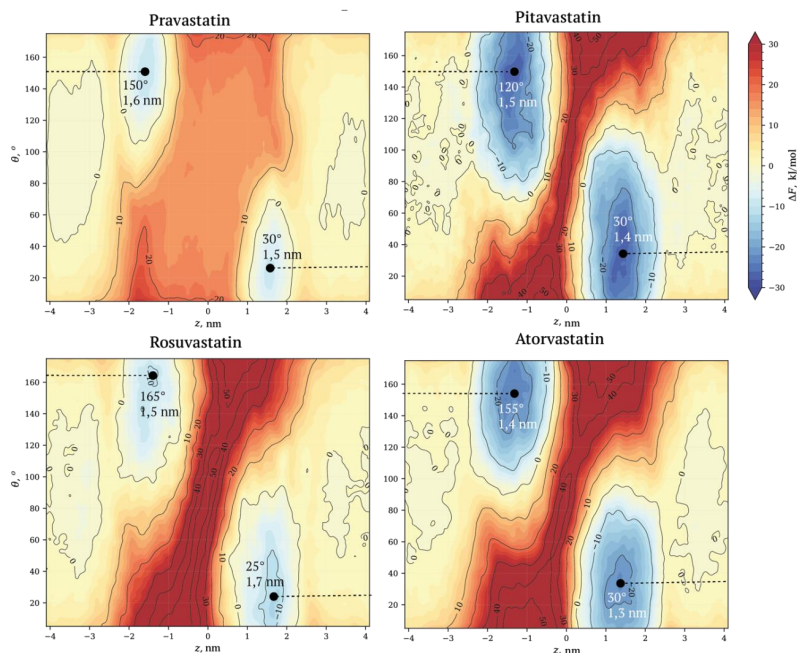


Figure 3. Free energy surface (FES) maps of pitavastatin, atorvastatin, rosuvastatin and pravastatin in a POPC bilayer.

For these systems we analyzed distributions of mass and electron density of the whole statin and its parts, as well as the bilayer and its parts, and acyl chain order parameters.

The obtained data indicate that pitavastatin is located deepest in the membrane, interacting predominantly with the hydrophobic core, atorvastatin is located slightly closer to the bilayer/solvent interface than pitavastatin and interacts with glycerol groups through its dihydroxy acid group, and pravastatin is localized near the bilayer surface, and its dihydroxy acids interact with the solvent and head groups. Rosuvastatin behaves similarly to pravastatin.

The change in bilayer parameters can be considered small for all statins — the overall decrease in ordering in fatty acids, the increase in area per lipid and the preservation of the overall membrane thickness are not sufficient to disrupt the membrane. We obtained S_{CD} data that are in agreement with the NMR experiment[2,3].

References

1. Schachter, M., *Fundamental & Clinical Pharmacology*, 2005, 19, 117-125.
2. G. Shurshalova, A. Sch. Holger, M. Fischer, D. Huster, A. V. Aganov, V. V. Klochov, *Biochemistry and Biophysics Reports*, 2021, 28, 101143.
3. Galiullina, L.F., Scheidt, H.A., Huster, D., Aganov, A., Klochov, V., *Biochimica et Biophysica Acta (BBA)-Biomembranes*, 2019, 1861 (3), 584–593.
4. Bonomi M., Branduardi D., Bussi G., Camilloni et al, *Computer Physics Communications*, 2009, 180, 1961-1972.

Modeling of spin-wave spectrum for YIG films at sub-THz frequencies

Daniil A. Khroshin, Alexey B. Ustinov

Department of Physical Electronics and Technology, Saint Petersburg Electrotechnical University "LETI", St. Petersburg, 197022, Russia

E-mail: Daniil.khroshin@gmail.com

Introduction

Nowadays, terahertz technologies are widely used in fields such as security, biomedicine, astronomy, non-destructive control and telecommunication [1,2,3]. The frequency range between 0.1 THz and 10 THz, known as the "THz gap," has been a challenging area due to the limited availability of efficient generators and detectors [4]. Currently, there are several studies proposing various approaches to fill this gap, such as designing devices based on the anisotropy of antiferromagnetic media [5-7] or utilizing Josephson junctions [8, 9], etc.

The goal of this work is to study the influence of the thickness of a ferromagnetic film on the form of dispersion characteristic of spin wave (SW) and calculate film thicknesses that would enable magnetization oscillations in the frequency range from 0.1 to 0.5 THz.

Statement of the problem and conditions

To search for spectrum in limited samples, in addition to solving Maxwell's equations with classical electrodynamic boundary conditions (BC), it's necessary take into account additional BC formulated by Rado and Weertman [11], for the Landau-Lifshitz equation.

In this work two extreme cases of these BC are considered: totally pinned and totally unpinned surface spins. Dipole-exchange SW spectra were calculated using the tensor Green's functions method [12] in perturbations theory approximation [10]. The static external magnetic field is directed perpendicularly relative to the film surface. For the further calculations, the values of saturation magnetization $M = 1750$ G and the exchange constant $\alpha = 3.1 \cdot 10^{-12}$ cm² characteristic of the yttrium-iron garnet (YIG) film are used. The internal static magnetic field $H_{int} = 3500$ Oe is twice the saturation magnetization. The spectrum was calculated for the lowest SW eigen-wave.

Results

The calculations demonstrated the difference between the obtained spectra for totally pinned and totally unpinned surface spins, and showed the influence of the film thickness on the form of dispersion characteristic (Fig.1).

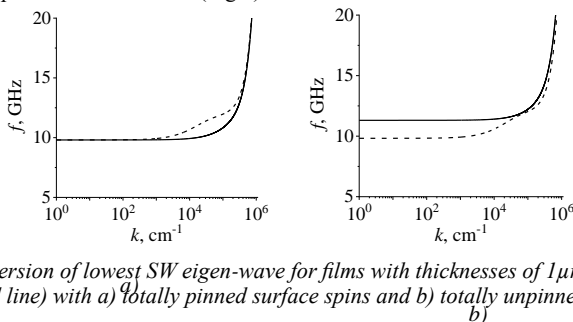


Figure 1. Dispersion of lowest SW eigen-wave for films with thicknesses of 1 μ m (dashed line), 100 nm (solid line) with a) totally pinned surface spins and b) totally unpinned surface spins

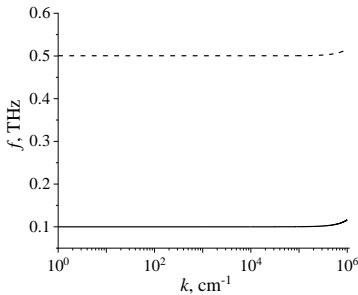


Figure 2. Dispersion of the lowest SW eigen-wave for films with thicknesses of 5.53 nm (dashed line) and 12.9 nm (solid line) with totally pinned surface spins

Conclusion

The simulation results show that to excite spin waves with a frequency above 0.1 THz, it is necessary to ensure that the film thickness is less than 12.9 nm.

Acknowledgements

The work was supported in part by the Ministry of Science and Higher Education of Russian (Grant № FSEE-2025-0008).

References

1. Leitenstrofer, A., Moskalenko, A. S., Kampfrath, T., Junichiro, K., Castro-Camus, E., Penq, K., Qureshi, N., Turchinovich, D., Tanaka, K. et al. The 2023 terahertz science and technology roadmap// Journal Phys. D: Appl. Phys. 56 (2023).
2. John F Federici et al. THz imaging and sensing for security applications — explosives, weapons and drugs // Semicond. Sci. Technol. 20 (2005).
3. Ashish Y. Pawar , Deepak D. Sonawane, Kiran B. Erande ,Deelip V. Derle. Terahertz technology and its applications// JPR Solutions: Drug invention today 5. – p.157 – 163 (2013).
4. Carlo Sirtori. Bridge for the terahertz gap. // Nature, Applied Physics, 417 – p.132 – 133 (2002).
5. A. R. Safin, E. E. Kozlova, D. V. Kalyabin and S. A. Nikitov. Detection of terahertz electromagnetic waves using conduction antiferromagnets. // Technical Physics Letters, Vol. 47, No. 11, p. 814–817 (2021).
6. A. Safin, V. Puliafito, M. Carpentieri, G. Finocchio, S. Nikitov, P. Stremoukhov, A. Kirilyuk, V. Tyberkevych and A. Slavin. Electrically tunable detector of THz-frequency signals based on an Antiferromagnet. // Appl. Phys. Lett. 117, (2020).
7. Safin, A., Nikitov, S., Kirilyuk, A., Tybekevych, V., Slavin, A. Theory of Antiferromagnet-Based Detector of Terahertz Frequency Signals// Magnetochemistry 8, 26, (2022).
8. L. Ozyuzer, A. E. Koshelev, C. Kurter et al. Emission of Coherent THz Radiation from Superconductors. // Science 318, 1291 – 1293 (2007).
9. Xiao Hu and Shi-Zeng Lin. Phase dynamics in a stack of inductively coupled intrinsic Josephson junctions and terahertz electromagnetic radiation. // Supercond. Sci. Technol. 23 (2010).
10. Kalinikos, B.A. and Slavin, A.N. Theory of dipole-exchange spin waves spectrum for ferromagnetic films with mixed exchange boundary conditions// Journal of Physics C: Solid State Physics, 19 (1986).
11. Rado, G.T. Observation of exchange interaction effects in ferromagnetics by spin wave resonance / G.T. Rado, J.R. Weertman // Phys. Rev.–V. 94, № 5. – P. 1386. (1954).
12. Vendik, O.G., Chartorizhsky, D.N. Dispersion equation for nonuniform oscillations of the magnetization in a ferromagnetic plate// J. SOV Phys. Solid State 12, №5. – p. 1538–1540 (1970).

Determination of Rotational Correlation Time of and Iridium Dihydride Complex in Aqueous Medium by Means of NMR Relaxometry with High-resolution

Alexey Kiryutin¹, Danil Markelov¹, Alexandra Yurkovskaya¹

¹International Tomography Center SB RAS, Institutskaya Str. 3A, Novosibirsk, 630090, Russia
E-mail: kalex@tomo.nsc.ru

Molecular mobility, specifically the correlation times of rotational motion in solution, is a crucial characteristic of substances, influenced by molecular size, temperature, and solvent properties. This parameter significantly affects spin relaxation times, as it determines whether the molecular motion is slow or fast relative to the Larmor frequency.[1] Field-cycling Nuclear Magnetic Resonance (NMR) relaxometry is a powerful technique for investigating molecular mobility and is applicable to a wide range of systems, including molecules in solution, polymers, molecular and liquid crystals, as well as biomolecules.[2-3] Previously, our group determined the correlation times of the neutral iridium complex [Ir(IMes)(COD)Cl] in methanol.[4] Here, COD refers to cyclooctadiene, and the structure of the IMes carbene is shown in Figure 1. This complex is one of the most widely used precatalysts in the SABRE (Signal Amplification By Reversible Exchange) method, which has proven to be an efficient and convenient approach for enhancing the NMR signal of molecules capable of reversibly binding non-covalently to an iridium hydride complex that continuously exchanges hydrogen atoms with dissolved para-hydrogen.[5-6]

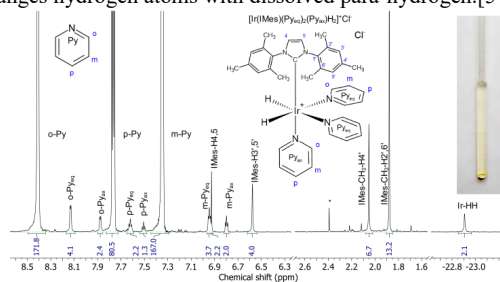


Figure 1. 700 MHz $^1\text{H}\{^{13}\text{C}\}$ NMR spectrum of $[\text{Ir}(\text{IMes})(\text{Py}_{\text{eq}})_2(\text{Py}_{\text{ax}})\text{H}_2]\text{Cl}$ detected in aqueous solution at 25 °C. Molecular structure and atom numbering is shown on inset. Signal from impurity is marked by *. Relative integrals of signals are shown under the signals.

In this study, we found that bubbling the pre-catalyst $[\text{Ir}(\text{IMes})(\text{COD})\text{Cl}]$ with para-hydrogen in an aqueous solution containing 1% pyridine led to the formation of a stable, positively charged iridium dihydride complex, $[\text{Ir}(\text{IMes})(\text{Py}_{\text{eq}})_2(\text{Py}_{\text{ax}})\text{H}_2]\text{Cl}$, featuring three pyridine ligands and the IMes carbene. Previously, the crystal structure of this complex was determined by X-ray diffraction using crystals obtained from organic solvents.[7] Additionally, the activation of the pre-catalyst in the presence of pyridine and nicotinamide was investigated by indirect detection via para-hydrogen.[8] SABRE experiments were conducted in a strong magnetic field,[9] and NMR parameters of the complex in methanol- d_4 were measured.[10] Here, we present the results of proton T_1 relaxation time measurements across a broad magnetic field range, from 0.5 T to 16.4 T, using a custom-built fast magnetic field cycling setup based on a high-resolution 700 MHz NMR spectrometer.[11]

A sample containing 1.1 mg of the pre-catalyst (synthesized according to the method described in ref. [12]), 6 μl of pyridine, 30 μl of D_2O , and 589 μl of H_2O was bubbled with hydrogen at 4 atm pressure and 45 °C in an NMR tube for 15 minutes. The color change from yellow to colorless indicated the completion of the cyclooctadiene hydrogenation reaction and

the formation of a stable iridium dihydride complex, stabilized by three pyridine molecules and the IMes carbene. The resulting solution's ^1H NMR spectrum is shown in Figure 1, with ^{13}C satellite suppression applied during FID acquisition. T_1 relaxation time measurements were performed using the inversion recovery method on a custom-built setup designed for rapid vertical displacement of the sample within the cryomagnet. The magnetic field for relaxation was determined by the sample's position relative to the center of the cryomagnet bore. The experimental protocol was as follows:

- Relaxation in a 16.4 T field for 15 s to establish initial Boltzmann polarization.
- Application of a 180-degree hard pulse to invert the magnetization of all protons.
- Rapid transfer of the sample to the selected magnetic field (within 290 ms).
- Holding the sample in the B_0 field for a variable time (0.01 to 10 s) to allow relaxation.
- Returning the sample to the detection field.
- A 150 ms delay to allow mechanical vibrations to settle.

NMR signal acquisition using excitation sculpting[13] sequences to suppress the strong H_2O solvent signal, along with ^{13}C decoupling to eliminate pyridine satellite signals. Each relaxation kinetics dataset consisted of 16 time points and was modeled using a decaying exponential function, yielding a set of T_1 values for each signal in the NMR spectra. The dependence of T_1 on the magnetic field was then plotted and fitted using equation (1), derived from the nuclear relaxation model based on local magnetic field fluctuations (Figure 2). As a result, the rotational correlation times (τ_c) for the protons in the complex were determined and are summarized in Table 1.

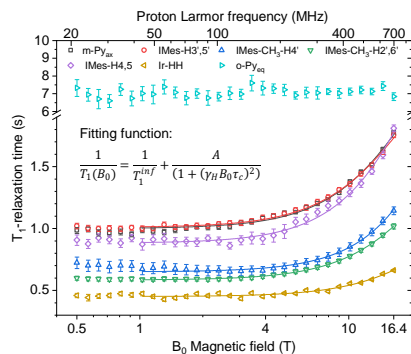


Figure 2. Proton relaxation dispersion data. (symbols) T_1 -relaxation times of individual protons, (lines) fitting curve using function (1) and correlation times from Table 1.

$$\frac{1}{T_1(B_0)} = \frac{1}{T_1^{\text{inf}}} + \frac{A}{(1 + (\gamma_H B_0 \tau_c)^2)}, \quad (1)$$

where T_1^{inf} , A , τ_c – fitting parameters, γ_H – ^1H gyromagnetic ratio

Table 1. Site specific rotational correlation times (τ_c) for the complex $\text{Ir}(\text{IMes})(\text{Py}_{\text{eq}})_2(\text{Py}_{\text{ax}}\text{H}_2)\text{Cl}$ in aqueous solution at 25 °C.

Proton	m-Py _{ax}	IMes-H4,5	IMes-H3',5'	IMes-CH ₃ -H4'	IMes-CH ₃ -H2',6'	Ir-HH	Common
τ_c (ps)	294±13	394±119	303±10	217±16	259±6	208±28	280±7

Conclusions

This study presents site-specific measurements of rotational correlation times for the $[\text{Ir}(\text{IMes})(\text{Py}_{\text{eq}})_2(\text{Py}_{\text{ax}})\text{H}_2]\text{Cl}$ complex, revealing significantly shorter values than those previously reported for its precursor, $[\text{Ir}(\text{IMes})(\text{COD})\text{Cl}]$, in methanol,[4] despite the larger size of the iridium hydride complex and the higher viscosity of the solvent (water). Variations in correlation times among different protons indicate that the molecule is not rigid.

The pronounced independence of T_1 relaxation times for the equatorial pyridine (Py_{eq}) protons is attributed to chemical exchange with free pyridine in solution, where the exchange rate exceeds the nuclear relaxation rate, consistent with data obtained in methanol.[14] In contrast, the axial pyridine (Py_{ax}) protons exhibit much shorter T_1 relaxation times, with a strong magnetic field dependence similar to that observed for the protons of the tightly bound IMes ligand.

Acknowledgements

This work was supported by the Russian Science Foundation (project #25-23-00607)

References

1. J. Kowalewski, L. Mäler, in Series in Chemical Physics, Vol. 2 (Eds.: H. J. Moore, N. D. Spencer), CRC Press Taylor & Francis Group Boca Raton, FL., 2006, p. 426 DOI: 10.1201/9781420012194
2. C. Luchinat, G. Parigi, J. Am. Chem. Soc. 2007, 129, 1055-1064. DOI: 10.1021/ja0633417
3. C. Charlier, S. N. Khan, T. Marquardsen, P. Pelupessy, V. Reiss, D. Sakellariou, G. Bodenhausen, F. Engelke, F. Ferrage, J. Am. Chem. Soc. 2013, 135, 18665-18672. DOI: 10.1021/ja409820g
4. A. N. Pravdivtsev, A. V. Yurkovskaya, P. A. Petrov, K. L. Ivanov, Z. Phys. Chem. 2017, 231, 857-865. DOI: 10.1515/zpch-2016-0849
5. R. W. Adams, J. A. Aguilar, K. D. Atkinson, M. J. Cowley, P. I. P. Elliott, S. B. Duckett, G. G. R. Green, I. G. Khazal, J. López-Serrano, D. C. Williamson, Science 2009, 323, 1708-1711. DOI: 10.1126/science.1168877
6. D. A. Barskiy, S. Knecht, A. V. Yurkovskaya, K. L. Ivanov, Prog. Nucl. Magn. Reson. Spectrosc. 2019, 114-115, 33-70. DOI: 10.1016/j.pnmrs.2019.05.005
7. M. J. Cowley, R. W. Adams, K. D. Atkinson, M. C. R. Cockett, S. B. Duckett, G. G. R. Green, J. A. B. Lohman, R. Kerssebaum, D. Kilgour, R. E. Mewis, J. Am. Chem. Soc. 2011, 133, 6134-6137. DOI: 10.1021/ja200299u
8. S. Knecht, S. Hadjiali, D. A. Barskiy, A. Pines, G. Sauer, A. S. Kiryutin, K. L. Ivanov, A. V. Yurkovskaya, G. Buntkowsky, J. Phys. Chem. Lett. 2019, 123, 16288-16293. DOI: 10.1021/acs.jpcc.9b04179
9. D. A. Barskiy, K. V. Kovtunov, I. V. Koptug, P. He, K. A. Groome, Q. A. Best, F. Shi, B. M. Goodson, R. V. Shchepin, A. M. Coffey, K. W. Waddell, E. Y. Chekmenev, J. Am. Chem. Soc. 2014, 136, 3322-3325. DOI: 10.1021/Ja501052p
10. A. S. Kiryutin, A. V. Yurkovskaya, H. Zimmermann, H.-M. Vieth, K. L. Ivanov, Magn. Reson. Chem. 2018, 56, 651-662. DOI: 10.1002/mrc.4694
11. I. V. Zhukov, A. S. Kiryutin, A. V. Yurkovskaya, Y. A. Grishin, H.-M. Vieth, K. L. Ivanov, Phys. Chem. Chem. Phys. 2018, 20, 12396-12405. DOI: 10.1039/C7CP08529J
12. I. Kownacki, M. Kubicki, K. Szubert, B. Marciniak, J. Organomet. Chem. 2008, 693, 321-328. DOI: 10.1016/j.jorganchem.2007.11.013
13. T. L. Hwang, A. J. Shaka, J. Magn. Reson. Ser. A 1995, 112, 275-279. DOI: 10.1006/jmra.1995.1047
14. O. G. Salnikov, C. D. Assaf, A. P. Yi, S. B. Duckett, E. Y. Chekmenev, J.-B. Hövener, I. V. Koptug, A. N. Pravdivtsev, Anal. Chem. 2024, 96, 11790-11799. DOI: 10.1021/acs.analchem.4c01374

NMR $^1\text{H}/^{13}\text{C}$ study of biocompatible copolymer of divinyl ether and maleic anhydride

Andrei V. Komolkin¹, Natalia P. Yevlampieva¹, Alexandr V. Sokol¹, Olga L. Alikhanova^{2,3},
Alexandr V. Serbin^{2,3}, Mikhail A. Vovk¹

¹St. Petersburg State University, St. Petersburg, 199034, Russia

²A.V. Topchiev Institute of Petrochemical Synthesis RAS, Moscow, Russia

³Research Center for Biomodulators and Drugs Systems, Health Research and Development Foundation, Moscow, Russia

E-mail: a.komolkin@spbu.ru

Introduction

The possibility and safety of synthetic polymers utilization in medicine and pharmacology today is beyond doubt. In this regard, the study of novel biocompatible high-molecular compounds and their derivatives remains in demand and relevant. Copolymer of the divinyl ether and maleic anhydride (DVEMAN) is one example of a universal compound, suitable for multiple biomedical applications due to biocompatibility, polyelectrolyte and complexation properties of its water-soluble carboxylic hydrolyzates (DIVEMA) [1-4]. Despite the fairly wide practical application of this copolymer, its structure is still not clear, especially when using the free-radical method of its synthesis. A great deal of discussion in the scientific literature, in particular, was caused by the fact that in the structure of a repeating unit of the chain it is possible to form both six-membered (pyran) bicycles (Figure 1, I) [1, 2] or five-membered (furan) bicycles (Figure 1, II) [5, 6].

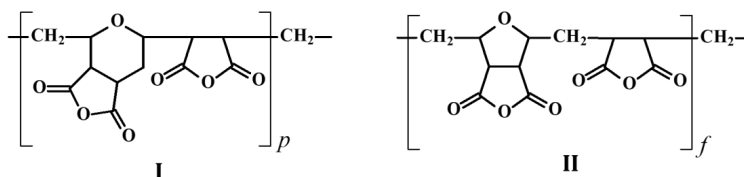


Figure 1. Chemical structure of repeat fragment of DVEMAN chain with the pyran (I) or furan bicycle (II).

As an explanation for this fact, a version of a possible dependence of the structure of the DVEMAN chain on the polarity of the solvent used for the synthesis of the copolymer was considered [1, 6, 7]. However, this version did not receive convincing evidence based on spectral data. Some studies have suggested a possible nonlinear structure of the DVEMAN chains [8].

Taking into account the practical importance of this copolymer and its derivatives for modern biomedical applications, the objective of present work was to clear the accumulated questions about the structural features of DVEMAN \rightarrow DIVEMA and the probable influence of synthesis conditions on the chain structure by means of ^1H and ^{13}C NMR spectra analysis.

Objects and methods

The objects of this investigation were the derivatives of the original DVEMAN obtained in three steps. First, the synthesis of DVEMAN was carried out in organic solvents of different polarity – chloroform (DVEMAN-1) and cyclohexanone (DVEMAN-2). Then, at the second stage, the DVEMAN samples were completely hydrolyzed and converted (third stage) into a uniform salt form. In the present work the hydrolyzed DIVEMA samples in salt form with the ratio $-\text{OH}/-\text{ONa}^+ = 1:1$ (commonly used for biomedical purposes) have been

studied (Figure 2). The stability of such DVEMAN derivatives in aqueous systems was shown earlier [3].

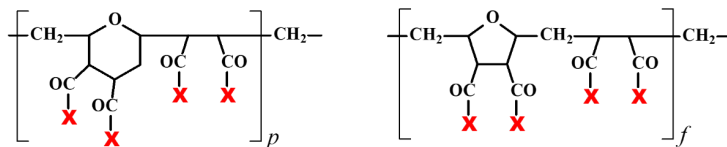


Figure 2. Chemical structure of the hydrolyzed DVEMAN derivatives of parent DVEMAN.
X = –OH or –ONa⁺

Proton and carbon-13 NMR spectra of both samples were recorded at 500 MHz and 125 MHz respectively. Samples were prepared in D₂O (99.5%). Four types of experiments were carried out: ¹H (proton spectra), ¹³C{¹H} (carbon spectra with proton decoupling), HSQC and HMBC spectra. In the figure 3, the central part proton spectra of the samples are shown. This part (chemical shifts from 2.0 to 3.75 ppm) corresponds to the hydrogen atoms of >CH– and –CH₂– groups in main chain and in pyran/furan rings (except to >CH– linked to oxygen atom).

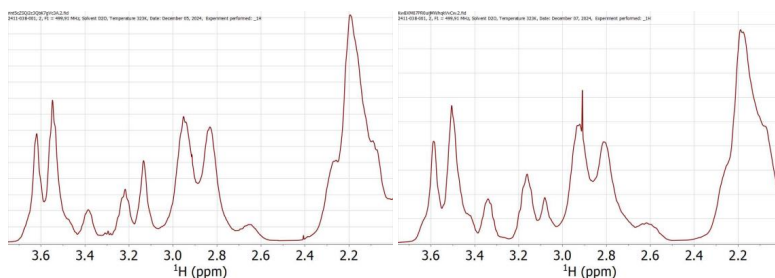


Figure 3. Central part of ¹H NMR spectra of DIVEMA-1 (left) and DIVEMA-2 (right) samples. Vertical scale is in arbitrary units

Computer simulation of chemical shifts of the substances was performed with Gaussian-16 software [9]. Geometry optimizations of parts of the backbone were performed in B3LYP/6-311G**+ theory level. Chemical shifts were calculated for the optimized conformations of the parts in RHF/6-311G**+ theory level. Calculated pairs of chemical shifts (σ_H , σ_C) are close to the experimental values obtained on the HSQC spectra. This allows us to conclude that both pyran and furan rings appears in the chain. Some of –CH₂– groups in the main chains of polymers are substituted with >CH– groups with cross-links to other polymers by oxygen atoms. Analysis of spectra shows that DIVEMA-1 in comparison to DIVEMA-2 has more cross-links.

Conclusions

The ¹H and ¹³C NMR-spectra of two modified DVEMAN samples, synthesized originally in chloroform (DVEMAN-1) and in cyclohexanone (DVEMAN-2), have been compared, and novel data on the structure of statistical copolymers have been obtained. The main results of the performed comparative analysis are the following:

1. as a whole, the free radical copolymerization of DVE and MAN leads to variable structure of DVEMAN copolymer backbone;

2. the both copolymer samples contain both the pyran and the furan cycles in the backbone chain; thus, a different solvent media could not be considered as the factor stimulating a formation of preferably pyran or furan cycles in its structure;
3. the analysis of spectral data showed that sample DVEMAN-1 \rightarrow DIVEMA-1 in comparison to DVEMAN-2 \rightarrow DIVEMA-2 contains a significant amount of cross-links with $>\text{CH}-\text{O}-\text{CH}<$ bridges;
4. the latter means that DVEMAN-1, synthesized in chloroform, is a predominantly cross-linked copolymer when DVEMAN-2 is not the same; so, the influence of solvent media on the process of copolymerization have been detected;
5. due to formation of different amount of oxygen-bridges in copolymer structure, it may be concluded that DVEMAN-2, obtained in cyclohexanone, has a slightly branched architecture of macromolecules when the macromolecules of DVEMAN-1, obtained in chloroform, are similar to nanoparticle taking into account its intermolecular cross-linkage.

Acknowledgments

Authors thank the Magnetic Resonance Research Center and Computing Center of Saint-Petersburg State University.

References

1. G. B. Butler. – J. Polym. Sci., Part A: Polym. Chem. 38, 3451(2000).
2. V. G. Kadajji, G. V. Betageri. – Polymers. 3, 1972 (2011).
3. A. V. Serbin, E. N. Karaseva, V. B. Tsvetkov, O. L. Alikhanova, I. L. Rodionov. – Macromol. Symp. 296, 466 (2010).
4. T. Kovshova, J. Malinovskaya, J. Kotova, M. Gorshkova, L. Vanchugova, N. Osipova, P. Melnikov, V. Vadekhina, A. Nikitin, Y. Ermolenko, S. Gelperina – Biomolecules 14, 1601 (2024).
5. T. Kunitake, M. Tsukino. – J. Polym. Sci. Polym. Chem. 17 (3), 877 (1979).
6. M. Gorshkova, T. Lebedeva, L. Stotskaya, I. Slonim. – Polym. Sci. Series A. 38(10), 1683 (1996).
7. R. Y. Samuels. – Polymer. 18, 452 (1977).
8. B. D. Bolshchikov, V. B. Tsvetkov, O. L. Alikhanova, A. V. Serbin. – Macro-molecular Chemistry and Physics, 220 (23), 1900389 (2019)
9. Gaussian 16, Revision C.01, M. J. Frisch, G. W. Trucks, H. B. Schlegel *et al.* – Gaussian, Inc., Wallingford CT, 2016. URL: <https://gaussian.com>

NMR analysis of surfactants characteristics based on methacrylic acid.

S.I. Levit², M.V.Kadnikov^{1,2}, P.A.Fetin², I.M.Zorin²

¹*Faculty of Physics, Saint Petersburg State University, Saint Petersburg, Russia*

²*Institute of Chemistry, Saint Petersburg State University, Saint Petersburg, Russia*

Email: si.levit@mail.ru

Introduction

Currently, there is a trend to transfer important and widely used organic reactions, particularly synthesis reactions, into aqueous solutions. This application of surfactants opens new horizons in the field of Green chemistry. Micellar catalysis is widely used in modern chemistry for achieving water solubility of insoluble compounds, which enables the conduction of pseudo-homogeneous reactions in water. One of the most effective micelles are formed from amphiphilic polyelectrolytes. Based on previous research, a surfactant derived from methacrylic acid has been synthesized[1]. NMR spectroscopy, being a crucial analytical technique in organic synthesis, allows to assess key characteristics in micelle synthesis, such as the degree of polymerization and potential impurities of oligomers.

Method

To obtain the target methacrylic acid based cationic monomer with a methoxypolyethylene glycol fragment a 4 stage synthesis was carried out (Fig. 2). Each stage was characterized by ¹H NMR spectroscopy analysis, including different synthesis methodic as well as a number of impurities (Fig. 1). Based on the obtained products, polyelectrolytes were synthesized and the degree of conversion of functional groups was measured by the same ¹H NMR method.

¹-H NMR Spectrum of MAU-Br in CDCl₃

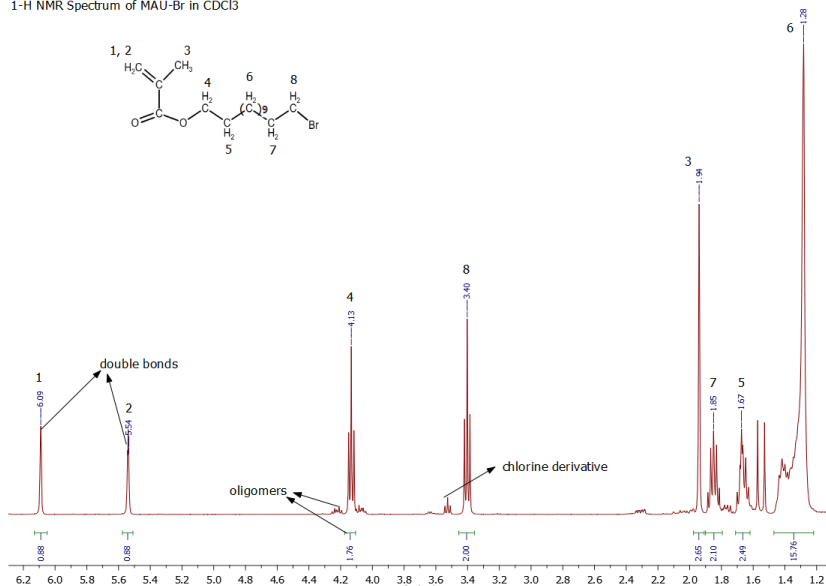


Figure 1. Conclusions from the ¹-H NMR spectrum for MAU-Br

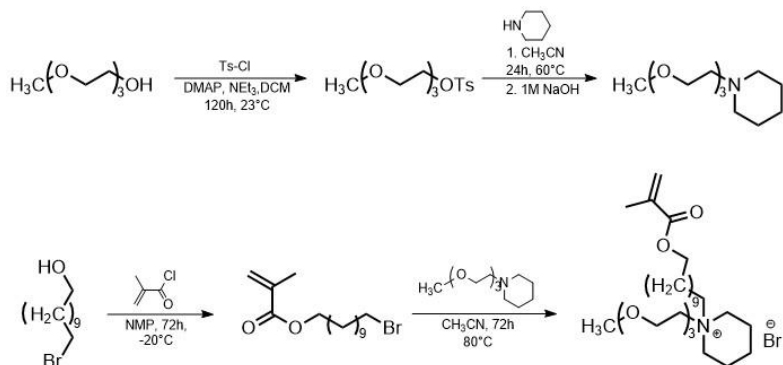


Figure 2. Scheme of macromonomer synthesis

Acknowledgements

Was supported by a grant RSF № 24-73-00193. The work was supported by the research park of St. Petersburg state university: RC of Magnetic resonance and cryogenic department.

References

1. I.M. Zorin, M.V. Kadnikov, P.A. Fetin. Cross-Coupling Reaction of Hydrophobic Substrates in Water: Micellar Catalysis with Macromolecular Surfactants. Russian Journal of General Chemistry, 2024, Vol. 94, Suppl. 1, pp. S148–S156.

Study of intramolecular mobility in ionic liquid [Bmim]₂Cd(SCN)₄ using NMR relaxation data.

*Daria A. Malakhova*¹, *Alexandr V. Ievlev*², *Konstantin V. Tyutyukin*²

¹Specialized educational and scientific center "Academic Gymnasium named after D.K. Faddeev of Saint Petersburg State University", St. Petersburg 198504 Russia

²Department of Nuclear Physics Research Methods, Saint Petersburg State University, St. Petersburg 198504 Russia

E-mail: a.ievlev@spbu.ru

Introduction

In this work, the main interest was directed to the study of intramolecular mobility in the complex ionic liquid [BMIM]₂Cd(SCN)₄, the study of this system was carried out to obtain additional information previously described here [1–3]. The term "ionic liquids" most often refers to salts whose melting point is below the boiling point of water, i.e. below 100 degrees Celsius. As a tool for studying intramolecular mobility, we used NMR relaxometry. For this purpose, changes in the integrated intensities in the ¹H and ¹³C NMR spectra were recorded at different temperatures depending on the interval between pulses in the standard inversion-recovery sequence. Based on the nature of the change in integrated intensities, the spin-lattice relaxation times for individual spectral lines were calculated. Then, from the obtained dependences, the reorientation times of individual molecular groups were calculated.

Results and discussions

All measurements were carried out in the resource center of Magnetic Resonance Research Methods of the St. Petersburg State University Science Park, on a Bruker Avance III spectrometer (500 MHz for protons and 127.5 MHz for carbon) in the temperature range from 263 K to 363 K with a step of 10 K, the interval between pulses varied from 0.01 to 15 seconds with a relaxation delay of 15 s.

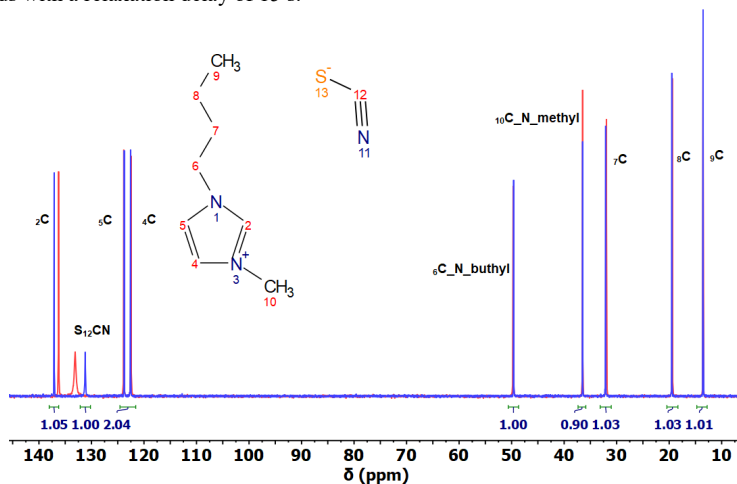


Figure 1. Full spectrum ¹³C at 298K, for pure BmimSCN – blue, and complexe IL with Cd [Bmim]₂Cd(SCN)₄ – red.

The measurement results and spectra were processed in the MestReNova software package version 14.2, and subsequent analysis and plotting of dependency graphs were performed in the MagicPlot 3.0 software.

As can be seen in Fig. 1, the ^{13}C spectra of our compound and the base IL are shown. The spectral line of carbon included in the thiocyanate is clearly visible here and has a chemical shift of $\delta = 135.39$ ppm, while the proton spectrum is quite standard for the butyl-methyl imidazolium cation and is therefore not shown here. The shift of the thiocyanate line by chemical shift relative to the base sample $\delta = 131.25$ ppm is caused by the entry of thiocyanate into a metal anion complex with cadmium.

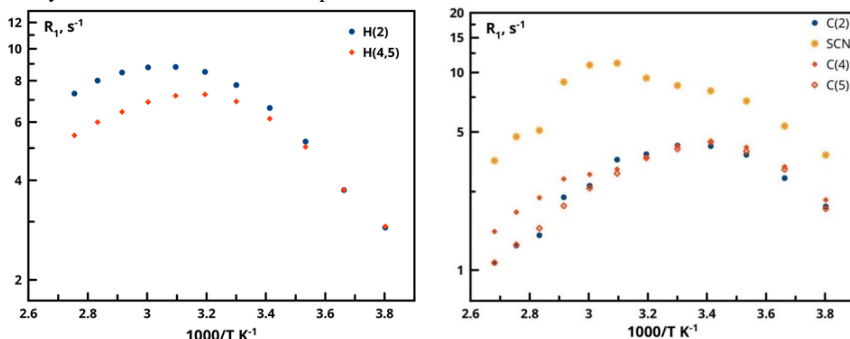


Figure 2. Temperature dependence of the spin-lattice relaxation rate of carbon nuclei ^{13}C - on the right, and protons ^1H - on the left.

The graphs in Fig. 2 show the temperature dependences of the spin-lattice relaxation rates of nuclei ^1H and ^{13}C for different molecular groups. Here we present only the information for carbons and protons of the imidazole ring and thiocyanate. As can be seen from the graphs, the temperature dependence of the relaxation rate has a maximum for all molecular groups considered. Using the information on the position of the maximum, we calculated the reorientation times for individual molecular groups using the BPP (Bloembergen-Purcell-Pound) relaxation model according to the equations 1 and 2 used in Refs. [4,5]. To solve these equations for the reorientation times τ_c , we used an auxiliary program written in Mathcad. Then, from two real and two imaginary roots, we selected only the root that has a physical meaning.

$$R_{1H}(\omega_H, T) = s_H^2 A_0 \left(\frac{\tau_c(T)}{1 + (\omega_H \tau_c(T))^2} + \frac{4\tau_c(T)}{1 + (2\omega_H \tau_c(T))^2} \right), \quad (1)$$

$$R_{1C}(\omega_C, T) = s_C^2 A_0 \left(\frac{6\tau_c(T)}{1 + (4.97\omega_C \tau_c(T))^2} + \frac{\tau_c(T)}{1 + (2.97\omega_C \tau_c(T))^2} + \frac{3\tau_c(T)}{1 + (\omega_C \tau_c(T))^2} \right), \quad (2)$$

where ω_H and ω_C – resonant angular frequency ($2\pi\nu_0$) for ^1H and ^{13}C , respectively, s_H^2 and s_C^2 (≤ 1) are order parameters, T is temperature of the sample, and A_0 is a constant.

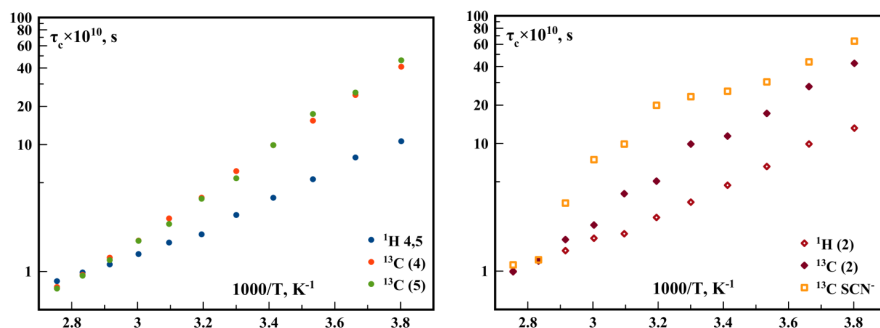


Figure 3. Temperature dependence of the reorientation time of proton nuclei and carbons of the 4th and 5th molecular groups - on the right, and of the 2nd molecular group (including carbon included in thiocyanate) - on the left.

As can be seen from the graphs shown in Fig. 3, the reorientation times of protons are shorter or comparable to those of carbon for each molecular group, which is quite consistent with the theory, since the carbon nucleus in the molecular group has fewer degrees of mobility. The activation energy of reorientation intramolecular motions for each group can be estimated from the slope of the temperature dependence of the reorientation time; from the graphs given, it is clear that for carbon it is longer than for protons.

Acknowledgements

This work is supported by Russian Science Foundation (RSF): grant № 23-23-00430. Thanks to the staff of Center for Magnetic Resonance of Research Park of St. Petersburg State University for fast and high-quality measurements.

References

1. O. Cabeza, L.M. Varela, E. Rilo, L. Segade, M. Domínguez-Pérez, D. Ausín, I. de Pedro, J.R. Fernández, J. González, M.P. Vazquez-Tato, Y. Arosa, E. López-Lago, R. de la Fuente, J.J. Parajó, J. Salgado, M. Villanueva, V. Matveev, A. Ievlev, J.A. Seijas, Synthesis, microstructure and volumetry of novel metal thiocyanate ionic liquids with [BMIM] cation, *J. Mol. Liq.* 283 (2019) 638–651. <https://doi.org/10.1016/j.molliq.2019.03.088>.
2. O. Cabeza, L. Segade, M. Domínguez-Pérez, E. Rilo, D. Ausín, J.A. Seijas, M.P. Vazquez-Tato, V. Matveev, A. Ievlev, J. Salgado, L.M. Varela, Strange behaviour of transport properties in novel metal thiocyanate based ionic liquids, *J. Mol. Liq.* 340 (2021) 117164. <https://doi.org/10.1016/j.molliq.2021.117164>.
3. A. V. Ievlev, K. V. Tyutyukin, N. V. Pokhvishcheva, Molecular and ionic mobility of ionic liquids with complex anions containing metals, in: *Magn. Reson. ITS Appl.*, St. Petersburg University Publishing House, Saint-Petersburg, 2024: pp. 91–93. <https://elibrary.ru/item.asp?id=67226989&pf=1>.
4. V. V. Matveev, D.A. Markelov, E.A. Brui, V.I. Chizhik, P. Ingman, E. Lähderanta, ¹³C NMR relaxation and reorientation dynamics in imidazolium-based ionic liquids: Revising interpretation, *Phys. Chem. Chem. Phys.* (2014). <https://doi.org/10.1039/c4cp00637b>.
5. V. V. Matveev, D.A. Markelov, A. V. Ievlev, E.A. Brui, K. V. Tyutyukin, E. Lähderanta, Molecular mobility in several imidazolium-based ionic liquids according to data of ¹H and ¹³C NMR relaxation, *Magn. Reson. Chem.* 56 (2018) 140–143. <https://doi.org/10.1002/mrc.4681>.

Effect of the disulfide reducing agent TCEP on the translational mobility of α - and κ -casein and their ability to form supramolecular structures

Daria Melnikova¹, Irina Nesmelova², Vladimir Skirda¹

¹*Department of Molecular Systems Physics, Institute of Physics, Kazan Federal University, Kazan, Russia*

²*Department of Physics and Optical Sciences and School of Data Science, University of North Carolina, Charlotte, North Carolina 28223, United States*

E-mail: melndaria@mail.ru

Introduction

The modern development of protein analysis methods has raised the question of studying factors affecting protein quality, such as chemical modifications of amino acids in protein composition. For example, this factor is most acutely sensitive in mass spectrometric studies, so the authors of [1] showed that during sample preparation for proteomic analysis an artifactual modification of a lysine residue with molecular mass equal to diglycine tags of ubiquitination sites is possible. Other studies [2] have established the fact that chemical treatment of proteins affects the results of phosphorylation sites. In other words, studying the effect of sample preparation methods on the results of a particular method in protein studies is important for improving the quality of the latter.

Tris(2-carboxyethyl)phosphine (TCEP) is known as a thiol free reductant of protein and peptide disulfide bonds and is widely used in sample preparation [3]. Compared to dithiothreitol (Cleland's reagent) and β -mercaptoethanol, TCEP is a more potent reducing agent than DTT, is resistant to air oxidation, and restores disulfide bonds quite rapidly and efficiently over a wide range of pH values [4,5]. It is generally accepted that the addition of a reducing agent results in the cleavage of disulfide bonds and the retention of all thiol groups in the reduced state. It is at the stage of disulfide bond reduction and subsequent alkylation of the formed free thiol groups that there is a rather high probability of artifacts formation [6], which will affect the final result of the analysis of the studied protein structures.

Results of a study of translational mobility of α - and κ -casein

The aim of this work was to determine the effect of the disulfide bond-reducing agent TCEP on the translational mobility of α - and κ -casein proteins and on their ability to form a supramolecular structure. NMR measurements were carried out on the equipment of the Federal Center of Shared Facilities at Kazan Federal University Bruker AVANCE III 400 NMR spectrometer.

In this study, the effect of TCEP on the molecular mobility of α - and κ -casein in dilute solutions was investigated on samples of dilute aqueous protein solutions without and with the addition of TCEP. Typical NMR spectrum of TCEP have several signals, in particular the region of chemical shifts from 2 ppm to 3.5 ppm according to [7] characterizes the proton groups of the TCEP: three carboxylates (carboxyl functional groups: carbonyl ($>C=O$) and hydroxyl ($-OH$)) and substituted phosphine. Thus, the translational mobility of TCEP molecules in aqueous solution can be quite unambiguously determined by analyzing the parameter dependence of the pulse gradient of the signal amplitude along the lines in the region of chemical shifts from 2 to 3.5 ppm. The diffusion attenuation characteristic of this region of chemical shifts is shown in Figure 1 A.

At the same time, comparison of NMR spectra of samples of aqueous protein solutions with α -casein concentration of 3% with and without TCEP showed that the lines of the spectrum attributed to TCEP molecules (chemical shift from 2 to 3.5 ppm) partially overlap with the range of chemical shifts of protein lines (from 0.16 to 3.61 ppm). Therefore, to

identify the diffusive attenuation of the spin echo signal of protein molecules, we integrated the signals in the chemical shift region from 0.16 to 2.0 ppm, since in this region the influence of TCEP on the spectral lines of protein molecules is rather small. The results of this approach are shown in Figure 1 B, where number 1 indicates the diffusion attenuation for the spectral line region from 0.16 to 2.0 ppm for the sample containing TCEP, and number 2 indicates the diffusion attenuations of the spin echo signal for the spectral line region from 0.16 to 3.61 ppm for the “pure” protein solution.

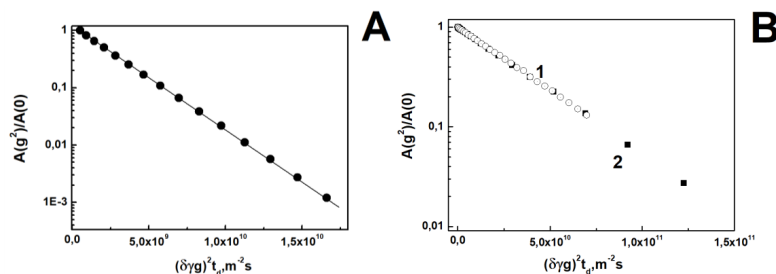


Figure 1. Spectrally resolved diffusion attenuations of the spin echo signal for: (A) an aqueous solution of TCEP with a molar concentration of 0.1048 mol/L. The solid line represents to the exponential form of diffusion attenuation; B) aqueous solution of protein at α -casein concentration of 3% with addition of TCEP, obtained from the spectral line areas from 0.16 to 2.0 ppm (curve 1 - empty circles \circ) and diffusion attenuation obtained over spectral lines from 0.16 to 3.61 ppm for the aqueous protein solution at an α -casein concentration of 3% without addition (curve 2 - black squares \blacksquare) of TCEP and NaOD

The diffusional attenuation for TCEP molecules in aqueous solution presented in Figure 1 A in a sufficiently large dynamic range (three decimal orders) is a monoexponential form. At the same time, a determined value of the self-diffusion coefficient of TCEP molecules ($D_{\text{TCEP}} = 4.2 \cdot 10^{-10} \text{ m}^2/\text{s}$) is almost an order of magnitude smaller than that for water molecules ($D_{\text{water}} = 2.7 \cdot 10^{-9} \text{ m}^2/\text{s}$). The obtained value of the self-diffusion coefficient for TCEP molecules in aqueous solution agrees well with the same value of the self-diffusion coefficient found in the study [8], where aqueous solutions with TCEP were studied by differential pulse and cyclic voltammetry.

Regarding the translational mobility of protein molecules, Figure 1 B shows that both diffusion attenuations for 3% aqueous solutions of α -casein (without and with TCEP addition) coincide with a good degree of accuracy and are described by an exponential law with the same value of the protein self-diffusion coefficient $D_{\text{protein}} = 2.97 \cdot 10^{-11} \text{ m}^2/\text{s}$. A similar result, i.e., the coincidence of diffusion attenuations and hence self-diffusion coefficients, was also observed for 1% α -casein solutions with and without the addition of TCEP.

It can be assumed that the α -casein under study either lacks protein fractions containing cysteine groups or TCEP used does not reduce disulfide bonds. A control experiment investigating covalently labeled cysteine residues of α S2-casein by fluorescence using thiol-reactive pyrene and Alexa-532 maleimides [9] failed to confirm both of these assumptions. Thus, the results obtained can be unambiguously interpreted as the absence of a significant effect of TCEP on the secondary structure of the protein and on its conformation (hydrodynamic size) in dilute aqueous solutions of α -casein. It can be hypothesized that this result is a consequence of the structure of α S2-casein, in which the two cysteines are located at a sufficiently close distance from each other. Therefore, the formation of disulfide bonds by them practically cannot significantly affect the conformation of the whole protein molecule.

To investigate the effect of TCEP on the molecular mobility of α - and κ -casein and the formation of supramolecular structures in concentrated protein solutions, we applied ^{31}P NMR, since both the reducing agent TCEP contains phosphate groups and the protein has a certain degree of phosphorylation [10,11].

On the example of α -casein and κ -casein solutions, the ambiguous nature of the effect of the disulfide bond reducing agent TCEP on the formation of supramolecular protein structure was established. Thus, the TCEP agent activates additional chemical processes in α -casein solutions that lead to the formation of an unlabile and insoluble gel. Based on the analysis of experimental data, a hypothesis about the formation of secondary intermolecular -S-S- bonds shielded for the reducing agent molecules in the presence of TCEP was formulated. At the same time, the opposite situation is observed in κ -casein solutions: the addition of TCEP molecules leads to the absence of all signs of gel formation.

Acknowledgements

This work was funded by the subsidy allocated to Kazan Federal University for the state assignment in the sphere of scientific activities number FZSM-2023-0016.

References

1. M. L. Nielsen, M. Vermeulen, T. Bonaldi, J. Cox, L. Moroder, M. Mann. – Nature methods, 5, 459-460 (2008).
2. R. Krüger et al. – Rapid Communications in Mass Spectrometry: An International Journal Devoted to the Rapid Dissemination of Up-to-the-Minute Research in Mass Spectrometry, 19,1709-1716 (2005).
3. E. B. Getz, M. Xiao, T. Chakrabarty, R. Cooke, P. R. Selvin. – Analytical biochemistry, 273, 73-80 (1999).
4. J. A. Burns, J. C. Bulter, J. Moran, G. M. Whitesides. – J. Org. Chem., 56, 2648-2650 (1991).
5. J. C. Han, G. Y. Han. – Analytical biochemistry, 220, 5-10 (1994).
6. E. S. Boja, H. M. Fales. – Analytical chemistry, 73, 3576-3582 (2001).
7. A. Krężel, R. Latajka, G. D. Bujacz, W. Bal. – Inorg. Chem., 42, 1994–2000 (2003).
8. I. B. Santarino, S. C. Oliveira, A. M. Oliveira-Brett. – Electrochemistry Communications, 23, 114-117 (2012).
9. D. L. Melnikova, V. D. Skirda, I. V. Nesmelova. – J. Phys. Chem. B, 123, 2305-2315 (2019).
10. H. E. Swaisgood. – Journal of dairy science, 76, 3054-3061 (1993).
11. P. F. Fox. – Advanced Dairy Chemistry – Proteins, 1-48 (2003).

NMR diffusometry and micellar solubilization using biological surfactants

*Daria L. Melnikova, Artem S. Alexandrov, Ruslan V. Arkhipov, Victor P. Arkhipov**

Molecular physics department, Institute of Physics, Kazan Federal University

E-mail: general_zh@mail.ru

** Department of Physics, Kazan National Research Technological University,*

E-mail: vikarch@mail.ru

The micellar extraction method uses the property of micelles and vesicles of surfactants, formed at concentrations above the critical micelle concentration, to solubilize organic compounds, aliphatic, aromatic and polycyclic hydrocarbons, metals and other pollutants. However, the use of synthetic surfactants in itself has a negative impact on the environment due to their toxicity and low biodegradability. Bio-surfactants produced by living microorganisms are used for environmental restoration, bioremediation and soil washing, biodegradation of hydrophobic organic compounds, in food production, cosmetics, pharmaceuticals and are a promising "green" alternative to synthetic surfactants.

An effective method for studying micellar solubilization is the NMR diffusometry method. Selective measurements of the self-diffusion coefficients (SDC) of all components in an aqueous solution of surfactant + solubilize make it possible to find the distribution of the solubilize between the bound (in micelles) and free (in water) states within the two-state model. Solubilization of hydrocarbon molecules by surfactant micelles is manifested, and its efficiency can be calculated from changes in the SDC of hydrocarbon molecules with a change in the concentration of surfactant in the solution. In the absence of solubilization, the SDC values of hydrocarbon molecules should not depend on the presence of micelles in the solution, and a possible decrease in the SDC can only be associated with changes in the dynamic viscosity of the solution with an increase in the concentration of rhamnolipid. In the presence of solubilization, one should expect a decrease in the SDC values of hydrocarbon molecules and their convergence with the SDC values of the surfactant with an increase in its concentration in the solution, and, finally, equality of the SDC values of hydrocarbons and rhamnolipid with complete solubilization.

The work summarizes and analyzes the results of studies [1-3] of micellar solubilization from aqueous solutions of substances of the BTEX group (benzene, toluene, ethylbenzene, xylene), phenol, and naphthalene, carried out by the NMR diffusometry method using rhamnolipid as a bio-surfactant.

Acknowledgements

This work was funded by the subsidy allocated to Kazan Federal University for the state assignment in the sphere of scientific activities number FZSM-2023-0016.

References

1. Arkhipov V. P., Arkhipov R. V., Petrova E. V., Filippov A. Magn. Reson. Chem., 61, 345–355. (2023) doi: 10.1002/mrc.5337
2. Arkhipov V. P., Arkhipov R. V., Filippov A. Magn. Reson. Chem., 62, 712–717, (2024) doi: 10.1002/mrc.5468
3. Arkhipov V. P., Arkhipov R. V., Filippov A. ACS Omega, 8, 30646–30654, (2023) doi.org/10.1021/acsomega.3c04367

Evaluation of plasma viscosity in patients with hyperviscosity syndrome using Proton Magnetic Relaxation.

Yulianela Mengana Torres¹, Manuel Arsenio Lores Guevara¹, Lilian Somoano Delgado¹, Claudia Camila García Cruz¹, Yamirka Alonso Geli¹, Fabián Tamayo Delgado¹, Juan Carlos García Naranjo¹, Yomaidis Araujo Durán², Lidia Clara Suárez Beyries², Yanet Obregón Segura², Yasmin Estrada Garrido².

¹ Centro de Biofísica Médica, Santiago de Cuba, Cuba, yulianela.mengana@uo.edu.cu

² Hospital General "Juan Bruno Zayas Alfonso", Santiago de Cuba, Cuba.

ABSTRACT

The determination of blood viscosity allows the clinical evaluation of various diseases, including multiple myeloma and sickle cell anemia, due to its usefulness in confirming the hyperviscosity syndrome and in making therapeutic decisions for its treatment. Magnetic Proton Relaxation has been proposed as a method for determining dynamic viscosity, so we propose to evaluate this parameter using this technique in patients with multiple myeloma in an asymptomatic state, debut and with VHS symptoms; To this end, an observational, descriptive and cross-sectional study was carried out in supposedly healthy individuals, patients with multiple myeloma and sickle cell anemia from the hematology service of the "Juan Bruno Zayas" Hospital in Santiago de Cuba. To obtain plasma, venous blood samples from the study subjects were centrifuged at 3500 rpm for 10 minutes. T2 was measured at 20°C, using the Carr-Purcell-Meiboom-Gill pulse sequence. No statistically significant differences were observed in plasma viscosity values in supposedly healthy subjects and patients with multiple myeloma in an asymptomatic state. Additionally, three patients with VHS were evaluated and monitored during treatment; statistically significant differences were observed in the plasma viscosity values of patients in an asymptomatic state and with VHS ($\alpha=0.05$). All these results showed the usefulness of the technique to determine the viscosity of protein solutions in patients with sickle cell anemia (asymptomatic and hospitalized state), as well as to evaluate the effect of the treatment.

Keywords: dynamic viscosity, hyperviscosity syndrome, multiple myeloma, sickle cell anemia, proton magnetic resonance.

INTRODUCTION

In clinical practice, blood components are usually evaluated in a differentiated way, hemoglobin, glucose, proteins, etc. are usually measured and it is compared with normal values, and when these deviate from these parameters, specific decisions are usually made. However, blood is not usually evaluated as a heterogeneous mixture that acquires its own identity and that carries specific properties, one of these properties consists of its viscosity, that is, the resistance that this fluid has to move.

Blood viscosity usually remains at values to which we have adapted and, therefore, under these conditions it could have little clinical implication; But in some diseases or in certain physiological conditions, such as living in high-altitude cities, blood viscosity can be increased and affect existing self-regulation mechanisms. We expose the role that blood viscosity has in human physiology, and some diseases where its importance may be greater and the difficulties in measuring it.

MATERIALS AND METHODS

Venous blood samples from the study subjects were centrifuged at 3500 rpm for 10 minutes and plasma, hemoglobin solution and blood serum were obtained. T₂ was measured at 20°C, using the Carr-Purcell-Meiboom-Gill pulse sequence.

RESULTS AND DISCUSSION

Table1. η_P values in “apparently healthy” individuals determined using the RMP method and the Ostwald viscometer as a reference method

Control individuals (n=20)	η_P (mPa·s) Ostwald viscometer	η_P (mPa·s) RMP
Average value	1,61 \pm 0,06	1,65 \pm 0,10
Range	1,57-1,65	1,60 - 1,77

Table 2 shows the results of the application of the method, based on RMP, for the determination of η_P in the case of “apparently healthy” individuals and patients with MM at the time of debut, with symptoms typical of hyperviscosity syndrome (HVS) and under treatment with chemotherapy. In the table 2 shows the η_P values obtained in these patients during hospital admission in cases where it was possible; observing, in general sense, a decrease with treatment. However, this reduction occurs at different times during treatment, which could be related to the initial conditions of each patient and their ability to respond to treatment.

Table 2. Use of the method developed for blood plasma viscosity in MM patients.

subjects	η_P (mPa·s)
“Apparently healthy” individuals (n=18)	1,65 \pm 0,10
Patients with MM (during debut) (n=18)	2.39 \pm 0.33
Patients with MM (follow-up by consultation) (n=191)	2.17 \pm 0.58
Patients with MM (admitted) (n=23)	2.09 \pm 0.56
Patients with MM (under treatment) (n=140)	2.1 \pm 0.3
Patients with MM (con SHV) (n=3)	4. 5 \pm 0.7

The η_P values obtained in patients with MM during the debut are significantly higher ($\alpha=0.05$, $P=9.86 \cdot 10^{-7} < 0.05$) than those determined in “apparently healthy” subjects; which can be explained by the increase in globulin concentrations (especially IgA and IgG). However, under treatment with chemotherapy, η_P values are significantly reduced ($\alpha=0.05$, $P=0.01 < 0.05$), becoming indistinguishable from the values obtained in “apparently healthy” adults ($\alpha=0.05$). , $P=0.30 > 0.05$). This last result supports the effectiveness of the treatment in reducing the concentration of globulins.

In patients with MM who have characteristic symptoms of VHS (hemorrhagic, neurological and ophthalmological) [4, 5] the η_P is statistically increased compared to “apparently healthy” individuals ($\alpha=0.05$, $P=0.01 < 0.05$), despite the limitations in the number of samples in the first case, because the concentrations of IgA and IgG are greater than 7000 mg/dl and 10,000 mg/dl respectively. In all patients with VHS, η_P values are greater than 3 mPa·s, which is the recognized threshold for the appearance of symptoms [7]. In general, patients with MM multiple myeloma with η_P values less than 3.0 mPa·s do not present symptoms of hyperviscosity. The η_P levels at which signs and symptoms of VHS begin to appear are difficult to define. The η_P is statistically increased because the concentrations of IgA and IgG are greater than 7000 mg/dl and 10000 mg/dl respectively. The

increase in IgA and IgG concentrations has a direct relationship with the increase in η_p according to the generalized Mooney equation [7].

Table 3. Use of the method developed for blood plasma viscosity in patients with AD

subjects	η_p (mPa·s)
“Apparently healthy” individuals (n=18)	2,15 ± 0,17
Patients with AD (follow-up by consultation) (n=122)	2,22 ± 0,86
Patients with AD (admitted) (n = 41)	2,01 ± 0,31

In the table 3 shows the η_p values obtained in these patients during hospital admission, as well as the follow-up patients through outpatient consultation; In general, a decrease in the viscosity of hospitalized patients was observed with treatment. However, this reduction occurs at different times during treatment, which could be related to the initial conditions of each patient and their ability to respond to treatment.

CONCLUSIONS

1. The results obtained in the measurement of the absolute dynamic viscosity in aqueous protein solutions using Nuclear Magnetic Relaxation statistically coincided with the reference method used with 95% reliability. Which validates the methods developed for use in the medical environment.
2. The usefulness of the methods developed in medical practice was demonstrated, observing statistically significant increases in absolute dynamic viscosity in samples of blood plasma, blood serum and hemoglobin solution in patients suffering from AD.

BIBLIOGRAPHICAL REFERENCES

1. Lores MA, Mengana Y, García J, Rodríguez N, Suárez L, Marichal M, et al. Plasma Dynamic Viscosity Determined by NMR. *Applied Magnetic Resonance*.2018, 49(10), 1075-1083.doi 10.1007/s00723-018-1026.
2. Rosenson RS, McCormick A, Uretz EF. Distribution of blood viscosity values and biochemical correlates in healthy adults. *Clin Chem*. 1996 Aug; 42(8 Pt 1):1189-95. PMID: 8697575.
3. Elblesy MA. Plasma viscosity and whole blood viscosity as tools of blood abnormalities by using simple syringe method. *Medical Instrumentation*.2014.doi: 10.7243/2052-6362-2-5.
4. Gertz MA. A cute hyperviscosity: syndromes and management. *Blood*. 2018, 132(13), 1379–1385. doi: 10.1182/blood-2018-06-846816.
5. Blanco-Santos Y, Areces López A, Gámez Pérez A. Síndrome de hiperviscosidad: características fisiopatológicas y clínicas. 16 de Abril [Internet]. 2020 [fecha de citación]; 59(278):e840.Disponible en:http://www.rev16deabril.sld.cu/index.php/16_4/article/view/840
6. Rosencranz R, Bogen SA. Clinical laboratory measurement of serum, plasma, and blood viscosity. *Am J Clin Pathol*. 2006, 125(Suppl), 78-86. doi: 10.1309/FFF7U8RRPK26VAPY.
7. Endre ZH, Kuchel PW. Viscosity of concentrated solutions and of human erythrocyte cytoplasm determined from nmr measurement of molecular correlation times. The dependence of viscosity on cell volume. *Biophys Chem*. 1986, 24, 337-356. doi: 10.1016/0301-4622(86)85039-6.

Modification approaches to the development of pervaporation sodium alginate-based membranes with enhanced properties

Olga Mikhailovskaya¹, Anna Kuzminova¹, Anton Mazur¹, Anastasia Penkova¹, Mariia Dmitrenko¹

¹ St. Petersburg State University, 7/9 Universitetskaya nab., Saint Petersburg 199034, Russia

E-mail: st113220@student.spbu.ru

<https://go.spbu.ru/rgpenkova>

Introduction

Pervaporation is a promising membrane method for the separation of liquid mixtures of low molecular weight substances, which finds application in various industries. The efficiency of this process largely depends on the choice of membrane material. One of the most progressive materials for creating membranes for pervaporation dehydration are polyelectrolyte complexes (PEC). They have high selectivity to water and allow for the effective separation of it from the mixture (namely, organic solvents).

Sodium alginate (SA) is a promising biopolymer for obtaining membranes with tailored characteristics. SA may be modified in two ways: by introducing a modifier (namely, carbon nanoparticles) into its matrix and by addition of polyelectrolyte (namely, polyethyleneimine (PEI)) to create PEC. Also, these modification approaches for the creation of mixed matrix membranes have now demonstrated their relevance.

Results and discussion

The aim of this study was to develop and study pervaporation membranes based on PEC of SA and PEI modified with graphene oxide (GO). Spectroscopic methods (FTIR and NMR) were used to confirm the formation of PEC and interaction it with GO. Scanning electron and atomic force microscopies were used to evaluate the membrane morphology and topography. It was shown that PEC membranes had a rough cross-sectional structure and a surface with "clusters". This was due to the ionic interaction between the anionic SA and the cationic PEI. In addition, SEM images confirmed the uniform miscibility of polymers associated with the formation of PEC (Fig. 1). The effectiveness of the membrane was tested in pervaporation for ethanol dehydration in a wide range of concentrations.

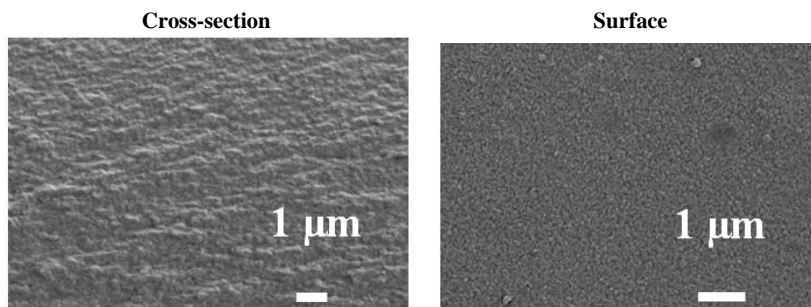


Figure 1. The cross-sectional and surface SEM micrographs of PEC membrane.

Conclusions

It was demonstrated that PEC-based (from SA/PEI) membranes modified with GO had significantly improved performance in pervaporation dehydration of ethanol compared to the

pristine SA membrane due to changes in structural and physicochemical properties during modifications. It makes them promising for use in the separation and purification of alcohols used in the production of biofuels and other chemical products.

Acknowledgements

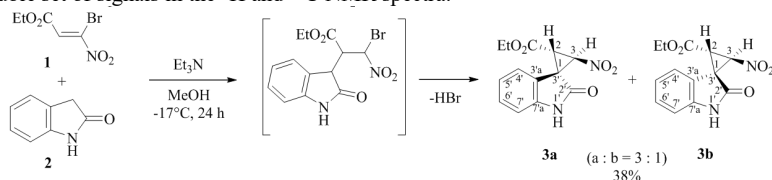
The study was supported by the Russian Science Foundation grant No. 23-73-01070, <https://rscf.ru/project/23-73-01070/>. The experimental work was facilitated by equipment from the Resource Centers for Nanotechnology, Magnetic Resonance, Cryogenic Department, Thermogravimetric and Calorimetric Research Center, Center for Physical Methods of Surface Investigation, Center for Innovative Technologies of Composite Nanomaterials, Chemical Analysis and Materials Research Center, and Center “Nanofabrication of Photoactive Materials (Nanophotonics)” at the St. Petersburg State University.

Determination of the spirocyclopropanoxindole fine structure using NMR spectroscopy

Mikhailap M. V., Pelipko V. V., Gomonov K. A., Makarenko S. V.

Herzen State Pedagogical University of Russia, Laboratory of nitro compounds, Center of collective use at the Faculty of Chemistry "Instrumental methods for the study of nitro compounds, coordination, biologically active substances and nanostructured substances"
 48 Moyka River Embankment, Saint Petersburg 191186, Russia
 E-mail: kohrgpu@yandex.ru

Alkyl 3-bromo-3-nitroacrylates, as Michael acceptors, form carbo- and heterocyclic structures in reactions with CH-acids [1, 2]. A study of the interaction of ethyl 3-bromo-3-nitroacrylate **1** with 1,3-dihydro-2H-indol-2-one **2** showed that the reaction ends with the formation of a mixture of regioisomeric spirocyclopropanoxindoles **3a, b**, which is reflected by a double set of signals in the ^1H and ^{13}C NMR spectra.



The rigidly fixed structure of these spirocyclopropanoxindoles **3a, b** makes them interesting objects for structural studies using 2D NMR spectroscopy experiments.

In the ^1H NMR spectrum of the mixture of spirocyclopropanoxindoles **3a, b** (Fig. 1), the H^2 protons signals appear as doublets at 3.85 (a), 3.78 (b) ppm, and the H^3 protons signals appear as doublets at 5.32 (a), 5.30 (b) ppm. In turn, the signals of the amino groups ($\text{H}^{1'}$) protons appear as broadened singlets at 8.73 (a), 8.95 (b) ppm. The vicinal J -coupling between methine protons of the cyclopropane ring observed in the ^1H NMR spectrum $^3J_{\text{H}^2\text{H}^3} = 6.07$ (a), 6.14 (b) Hz indicates their *trans*-configuration, which is consistent with the literature data [3].

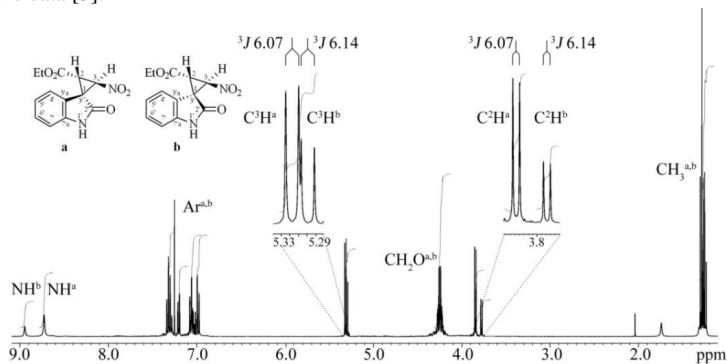


Figure 1. ^1H NMR spectrum of isomers **3a, b** (CDCl_3)

This assignment of signals in the ^1H NMR spectrum is confirmed by the results of the study these substances by the ^1H - ^1H NOESY NMR method. The results of ^1H - ^1H NOESY

(obtained with a variable value mix. time) of the isomer mixture, demonstrate NOE correlations of the protons $C^2H/C^4'H$ for isomer a and $C^3H/C^4'H$ for isomer b (Fig. 2).

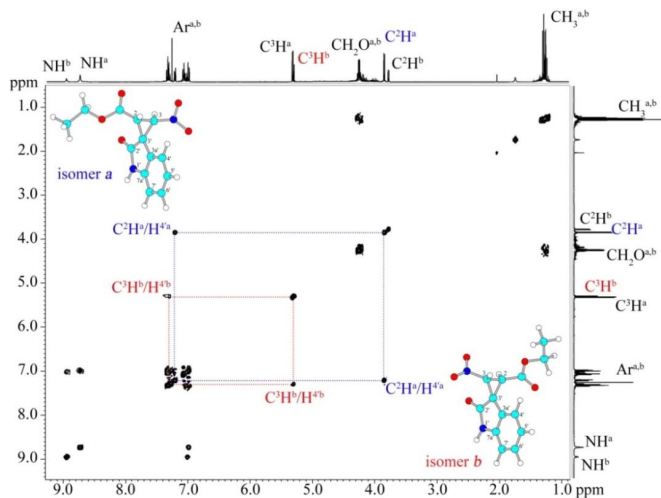


Figure 2. 1H - 1H NOESY spectrum of isomers **3a**, **b** ($CDCl_3$) with their models

The assignment of signals in the ^{13}C NMR spectra for both isomers was carried out on the results of the 1H - ^{13}C HMQC and 1H - ^{13}C HMBC NMR experiments. Unprotonated carbon atoms were assigned based on 1H - ^{13}C HMBC NMR experiment. Thus, spectrum of the mixture of two isomers **3a**, **b** showed cross-peaks between protons H^3 , H^2 , $H^{5'}$, $H^{1'}$ and carbon atom $C^{3a'}$ (121.7 (a), 122.6 (b) ppm), protons $H^{4'}$, $H^{6'}$, $H^{1'}$ and carbon atom $C^{7a'}$ (141.9 (a), 141.7 (b) ppm), proton $H^{1'}$ with spiro carbon $C^{3'}$ (40.0 (a), 39.2 (b) ppm). Cross peaks of methylene protons with the ester carbonyl carbon atom (163.4 (a), 165.0 (b) ppm) are also observed.

Thus, based on the 2D NMR spectroscopy experiments results, the fine structure of two isomers of spirocyclopropaneoindoles was determined, and the signals of their protons and carbon atoms were assigned.

The studies were carried out in the Center of collective use at the Faculty of Chemistry of the Herzen State Pedagogical University of Russia on the Jeol ECX-400A spectrometer (Royal Probe) at 399.78 (1H) and 100.53 (^{13}C) MHz with standard experimental settings. The residual signals of a non-deuterated solvent (for 1H nuclei) or the signals of a deuterated solvent (for ^{13}C nuclei) were used as a standard.

References

1. V. V. Pelipko, R. I. Baichurin, K. A. Lyssenko, E. V. Kondrashov, S. V. Makarenko – Mendelev Commun., 33, 451-454 (2023).
2. V. V. Pelipko, R. I. Baichurin, K. A. Lyssenko, V. V. Dotsenko, S. V. Makarenko – Mendelev Commun., 32, 454-456 (2022).
3. A. J. Gordon, R. A. Ford. The Chemist's Companion. New York: Wiley, 1972.

Novel blend cellulose nitrate/cellulose acetate ultrafiltration membranes for enhanced water treatment

Anna Mikulan¹, Roman Dubovenko¹, Mariia Dmitrenko¹, Anna Kuzminova¹, Anton Mazur¹, Anastasia Penkova¹

¹ St. Petersburg State University, 7/9 Universitetskaya nab., Saint Petersburg 199034, Russia

E-mail: st097675@student.spbu.ru

https://go.spbu.ru/rqpenkova

Introduction

Protein separation presents a fundamental challenge in modern water treatment, biotechnology and the pharmaceutical industries, as they play a central role in various cellular processes. A highly effective and widespread method employed for protein separation is ultrafiltration (UF), which utilizes semipermeable membranes to selectively remove molecules of specific sizes. Ultrafiltration is the most actively used membrane method in various industries (food, chemical, microbiological, water purification, etc.). Due to its active use, the creation of new ultrafiltration membranes with improved transporting and antifouling properties is required.

The choice of eco-friendly cellulose derivatives, in particular nitrocellulose (CN) and cellulose acetate (CA) for the fabrication of UF membranes offers a promising solution for this purpose, combining ecological sustainability with good functional properties. Bulk modification of membranes plays a crucial role in the development of highly effective filtration materials. This approach significantly enhances the operational characteristics of membranes by creating composite membranes, wherein the incorporation of various additives allows for a synergistic effect. As a result, the final properties of the membranes surpass the simple sum of the characteristics of their individual components. The use of metal-organic frameworks (MOFs), which are unique porous structures with a high specific surface area, significantly influences the structure, permselectivity and hydrophilic-hydrophobic balance of the material and represent a promising class of modifiers that have found widespread application in the creation of composite membranes. Another classical class of additives includes porogens, which affect the transport characteristics and morphology of the resulting membranes. They allow for the control of pore size and distribution within the membranes, directly impacting their ability to separate molecules of varying sizes. Furthermore, one of the most popular synthetic polymer – polysulfone (PSU) was utilized as an additive due to its excellent film-forming properties, remarkable thermal and chemical stability, and its widespread application in membrane technology.

Results and discussion

This study focuses on the development and investigation of membranes from cellulose nitrate (CN) by blending it with cellulose acetate (CA) and modifying it with additives such as polysulfone (PSU), polyvinylpyrrolidone (PVP K-30), and a Zn-based metal-organic framework (ZnBIM) for efficient ultrafiltration separation of proteins. It has become important to study the structure of polymers, as this makes it possible to more accurately predict and study the properties of the resulting membranes. Among the methods that make it possible to determine the characteristics of polymers, nuclear magnetic resonance (NMR) is the best tool. NMR allowed us to study the degree of substitution of cellulose derivatives (CA, CN) in this work. Additional characteristics of the membrane samples were studied using Fourier transform infrared spectroscopy, scanning electron microscopy, atomic force microscopy and contact angle measurement. The transport properties of the developed membranes were studied by ultrafiltration during separation of protein mixtures.

Conclusions

Thus, the results clearly demonstrated that mixing CN with CA and the strategic use of additives can lead to the successful development of highly efficient CN-based membranes for UF separation of proteins. This makes them promising for use for separation and purification in the pharmaceutical industry.

Acknowledgements

The study was supported by the Russian Science Foundation grant No. 20-79-10064, <https://rscf.ru/en/project/20-79-10064/>. The experimental work was facilitated by equipment from the Resource Centers for Nanotechnology, Magnetic Resonance, Cryogenic Department, Thermogravimetric and Calorimetric Research Center; Center for Physical Methods of Surface Investigation, Center for Innovative Technologies of Composite Nanomaterials, Chemical Analysis and Materials Research Center, and Center “Nanofabrication of Photoactive Materials (Nanophotonics)” at the St. Petersburg State University.

Determination of the structure of regioisomeric furan-containing naphthofuranes based on 1D and 2D NMR spectroscopy experiments

Minaeva V. Yu., Ozerova O. Yu., Makarenko S. V.

Herzen State Pedagogical University of Russia, Department of Organic Chemistry

48 Moyka River Embankment, Saint Petersburg 191186, Russia

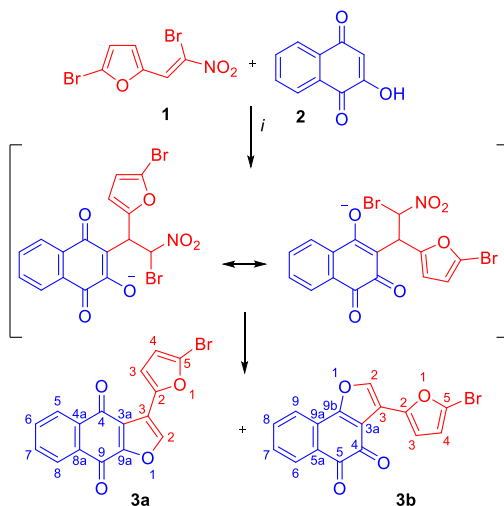
E-mail: kohrgpu@yandex.ru

http://kohrgpu.ru

We have previously shown that the interaction of furan-containing *gem*-bromonitroethenes with representatives of cyclic CH-acids leads to the formation of tri- and tetracyclic heterocyclic structures of the dihydrofuran and furan series [1].

The study of the reaction of a representative of furan-containing *gem*-bromonitroethenes – 2-(5-bromofuryl)-1-bromo-1-nitroethene **1** with 2-hydroxynaphthoquinone-1,4 **2** showed that the process leads to the formation of a mixture of regioisomeric 3-(5-bromofuran-2-yl)naphtho[2,3-*b*]furan-4,9-dione **3a** and 3-(5-bromofuran-2-yl)naphtho[1,2-*b*]furan-4,5-dione **3b** (ratio 1:1.17 according to the ^1H NMR spectrum), which was successfully separated into individual isomers by recrystallization (Scheme 1).

Scheme 1.



i: C_6H_6 , Et_3N , 3 h, reflux or MeOH, AcOK, 3d, r.t.

The synthesized 3-(5-bromofuran-2-yl)naphtho[2,3-*b*]furan-4,9-dione **3a** and 3-(5-bromofuran-2-yl)naphtho[1,2-*b*]furan-4,5-dione **3b** can exist as *s-cis*- and *s-trans*-conformers (Fig. 1). The presence of one set of signals in the ^1H and ^{13}C NMR spectra of individual substances **3a**, **b** indicates that they are formed by configurationally homogeneous (Fig. 1).

Thus, the aim of this work is to determine the fine structure of 3-(5-bromofuran-2-yl)naphtho[2,3-*b*]furan-4,9-dione **3a** and 3-(5-bromofuran-2-yl)naphtho[1,2-*b*]furan-4,5-dione **3b** by 1D and 2D NMR spectroscopy experiments.

Two doublets at 6.46 and 7.63 ppm ($^3J = 3.5$ Hz) of the C³H and C⁴H protons of the furan ring, a singlet at 8.14 ppm of the C²H proton and two multiplets of the protons of the condensed benzene ring in the regions 7.86–7.75 ppm и 8.27–8.19 ppm are observed in the ¹H NMR spectrum of isomer 3a (Fig. 2).

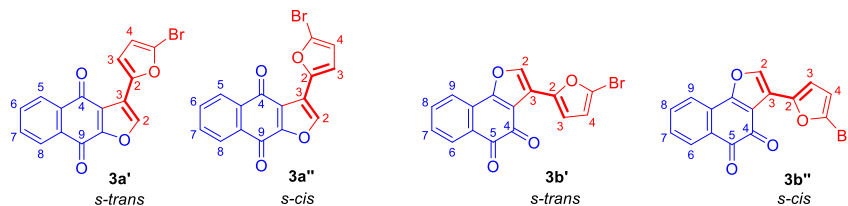


Figure 1. Possible conformational isomers of compounds 3a and 3b.

In the ¹H-¹³C HMBC spectrum of isomer 3a, cross peaks of the downfield multiplet of the benzene ring in the region of 8.27–8.19 ppm and signals of carbon atoms at 173.63 and 180.20 ppm are observed, which is possibly a consequence of the interaction of the C⁵H and C⁸H protons with the carbonyl carbon atoms C⁴ and C⁹, confirming the structure of the regioisomer 3a (Fig. 3).

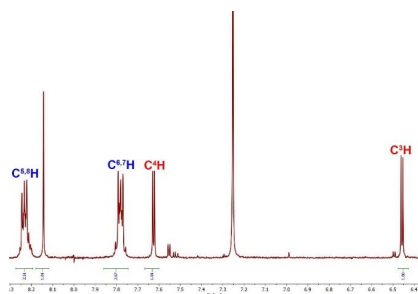


Figure 2. ¹H NMR spectrum of the compound 3a (CDCl₃).

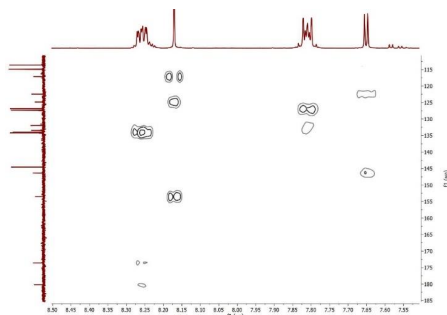


Figure 3. ¹H-¹³C HMBC NMR spectrum of the compound 3a (CDCl₃).

The study of compound 3a by the ¹H-¹H NOESY experiment showed that the C³H and C⁴H protons of the furan ring, as well as C⁵H, C⁶H, C⁷H, C⁸H, regularly demonstrate the Nuclear Overhauser Effect, while the C²H proton does not correlate with the C³H and C⁴H protons of the furan ring, which allows us to assign the *s-trans* configuration to this compound (Fig. 4).

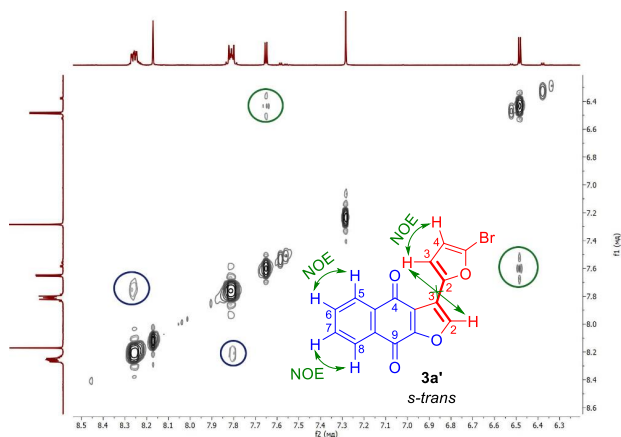


Figure 4. ^1H - ^1H NOESY spectrum of the compound **3a** (CDCl_3)

Thus, based on the results of the ^1H - ^1H NOESY experiment, the *s-trans* configuration of the obtained 3-(5-bromofuran-2-yl)naphtho[2,3-*b*]furan-4,9-dione **3a** was established. The configuration of 3-(5-bromofuran-2-yl)naphtho[1,2-*b*]furan-4,5-dione **3b** is undergoing further studies.

References

1. Minaeva V.Yu., Marshev E.D., Popov G.S., Pilipenko I.A., Stepanova A.M., Ozerova O.Yu., Makarenko S.V. Synthesis of tri- and tetracyclic bifuran structures based on furan-containing gem-bromonitroethenes // Abstracts of the II Interdisciplinary All-Russian youth scientific school-conference with international participation "Molecular design of biologically active substances: biochemical and medical aspects". Kazan. September 16-20 2024. P. 115.

Conformational behavior of cyclic peptides cyclosporin C and alisporivir in acetonitrile and their interaction with Dy^{3+} ions

Guzel A. Minnullina, Islam N. Garifullin, Sergey V. Efimov, Vladimir V. Klochkov

Institute of Physics, Kazan Federal University, Kazan, 420008 Russia

E-mail: g.minnullina2010@yandex.ru

Introduction

Cyclosporins are cyclic undecapeptides with immunosuppressive, antiviral, antifungal and anti-inflammatory properties. For example, cyclosporin A (CsA) is widely used to prevent graft rejection in organ transplants [1]. There are analogues of CsA with pharmacologically valuable properties, most of which are different from CsA in one or two sites by a change of amino acid or N-methylation state. Cyclosporin C is one of those candidates: it is a natural analogue of CsA, a cyclic undecapeptide in which aminobutyric acid is replaced by threonine (Fig. 1). The results of studies with CsC showed that it has a strong immunosuppressive activity while being less nephrotoxic than CsA [2].

Another analogue of CsA is alisporivir (Debio-025): it is a non-immunosuppressive derivative of CsA which is known for its antiviral activity and ability to modulate the immune response (Fig. 1).

It is known that the activity of peptides, including bioavailability, depends on their conformation in solution, which can be affected by the environment: interaction with metal ions or various solvents. The aim of this work was to investigate the effect of the dysprosium ion Dy^{3+} on the structure of alisporivir and CsC in acetonitrile (CD_3CN) using an approach based on nuclear magnetic resonance (NMR) spectroscopy in the presence of paramagnetic ions [3].

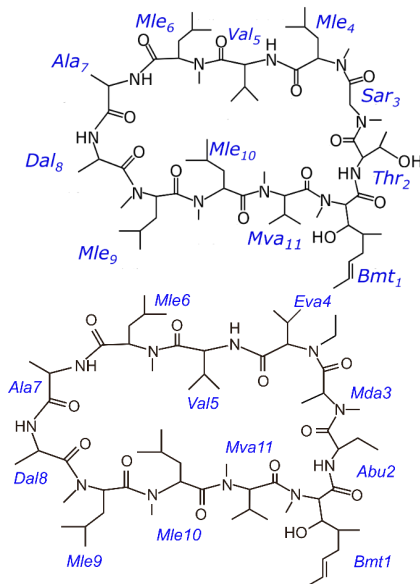


Figure 1. Chemical structures of cyclosporin C (left) and alisporivir (right).

Method

NMR measurements were carried out on a Bruker Avance III HD 700 spectrometer (700 MHz for ^1H , 175 MHz for ^{13}C). The temperature of 298 K was stabilized during the experiments.

Samples were prepared by dissolving the peptides in deuterated acetonitrile (CD_3CN) at a concentration of 1.0 – 1.4 mM. Dy^{3+} ions were added to achieve the relative ion:peptide molar ratio of 1:4. Two-dimensional spectra (DQF-COSY, TOCSY, ROESY, ^1H - ^{13}C HSQC, and ^1H - ^{13}C HMBC) were recorded before adding the ion, afterward the ^1H - ^{13}C HSQC spectrum of the CsC- Dy^{3+} complex was obtained. Data acquisition and processing were carried out using TopSpin 3.5. The spectral analysis and peak integration in HSQC spectra were made with the aid of the Sparky program.

Simulated annealing was carried out using XPLOR-NIH. Molecular dynamics was simulated in GROMACS 2018.6 with explicit solvent. Cubic cell had the size of $3 \times 3 \times 3$ nm and contained one alisporivir molecule (199 atoms) and 839 H_2O molecules (tip4p). Conformational screening was made using CREST software [4].

Results and Discussion

A total assignment of ^1H and ^{13}C signals for the major conformer of CsC was obtained and the chemical shifts of some signals of the minor conformer were determined. The effect of adding Dy^{3+} on the HSQC spectrum was examined by comparing HSQC spectra that have been recorded in the absence and the presence of Dy^{3+} : the fragment of superposed spectra is shown in Fig. 2. Leucine Mle*4 CH_α signal of the second conformer was not observed, so the fragment of spectra includes CH_α signals of 11 residues of the major conformer (written in black letters) and CH_α signals of 10 residues of the minor conformer (written in green letters). Adding dysprosium ions induces a slight broadening of CsC resonances and slightly shifts the peaks. Upon the addition of Dy^{3+} ions, the CH_α signals of all residues of the main conformer remain, and the signal of leucine Mle*9 of the minor conformer disappears.

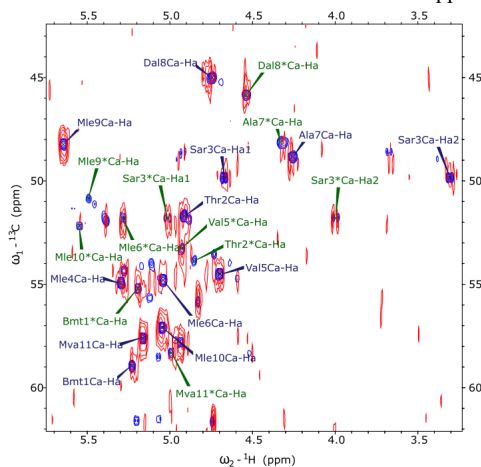


Figure 2. Fragment of ^1H - ^{13}C HSQC spectra of CsC in CD_3CN before and after the addition of Dy^{3+} ions: blue peaks correspond to the spectrum recorded with the pure CsC sample; red peaks, to the spectrum of the CsC- Dy^{3+} mix. Signals of the minor (second) conformer are marked with the asterisk (*).

The signal intensities of these two conformers for free CsC and CsC–Dy³⁺ mix were measured. To compare intensities of signals, autoscaled integral intensities in the 2D HSQC spectra were calculated for the both conformers [3]. The analysis of the obtained results allowed us to conclude that the Dy³⁺ ions bind to the cyclosporin backbone so that it is placed closer to alpha protons of residues Bmt1, Sar3, Mle6 and Ala7; this conclusion is corroborated by selective broadening of the CH α signals in the mentioned residues. However, the structure of the peptide (first of all, distribution of *cis*- and *trans*-peptide bonds in the backbone) does not change significantly upon binding to the ion.

A similar behavior is observed in the case of alisporivir in CD₃CN. Two conformers of Debio-025 were observed in acetonitrile, one of which shows signals similar to those of the single conformer of alisporivir in chloroform. The addition of Dy³⁺ ions affects the two conformers differently: clear trend was not found for the first conformer, but CH α signals of residues from Val5 to Mva11 decreased significantly. It means that one of the conformers of Debio-025 has an interaction with the dysprosium ion.

To obtain information on peptide bonds, a model structure with two *cis*-bonds between residues Bmt1-Abu2 and Mda3-Eva4 was prepared using XPLORE-NIH software. This model served as the initial structure in the MD simulation in GROMACS. Next, the structure was optimized by a semiempirical calculation.

A conformational search for alisporivir in CD₃CN was performed using CREST (Conformer-Rotamer Ensemble Sampling Tool) with the continuum solvent model. Low-energy conformers were isolated to be used for subsequent construction of complexes with the metal ion; the most favorable conformer had the relative population of 59%.

Acknowledgements

The work was supported by the Russian Science Foundation (project no. 24-23-00427).

References

1. M. Hamawy, S. Knechtle. Overview of the Actions of Cyclosporine and FK506. Transplantation Reviews, 2003, Vol. 17 (4), P. 165-171.
2. N. Sadeg, C. Pham-Huy, P. Rucay et al. In Vitro and In Vivo Comparative Studies on Immunosuppressive Properties of Cyclosporines A, C, D and Metabolites M1, M17 and M21. Immunopharmacology and Immunotoxicology, 1993, Vol. 15, P. 163-177.
3. A. Bernini, O. Spiga, V. Venditti et al. The use of a ditopic Gd(III) paramagnetic probe for investigating α -bungarotoxin surface accessibility. Journal of Inorganic Biochemistry, 2012, Vol. 112, P. 25-31.
4. P. Pracht, S. Grimme, C. Bannwarth et al. CREST – A program for the exploration of low-energy molecular chemical space. The Journal of Chemical Physics, 2024, Vol. 160 (11), P. 114110.

Hydrogen/deuterium isotope effects on the microstructure and molecular mobility in the aqueous solution of europium nitrate. A molecular dynamics simulation study

D.A. Mizyulin, A.V. Egorov

Faculty of Physics, St. Petersburg State University, Russia

E-mail: st084970@student.spbu.ru

Trivalent europium ion (Eu^{3+}) plays an important role in chemistry, materials science, and biology. Investigation of its interactions with water is important for a large number of applications. In the present work, hydrogen/deuterium isotope effects on Eu^{3+} hydration are studied using molecular dynamics simulations.

Simulations were carried out using the MDynaMix v.5.0 software package [1]. Solutions of $\text{Eu}(\text{NO}_3)_3$ in H_2O and D_2O at 10 different concentrations (from 0.05 to 4 mol/kg) were considered. The calculations were performed in an NPT ensemble at 298 K and 1 atmosphere. The temperature was kept constant using a Nose-Hoover thermostat [2], and the pressure was maintained by a Hoover barostat [3]. The SPC/E [4] water model was considered. Model for heavy water was developed by merely changing the hydrogen mass in a classical concept. The Eu^{3+} cation was modeled using the potential described in Ref. [5]. Model nitrate anion was treated as a 4-site planar structure with a central nitrogen atom and three oxygen atoms at a distance of 1.22 Å with all O-N-O angles of 120° [6]. Intermolecular interactions were described as the sum of Coulomb and Lennard-Jones (6-12) potentials. Their parameters were taken from Ref. [7]. The equations of motion were solved using the Verlet algorithm with a time step of 2 fs. The electrostatic interactions were treated using Ewald method. The geometry of the model water molecules and nitrate anions was maintained using the SHAKE algorithm [8]. For each system the equilibration time was equal to 1 ns, the following simulation run was 1 ns long.

Based on the simulation results, the radial distribution functions between all atoms were calculated. A special attention was given to the changes in the composition of the first solvation shell of the europium ion with increasing salt concentration. Hydrogen/deuterium isotope effects on the molecular mobility (diffusivity and rotational reorientation of the solution components) were considered in detail.

References

1. A.P. Lyubartsev, A. Laaksonen, MDynaMix / A scalable portable parallel MD simulation package for arbitrary molecular mixtures / – 2000. – 128. – P 565.
2. Nosé, S. / A molecular dynamics method for simulations in the canonical ensemble. *Molecular Physics* / – 1984. – 52(2). – P 255.
3. Martyna, G. J., Tuckerman, M. E., Tobias, D. J., & Klein, M. L. / Explicit reversible integrators for extended systems dynamics. *Molecular Physics* / – 1996. – 87(5), – P 1117.
4. H. J. C. Berendsen, J. R. Grigera, and T. P. Straatsma / The missing term in effective pair potentials / – 1987. – 912. – 4. – P 6269.
5. J. Chem. / *Thermodynamics* / – 1984. – 16. – P 921.
6. C. Ebner, R. Sansone, S. Hengrasmee, M. Probst. – *Int. J. Quant. Chem.*, 75, 805-814 (1999).
7. Egorov A.V., Komolkin A.V., Chizhik V.I., et al. / Temperature and concentration effects on Li - ion hydration. A molecular dynamics simulation study / *J. Phys. Chem. B* – 2003. – 107. – P. 3234.
8. Jean-Paul Ryckaert, Giovanni Ciccotti, Herman J.C Berendsen / Numerical integration of the cartesian equations of motion of a system with constraints: molecular dynamics of n-alkanes, *Journal of Computational Physics* / – 1977. – 23. – 3. – P 327.

Computer simulation of interaction of fullerenes C60 with short amyloid peptides

Polina A. Anufrieva, Sofia E. Mikhtaniuk, Alina S. Zaitseva, Valeriy V. Bezrodnyi, Emil I. Fatullaev, Igor M. Neelov

¹ St. Petersburg State University, St. Petersburg, 199034, Russia St. Petersburg

² National Research University of Information Technologies, Mechanics and Optics (ITMO University), St. Petersburg, 197101, Russia

³ "Kurchatov Institute"-PNPI-IVS, St. Petersburg, 199004, Russia;

E-mail: i.neelov@mail.ru

Introduction

Alzheimer's disease is incurable neurodegenerative diseases. Inhibition of aggregation of amyloid peptides is one of the promising ways of control of this disease [1-12]. Fullerenes has many applications in biomedicine including drugs and gene delivery, as antibacterial, antiviral and anti-amyloid agents. [13-16].

Molecular dynamics (MD) method was frequently used for simulation of interaction of anti-amyloid agents with amyloid fibrils. In this work the MD simulation of interaction of fullerenes with stack of short amyloid peptides (LMVGGVVIA) was performed in water solvent at temperature $T=300\text{K}$ and pressure $P=1\text{atm}$ using the program package Gromacs-23 with AMBER99SB-ildn force field.

The Results and discussion

Snapshots of systems consisting of fullerenes, peptides during simulation are shown on Fig. 1 (water molecules are not shown for clarity). One can see that at the beginning of simulation (Fig. 1, a) stack of peptide molecules is not in contact with fullerenes. After 5 ns (Fig. 1, b) the stack was already destroyed by interaction with fullerenes but peptide molecules are only partly adsorbed on fullerenes. At 20-25 ns (Fig. 1, c) all peptide molecules are adsorbed on fullerenes.

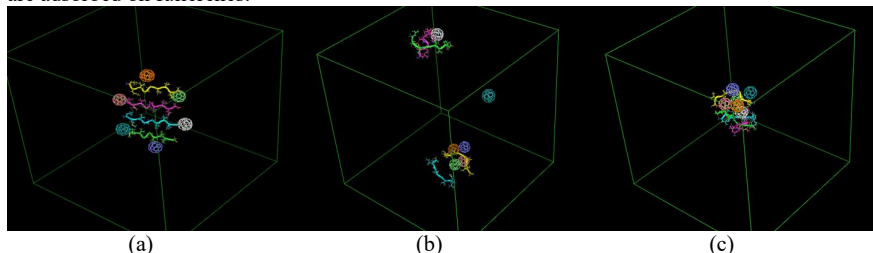


Figure 1. Snapshots of process of destruction of amyloid stack by fullerenes and fullerene-peptide complex formation : system consisting of 6 fullerenes C_{60} and 4 peptides at $t = 0$ (a), $t = 5$ ns (b), $t = 20$ ns (c);

The distance between peptide molecules and fullerenes (Fig.2) is important characteristic of complex formation between them. This distance during the first 20 ns (during the peptide stack destruction) fluctuates strongly. After 20 ns it decreases and then goes to plateau (because all peptides are already in contact with fullerenes). And after that all distances fluctuate only slightly because stable complex is created.

We demonstrated that fullerenes could destroy stack of amyloid peptides and form complex with separate amyloid peptides using molecular dynamics simulation approach. Thus fullerene probably could be used in future as anti-amyloid agent for curing of Alzheimer disease.

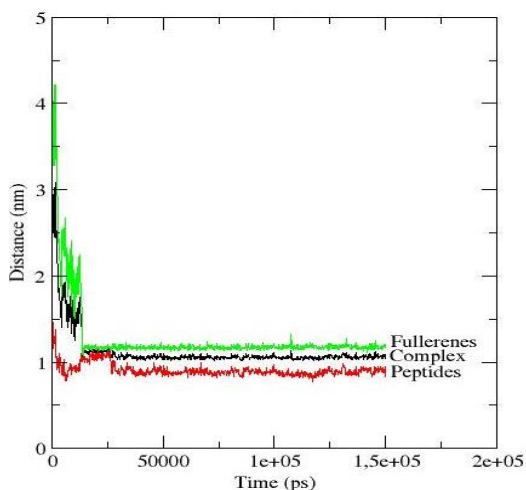


Fig. 2. Changes in distance between fullerenes and amyloid peptides during destruction of amyloid stack and complex formation.

Acknowledgements

The work was carried out with the support of St. Petersburg State University, project code 125022002755-5. The simulations were performed at the Computer Resources Center of SPbSU.

References

1. Petkova A.T., Yau W.M., Tycko R. "Experimental Constraints on Quaternary Structure in Alzheimer's β -Amyloid Fibrils". *Biochemistry*, 2006, 45, 498–512.
2. Klajnert B., Bryszewska M., Cladera J. "Molecular Interactions of Dendrimers with Amyloid Peptides: pH Dependence". *Biomacromolecules*, 2006, 7, 2186–2191.
3. Stelzmann, R.A.; Norman Schnitzlein, H.; Reed Murtagh, F. An English Translation of Alzheimer's 1907 Paper, "Über Eine Eigenartige Erkrankung Der Hirnrinde." *Clin. Anat.* 1995, 8, 429–431.
4. Knopman, D.S.; Amieva, H.; Petersen, R.C.; Chételat, G.; Holtzman, D.M.; Hyman, B.T.; Nixon, R.A.; Jones, D.T. Alzheimer Disease. *Nat. Rev. Dis. Prim.* 2021, 7, 33.
5. Lynch, C. World Alzheimer Report 2019: Attitudes to Dementia, a Global Survey. *Alzheimer's Dement.* 2020, 16,
6. DeTure, M.A.; Dickson, D.W. The Neuropathological Diagnosis of Alzheimer's Disease. *Mol. Neurodegener.* 2019, 14, 32,
7. 50. Tolar, M.; Hey, J.; Power, A.; Abushakra, S. Neurotoxic Soluble Amyloid Oligomers Drive Alzheimer's Pathogenesis and Represent a Clinically Validated Target for Slowing Disease Progression. *Int. J. Mol. Sci.* 2021, 22, 6355.
8. Bejanin, A.; Schonhaut, D.R.; La Joie, R.; Kramer, J.H.; Baker, S.L.; Sosa, N.; Ayakta, N.; Cantwell, A.; Janabi, M.; Lauriola, M.; et al. Tau Pathology and Neurodegeneration Contribute to Cognitive Impairment in Alzheimer's Disease. *Brain* 2017, 140, 3286.
9. Kollmer, M.; Close, W.; Funk, L.; Rasmussen, J.; Bsoul, A.; Schierhorn, A.; Schmidt, M.; Sigurdson, C.J.; Jucker, M.; Fändrich, M. Cryo-EM Structure and Polymorphism of A β Amyloid Fibrils Purified from Alzheimer's Brain Tissue. *Nat. Commun.* 2019, 10, 4760.
10. Makin, S. The Amyloid Hypothesis on Trial. *Nature* 2018, 559, S4–S7.

11. Chen, Z.; Krause, G.; Reif, B. Structure and Orientation of Peptide Inhibitors Bound to Beta-Amyloid Fibrils. *J. Mol. Biol.* 2005, 354, 760–776.
12. Takahashi, T.; Mihara, H. Peptide and Protein Mimetics Inhibiting Amyloid β -Peptide Aggregation. *Acc. Chem. Res.* 2008, 41, 1309–1318.
13. Kim, J.E.; Lee, M. Fullerene Inhibits β -Amyloid Peptide Aggregation. *Biochem. Biophys. Res. Commun.* 2003, 303, 576–579
14. Siposova, K.; Petrenko, V.I.; Ivankov, O.I.; Musatov, A.; Bulavin, L.A.; Avdeev, M. V.; Kyzyma, O.A. Fullerenes as an Effective Amyloid Fibrils Disaggregating Nanomaterial. *ACS Appl. Mater. Interfaces* 2020, 12, 32410–32419.
15. Podolski, I.Y.; Podlubnaya, Z.A.; Kosenko, E.A.; Mugantseva, E.A.; Makarova, E.G.; Marsagishvili, L.G.; Shpagina, M.D.; Kaminsky, Y.G.; Andrievsky, G. V.; Klochkov, V.K. Effects of Hydrated Forms of C 60 Fullerene on Amyloid β -Peptide Fibrillization In Vitro and Performance of the Cognitive Task. *J. Nanosci. Nanotechnol.* 2007, 7, 1479–1485.
16. Wang, X.; Weber, J.K.; Liu, L.; Dong, M.; Zhou, R.; Li, J. A Novel Form of β -Strand Assembly Observed in A β 33–42 Adsorbed onto Graphene. *Nanoscale* 2015, 7, 15341–15348

Investigation of interaction of cyclic peptide with short amyloid peptides by computer simulation

Alexey V. Vakulyuk, Sofia E. Mikhtaniuk, Valeriy V. Bezrodnyi, Emil I. Fatullaev,
Igor M. Neelov

¹ St. Petersburg State University, St. Petersburg, 199034, Russia St. Petersburg

² National Research University of Information Technologies, Mechanics and Optics (ITMO University), St. Petersburg, 197101, Russia

³ "Kurchatov Institute"-PNPI-IVS, St. Petersburg, 199004, Russia;

E-mail: i.neelov@mail.ru

Alzheimer's disease is known for over a hundred years and is considered the most common neurodegenerative disease worldwide. The incidence increases in proportion to the aging society and is most common among people over 75 year old [1-10]. Inhibition of aggregation of amyloid peptides is one of the promising ways of control of this disease. Linear [11-13] and cyclic peptides [13-20] have many applications in biomedicine including drugs and gene delivery, as antibacterial, antiviral and anti-amyloid agents.

Molecular dynamics (MD) method was frequently used for simulation of interaction of anti-amyloid agents with amyloid fibrils. In this work the MD simulation of interaction of cyclic peptide with stack of four short amyloid peptides (LVFFAE) was performed in water solvent at temperature $T=300\text{K}$ and pressure $P=1\text{atm}$ using the program package Gromacs-23, AMBER99SB-ildn force field and PME method for account of electrostatic interactions.

The Results and discussion

Snapshots of systems consisting of cyclic peptide RRRKKR and stack of four amyloid peptides (LVFFAE) during simulation are shown on Fig. 1 (water molecules are not shown for clarity). One can see that at the beginning of simulation (Fig. 1, a) stack of linear peptide molecules is not in contact with cyclic peptide. After 100ns (Fig. 1, b) the stack is already destroyed by interaction with cyclic peptide but linear peptide molecules are only partly adsorbed on cyclic peptide. At 500 ns (Fig. 1, c) all peptide molecules are adsorbed on the surface of cyclic peptide.

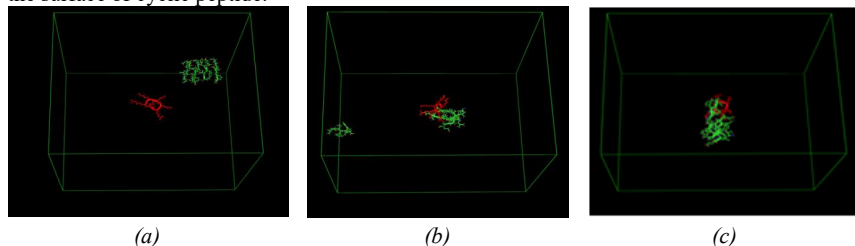


Figure 1. Snapshots of process of destruction of amyloid stack by cyclic peptide and cyclic-linear peptide complex formation: system consisting of one cyclic peptide and four linear amyloid peptides at $t = 0$ (a), $t = 15$ ns (b), $t = 75$ ns (c);

The distances between linear peptide molecules in amyloid stack increase in the begin of simulation (Fig.2b) due to desintegration of amyloid stack. At the same time cyclic peptide attracts linear peptides and distance between them decrease during first 30ns when short living complex occurs (Fig2a). Than there are large fluctuations of both distances until 70-80ns when stable complex of cyclic and linear peptides forms. After that all distances go to plateau because all linear peptides already adsorbed on cyclic peptide and form stable complex with it.

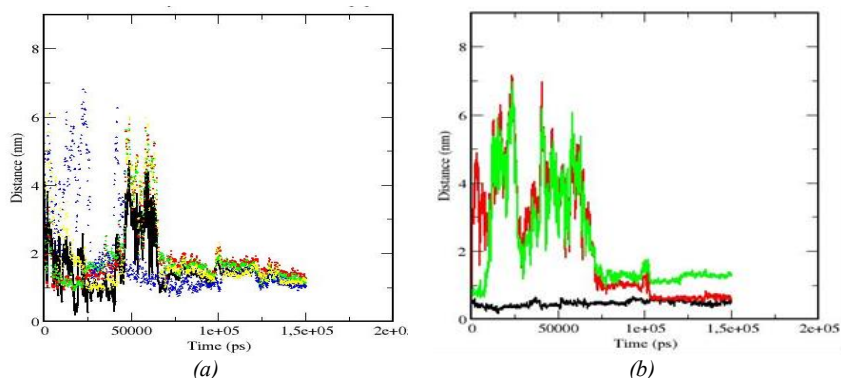


Fig. 2. Changes in distance a) between cyclic peptide and all (1st, 2nd, 3rd and 4th) linear amyloid peptides together (black) or separately: 1st (red), 2nd (green), 3rd (blue) and 4th (yellow) peptide in stack and b) between linear amyloid peptides 1-2 (black), 2-3 (red) and 3-4 (green) pairs of linear peptides in stack) during destruction of stack (0-50 ns) and complex formation (70-80 ns).

We demonstrated that cyclic peptides could destroy stack of amyloid peptides and form complex with separate amyloid peptides using molecular dynamics simulation approach. Thus, fullerene probably could be used in future as anti-amyloid agent for curing of Alzheimer disease.

Acknowledgements

The work was carried out with the support of St. Petersburg State University, project code 125022002755-5. The simulations were performed at the Computer Resources Center of SPbSU.

References

1. Petkova A.T., Yau W.M., Tycko R. "Experimental Constraints on Quaternary Structure in Alzheimer's β -Amyloid Fibrils". *Biochemistry*, 2006, 45, 498–512.
2. Klajnert B., Bryszewska M., Cladera J. "Molecular Interactions of Dendrimers with Amyloid Peptides: pH Dependence". *Biomacromolecules*, 2006, 7, 2186–2191.
3. Stelzmann, R.A.; Norman Schnitzlein, H.; Reed Murtagh, F. An English Translation of Alzheimer's 1907 Paper, "Über Eine Eigenartige Erkrankung Der Hirnrinde." *Clin. Anat.* 1995, 8, 429–431.
4. Knopman, D.S.; Amieva, H.; Petersen, R.C.; Chételat, G.; Holtzman, D.M.; Hyman, B.T.; Nixon, R.A.; Jones, D.T. Alzheimer Disease. *Nat. Rev. Dis. Prim.* 2021, 7, 33.
5. Lynch, C. World Alzheimer Report 2019: Attitudes to Dementia, a Global Survey. *Alzheimer's Dement.* 2020, 16.
6. DeTure, M.A.; Dickson, D.W. The Neuropathological Diagnosis of Alzheimer's Disease. *Mol. Neurodegener.* 2019, 14, 32.
7. 50. Tolar, M.; Hey, J.; Power, A.; Abushakra, S. Neurotoxic Soluble Amyloid Oligomers Drive Alzheimer's Pathogenesis and Represent a Clinically Validated Target for Slowing Disease Progression. *Int. J. Mol. Sci.* 2021, 22, 6355.
8. Bejanin, A.; Schonhaut, D.R.; La Joie, R.; Kramer, J.H.; Baker, S.L.; Sosa, N.; Ayakta, N.; Cantwell, A.; Janabi, M.; Lauriola, M.; et al. Tau Pathology and Neurodegeneration Contribute to Cognitive Impairment in Alzheimer's Disease. *Brain* 2017, 140, 3286.

9. Kollmer, M.; Close, W.; Funk, L.; Rasmussen, J.; Bsoul, A.; Schierhorn, A.; Schmidt, M.; Sigurdson, C.J.; Jucker, M.; Fändrich, M. Cryo-EM Structure and Polymorphism of A β Amyloid Fibrils Purified from Alzheimer's Brain Tissue. *Nat. Commun.* 2019, 10, 4760.
10. Makin, S. The Amyloid Hypothesis on Trial. *Nature* 2018, 559, S4–S7.
11. Chen, Z.; Krause, G.; Reif, B. Structure and Orientation of Peptide Inhibitors Bound to Beta-Amyloid Fibrils. *J. Mol. Biol.* 2005, 354, 760–776.
12. Takahashi, T.; Mihara, H. Peptide and Protein Mimetics Inhibiting Amyloid β -Peptide Aggregation. *Acc. Chem. Res.* 2008, 41, 1309–1318.
13. Ribarić S. Peptides as potential therapeutics for Alzheimer's disease, *Molecules.* 2018, 23, 283.
14. Appelt C. et al. Structures of cyclic, antimicrobial peptides in a membrane-mimicking environment define requirements for activity, *Journal of Peptide Science.* 2007. T. 14. № 4. C. 524–527.
15. Costa L., Sousa E., Fernandes C. Cyclic peptides in pipeline: What future for these great molecules? *Pharmaceuticals.* 2023, 16, 996.
16. Dougherty P. G., Sahni A., Pei D. Understanding cell penetration of cyclic peptides // *Chemical Reviews.* 2019, 119, 10241–10287.
17. Falanga A. et al. Cyclic peptides as novel Therapeutic microbicides: Engineering of Human Defensin Mimetics, *Molecules,* 2017. T. 22. № 7. C. 1217.
18. Miao J., Descoteaux M. L., Lin Y.-S. Structure prediction of cyclic peptides by molecular dynamics + machine learning, *Chemical Science,* 2021, 12, 14927–14936.
19. Pham J. D. et al. A Fibril-Like Assembly of Oligomers of a Peptide Derived from β -Amyloid // *Journal of the American Chemical Society.* 2014, 136, 12682–12690.
20. Zhang H., Chen S. Cyclic peptide drugs approved in the last two decades (2001–2021), *RSC Chemical Biology,* 2021. T. 3, 18–31.

Investigation of magnetic characteristics of magnetite nanoparticles in various organic shells

Yaroslav Yu. Marchenko¹, Vyacheslav A. Ryzhov¹, Vladimir V. Deriglazov¹,

Anastasia S. Dmitrieva^{1,2}, Anastasia V. Nikitina^{3,4}, Yuriy V. Bogachev³

¹ Petersburg Nuclear Physics Institute Named by B.P. Konstantinov of National Research Centre «Kurchatov Institute», Gatchina, Russia;

² Saint-Petersburg State Institute of Technology, St. Petersburg, Russia

³ Saint Petersburg Electrotechnical University, St Petersburg, Russia

⁴ Saint Petersburg State University (SPbSU), Saint Petersburg, Russia

E-mail: marchenko_yy@pnpi.nrcki.ru

Introduction

For such biomedical applications of magnetic nanoparticles (NP) as MRI diagnostics and therapy based on the hyperthermia effect, their magnetic and dynamic parameters are key. Their reliable determination is possible using a highly sensitive method of longitudinal nonlinear response to a weak alternating (AC) magnetic field $h(t)$ in the presence of a constant field H with registration of field dependences of the phase components $\text{Im}M_2(H)$, $\text{Re}M_2(H)$ of the second harmonic of magnetization (NLR- M_2) [1,2]. At frequencies of the megahertz order, nanoparticles with a magnetic moment in the range of $10^3 - 10^6 \mu_B$ generate a nonlinear response with pronounced extremes in magnetic fields of the order of $\sim (10 - 100)$ Oe. Greater information content is provided due to comparable values of the real and imaginary phase components of the nonlinear response signal. In this work, aqueous colloidal solutions of iron oxide nanoparticles were studied using the NLR- M_2 and electron magnetic resonance (EMR) methods. Processing the obtained experimental data based on the Fokker-Planck (FP) formalism allowed us to obtain comparative estimates of the magnetic and dynamic parameters of magnetite nanoparticles in dextran (NP-Dx) and citrate (NP-Cyt) shells and the degree of their aggregation in aqueous colloidal solutions. The both methods used in this work are non-destructive and NLR- M_2 allows us to characterize the state of NPs in a concentrated suspension.

Results and discussion

The NLR- M_2 signals from an aqueous suspension of NPs in dextran and citrate shells recorded at room temperature at a field scanning frequency of $F_{SC} = 0.25$ Hz are shown in Figure 1. An increase in the time allocated for relaxation during the field sweep H to 4 sec led to the disappearance of the field hysteresis observed at $F_{SC} = 10$ Hz, which indicated the dynamic nature of the field hysteresis and the superparamagnetic regime of NP ensembles both in dextran and citrate shells in an aqueous colloidal solution, which made it possible to use the FP formalism to approximate the M_2 signals [1]. The solid black lines in Fig. 1 represent the approximation of the field dependences of the phase components $\text{Re}M_2(H)$ and $\text{Im}M_2(H)$ of the nonlinear response by numerical solutions of the FP equation. The experimental dependencies are represented by symbols (forward scanning – circles, reverse scanning – triangles). As can be seen from Fig. 1, the theoretical curves describe the experimental signals well. The following parameters of magnetic centers in colloidal aqueous solutions of NPs in dextran and citrate shells, obtained by approximating the hysteresis-free M_2 response curves, are given in Table 1: saturation magnetization – M_S ; magnetic moment – M_C ; concentration of magnetic centers – N_C ; anisotropy energy – E_a ; dispersion of magnetic moment – σ ; attenuation coefficient – α ; Neel relaxation time – τ_N ; iron concentration in NP suspension, C_{Fe} , determined by the thiocyanate method; average nanoparticle concentration in suspension – N_{NP} , determined from the ratio of C_{Fe} to the average mass of the nanoparticle

magnetic core, $m_{\text{NP}} = 2.6 \cdot 10^{-15}$ mg, determined previously [1] for NPs in a dextran shell, synthesized using the technology used in this work; average number of NPs in an aggregate, N_a , determined from the N_{NP}/N_C ratio. Different organic shells lead to differences in NP aggregation, $N_a \approx 6$ for NP-Dx and $N_a \approx 4$ for NP-Cyt. This is probably due to the contribution to the stabilization of the resulting aggregates of not only magnetic (dipole) interactions of the magnetite cores of the NPs, but also Van der Waals interactions of the polar groups of the organic shells. The latter are apparently more effective in NP-Dx, which leads to a larger average number of particles in the aggregate. Dipole interactions of the NPs included in the aggregate lead to a decrease in the value of the magnetic moment of the aggregate compared to the sum of the magnetic moments of the NPs included in it, which is accompanied by a decrease in the free energy of the NP ensemble associated with a decrease in the magnetostatic energy of the aggregates.

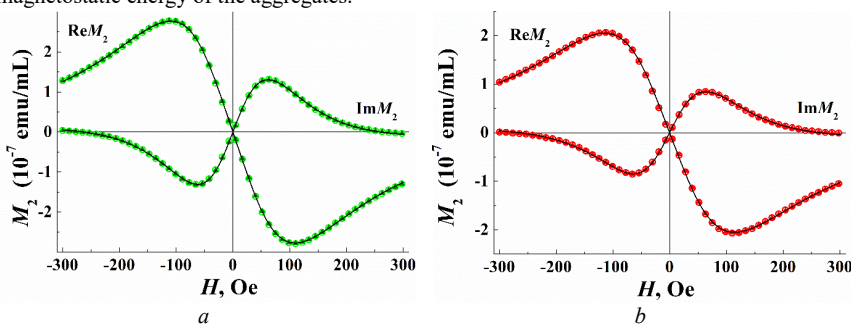


Figure 1. Real and imaginary parts of the nonlinear magnetic response as a function of the constant magnetic field for the nanoparticle in aqueous suspensions NP-Dx (a) and NP-Cyt (b)

Table 1. Parameters of nanoparticles

	M_S , emu/mL	M_C , μ_B	N_C , mL^{-1}	E_a , K	σ	α	τ_N , ns	C_{Fe} , mM/L	N_{NP} , mL^{-1}	N_a , agr $^{-1}$
NP-Dx	0.118(4)	42160(40)	$3.02(1) \cdot 10^{14}$	0.1(6)	0.545(2)	0.1326(3)	2.08(1)	87.5(2.5)	$1.89(6) \cdot 10^{15}$	6(1)
NP-Cyt	0.0963(6)	38280(60)	$2.71(2) \cdot 10^{14}$	0.2(6)	0.546(3)	0.139(1)	1.784(9)	57.2(1.9)	$1.23(5) \cdot 10^{15}$	4(1)

To obtain the EMR spectra of aqueous colloidal solutions of NP-Dx and NP-Cyt nanoparticles, a specialized X-band spectrometer ($F = 8.54$ GHz) was used to record broad lines in the modulation-free mode, developed at PNPI [1]. The spectrum was approximated by numerical solutions of the FP equation for magnetically correlated NP aggregates, which made it possible to estimate the crossover field between the region of magnetically correlated aggregates ($H < 1250$ Oe) and for independent NPs ($H > 1650$ Oe), which was $H_C \sim 1430$ Oe. As the field increases above H_C , the spin dynamics changes significantly. The attenuation constant α decreases to ≈ 0.125 , while the Neel time τ_N increases by ~ 5 times. This is important to consider in the practical application of magnetic NP colloids. Spectra with a g-factor of 2.3502 (NP-Dx) and 2.1183 (NP-Cyt) and approximately the same line width were obtained on a Bruker Elexsys E580 spectrometer in the modulation mode. Higher g-factor value for NP-Dx is probably explained by the presence of significant magnetic anisotropy associated with stronger bonds of the dextran molecules of the shell with the magnetic core of the NP. This, apparently, slightly deforms the magnetite core and leads to the appearance of shape anisotropy. In weak fields, in the region of dipole-correlated aggregates, the dipole interactions of NPs in the aggregate, which do not commute with the Zeeman interaction, lead to the formation of a complex pattern of electron levels and the appearance of a non-resonant

absorption signal in weak fields. Since the recorded signal is proportional to the diagonal component of the susceptibility tensor χ_{xx} symmetrical with respect to H , absorption is also present at $H = 0$. For NP-Cyt, the contribution of the weak-field absorption is noticeably smaller compared to NP-Dx, which indicates weaker dipole interactions in the aggregates of NPs in the citrate shell, i.e., a looser structure of these aggregates and correlates with a smaller average number of NPs in the aggregates (4 NPs/aggregate) compared to NP-Dx aggregates (6 NPs/aggregate) according to the nonlinear response data.

Conclusion

It was found that nanoparticles form aggregates in which NPs are linked by dipole-dipole interactions, the behavior mode of which corresponds to the superparamagnetic one. The formation of aggregates leads to a decrease in the magnetic moment of the aggregate with respect to the sum of the moments of the NPs included in it, due to dipole correlations, and, accordingly, to a decrease in the magnetostatic energy of the aggregate, which is accompanied by a decrease in the free energy of the entire ensemble of NPs. The organic shell affects the formation of aggregates and, accordingly, the number of NPs in the aggregate. The EMR studies of an aqueous colloidal solution of NP-Dx made it possible to estimate the crossover field from the mode of magnetically correlated aggregates to the mode of independent NPs $H_c \approx 1430$ Oe. For the NP-Cyt suspension, the low zero-field absorbance indicates a weaker magnitude of NP dipole interactions in the aggregate and a lower field of crossover, which is likely due to the looser structure of the aggregate. This correlates with the lower number of NPs in the NP-cyt aggregate (~ 4) compared to NP-Dx (~ 6) obtained from the analysis of NLR- M_2 results (Table 1).

Acknowledgments

The work was supported by the Russian Science Foundation grant № 23-25-00273, <https://rscf.ru/project/23-25-00273/>

References

1. Ryzhov V.A. et al. Comprehensive characterization of magnetite based colloid for biomedical applications. *Applied Physics A*, 2019. Vol. 125, No. 322. Pp. 1-11. doi: 10.1007/s00339-019-2596-7.
2. Ryzhov V.A. et al. On the spurious signal in the longitudinal nonlinear magnetic susceptibility of magnets at the second harmonic of the excitation frequency. *Tech. Phys.* 1996. Vol. 41, No. 6. Pp. 620-626.

Application of ^1H - ^{13}C HMBC NMR spectroscopy for identification of regioisomeric polycyclic dihydrofurans

Pilipenko I. A.,^{a,b} Ozerova O. Yu.,^a Makarenko S. V.^a

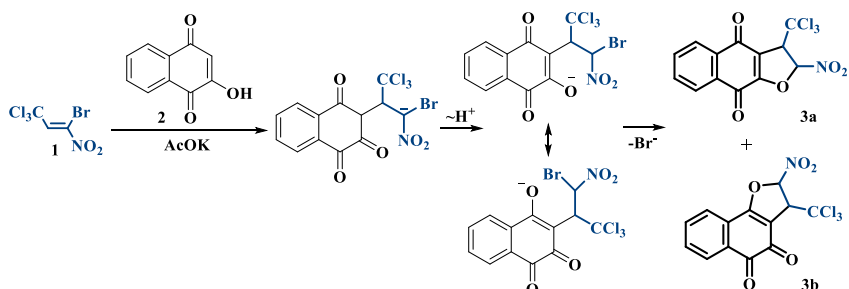
^a Herzen State Pedagogical University of Russia, Department of Organic Chemistry, Laboratory of Nitrocompounds, Center of collective use at the Faculty of Chemistry "Instrumental methods for the study of nitro compounds, coordination, biologically active substances and nanostructured substances", 48 Moyka River Embankment, Saint Petersburg 191186, Russia

^b Saint Petersburg State Forest Technical University, Department of Chemistry Institutsky per., 5, Saint Petersburg, 194021, Russia.

E-mail: kohrgpu@yandex.ru

<http://kohrgpu.ru>, <http://ckpo.herzen.spb.ru/?page=organic-chemistry>

The study of the interaction of 1-bromo-1-nitro-3,3,3-trichloropropene 1 with 2-hydroxy-1,4-naphthoquinone (lawsone) 2 showed that the reaction leads to the formation of a mixture of isomers – condensed 2-nitro-3-trichloromethyl-2,3-dihydrofurans of linear 3a and angular 3b structures, the ratio is ~1:1. The regioisomers were separated using preparative thin-layer chromatography.



The ^1H NMR spectra of the isolated compounds 3a, b contain doublets of protons of the dihydrofuran fragment C^3H 5.08 ppm and C^2H 6.46 ppm ($^3J = 1.9$ Hz) for 3a; C^3H 5.02 ppm and C^2H 6.51 ppm ($^3J = 1.6$ Hz) for 3b. J-coupling constants 3J ($\text{C}^2\text{H}/\text{C}^3\text{H}$) of the methine protons of the dihydrofuran ring for both isomers indicate their *trans* configuration. The signals of the protons of the naphthoquinone ring C^bH appear in multiplets at 7.76-7.92 ppm, the protons of C^aH form pairs of doublets at 8.17 and 8.23 ppm (3a), 7.93 and 8.25 ppm (3b). The close value of the chemical shifts of C^aH protons in 3a allows us to attribute to it the structure of linear dihydrofuran, a significant difference in the chemical shifts of isomer 3b allows us to consider its structure as angular.

The hypothesis is confirmed by the results of the ^1H - ^{13}C HMBC NMR spectroscopy experiment. Thus, in the HMBC spectrum of compound 3a (Figure 1), cross peaks of doublets of C^5H and C^8H and two carbonyl carbons C^4 and C^9 (8.17/178.92 ppm and 8.22/175.70 ppm) are observed, which clearly proves its linear structure.

Our accepted assignment of regioisomers is additionally confirmed by X-ray diffraction analysis performed for their representative, compound 3a (Figure 2). Its molecule is a linear tricyclic condensed dihydrofuran with a *trans* configuration of C^2H and C^3H protons.

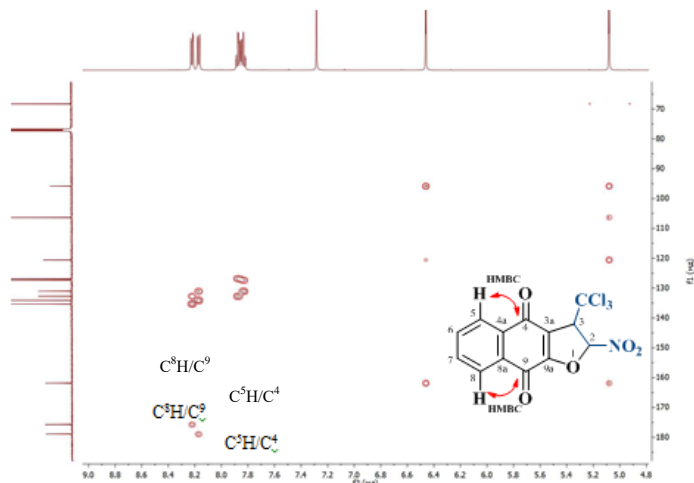


Figure 1. The fragment of ^1H - ^{13}C HMBC spectrum of compound 3a

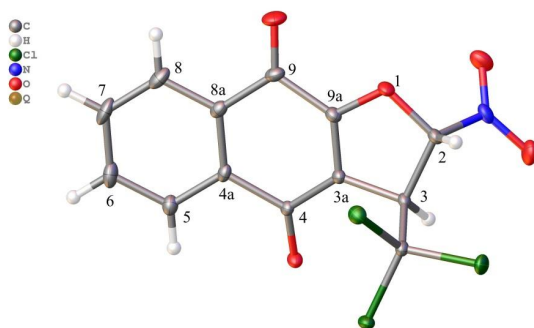


Figure 2. X-ray diffraction analysis of compound 3a

Thus, 1D ^1H NMR spectroscopy in combination with 2D methods (^1H - ^{13}C HMBC) makes it possible to unambiguously determine the structure of polyheterocyclic structures.

Acknowledgements

The research was supported by an internal grant of the Herzen State Pedagogical University of Russia (project 51-VG).

The spiro[1-azabicyclo[3.2.0]heptane] frameworks: structures determination using NMR methods

Julia A. Pronina¹, Alexander V. Stepakov², Stanislav I. Selivanov³

¹Saint-Petersburg State Institute of Technology (Technical University), Moskovsky prospect 26, 190013, Saint-Petersburg, Russia

²Institute of Chemistry, State University of Saint-Petersburg, University prospect 26, 198504, Saint-Petersburg, Russia

³Laboratory of Biomolecular NMR, St. Petersburg State University, 7/9 Universitetskaya nab., St. Petersburg, 199034, Russia

E-mails: ¹pronina.iuli05@yandex.ru; ³nmr.group.spbu@gmail.com

Introduction

NMR spectroscopy has changed the approach to studying the structures of the obtained compounds, thereby giving impetus to the development of organic chemistry. In a short time, NMR has become one of the most important methods not only for structural proof but also for studying the nature of chemical and physical processes. Currently, the attention of many scientists is focused on the development of simpler NMR approaches for the analysis of complex low- and high-molecular compounds [1, 2] and multicomponent mixtures [3].

Here, we present a study of the spatial structures of spiro (1) and dispiro[1-azabicyclo[3.2.0]heptane] (2) using NMR spectroscopy methods. These structures were obtained by an efficient one-pot three-component [3+2]-cycloaddition reaction of azomethine ylide, obtained *in situ* from isatin (3) and azetidine-2-carboxylic acid (4), with maleimide (5) and itaconimide (6), correspondingly (Fig. 1). This efficient synthetic protocol may have potential implications for medicinal chemistry and diversity-oriented synthesis.

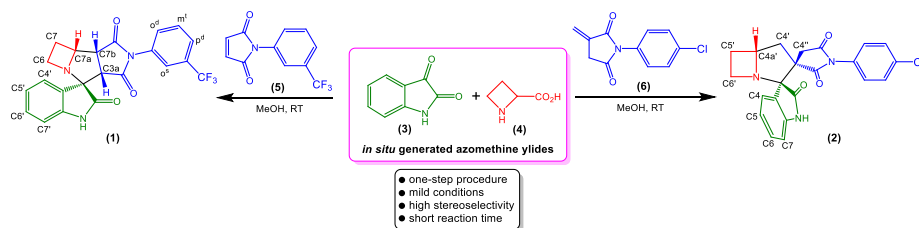


Figure 1. Scheme of reaction and structures of spiro (1) and dispiro[1-azabicyclo[3.2.0]heptane] (2) (Numbering of rings and some atoms are shown by figures)

Experiments and results

This report presents the results of studying the ¹H NMR spectrum of structures spiro (1) and dispiro (2) compounds in order to prove the structure of each of them. The identification of signals in the ¹H spectrum of compound (1) turns out to be somewhat simpler than in the case of (2) analysis. For example, in the case of identification of compound (1) based on NOESY data, the signals of protons NH, H7', H6', H5', H4', H6a do not overlap with others, as in compound (2). In addition, there are 3 identical protons for H6a in (1), and for (2), the signal of a similar proton was observed as a triplet of doublets (J = 8.8 and 5.2 Hz), indicating a difference in the spatial structure of the four-membered ring.

Other attributions of the signals in the aliphatic region of the proton spectrum of compound (1) were made based on the scalar and spatial interactions of the H6a α proton using the COSY and NOESY methods (Fig. 2a, b). In the aliphatic fragment of the NOESY spectrum spatial α - or β -orientation affiliation is inferred from comparing the intensities of the corresponding cross-peaks with the nearest neighboring protons. A good example of this

approach is the spatial interaction of proton 7a at 4.49 ppm. with protons at C7, the signals of which are at 2.55 and 2.01 ppm. The intensity of the cross-peak with the first of approximately 7 times exceeds the intensity of the cross peak with the second one. Hence, the proton at 2.55 ppm has the same spatial β -orientation with H7a, and the proton at 2.01 ppm, respectively, the opposite α -orientation. We quantified the interproton distances and obtained their experimental values using the MM2 method with an accuracy of $\pm 5\%$ for long-range sizes of the order of 5.5 Å for small molecules in liquid under the condition of extreme narrow limit: $\omega_0\tau_c < 1$ (Fig. 2c).

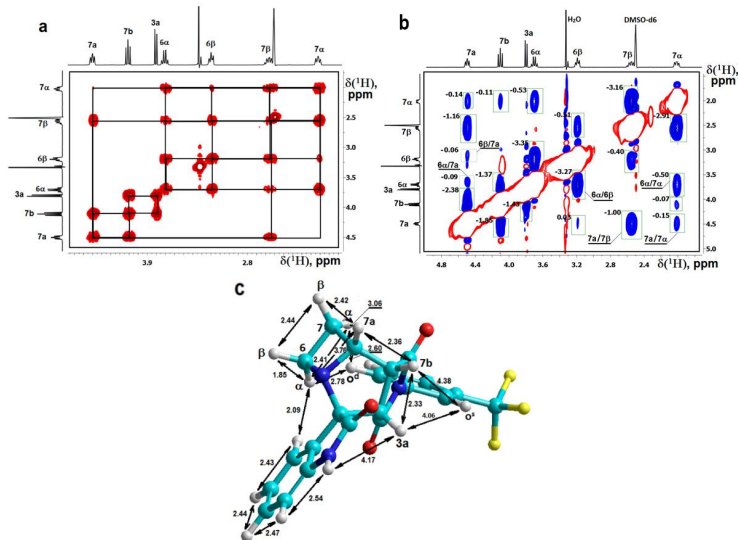


Figure 2. Aliphatic region of a) COSY and b) NOESY ($\tau_m = 0.5$ s) spectra of compound (1); c) spatial structure of this molecule.

We analyzed cross-peaks in the COSY and NOESY spectra of compound (2), which allowed us to determine the positions of aromatic proton signals (Fig. 3a, b). The key to the subsequent conformational analysis was the identification of the proton H4. After that, it was necessary to detect a weak spatial interaction of the NH proton with a proton at a frequency of 2.52 ppm, which has a doublet structure with a large constant of 18.5 Hz. This signal can be attributed to proton H4'' β , and the second doublet signal 3.19 belongs to proton H4'' α . The H4' α and H4' β protons have different values of the scalar vicinal constants $^3J_{\text{H-H}}$ 2.8 and 8.7 Hz with the H4a' proton which, according to the COSY spectrum data, has a multiplet signal at 4.54 ppm in the proton spectrum, reflecting the difference in the corresponding dihedral angles.

The key argument in favor of the dominance of conformer (B) of compound (2) in this case is the absence of spatial interactions of the H4 proton with two α -protons H4' α and H5' α , the calculated distances with which for conformer (A) are, respectively, 2.23 and 2.42 Å, and for conformer (B), respectively, 4.83 and 4.18 Å. Such large (more than 2 times) differences in these distances provide a qualitative (but not quantitative) assessment of the ratio of these conformers in favor of the dominance of (B), which is independently confirmed by the calculated values of their energies of formation: $E^{(A)} = 79.86$ kcal/mol and $E^{(B)} = 78.37$ kcal/mol. The difference in these energies (ΔE) is 1.49 kcal/mol and suggests the existence in

solution of a small (about 10%) amount of conformer (A) in the state of fast (in the NMR time scale) conformational equilibrium with the dominant conformer (B). This equilibrium is associated with the change in the type of the 3'-envelope of the five-membered ring $N^1-C^2-C^3-C^4-C^{4a}$ in the region of two spiro junctions, which is shown in Fig. 3d. According to calculations (MM2), the transition from conformer (A) to (B) corresponds to a pseudo-rotation around the C^2-C^3 bond at an angle of 74.6° clockwise (Fig. 3e) and leads to a significant change in the spatial structure of the (2) molecule.

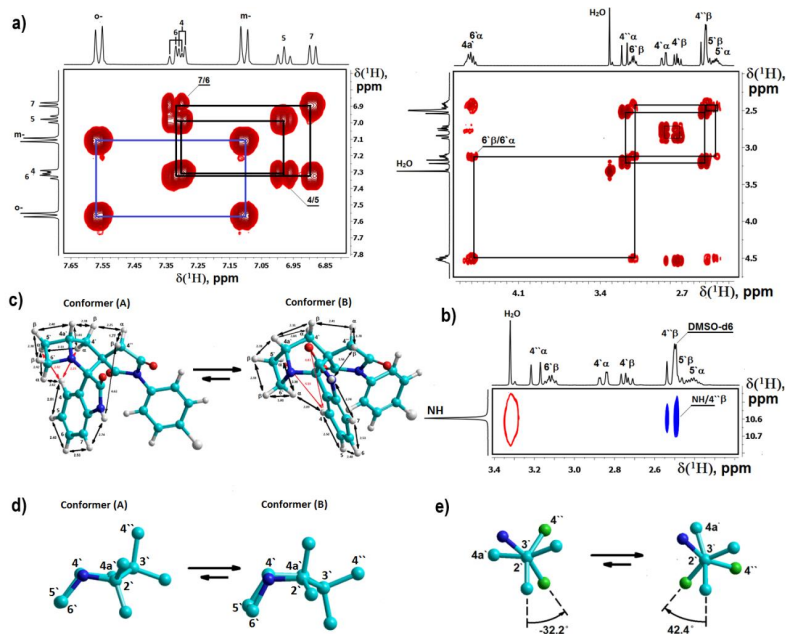


Figure 3. a) – Aromatic and aliphatic regions of COSY spectrum and b) – fragment of NOESY spectrum (at mixing time 0.5 s) of compound (2); c) – spatial structures of conformers (A) and (B) for compound (2); d) – the proposed conformational equilibrium of compound (2); e) – Newman projections along the C^2-C^3 bond for conformers (A) and (B) of compound (2)

Conclusion

Thus, the NMR study of compound (1) and (2) resulted not only in the complete identification of all proton signals but also provided argumentative confirmation of its spatial structure, both at the qualitative and/or quantitative levels.

Acknowledgements

NMR experiments were performed on spectrometer Bruker – 400 in the Resource Center “Magnetic Resonance Research Centre” of the Saint-Petersburg State University. SSI thanks Saint-Petersburg State University for supporting - research project 127400313.

References

1. W.F. Reynolds, R.G. Enriquez. J. Nat. Prod., 65, 221–244 (2002).
2. D. P. Frueh. Progress in NMR Spectroscopy, 78, 47–75 (2014).

3. M. Tiainen, P. Soininen, R. Laatikainen. J. Magn. Reson., 242(1), 67–78 (2014).

The spiro[1-azabicyclo[3.3.0]octane] frameworks: structures determination using NMR methods

*Julia A. Pronina*¹, Ekaterina V. Berezhnaya¹, Alexander V. Stepanov², Stanislav I. Selivanov³

¹Saint-Petersburg State Institute of Technology (Technical University), Moskovsky prospect 26, 190013, Saint-Petersburg, Russia

²Institute of Chemistry, State University of Saint-Petersburg, University prospect 26, 198504, Saint-Petersburg, Russia

³Laboratory of Biomolecular NMR, St. Petersburg State University, 7/9 Universitetskaya nab., St. Petersburg, 199034, Russia

E-mails: ¹pronina.iuli05@yandex.ru; ³nmr.group.spbu@gmail.com

Introduction

In NMR the main sources of information are indirect (scalar) and direct (through space) interactions between pairs of magnetic nuclei, which are characterized by a scalar constant (*J*) and the rate of cross relaxation (σ), respectively [1, 2]. The strategy of using NMR in structural and conformational analysis is based on the analysis of direct and indirect pair interactions, since they reflect the structural features of the compounds under study at a qualitative or quantitative level. Therefore, in most cases, two types of correlation experiments COSY and NOESY are necessary and (most often) sufficient tools for determining the structure and spatial arrangement of molecules in solution.

The effective use of this minimal set of NMR analysis methods is demonstrated by the example of studying three compounds (1-3), for each of which 4 possible variants of their structure are given and the one that corresponds to the NMR data is selected. Compounds (1-3) were obtained by an efficient [3+2]-cycloaddition reaction of stable azomethine ylide (4) with the corresponding inactive alkene (5-6) (Fig. 1).

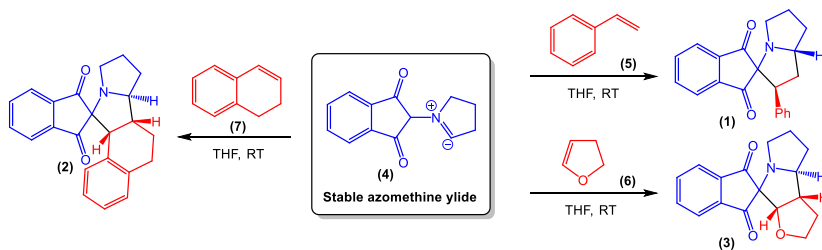


Figure 1. Scheme of reactions for the preparation and structures of derivatives spiro[1-azabicyclo[3.3.0]octane](1-3)

Experiments and results

In this work, when studying the ¹H NMR spectrum of compounds (1-3), the corresponding structure was selected and proved for each of them. Figure 2 shows four proposed structures of compound (1) and scalar bonding schemes between geminal and vicinal protons, which clearly show the structural differences between variants A, B and C, D. The simplest choice of one of the pairs is based on the number of scalar interactions of the C-H proton ("a") located next to the nitrogen atom. Based on the analysis of the cross-peaks of the COSY spectrum, it can be easily argued that (1) has the structure of A or B. This is based on the fact that the multiplet signal of proton a (at 4.95 ppm) has 5 (not 4) cross-peaks.

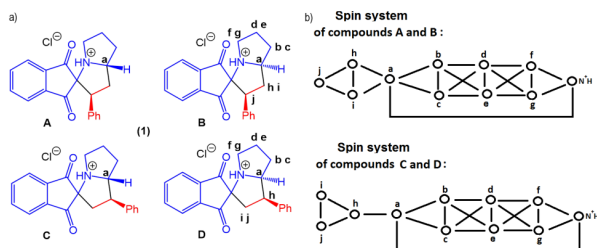


Figure 2. Four proposed structures of compound (1) (left) and scalar network (right) for A, B and C, D structures

The choice between structures A and B requires a correct analysis of the NOESY spectrum (Fig. 3). The NOESY data proved that in compound (1), proton a has the β -orientation. First of all, this is proved by the extremely intense cross-peak NH/a (3.99), the value of which indicates that proton a is the closest to the proton N⁺H. In addition, the proton a is characterized by intense cross-peaks a/h (5.11) and a/b (2.88) with the neighboring β -protons h and b, as well as a less intense cross-peak a/i (1.41). The structure of the 1-A molecule was optimized using the MM2 method. A comparison of experimental and calculated values revealed the absence of a/f cross-peak. This fact has given grounds for searching for the corresponding conformation of the five-membered ring in compound 1-A, in which the protons a and f are at a distance of more than 3.5 Å. Such a conformation (2) was found and is presented in the lower part of Figure 3D. The transition to considering conformation (2), stimulated by the absence of the a/f cross-peak in the NOESY spectrum, led to an improvement (more than 3 times) in the ratio of experimental and calculated values both at the quantitative (for the r_{a-i} distance) and qualitative (for the r_{a-f} distance) levels.

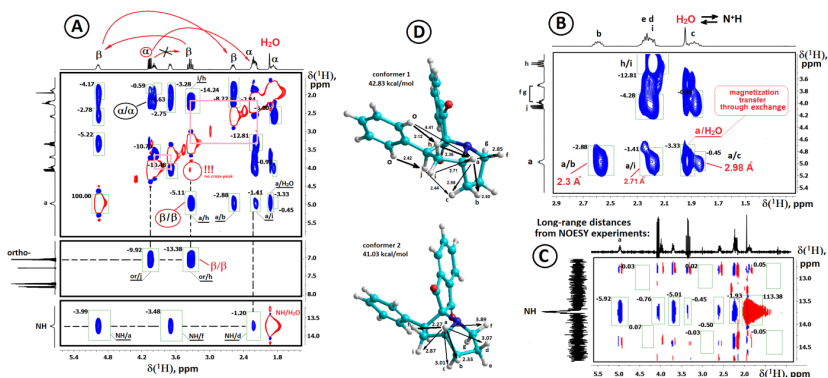


Figure 3. Fragments of NOESY ($\tau_m = 0.5$ s) spectrum (A, B, C) for compound 1 in $CDCl_3$ and calculated (MM2) its spatial structure. Cross-peak relative intensities are shown by numbers

The above approach was also applied to molecules (2) and (3) (Fig. 4). For both compounds, based on the data from the COSY spectrum, structures C and D can be excluded from consideration, as they both have only one scalar interaction for proton a. The position of protons b and c in the signal spectrum can also be easily determined.

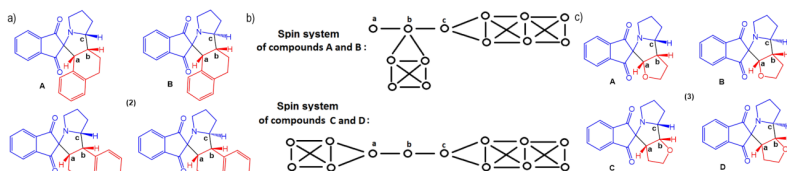


Figure 4. Four proposed structures of compound (2) and (3) (a, c) and scalar network (c) for A, B and C, D structures

Similarly to the previous case, it was possible to determine the β - or α -orientation of proton c by analyzing the NOESY spectrum and optimizing the geometry of the molecule using the MM2 method (Fig. 5). In the case of compound (2), there is a good (within $\pm 1.3\%$) quantitative agreement between the experimental and calculated distances. However, the assumption about the structure of B in compound (3) is more qualitative. The quantification is inaccurate due to the superposition of signal b on an unknown proton x, which also has a NOE with proton c. However, separating the integrals of overlapping cross-peaks is too difficult a task.

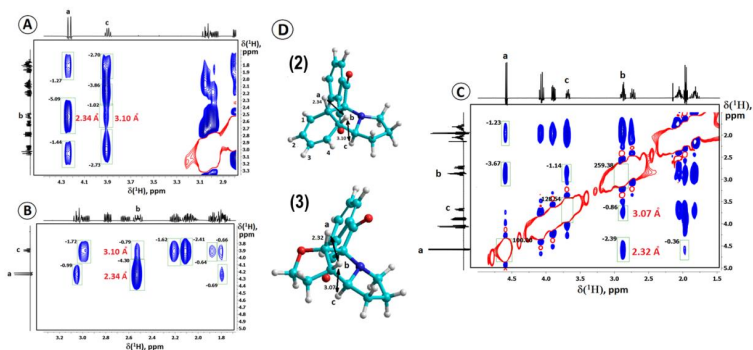


Figure 5. Fragments of NOESY ($\tau_m = 0.5$ s) spectrum (A, B) for compound (2) and (C) for compound (3) in CDCl_3 and calculated (MM2) its spatial structure (D), where proton-proton distances (r_{H-H}) are shown by numbers in Å

Conclusion

Using two methods of correlation experiments COSY and NOESY made it possible to achieve a complete solution to the problem. Thus, based on NMR spectroscopy data, compound (1) corresponds to regioisomer A, and compounds (2) and (3) correspond to regioisomer B.

Acknowledgements

NMR experiments were performed on spectrometer Bruker – 400 in the Resource Center “Magnetic Resonance Research Centre” of the Saint-Petersburg State University. SSI thanks Saint-Petersburg State University for supporting - research project 127400313.

References

1. M. Eberstadt, G. Gemmecker, D. F. Mierke, H. Kessler, *Angew. Chem. Int. Ed.*, **34**, 1671–1695 (1995).
2. B. Vögeli, *Progress in NMR Spectroscopy*, **78**, 1–46, (2014).

Different mechanisms of spin-lattice relaxation of gallium in semi-insulator GaAs

Andrey M. Rochev, Vladimir M. Mikushev, Elena V. Charnaya, Denis Yu. Nefedov

Physics Faculty, St. Petersburg State University, St. Petersburg

E-mail: st098173@student.spbu.ru

Introduction

Spin-lattice relaxation (SLR) of quadrupole nuclei in solids is due to several mechanisms. The "crystalline" quadrupole mechanism, which is an attribute of ideal insulator materials, is related to the interaction of nuclear quadrupole moments with dynamic gradients of electric fields caused by modulation of the interatomic distances by thermal phonons [1]. In conductors, SLR occurs due to the hyperfine coupling of nuclear magnetic moments with conduction electrons [2]. In real materials, which have both native paramagnetic defects and paramagnetic impurity atoms, there is a pronounced contribution of the "impurity" SLR mechanism, which involves spin diffusion [3]. In this case, the SLR acceleration is caused by the enhanced spin-lattice interaction near the paramagnetic centers due to dipole magnetic and quadrupole electric hyperfine coupling [4-6]. The use of NMR allows studying separately these mechanisms of SLR and obtaining information about properties of defects, which exist in real crystals. It was previously shown [4] that point paramagnetic centers and spin diffusion are involved in the continuous saturation of gallium spin systems in semi-insulator GaAs single crystals. This made it possible to develop a technique for separating contributions to gallium SLR using the additional resonance continuous fields applied during observation of the nuclear magnetization recovery [7]. Recently, it was proposed [8] to use a more accurate and sensitive technique for evaluating the slow component of nuclear magnetization restoration at positive spin temperatures under magnetic continuous saturation of the nuclear spin system.

Sample and experiment

The samples are semi-insulator GaAs single crystals with an electrical resistivity of $10^8 \Omega \text{ cm}$ at room temperature: undoped one with a concentration of uncontrolled impurities of no more than 10^{15} cm^{-3} and doped with chromium and copper up to concentrations of 10^{17} cm^{-3} . Two gallium isotopes can be observed by NMR: ^{69}Ga with a natural abundance 60.2% and a quadrupole moment $Q = 17.1 \cdot 10^{-30} \text{ m}^2$ and ^{71}Ga with a natural abundance 39.8% and a quadrupole moment $Q = 10.7 \cdot 10^{-30} \text{ m}^2$. These isotopes have different SLR rates.

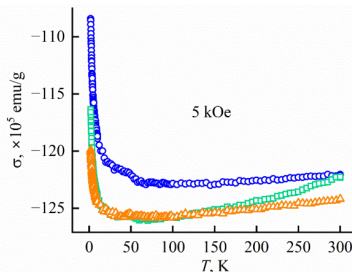


Figure 1. Temperature dependences of the magnetization σ of GaAs crystals at 5 kOe. Blue circles, green squares, and orange triangles correspond to the undoped GaAs and GaAs doped with Cr and Cu, respectively.

Studying the three samples using a Quantum Design MPMS SQUID VS magnetometer revealed very weak paramagnetism at low temperatures due to paramagnetic centers against the background of diamagnetic magnetization (Fig. 1). One can see that doping does not affect noticeably the magnetization of the samples.

NMR measurements were performed using a Bruker Avance III 400 pulse spectrometer optimized for solid samples in the range from room temperatures to 80 K. Relaxation of the ^{69}Ga and ^{71}Ga isotopes was observed under the inversion recovery protocol under additional continuous resonance magnetic saturation of the spin systems following the procedure described in detail in [8].

Results and discussion

The dependence of the relative integral intensity of the ^{69}Ga or ^{71}Ga NMR signal $Z(t)=A(t)/A_0$ on the time interval t between the 180° and 90° pulses was measured under application of additional weak long electromagnetic pulses at the Larmor frequency, which produced saturation of the gallium nuclear spin system to the value Z^{st} in the range from 1 to 0.1. The saturation factor is defined here as $Z^{st}=A^{st}/A_0$, where A^{st} and A_0 are the integral intensities of the NMR signals after a single 90° pulse under additional saturation and without it. When the mean spin temperature over the crystal volume is negative that corresponds to $Z(t)<0$ the recovery of nuclear magnetization follows the exponential law

$$Z(t) = Z^{st} [1 - b \exp(-t/\tau_1)], \quad (1)$$

where b is a numerical coefficient ($b<2$). For the positive average spin temperature ($Z(t)>0$), the magnetization recovery is described by the sum of two exponentials similar to [9] for any factors Z^{st} of continuous saturation:

$$Z(t) = Z^{st} \left\{ \rho \exp(-(t-t_0)/\tau_1) + (1-\rho) \exp(-(t-t_0)/\tau_2) \right\}, \quad (2)$$

where ρ is the coefficient characterizing the fraction of nuclei, which relax with relaxation time τ_1 . The emergence of the second exponential with a longer time of nuclear magnetization recovery demonstrates a decrease in the efficiency of spin-phonon coupling for the fraction $(1-\rho)$ of nuclei and corresponds to a decrease in the SLR rate. We emphasize that the second exponential appeared only at Z^{st} below a particular threshold value.

The dependences of the restoration times τ_1 and τ_2 on the saturation factor Z^{st} is shown in Fig. 2. The general analysis of relaxation under continuous saturation, which neglects the impact of paramagnetic centers, predicts the linear decrease of the restoration time with decreasing the saturation factor

$$\tau = T_1^\Sigma Z^{st}, \quad (3)$$

where T_1^Σ is the total relaxation time.

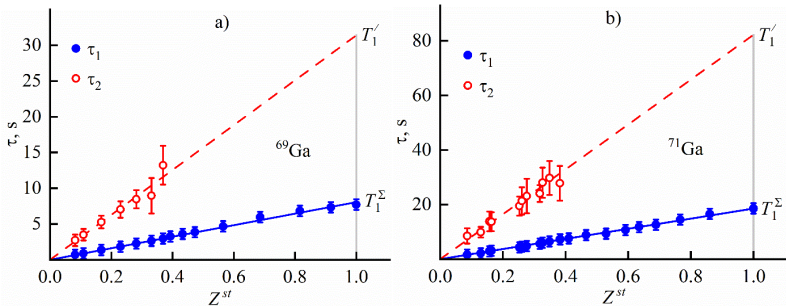


Figure 2. The restoration times τ_1 and τ_2 for a) ^{69}Ga and b) ^{71}Ga , depending on the continuous magnetic saturation factor Z^{st} in an undoped GaAs crystal at 90 K.

This agrees with the straight line shown for the $\tau_1(Z^{sf})$ dependence in Fig. 2, which is extended to T_1^Σ at $Z^{sf} = 1$.

The emergence of the contribution to nuclear SLR with the time τ_2 , which is longer than τ_1 , means the suppression of the “impurity” relaxation as a result of strong enough saturation ($Z^{sf} < 0.4$). Such suppression can occur only at positive spin temperatures. When «impurity» relaxation involving spin diffusion breaks down, the dependence $\tau_2(Z^{sf})$ should correspond to the time $T_1' > T_1^\Sigma$. The temperature dependences of T_1' is well described by the expression for the quadrupole SLR [1]. This agrees with the suggestion that the time T_1' corresponds to the “crystalline” mechanism of SLR while the “impurity” SLR is fully suppressed for the fraction $(1-\rho)$ of nuclei. This conclusion is also in agreement with the ratio between the relaxation times T_1' for the gallium isotopes, which is equal to the reciprocal ratio of the squared quadrupole moments. The defects responsible for the “impurity” relaxation could be the well known EL2 centers [9], which comprise the As ions on the gallium sites. At enough high temperatures such centers behave as elastic dipoles and generate local dynamic gradients of electric fields interacted with the nuclear quadrupole moments.

Acknowledgements

The measurements were carried out using the equipment of the Resource Centers of the St. Petersburg State University Scientific Park "Center for Diagnostics of Functional Materials for Medicine, Pharmacology and Nanoelectronics".

References

1. A. R. Kessel'. Nuclear Acoustic Resonance (in Russian). - Nauka, Moscow, 1969.
2. A. Abragam. The principles of nuclear magnetism. - Clarendon Press, Oxford, 1962.
3. G. R. Khutsishvili. - Sov. Phys. Uspekhi, 8, 743-768 (1966). DOI: 10.1070/PU1966v008n05ABEH003035
4. A. A. Kuleshov, V. M. Mikushev, A. L. Stolypko, E. V. Charnaya, and V. A. Shutilov. - Sov. Phys. Solid State, 28, 1837-1839 (1986).
5. E. V. Charnaya, V. M. Mikushev, E. S. Shabanova. - J. Phys.: Condens. Matter, 6, 7581-7588 (1994). DOI: 10.1088/0953-8984/6/37/012
6. A. A. Kuleshov, V. M. Mikushev, A. L. Stolypko, E. V. Charnaya. - Sov. Phys. Acoust., 35, 276-279 (1989).
7. P. Yu. Efitsenko, V. M. Mikushev, E. V. Charnaya. - JETP Lett., 54, 587-589 (1991).
8. V. M. Mikushev, A. M. Rochev, E. V. Charnaya. - Acoust. Phys., 69, 782-787 (2023). DOI: 10.1134/s1063771023601103
9. D. Laszig, H. G. Brion, P. Haasen. - Phys. Rev. B, 44, 3695-3701 (1991). DOI: 10.1103/PhysRevB.44.3695

Effect of rare earth impurities on structural properties of calcium phosphate-based materials by EPR spectroscopy

Margarita A. Sadovnikova¹, George V. Mamin¹, Darya V. Shurtakova¹, Margarita A. Goldberg², Nataliya V. Petrakova², Vladimir S. Komlev², Marat R. Gafurov¹

¹ Institute of Physics, Kazan Federal University, 420008 Kremlyovskaya 18, Kazan, Russia

² A.A. Baikov Institute of Metallurgy and Materials Science, Russian Academy of Sciences, 49 Leninsky pr., 119334 Moscow, Russia

E-mail: margaritaasadov@gmail.com

Introduction

A significant area of development in modern science and technology is the search for and creation of new materials with a predetermined set of physical and chemical properties. Doping crystalline structures with various impurities greatly extends their application range. The calcium phosphate (CaP) systems under investigation are widely used in biomedical applications, particularly in orthopaedics and maxillofacial surgery, as fillers for bone defects resulting from injuries or various diseases [1]. CaPs play an important role in tissue engineering, drug and gene delivery and many other biomedical applications [1]. The introduction of a number of rare earth (RE) elements into the CaP crystal structure, namely cerium (Ce^{3+}), neodymium (Nd^{3+}), europium (Eu^{2+}), gadolinium (Gd^{3+}) and erbium (Er^{3+}), allows us to obtain bioimaging systems that increase contrast when studying the dynamics of bone repair [2]. Modern diagnostics widely uses non-invasive imaging methods, including radiography, computed tomography (CT), single-photon emission computed tomography (SPECT), and magnetic resonance imaging (MRI). Ionizing radiation-based methods (radiography and CT), despite their high resolution and throughput, are associated with radiation risk and do not always provide sufficient contrast for accurate tissue differentiation. The search for new biocompatible and safe agents with more effective contrast enhancement is a popular area in practical diagnostics.

Thus, the present study focuses on the characterization of synthetic CaP doped with rare earth ions using continuous and pulsed electron paramagnetic resonance (EPR) techniques. The synthesis of CaP containing RE ions was carried out by precipitation from aqueous salt solutions [3].

Materials and methods

EPR measurements were performed in the continuous wave (CW) and pulsed modes in X-band ($\nu_{\text{mw}} = 9.6$ GHz) on a Bruker Elexsys E580 spectrometer. Field-swept electron spin-echo (ESE) spectra were recorded with the standard Hahn pulse sequence $\pi/2 - \tau - \pi$ with a $\pi/2$ pulse duration of 16 ns, and a minimal time delay $\tau = 240$ ns.

Results

Samples of magnesium-calcium phosphate powders with gadolinium impurity centers were studied by EPR at a temperature of $T = 297$ K, since the Gd^{3+} ion with the electron configuration $4f^7$ ($^8S_{7/2}$ is the ground state) is the only trivalent RE element that can be observed at room conditions. The CaP crystal lattice without paramagnetic impurities does not contain ions with a non-zero electron spin, which leads to the absence of an EPR signal. The presence of a resonance low-intensity signal ($g \approx 2$) for a nominally pure sample (Fig. 1 (a), blue inset) indicates the presence of an uncontrolled impurity in the structure due to the reagents used, presumably indicating the presence of oxide groups or a free radical on the surface of magnesium-calcium phosphate powder nanoparticles. Since the sample is in the form of powder, and the fine structure parameters have a strong dependence of the orientation of the nanocrystal on the external magnetic field B_0 , respectively, the EPR spectrum contains resonance contributions from all equally probable positions of the nanocrystals, which leads

to an inhomogeneous broadening of the EPR spectrum lines. It is also worth noting that the broadening of the resonance absorption line is due to the fact that the Gd^{3+} ion is characterized by a strong spin-lattice interaction and due to extremely short longitudinal relaxation times ($T_1 \approx 1/T_n$ (K), where n is the exponent depending on the relaxation mechanisms). Based on the characteristic EPR signals with g-factors ($g_{eff} = 5.8$, $g_{eff} = 2.8$ and $g = 1.9$), we can unambiguously conclude that Gd^{3+} is embedded in the crystal lattice of the sample under study. Analysis of the intensities of the EPR spectra for two different concentrations of gadolinium (0.5% Gd and 1% Gd) indicates that the proposed synthesis method allows the introduction of the amount of impurity centers declared during chemical synthesis into the CaP structure (the integral intensity differs by a factor of 2).

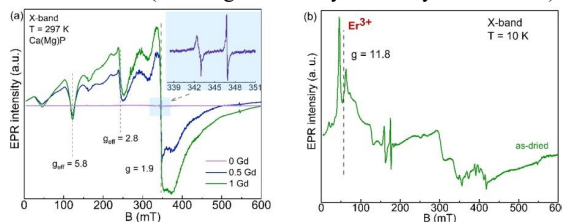


Figure 1. (a) Concentration dependence of CW EPR spectra in the X-band for magnesium-calcium phosphate powders with Gd^{3+} ; (b) EPR spectra recorded in CW mode in the X-band for hydroxyapatite with 0.25Er

The typical detection range of the Er^{3+} signal is up to 20 K, at temperatures above 30 K the EPR signal is usually not observed, so the experiment was carried out at a sample temperature of 10 K (Fig. 1(b)). In polycrystalline systems, all crystal orientations are statistically equally probable. As a result, the EPR spectrum of the powder is the superposition of all nanocrystal orientations. Figure 1(b) shows the EPR spectra recorded at a sample temperature of 10 K. According to the literature data [4] the signal at the g-factor of 11.8 refers to the RE element Er^{3+} . The weak structural inflections detected in the spectrum (Fig. 1(b)) are possibly associated with the emergence of a hyperfine structure as a result of interaction with the ^{167}Er isotope with a nuclear spin of $I = 7/2$ (abundance of 23%). Also, the presence of low-intensity resonance curves can be caused by the presence of various uncontrolled impurities on the sample surface or in the interstitial sites of the crystal lattice. Thus, the obtained results indicate the introduction of Er^{3+} ions into the crystalline lattice of hydroxyapatite in the proposed synthesis method.

Thus, it is shown that the EPR method is effective experimental tool for studying cationic doping. Based on the obtained results using the capabilities of modern methods of pulsed EPR spectroscopy, it can be used for the study of functional biomaterials doped with rare earth elements.

Acknowledgements

This research was funded by the RSF grant No 23-63-10056

References

1. N. A. Abdul Halim, M. Z. Hussein, M. K. Kandar. – *International Journal of Nanomedicine*, 6477-6496 (2021).
2. S. Mondal, S. Park, J. Choi, et al. – *Ceramics International*, **46** (18), 29249-29260 (2020).
3. N. V. Petrakova, Y. O. Zobkova, V. S. Komlev, et al. – *Ceramics International*, **50** (12), 20905-20916 (2024).
4. G. Gorni, A. Serrano, D. Bravo, et al. – *Journal of the American Ceramic Society*, **103** (7) 3930-3941 (2020).

Effect of alkaline treatment on structure, morphology, CO₂ sorption of mesoporous ZSM-5 zeolites

A. Samadov¹, I.A. Zvereva¹, G.A. Valkovskiy², M.G. Shelyapina², V. Petranovskii³

¹ Institute of Chemistry, St. Petersburg State University, Saint Petersburg 199034, Russia

² Faculty of Physics, St. Petersburg State University, Saint Petersburg 199034, Russia

³ CNyN, Universidad Nacional Autónoma de México, Ensenada 22860, B.C., Mexico

E-mail: azamatsamadov1245@gmail.com

Introduction

Zeolites are crystalline aluminosilicates those properties such as high ion exchange capacity, action as molecular sieves, and catalytic activity make them very attractive for application in a number of industrial processes. To tailor structures and properties of zeolites for a specific application, it is necessary to understand the effects of various modifications (either during synthesis or post-synthetic treatments) on their physico-chemical properties. The crystal structure of zeolites can be represented as an open three-dimensional framework formed by [SiO₄]⁴⁻ and [AlO₄]⁵⁻ tetrahedra connected by vertices that create regular voids: cavities and channel systems extended in one, two or three dimensions.

Zeolites normally belong to microporous materials as the size of the formed voids d does not extend 1 nm (according to IUPAC porous materials are classified on microporous ($d < 2$ nm), mesoporous ($2 < d < 50$ nm) and macroporous ($d > 50$ nm)). The uniformity of the pore size allows applying zeolites as molecular sieves. However, several studies showed the benefit of mesoporosity in a specific application due to the efficient mass-transport properties [1]. One such application is the capture of CO₂ [2] and its subsequent utilization, for example, in the carboxylation reaction of glycerol [3].

In this contribution, we report on the synthesis of a series of mesoporous ZSM-5 zeolites, their comprehensive characterization using various complementary methods, and the study of their sorption properties with respect to CO₂.

Synthesis

The samples of microporous NH₄-ZSM-5 zeolites with nominal Si/Al ratio 15, 25 and 40 were supplied by Zeolyst int. To prepare ZSM-5 with controlled hierarchical porosity they were treated in 0.2M or 0.4M of NaOH aqueous solution under stirring (350 rpm) at 65 °C for 30, 60, 90, 120 and 150 minutes. The resulting product was centrifuged for 10-15 min, washed in distilled water, and dried at 100 °C for 5-6 hours. The crystal structure of synthesized materials was controlled by X-ray diffraction (XRD) with Bruker D8 DISCOVER diffractometer. The elemental composition was determined by energy dispersive X-ray spectroscopy (Shimadzu EDX 800 HS). ¹H, ²³Na, ²⁷Al and ²⁹Si nuclear magnetic resonance (NMR) spectra were recorded under magic angle spinning (MAS) condition with rotation frequency 10 kHz using Bruker WB Avance III (400 MHz) spectrometer. Gas sorption isotherms (N₂ (at 77 K) and CO₂ (within the temperature range from 298 to 363 K)) were obtained using the Quadrasorb SI equipment.

Results and discussion

XRD confirms that after alkaline treatment the samples keep the zeolite crystal structure. EDX shows that the Si/Al ration for the parent commercial samples differs from the nominal one (19.8, 30 and 44 instead of 15, 20 and 40, respectively). The alkaline treatment leads to a gradual decrease in the Si/Al ratio over the treatment time, more pronounced for 0.4M NaOH, see Fig. 1, which confirms the leaching of silicon.

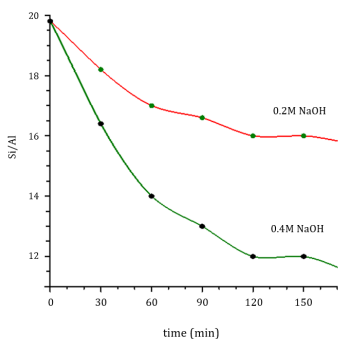


Figure 1. Change in the Si/Al ratio for ZSM-5 (nominal Si/Al = 15) during leaching at different NaOH concentrations.

According to ^{29}Si MAS NMR spectra the treatment leads to a decrease in silicon in $\text{Q}^4(0\text{Al})$ sites, mainly the signal at -116 ppm, with simultaneous increasing of $\text{Q}^3(1\text{Al})$ population (a signal at -107 ppm). It should be noted that all extra-framework Al, if any, are washed away after treatment in NaOH – no signal corresponding to octahedral Al are observed in ^{27}Al MAS NMR. ^1H and ^{23}Na MAS NMR spectra confirm the substitution of NH_4 by Na.

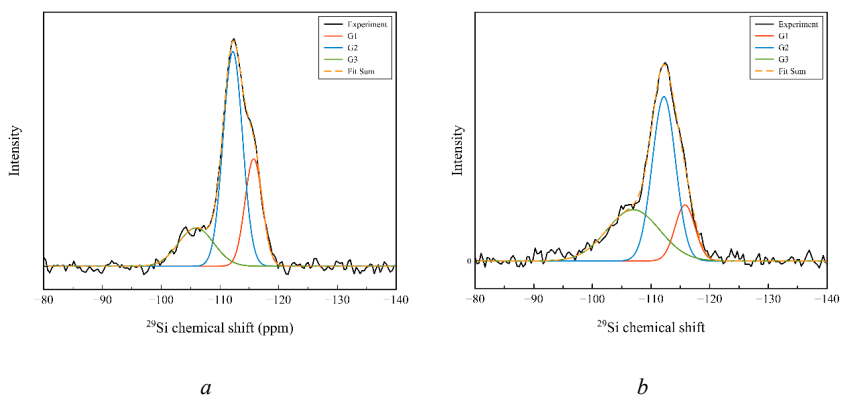


Figure 2. ^{29}Si MAS NMR spectra of the parent ZSM-5 zeolite (nominal Si/Al = 25) (a) and after treatment in 0.2M NaOH for 120 min (b).

Nitrogen porosimetry studies confirm that as the leaching time and/or the alkali concentration increases, the proportion of mesoporosity increases. For example, for ZSM-5 zeolite with nominal Si/Al = 15 the pore size increases up to 20 nm (for 0.2M NaOH, 120 min) and 28 nm (for 0.4M NaOH, 120 min).

The curves of the differential isosteric enthalpy of CO_2 adsorption (H_{iso}) for samples ZSM-5 zeolite with nominal Si/Al = 15 before and after treatment in 0.2M and 0.4M NaOH for 120 min are shown in Fig. 3. The enthalpy of CO_2 adsorption for these samples is of about ~30-40 kJ/mol (extrapolation to zero volume of the adsorbed gas), however, the samples show different dependence of H_{iso} on the adsorbed volume: for the parent zeolite sample it weakly depends on the adsorbed volume, that is typical for microporous systems. With increasing mesoporosity (leaching) an increase in the slope is observed. It indicates that the surface becomes more energetically heterogeneous. Nevertheless, for the sample treated in 0.2M

NaOH for 120 min even with maximum CO₂ coverage the enthalpy of adsorption is not lower than ~20 kJ/mol, which indicates that such a mild condition for creating mesoporosity ensures a fairly good interaction of CO₂ with the zeolite surface.

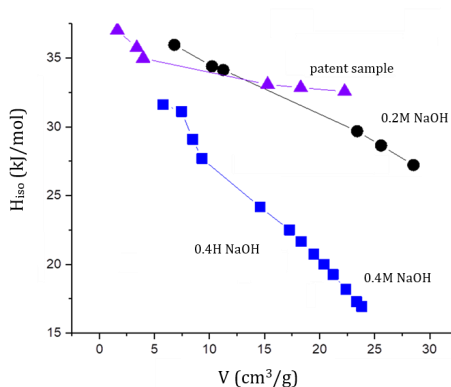


Figure 3. The enthalpy of adsorption of CO₂ for samples ZSM-5 with nominal Si/Al = 15 before and after treatment in 0.2M and 0.4M NaOH for 120 min, depending on the adsorbed volume.

Conclusion

It has been shown that by selecting the initial zeolite matrix and post-treatment conditions, it is possible to achieve a combination of mesoporosity with a moderately pronounced heterogeneity of the surface, and enthalpy of CO₂ adsorption, which is close to that in microporous zeolite, which makes these materials promising for use in the field of CO₂ capture and subsequent use in catalytic reactions.

Acknowledgements

The research was funded by the Ministry of Science and Higher Education of Russia, Agreement No 075-15-2023-611 from 30.08.2023. V.P. is grateful for the grant DGAPA-PAPIIT IG101623. The studies were carried out at the Research Park of Saint Petersburg State University: Centre for X-ray Diffraction Studies, Centre for Magnetic Resonance, Centre for Diagnostics of Functional Materials for Medicine, Pharmacology and Nanoelectronics, Center for Innovative Technologies of Composite Nanomaterials.

References

1. M. Milina, S. Mitchell, P. Crivelli, D. Cooke, J. Pérez-Ramírez, Nat. Commun. 5 3922 (2014).
2. M.G. Shelyapina, I. Rodríguez-Iznaga, V. Petranovskii, Materials for CO₂, SO_x, and NO_x emission reduction, in: O.V. Kharissova, L.M.T. Martínez, B.I. Kharisov (Eds.), Handb. Nanomater. Nanocomposites Energy Environ. Appl., Springer, Cham, 2020: pp. 1–30
3. A. Kojcinovic, B. Likozar, M. Grilc, J. CO₂ Util. 66 102250 (2022).

Phase structure and molecular mobility of drug delivery systems based on liposomes with Pluronics by nuclear magnetic resonance method

A.N. Sashina¹, A.V. Filippov², A.V. Khaliullina¹

¹Kazan Federal University, Kremlevskaya str, 18, Kazan, 420008, Russia

²Chemistry of Interfaces, Luleå University of Technology, Luleå, 97187, Sweden

E-mail: AlNSashina@kpfu.ru

Introduction

The application of traditional liposomes as drug delivery systems (DDSs) faces difficulties due to their instability and very short life time. To solve this problem liposome are supplemented with various polymers/copolymers, which help prevent the degradation of lipid DDSs in biological media and prolong the circulation time of the drug in the body [1, 2]. For example, Pluronics consisting of blocks of polypropylene oxide (PPO) and polyethylene oxide (PEO) can be used as copolymers [3].

In this work, the effect of Pluronic F127 on the phase behaviour of systems based on phosphatidylcholine liposomes was studied by ³¹P NMR spectroscopy, the molecular mobility of the system components was analyzed by ¹H NMR relaxometry and translational diffusion by ¹H NMR diffusometry.

Results and discussions

Comparative analysis of ³¹P NMR spectra of multilamellar lipid liposomes without Pluronic and with Pluronic showed that in the first case there is only lamellar liquid crystalline (LC) phase in the system, and when Pluronic is added, an isotropic peak appears in the whole temperature range studied (Fig. 1). The presence of an isotropic phase can be explained by the formation of micelles containing lipids.

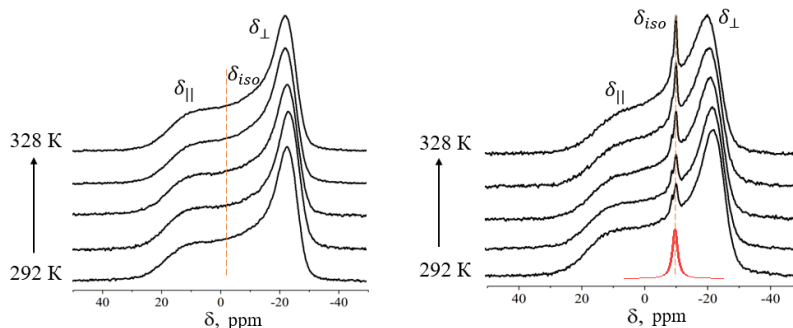


Figure 1. ³¹P NMR spectra for a suspension of phosphatidylcholine (left) and phosphatidylcholine with Pluronic F127 concentration of 2.5 mol% (right) at varying temperatures

According to ¹H NMR relaxometry data, the decay of transverse magnetization for the phospholipid system with Pluronic are due to the sum of contributions from the “liquid-phase” components and the “solid component” with a characteristic transverse relaxation time $T_{2s} \sim 20$ ms. Thus, the system of phosphatidylcholine with Pluronic combines the properties of both liquid and solid.

According to NMR diffusometry data, diffusion decay can be divided into two components with quite different self-diffusion coefficients. One of the components D_1 grows

from $1 \cdot 10^{-12}$ to $5 \cdot 10^{-12} \text{ m}^2/\text{c}$ with increasing temperature. The other component is independent of temperature and is characterized by an average value of $D_2 \sim 2 \cdot 10^{-15} \text{ m}^2/\text{c}$.

References

1. de Castro K. C. et al. Pluronic triblock copolymer-based nanoformulations for cancer therapy: A 10-year overview. – *Journal of Controlled Release*, 355, 802-822 (2023).
2. Khaliq N. U. et al. Pluronic F-68 and F-127 based nanomedicines for advancing combination cancer therapy. – *Pharmaceutics*, 8, 2102 (2023).
3. Pluronic F. Applications of thermo-reversible Pluronic F-127 gels in pharmaceutical formulations. – *J. Pharm. Sci.*, 9, 3, 339-358 (2006).

Synthesis of 4,5-diethynyl-1,2,3-triazoles and structure analysis by NMR spectroscopy

G.A. Shonin¹, I.A. Balova¹, A.I. Govdi¹

¹Saint Petersburg State University, Saint-Petersburg, Russia

E-mail: st128251@student.spbu.ru

Introduction

Nowadays, 1,2,3-triazoles and their derivatives are actively studied by scientists, as they find wide application in many areas of life. Some of them have antimicrobial and antiviral properties, are used as dyes, photostabilizers, as well as insecticides and fungicides¹.

Today, a new field of application of triazoles is rapidly developing – using as dyes and fluorophores². Recently, we reported the synthesis of 4,5-diethynyl-1,2,3-triazoles with fluorescent properties³, which can be used as fluorescent tags and are promising agents for cancer diagnosis and therapy. Fluorescence imaging is one of the most reliable methods for determining the presence of malignant tumors in the human body.

NMR spectroscopy helps to accurately determine whether the obtained compound is pure, because often during the preparation of 5-iodo-1,2,3-triazoles by 1,3-dipolar cycloaddition⁴ may occur deiodination process and the formation of 1,2,3-triazole, difficult to separate on column chromatography.

Method

We have prepared some new 4,5-diethynyl-triazoles, distinguished by different substituents exerting different effects on the molecule by a four-step synthesis involving 1,3-dipolar cycloaddition and Sonogashira reaction in good yields, from 4-methoxybenzylazide and 2-methylbut-3-yn-2-ol. The precursors and each of the intermediate products were characterized by ¹H and ¹³C NMR spectroscopy.

As can be seen in these spectra, the substances have no impurities of other products and can be further investigated as promising fluorescent tags.

Figure 1. Scheme of synthesis

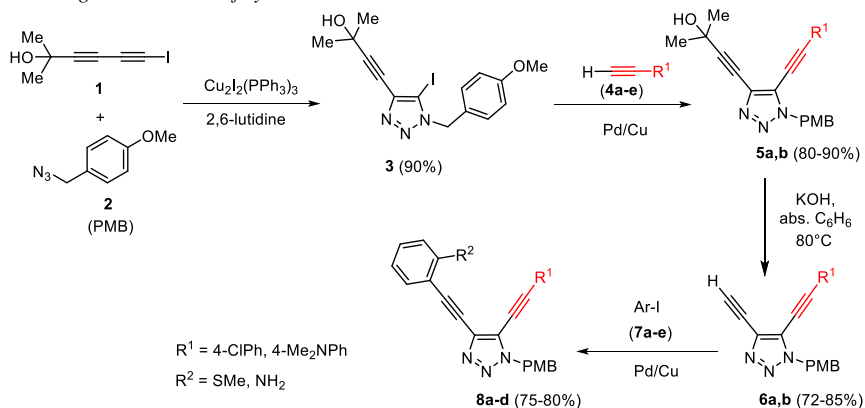
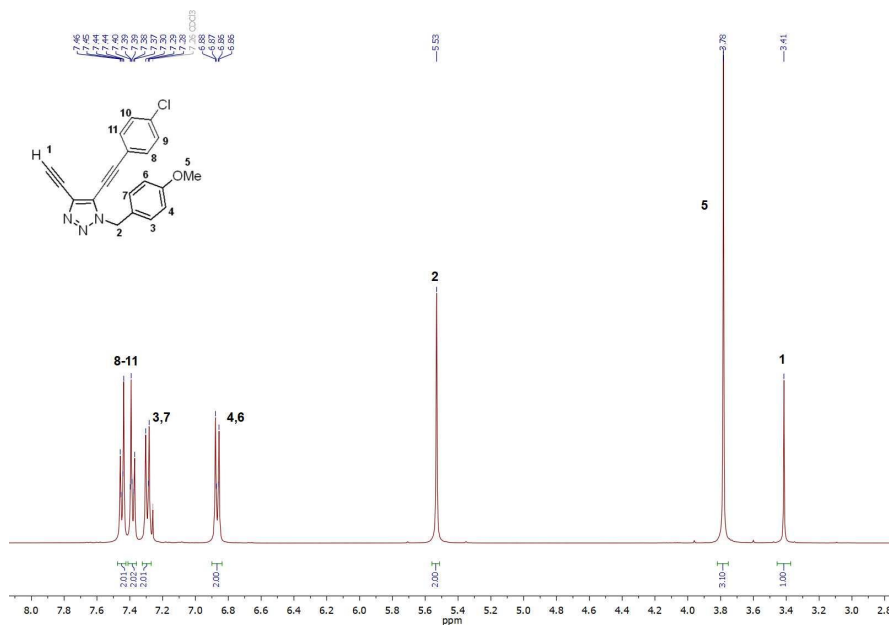


Figure 2. ¹H NMR spectra of the 1,2,3-triazole 6a



Acknowledgements

The research was carried out by using the equipment of the SPSU Resource Centres: the Magnetic Resonance Research Centre.

References

1. Sahu, A.; Sahu, P.; Agrawal, R. A Recent Review on Drug Modification Using 1,2,3-Triazole. *Curr. Chem. Biol.* 2020, 14 (2), 71–87. <https://doi.org/10.2174/2212796814999200807214519>.
2. Brunel, D.; Dumur, F. Recent Advances in Organic Dyes and Fluorophores Comprising a 1,2,3-Triazole Moiety. *New J. Chem.* 2020, 44 (9), 3546–3561. <https://doi.org/10.1039/c9nj06330g>.
3. Govdi, A. I.; Tokareva, P. V.; Romyantsev, A. M.; Panov, M. S.; Stellmacher, J.; Alexiev, U.; Danilkina, N. A.; Balova, I. A. 4,5-Bis(Arylethynyl)-1,2,3-Triazoles—A New Class of Fluorescent Labels: Synthesis and Applications. *Molecules* 2022, 27 (10). <https://doi.org/10.3390/molecules27103191>.
4. Govdi, A. I.; Danilkina, N. A.; Ponomarev, A. V.; Balova, I. A. 1-Iodobuta-1,3-Diynes in Copper-Catalyzed Azide–Alkyne Cycloaddition: A One-Step Route to 4-Ethynyl-5-Iodo-1,2,3-Triazoles. *J. Org. Chem.* 2019, 84 (4), 1925–1940. <https://doi.org/10.1021/acs.joc.8b02916>.

Spectral characteristics of cyclosporin G and L in deuterated acetonitrile with water solution determined by NMR spectroscopy

Artiom S. Tarasov, Anastasia F. Petrova, Sergey V. Efimov, Vladimir V. Klochkov

¹Institute of Physics, Kazan Federal University, Kazan, Kremlevskaya Str., 18, Russian Federation

E-mail: tarasov_as2010@mail.ru

Introduction

The spectral characteristics of cyclosporins G and L (CsG, CsL) in deuterated acetonitrile (CD_3CN) solution in the absence or presence of water (H_2O) were investigated by using high-resolution nuclear magnetic resonance (NMR) spectroscopy methods. The study focused on the search for possible structural changes of CsG and CsL in the presence of water molecules H_2O in CD_3CN solution. Information on the spectral features and possible conformations for CsG and CsL in a CD_3CN - H_2O solution was revealed by employing a combination of one-dimensional (^1H , ^{13}C) and two-dimensional (^1H - ^1H TOCSY, ^1H - ^{13}C HSQC, ^1H - ^1H ROESY) NMR spectroscopy methods. The obtained information will help to better understand the features of conformational transitions in biomolecules under the influence of various factors.

Cyclosporins are natural or synthetic organic biologically active compounds consisting of 11 amino acids. The cyclosporin family is quite diverse and includes more than 20 different molecules [1-3]. Cyclosporines are hydrophobic peptide compounds that are poorly soluble in pure water. However, they are well soluble in acetonitrile. A mixture of acetonitrile and water creates a medium that ensures the solubility of cyclosporine and at the same time ensures the formation of hydration shells around the polar groups of the peptide molecules, which can affect its conformation.

Cyclosporin G (CsG) and Cyclosporin L (CsL) (Fig. 1) are used in this study. CsG and CsL are two of many derivatives of this class of compounds that differ from each other in the amino acid residues at positions 1 and 2, biological activity, and physicochemical properties [4, 5]. CsG is an immunosuppressor structurally similar to cyclosporin A (CsA). Although this drug is pharmacologically as active as CsA, it is less toxic, in particular at the kidney level [4].

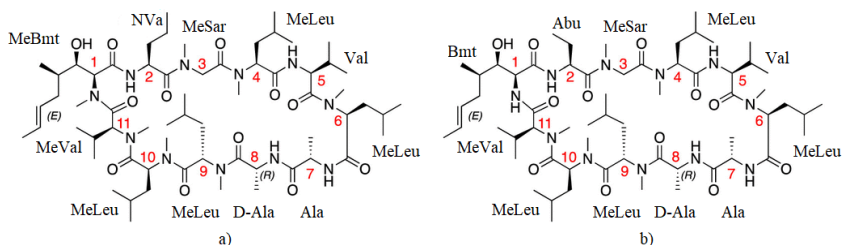


Figure 1. Chemical structure of CsG (a) and CsL (b) (from [2])

Method

NMR measurements were carried out on a Bruker Avance III HD 700 (700 MHz for ^1H , 175 MHz for ^{13}C) and Bruker Avance II 500 (500 MHz for ^1H , 125.2 MHz for ^{13}C) spectrometers. All samples were prepared in standard 5-mm NMR tubes. The solution volume was 0.6 ml. Solution was prepared in CD_3CN , the samples concentrations of CsG and CsL

were 1.5 mM. Two-dimensional spectra (^1H - ^1H TOCSY, ^1H - ^{13}C HSQC) were recorded at the temperature of 303 K. The spectral window was 12 ppm. A series of one-dimensional ^1H and two-dimensional ^1H - ^{13}C HSQC NMR spectra were obtained with the addition of H_2O to the sample in a 1:10 ratio.

Results and Discussion

A correlation of ^1H and ^{13}C NMR signals corresponding to the major and minor conformers of CsG and CsL in a polar medium (CD_3CN and CD_3CN - H_2O) is observed based on a comparative analysis of two-dimensional spectra.

The CsL molecule exists in the form of two equilibrium conformers (the fraction of the minor conformer in CDCl_3 is 22% according by the integrated intensities) in acetonitrile, acetone and chloroform. The number of conformers increases (6 were found) in the CD_3CN - H_2O solution. They differ from each other in the values of the chemical shifts of the ^1H and ^{13}C nuclei of the main chain atoms, which indicates a difference in the overall spatial structure of the molecules. Strongly broadened signals appear in the low-field part of the spectrum ($\delta > 8$ ppm). Nevertheless, the number of detectable conformers with comparable intensity remains small is three, according to the 2D EXSY exchange spectra.

In the ^1H NMR spectrum of CsG in CD_3CN solution, 2 conformers are initially observed. Similarly with CsL, when H_2O is added to the solution, several new conformers can be observed, which also differ in chemical shift values (Fig. 2).

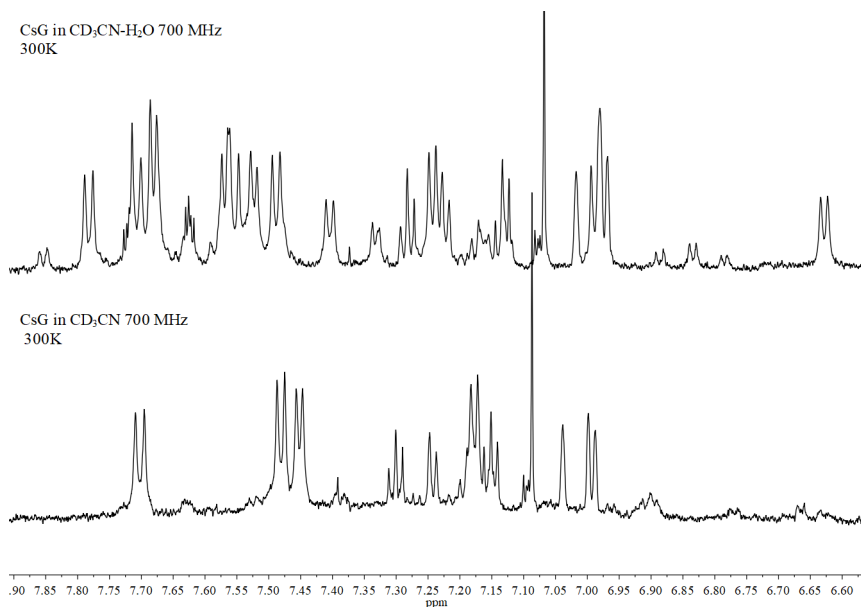


Figure 2. Fragment of ^1H NMR spectra of CsG in different solutions (upper picture, CD_3CN - H_2O ; lower picture, CD_3CN) (700 MHz, 300 K)

It is interesting to note that in chloroform and acetonitrile not only the chemical shift values of carbon nuclei are similar, but also protons: most signals of nuclei close to the main chain of the peptide (NCH_3 , as well as the $\beta\text{-CH}_3$ groups of alanines) are obtained in the

spectrum in CD_3CN by a shift to the right and upward relative to the spectrum in CDCl_3 . Thus, the structure of CsG turns out to be more stable before changing the solvent to polar acetonitrile than, for example, the cyclosporine molecule CsC.

In general, the conformational diversity of cyclosporins A, B, C in polar media such as DMF or DMSO is quite large (6-8 conformers and more), while in chloroform or benzene they exist as a single conformer. The behavior of CsG and CsL is more interesting and does not fit into this simple scheme. In addition, adding a small amount of water to acetonitrile in this case turns out to be a convenient tool for initiating the exchange, which will allow a more detailed study of the properties of cyclosporins and their individual conformers.

Acknowledgements

The work was supported by the Russian Science Foundation (project no. 24-23-00427).

References

1. S.V. Efimov, et al. – Biochemical and Biophysical Research Communications, Vol. 526, Issue 4, Pages 1054-1060 (2020).
2. K.M. Corbett, et al. – J. Med. Chem., Vol. 64, Issue 18, Pages 13131-13151 (2021).
3. D.Gang. – Genes, Vol. 9, Issue 11, P. 557 (2018).
4. L. Pichard, et al. – Biochem Pharmacol., Vol. 51, Issue 5, Pages 591-598 (1996).
5. R. Traber, et al – ChemInform, Vol 18, Issue 20, P. 311 (1987).

The structural features of the fibril-forming peptide SEM2(49-107) by NMR spectroscopy and its role in enhancing HIV activity

Anastasia A. Troshkina, Dmitriy S. Blokhin, Vladimir V. Klochkov

Kazan Federal University, Kremlevskaya Str., 18, 420008 Kazan, Russia

E-mail: AnaATroshkina@kpfu.ru

Introduction

The SEM2(49-107) peptide is a fragment of the semenogelin 2 protein which is a constituent of the human semen coagulum [1]. Semenogelin 2 is synthesized and secreted by the seminal vesicles [2]. Scientific research indicates that the seminal fluid of humans is crucial in enhancing the activity of HIV [3]. However, the exact mechanisms behind viral transmission and infection are not fully understood and require further research. The electrostatic repulsion between the negatively charged HIV virus particles and the target cells usually inhibits their interaction. Research has shown that certain components of seminal fluid can aggregate into amyloid fibrils, which have cationic surfaces. These surfaces act as electrostatic bridges, promoting the attachment of HIV to host cells. This is mechanism significantly increases HIV infectivity [4]. Aggregation of the SEM2(49-107) peptide leads to the formation of amyloid fibrils which contribute the interaction of HIV virions with target cells. To identify the physical mechanisms that determine the interaction between amyloid fibrils, HIV virions and target cells, it is necessary to investigate the structural changes in the SEM2(49-107) peptide that cause its aggregation. In this study, nuclear magnetic resonance (NMR) spectroscopy was used as the primary method to analyze the structure of the SEM2(49-107) peptide under conditions that closely imitate physiological properties.

Experiment and results

The object of the study is a fragment of the protein semenogelin 2 is the peptide SEM2(49-107) that labeled with isotopes $^{13}\text{C}/^{15}\text{N}$. The studied sample SEM2 peptide (49-107) was synthesized at the Research Institute of Structural Biology at Kazan Federal University. The amino acid sequence of the SEM2(49-107) peptide is presented in Figure 1.

49	54
PHE-GLY-GLN-LYS-ASP-GLN-GLN-HIS-THR-LYS-	
59	64
SER-LYS-GLY-SER-PHE-SER-ILE-GLN-HIS-THR-	
69	74
TYR-HIS-VAL-ASP-ILE-ASN-ASP-HIS-ASP-TRP-	
79	84
THR-ARG-LYS-SER-GLN-GLN-TYR-ASP-LEU-ASN-	
89	94
ALA-LEU-HIS-LYS-ALA-THR-LYS-SER-LYS-GLN-	
99	104
HIS-LEU-GLY-GLY-SER-GLN-GLN-LEU-LEU	

Figure 1. The amino acid sequence of peptide SEM2(49-107)

The 1D, 2D, and 3D NMR spectra of SEM2(49-107) peptide ($\text{C} = 0.46 \text{ mM}$, $\text{pH} = 6.0$) were acquired using a Bruker AVANCE III 700 NMR spectrometer equipped with a quadruple resonance (^1H , ^{13}C , ^{15}N , ^{31}P) CryoProbe at the temperature 293 K. Data processing was performed using Bruker's Topspin 3.6, and spectral analysis was conducted in CCP-NMR [5]. Based on the NMR spectra, the chemical shifts of ^1H , ^{13}C , and ^{15}N were determined, and the internuclear distances and dihedral angles for the SEM2(49-107) peptide were also established. During the analysis of the spectral chemical shifts, 48 out of the 59 amino acid

residue (86%) of the SEM2(49-107) peptide were determined. The obtained data from NMR spectra on the assignment of chemical shifts (^1H , ^{13}C , ^{15}N) were published in the article [6].

The secondary structure of the SEM2 (49-107) was evaluated using two methods: using chemical shift index (CSI) which was obtained by CCPNMR program and prediction of the secondary structure according to TALOS-N (Torsion Angle Similarity Obtained from Shift) [7] [8]. Both methods showed that the SEM2(49-107) peptide contains alpha-helical fragments at the C-terminus in the range from 89(Ala) to 98 (Gln) amino acids residues.

The three-dimensional structure of peptide SEM2 (49—107) were calculated using the constrained annealing simulation protocol using the XPLOR-NIH software [9].

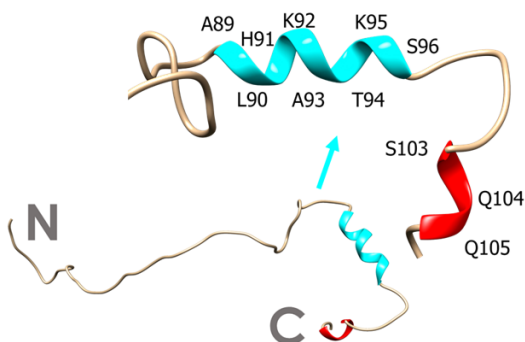


Figure 2. Spatial structure of peptide SEM1(86—107) in an aqueous solution

The cross-peaks in the ^1H , ^{13}C , ^{15}N NOESY (3D) NMR spectrum and torsion angles as determined by the TALOS-N program were used into experimental distance limits. Visualization of spatial structures was done using the UCSF Chimera program [10]. The spatial structure calculation data indicate a relatively limited conformation of the peptide in the amino acid residues range from 89 (Ala) to 96 (Ser) and 103 (Ser) to 105 (Gln). These data are consistent with the results of the secondary structure analysis, which show the presence of a secondary structure in the form of an alpha helix in this area.

Acknowledgements

This work was supported by the Russian Science Foundation (D.S. Blokhin, project no. 20-73-10034).

References

1. N. R. Roan, et al. – Cell Host and Microbe, Vol. 10, Pages 541-550 (2011).
2. H. Lilja, et al. – J Biol Chem., Vol. 264, Issue 3, Pages 1894–1900 (1989).
3. P. Westermark. – FEBS J., Vol. 272, Issue 23, Pages 5942–5949 (2005).
4. J. Münch, et al. – Cell, Vol. 131, Issue 6, Pages 1059–1071 (2007).
5. W.F. Vranken, et al. – Proteins, Vol. 59, Pages 687–696 (2005).
6. A.A. Troshkina, et al. – Biomol NMR Assign., P. 8 (2024).
7. D.S. Wishart, et al. – Biochemistry, Vol. 31, Issue 6, Pages 1647–1651 (1992).
8. Y. Shen, et al. – J Biomol NMR., Vol. 44, Issue 4, Pages 213–223 (2009).
9. C. D. Schwieters, et al. – Journal of magnetic resonance, Vol. 160, Issue 1, Pages 65–73 (2003).
10. E. F. Pettersen, et al. – Journal of computational chemistry, Vol. 25, Issue 13, Pages 1605–1612, (2004).

Study of slow molecular motions by NMR relaxation.

Konstantin V. Tyutyukin, Alexandr V. Ievlev

*Department of Nuclear Physics Research Methods, Saint Petersburg State University,
St. Petersburg State University, St. Petersburg 198504 Russia*

E-mail: a.ievlev@spbu.ru

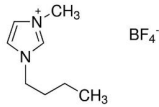
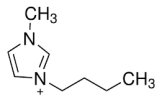
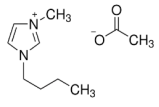
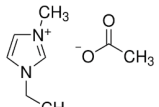
Introduction

Ionic liquids have been studied many times using NMR, as it is one of the most informative methods for obtaining information about the structure and molecular mobility of the compounds themselves. In cases with imidazolium-based ILs, it is possible to obtain complete information on the structure of the carbon skeleton of the ion, as well as on intramolecular interactions with protons. However, in such systems with strong electrostatic interactions, larger scale motions can be expected to exist. In the works of the Kruk group [1] such scales of correlation times are associated with translational mobility. In the present work it is proposed to test this hypothesis using relaxation NMR methods.

Results and discussions

To test the above hypothesis, 4 different ILs were used (see Table 1), which were examined on 3 different devices. The first two are standard NMR spectrometers (such as Bruker Avance-III) from the St. Petersburg State University scientific park, operating at frequencies of 300 MHz and 400 MHz for protons. The third device is a modernized version of the Bruker SXP 2-100 with the ability to reconfigure the field in a wide range. In our case, a frequency of 13.5 MHz for protons was selected.

Table 2. The studied ILs

1	2	3	4
[BMIM]BF ₄ CAS-Number: 174501-65-6	[BMIM]Cl CAS Number: 79917-90-1	[BMIM]Ac CAS Number: 284049-75-8	[EMIM]Ac CAS Number: 143314-17-4
			

In all cases, spin-lattice relaxation rates were measured using a standard inversion-recovery pulse sequence. In the case of low-frequency measurements (3rd device) it was not possible to resolve individual lines in the spectrum. Therefore, for a comparative analysis of the temperature dependences of relaxation rates, the NMR relaxation data on high-frequency devices were processed by one integral over the entire range of chemical shifts. Figure 1 shows a comparison of the data averaged in this way in the form of a solid line, and provides data on the temperature dependences for individual lines corresponding to different molecular groups.

In this work, relaxation dependences with maxima in the operating temperature range of the IL were obtained. According to Bloembergen-Purcell-Pound model [2] the maximum of the relaxation curve shifts to the low temperature region as the operating frequency of the device decreases, so in some cases there is a chance to observe in a low-frequency experiment a maximum responsible for slower movements, which can usually be explained by the

movement of molecular segments and are not visible in experiments in strong fields. The results of experimental data processing are shown in Figure 2.

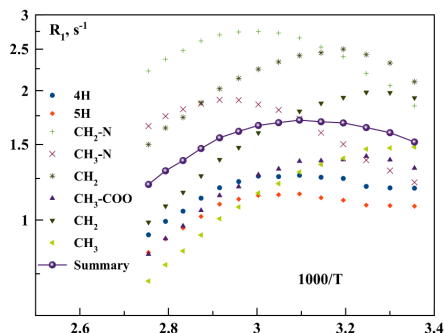


Figure 1. Temperature dependences of spin-lattice relaxation rates for individual spectral lines of BmimAc and averaged over all spectral lines

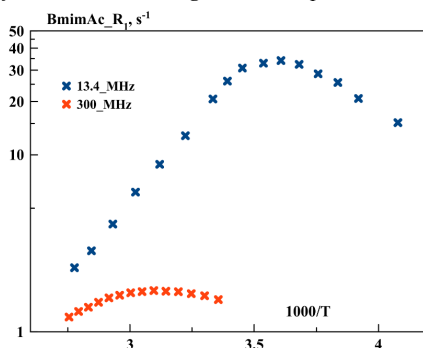


Figure 2. Dependence of the spin-lattice relaxation rate on the inverse temperature for different resonance frequencies (IL: BmimAc)

As can be seen from Figure 2, the maximum in the cation relaxation rates is observed at both frequencies, however, the correlation times calculated from the low-frequency maximum reflect some larger-scale motion than the rotation of individual molecular groups.

Acknowledgements

This work is supported by an internal grant from St. Petersburg State University (ID: 132193705). Thanks to the staff of Center for Magnetic Resonance of Research Park of St. Petersburg State University for fast and high-quality measurements.

References

1. D. Kruk, R. Meier, A. Rachocki, A. Korpala, R. K. Singh, and E. A. Rössler, "Determining diffusion coefficients of ionic liquids by means of field cycling nuclear magnetic resonance relaxometry," *Journal of Chemical Physics*, vol. 140, no. 24, Jun. 2014, doi: 10.1063/1.4882064.
2. N. Bloembergen, E. M. Purcell, and R. V. Pound, "Relaxation effects in nuclear magnetic resonance absorption," *Physical Review*, vol. 73, no. 7, pp. 679–712, 1948, doi: 10.1103/PhysRev.73.679.

Study of NV⁻ centers in natural diamonds (carbonado) by micron scale scanning spectroscopy

Valentina V. Yakovleva¹, Kirill V. Likhachev¹, Marina V. Muzafarova¹, Anna P. Bundakova¹, Roman A. Babunts¹, Sergey V. Titkov², Pavel G. Baranov¹

¹Ioffe Institute, Saint-Petersburg, 194021, Russia

²(IGEM) RAS, Moscow, 119017, Russia

E-mail: valya_yakovleva_1999@mail.ru

Introduction

Cryptocrystalline diamond aggregates (carbonado) with grain sizes of 1-10 μm from Siberian deposits were studied using optically detected magnetic resonance (ODMR) and photoluminescence (PL) methods based on confocal spectroscopy. They were found to have high contents of NV⁻ centers. Based on the analysis of the parameters of the PL and ODMR spectra, various characteristics were obtained, such as the ratio of the charge states of NV centers, mechanical stresses and strains, and local nitrogen concentration.

Features of cryptocrystalline diamond aggregates

Among polycrystalline diamond aggregates, a special type of cryptocrystalline aggregates was identified, consisting of grains smaller than 20 μm in size and giving ring reflections on X-ray images, which is typical for finely dispersed substances [1]. According to the mineralogical classification of diamonds by Yu. L. Orlov, such polycrystalline aggregates belong to the X variety and are called "carbonado". Fig. 1 shows AFM-image of one of the carbonado samples. It can be seen that analyzed sample consists of many irregular closely intergrown diamond grains, the sizes of which vary from dozens of nm to micron units.

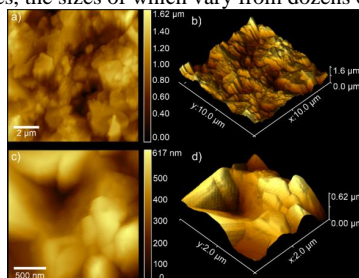


Figure 1. AFM-images of carbonado, made on a different scale: (a and b) – micron scale, (c and d) – nanometer scale.

Features of NV⁻ centers in diamonds

Nowadays negatively charged nitrogen-vacancy centers are of great interest for many scientists since it is possible to register optically detected magnetic resonance signal on them under room temperature [2]. However, the major part of research is related to NV⁻ centers in synthetic diamonds, where they were created artificially by radiation and annealing. This work is devoted to NV centers in natural cryptocrystalline diamond aggregates, where they were formed naturally. Earlier the unique magneto-optical properties of NV⁻ centers were also recently studied in natural diamond single crystals [3]. Scanning PL signals showed that in natural cubic crystals NV⁻ centers are concentrated in deformation slip planes. This indicates their formation as a result of high-temperature post-crystallization plastic deformation.

The NV center represents a substitutional nitrogen atom in diamond crystal lattice and a carbon vacancy in the nearest coordination sphere (Fig. 2).

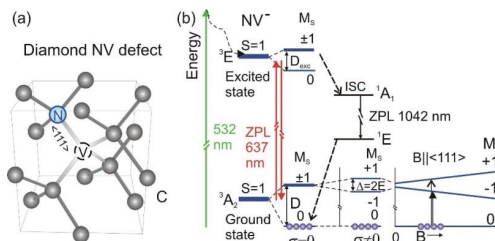


Figure 2. Structure of the NV center inside the diamond unit cell (a) and the scheme of optically induced population alignment of spin levels in the ground state of a negatively charged NV center (b)

The scheme of optical excitation cycle shows that while excitation of the NV⁻ center with green laser the spin sublevel with spin projection equal to zero is predominantly populated. But when we apply a resonant microwave frequency equal to 2.87 GHz, an additional redistribution of electronic population occurs, which leads to a relative change in photoluminescence, in particular to its decrease. And we can detect this PL change.

PL and ODMR registration technique

The present studies were performed on an ODMR spectrometer based on scanning confocal microscope and equipped with a confocal optical circuit (NTMDT SI), which was constructed at the Ioffe Institute (Fig. 3) [4]. This spectrometer allows registration of PL and ODMR signals in the region of $\sim 1 \mu\text{m}^3$ at room temperature and revealing spatial distribution of PL and ODMR signals using confocal 3D (z, x, y) scanning with a submicron resolution. The combination of confocal optics with the atomic force microscope allows positioning of measurements with nanometer accuracy.

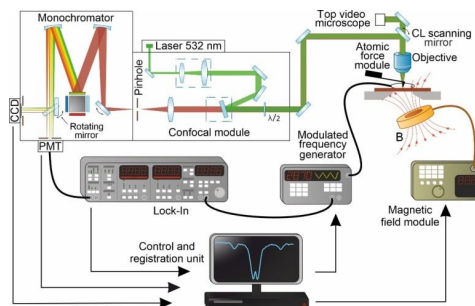


Figure 3. Block diagram of an ODMR spectrometer based on optical confocal and atomic force microscopes

Acknowledgements

This work is supported by the Ministry of Science and Higher Education of the Russian Federation (No. FFUG-2024-0046).

References

1. Yu. L. Orlov. The Mineralogy of the Diamond. – John Wiley & Sons, 1960.
2. A. Gruber, A. Draebenstedt et al. – Science, 276, 2012-2014 (1997).
3. S. V. Titkov, V. V. Yakovleva et al. – Diamond & Related Materials, 136, 109938 (2023).
4. R. A. Babunts, M. V. Muzafarova et al. – Technical Physics Letters, 41 (6), 583-586 (2015).

NMR study of the fibril-forming peptide SEM(86-107)

Ekaterina M. Zaitseva, Aydar R. Yulmetov, Daria A. Osetrina, Dmitry S. Blokhin

Kazan Federal University, Kremlevskaya Str., 18, 420008, Kazan, Russia

E-mail: EkMZayceva@stud.kpfu.ru

Introduction

Since the 1980s, researchers have been actively studying factors that can influence the transmission of HIV-1 (human immunodeficiency virus-1), one of the most dangerous sexually transmitted infections leading to AIDS (acquired immunodeficiency syndrome).

It was soon discovered that one of the factors was the amyloid fibrils contained in human semen. Amyloid fibrils are insoluble aggregates formed by peptides and proteins with different primary, secondary and tertiary structures of their functionally folded states. These fibrils are usually associated with neurodegenerative diseases such as Alzheimer's or Parkinson's disease. More recently, it became apparent that amyloid fibrils significantly contribute to accelerated HIV transmission. It is hypothesized that amyloid fibrils enhance the adhesion of HIV virus particles to cell membranes by reducing electrostatic repulsion between the membranes of the virus and the target cell [1].

Semenogelin, a protein found in the human seminal coagulum (accounting for approximately 60% of its volume), is secreted by seminal vesicles and is responsible for the immobilization and fixation of spermatozoa within the seminal coagulum, a gel—like reservoir for capturing and transporting sperm. To liquefy semen and initiate sperm motility, semenogelin must be cleaved by prostate-specific antigen (PSA; before activation, PSA is present in the prostate and is inhibited by elevated concentrations of zinc ions), which cleaves the molecules of semenogelin I (SEM1) and semenogelin II (SEM2), resulting in the formation of soluble fragments that can form amyloid fibrils. It is also known that zinc ions inhibit the fibrillation of certain peptides into active fibrils, which leads to the formation of oligomeric complexes [2,3].

One of the fragments formed as a result of the cleavage of PSA is the semenogelin-1 peptide SEM1(86-107): 22 amino acid residues in the sequence DLNALHKTTKQRH-LGGSQQLL. In this study, we investigated the structure of the SEM1(86-107) peptide using high-resolution NMR spectroscopy. This methodology allowed us to obtain the spatial structure of the peptide, as well as to find out the structural changes occurring within the peptide when zinc ions are added to the solution, and to study the mechanisms of its aggregation.

Results

At the initial stage, a series of two-dimensional NMR experiments with the peptide SEM1 (86-107) was carried out. The pre-established amino acid sequence of the peptide, as well as the assigned chemical shifts of amino acid residues and internuclear distances and dihedral angles obtained from spectral data analyzed using the TALOS+ program, were used to calculate the spatial structure using the simulated annealing method in the XPLOR-NIH software. The spatial structure of the peptide was visualized using the UCSF Chimera. The analysis of the spatial conformation led to the conclusion that the predominant type of secondary structure in the SEM1(86-107) peptide is horseshoe shaped (Fig. 1). Calculated Ramachandran plot of SEM1(86-107) validated the obtained peptide's structure (residues in the most favored region: 100,0%; residues in the additionally allowed region: 90,7%; residues in the disallowed region: 0,0%).

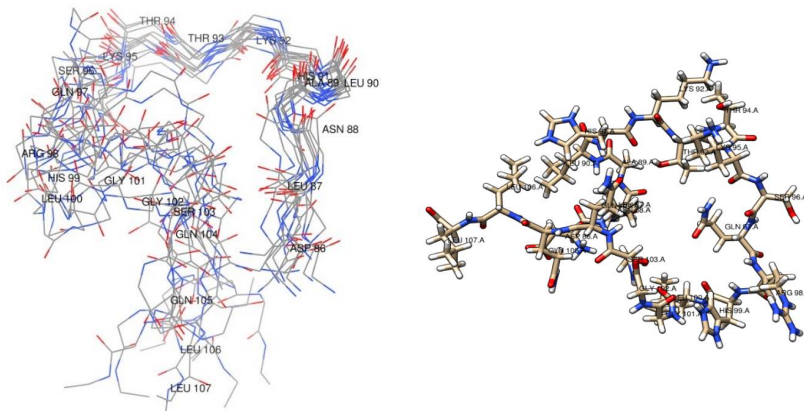


Figure 1. Spatial structure of the peptide SEM1(86–107) as an ensemble of 14 structures

At the next stage, the effect of zinc ions on the peptide was investigated. It has been hypothesized that the zinc ion forms an ionic bond with the charged side chain of histidine residue adjacent to leucine, a phenomenon previously described in other studies involving various peptides [3].

To substantiate our assumption of binding, the longitudinal relaxation times (T_1) of the peptide in an aqueous solution and in a solution containing zinc ions were determined from the ^1H - ^{15}N HSQC spectra obtained at eight different delay times. Analyzing the obtained data on relaxation times, it can be noted that when zinc ions are added, their values decrease. Presumably, this change is due to the fact that zinc ions bind to the charged side chain of the amino acid residue histidine (91His), which can be observed by the change in the values of chemical shifts of the signals from the neighboring leucine (90Leu), which, in turn, occurred as a result of a change in the electron environment of the molecule and acted as a factor for increased relaxation rates.

At the last stage, to study the binding mechanism, molecular dynamic simulations of the peptide-zinc ion complex (including 1 peptide molecule, 1 zinc ion and 3158 water molecules, with a modeling cell size of 4.7 x 4.7 x 4.7nm) was performed using the GROMACS package. The simulation was performed in parallel in 36 threads, which amounted to a total of 36x100=3600ns of system evolution. The coordinates of all the atoms were recorded every 0.01ns. The trajectory obtained as a result of the simulation was analyzed using the GROMOS clustering method: for each recorded step, the interaction energies of all amino acid residues were calculated, and pairs of configurations with a standard deviation (RMSD) of no more than 1.1 kJ/mol were identified and grouped into clusters (Fig. 2).

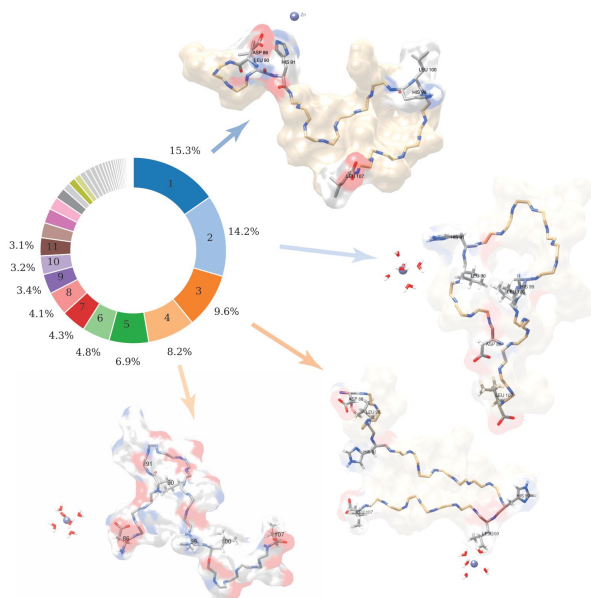


Figure 2. The obtained clusters of the peptide SEM1(86-107) with zinc ion complex structures resulting from the molecular dynamics simulation using the GROMOS clustering method

Conclusion

During this study, the structure of the peptide SEM1(86-107) was obtained and visualized for the first time based on nuclear magnetic resonance (NMR) spectroscopy data. Analysis of the data collected during the study of the peptide with zinc ion solution led to the conclusion that their interaction leads to the formation of a stable peptide-ion complex due to the presence of a charged side chain from the histidine residue in the peptide. Using molecular dynamic simulation in the GROMACS software package, we were able to observe the formation of this complex.

Therefore, SEM1 and SEM2 have the potential to indirectly modulate the enzymatic activity of prostate-specific antigen (PSA), since it is known that this protease is inhibited by Zn_2^+ . In the light of this knowledge, it is possible to further explore the possibilities of SEM1, SEM2 and related peptides to activate PSA in the presence of Zn_2^+ and also to study how the inhibition of SEM1 peptides by zinc ions slows down the spread of HIV infection.

References

1. Cohen, F.S. The Energetics of Membrane Fusion from Binding, through Hemifusion, Pore Formation, and Pore Enlargement / F. C. Cohen, G. B. Melikyan. // J. Membr. Biol. – 2004. – V. 199. – P.1-14.
2. Jonsson, M. Semenogelins I and II bind zinc and regulate the activity of prostate-specific antigen. / S. Linse, B. Frohm, A. Lundwall, J. Malm // J. Biochem. – 2005, 387 (2): 447–453. <https://doi.org/10.1042/BJ20041424>.
3. Sheftic, S.R. Inhibition of semen-derived enhancer of virus infection (SEVI) fibrillogenesis by zinc and copper / J. M. Snell, S. Jha, A. T. Alexandrescu // J. Eur. Biophys., 2012, 41, 695–704.

Poems about School

* * *

Spinus, Spinus, where you were?
Did you dive in the Resonance world?
– “Yes! I dived with my great joy –
Resonance is a pleasant toy!”

“Spinus” school invited you
To look for a knowledge clue.
We will show the signal birth
In the field of our Earth!

If you wish to have success,
At the School achieve progress!
We will teach you all to fly
In the scientific sky!

We desire you to get
Many victories-побед!
It will be a good surprise
If you catch the Nobel prize!

2010

Author Index

- Abiev R. Sh.*, 142
Abzianidze V. V., 172
Alakshin E. M., 55, 95
Aldoshin S. M., 156
Alexandrov A. S., 133, 204
Alikhanova O. L., 193
Alkhuder O., 134
Alonso-Geli Y., 137, 205
Andronenko S. I., 142
Anisimov N. V., 48, 145, 147
Antonenko A. O., 149
Antonov A. S., 168
Anufrieva P. A., 221
Araujo Durán Y., 205
Arkhipov R. V., 204
Arkhipov V. P., 204
Babunts R. A., 50, 257
Baichurin R. I., 179
Balova I. A., 248
Baranov P. G., 50, 257
Batueva A. V., 50
Batueva E. E., 152
Berezhnaya E. V., 235
Bezrodnyi V. V., 153, 221, 224
Blokhin D. S., 253, 259
Bochkin G. A., 52
Bogachenkov A. S., 172
Bogachev Yu. V., 227
Bogaychuk A. V., 55, 95
Boltenkova E. I., 55, 95
Bozhenko K. V., 156
Bundakova A. P., 257
Bunkov Yu. M., 28
Bystrov E. S., 57
Bystrov S. S., 57
Cabal-Mirabal C., 30, 89
Cabeza O., 77
Chang L. J., 149
Charnaya E. V., 33, 149, 238
Chekmenev E. Y., 124
Cheremensky S. O., 157
Chernyak A. V., 104
Chetverikova D. A., 60
Chisty L. S., 172
Chizhik V. I., 35, 111
De Maissin H., 124
Demir A. T., 97
Deriglazov V. V., 227
Djapic N., 158
Dmitrenko M., 208, 212
Dmitrieva A. S., 160, 227
Dmitrieva E. V., 163
Dolgorukov G. A., 63
Dubovenko R., 212
Dvinskikh S. V., 65
Efimov S. V., 217, 250
Egorov A. V., 111, 157, 220
Egorova P. V., 170
Estrada Garrido Y., 205
Fatullaev E. I., 221, 224
Fedorov V. S., 160
Fel'dman E. B., 52, 117
Fetin P. A., 129, 196
Filimonenko D. S., 66
Filippov A. V., 246
Fishman N. N., 110
Frolova E. N., 152
Gafarova A. R., 166
Gafurov M. R., 163, 241
Galiakhmetov S. A., 168
Galimova A., 69
Garaeva A. M., 55, 95
Garaeva N. S., 170
García Cruz C. C., 205
García Naranjo Ju. C., 89, 205
Garifullin I. N., 217
Gayathri A., 41
Godovikov I. A., 92, 179
Goldberg M. A., 241
Gomonov K. A., 210
Gonyalin V. E., 170
González-Dalmau E., 30
Gorkovaia K. S., 172
Govdi A. I., 248
Gracheva I. N., 163
Gridnev I. D., 38
Grishanovich I. A., 174
Gromova N. R., 73
Grunin L., 75
Grunin Yu., 75
Gumarov G. G., 166
Gurin A. S., 50
Gutsev G. L., 156
Gutsev L. G., 156
Haponchyk R. V., 176
Hövenner J.-B., 124
Hurshkainen A., 145
Ievlev A. V., 60, 77, 198, 255

- Igonin A. S.*, 179
Isaeva E. I., 179
Ivanov D., 182
Ivanova A. G., 142
Ivanova M., 75
Kadnikov M. V., 129, 196
Kaliaperumal K., 41
Karmanova N. V., 185
Khaliullina A. V., 246
Khatmullina K. G., 104
Khroshin D. A., 188
Khrustalev A.A., 57
Khudozhnikov A. E., 42, 80
Khusnutdinov R., 69
Kilin S. Ya., 66
Kirilenko V. D., 57
Kiryutin A. S., 92, 110, 190
Klochkov V. V., 217, 250, 253
Kocharyan G., 81
Kolokolov D. I., 42, 80
Komlev V. S., 241
Komolkin A. V., 73, 193
Koptyug I. V., 124
Kosenko I. D., 92
Kostin M. A., 134
Kovalenko A. S., 100, 142
Kozhevnikov A. Yu., 174
Kramushchenko D. D., 50
Krivorotov D. V., 172
Kupriyanov P., 83
Kupriyanova G., 86
Kustov L. M., 100
Kuular V. I., 121
Kuzmichev A. N., 28
Kuzmin V. V., 63
Kuzminova A., 208, 212
Kuznetsova E. I., 52, 117
Lapina O. B., 120
Laurent S., 89
Lebedev V. T., 121
Lee M. K., 149
Levit S. I., 196
Likhachev K. V., 257
López-Alexander R., 137
Lores Guevara M. A., 89, 137, 205
Ludwig R., 42
Lukzen N. N., 110
Lyatun I., 86
Makarchenko A. S., 63
Makarenko S. V., 210, 214, 230
Malakhova D. A., 198
Mamin G. V., 163, 241
Marchenko Ya. Yu., 227
Marchenkov V. V., 149
Markelov Danil A., 92, 190
Markelov Denis A., 73, 153
Matveev V. V., 111
Mazur A., 208, 212
Melnikova D. L., 133, 201, 204
Mengana Torres Yu., 205
Mikailzad F., 69
Mikhailovskaya O., 208
Mikhalap M. V., 210
Mikhtaniuk S. E., 153, 221, 224
Mikulan A., 212
Mikushev V. M., 238
Minaeva V. Yu., 214
Minnullina G. A., 217
Mizyulin D. A., 220
Moiseev S. A., 69
Mozhukhin G., 83
Mukhamadullin B. M., 95
Mukhin K. A., 111
Muller R. N., 89
Mulloyarova V. V., 168
Muratova A. D., 73
Murzakanov F. F., 163
Musaelyan M., 81
Muzafarova M. V., 257
Naumov S. V., 149
Neelov I. M., 153, 221, 224
Nefedov D. Yu., 33, 238
Nesmelova I., 201
Nikitina A. V., 227
Nikolaev A. M., 100, 142
Nikolaev B. P., 160
Nizovtsev A. P., 66
Obregón Segura Y., 205
Okay C., 97
Osetrina D. A., 259
Osmanov V. K., 92
Ozerova O. Yu., 214, 230
Papulovskiy E. S., 120
Pelipko V. V., 210
Penkova A., 208, 212
Peshkova M. A., 60
Petrakova N. V., 241
Petranovskii V., 243
Petrova A. F., 250
Pilipenko I. A., 230

- Pişkin H.*, 69
Pokhvishcheva N. V., 60
Pomogailo D. A., 100
Popova M. V., 121
Pravdivitsev A. N., 124
Price W. S., 43
Pronina Ju. A., 232, 235
Ramakrishnan T., 41
Rameev B., 69, 83, 97
Rochev A. M., 238
Rodríguez de la Cruz N. Ju., 89
Rybin D. S., 166
Ryzhov V. A., 227
Sadovnikova M. A., 241
Salikhov K. M., 102
Salnikov O. G., 124
Samadov A., 243
Samodelrin D. A., 28
Sarıbaş N. G., 83
Sashina A. N., 246
Schmidt A. B., 124
Selivanov S. I., 232, 235
Serbin A. V., 193
Sharipova A. R., 152
Shavykin O. V., 153
Shelyapina M. G., 243
Shestakov S. L., 174
Sheveleva N. N., 153
Shevtsov M., 160
Shilova O. A., 100, 142
Shipulya E. I., 117
Shonin G. A., 248
Shubin A. A., 120
Shurtakova D. V., 241
Shvidchenko A. V., 121
Sinelnikov A. A., 142
Skirda V. D., 133, 182, 201
Slesarenko A. A., 104
Slesarenko N. A., 104
Smirnov M., 86
Snadin A. V., 110
Sokol A. V., 193
Soltamov V. A., 163
Somoano Delgado L., 205
Stepakov A. V., 232, 235
Stepanov B. I., 66
Suárez Beyries L. C., 205
Suharzhevsky S. M., 142
Sukhanov A. A., 152
Suponina D. S., 172
Tamayo Delgado F., 89, 205
Tarasov A. S., 250
Tarasova A. A., 147
Tikhonov P., 145
Titkov S. V., 257
Toktarev A. V., 120
Tolstoy P. M., 134
Trofimov I. A., 124
Troshkina A. A., 253
Tudupova B. B., 121
Turanov A. N., 152
Turanova O. A., 152
Tyutyukin K. V., 77, 198, 255
Ubovich M., 111
Usachev K. S., 170
Uskov A. V., 33
Ustinov A. B., 176, 188
Utenyshev A. N., 156
Vakulyuk A. V., 224
Valkovskiy G. A., 243
Varela L. M., 77
Vasil'ev S. G., 52, 117
Vasilev A. A., 33
Volkov M. Yu., 55
Vovk M. A., 121, 193
Xia B., 44
Yakovlev I. V., 120
Yakovleva L. Yu., 160
Yakovleva V. V., 257
Yarmolenko O. V., 104
Yevlampieva N. P., 121, 193
Yi A. P., 124
Yulmetov A. R., 185, 259
Yurkovskaya A. V., 92, 190
Yushmanov P., 127
Yusupov M. M., 170
Zaitseva A. S., 221
Zaitseva E. M., 259
Zaripov R. B., 166
Zefirova P. M., 129
Zenchuk A. I., 117
Zolotov D. R., 57
Zorin I. M., 129, 196
Zozulya A., 86
Zvereva I. A., 243
Zyubin A., 86

Magnetic Resonance and its Applications. Spinus

Proceedings

Volume 22

Saint Petersburg State University

31 March — 4 April, 2025

Подписано в печать 25.03.2025. Формат $84 \times 90^{1/16}$.
Бумага офсетная. Гарнитура Таймс. Печать цифровая.
Усл. печ. л. 15,52. Тираж 150 экз. Заказ № 2423.

Отпечатано в Издательстве ВВМ.
196247, Санкт-Петербург, ул. Бассейная, д. 5, литера А, кв. 52.